Femtosecond pulsed laser deposition as a novel route for nanocomposite photonic materials on silicon

Matthew J. M. Murray

Submitted in accordance with the requirements for the degree of
Doctor of Philosophy

The University of Leeds
School of Process, Environment, and Materials Engineering
Institute for Materials Research

September, 2013

This thesis is dedicated to my incredible partner,

Amanda Kaplanski

The following publications all relate to the results of chapter 4.

List of publications:

(1) *M. Murray, T Toney Fernandez, B Richards, G Jose and A Jha, "Tm^{3+} doped silicon thin film and waveguides for mid-infrared sources", Applied Physics letters,* ***101****, (14), 141107-141107-4*

(2) *M. Murray, G. Jose, B. Richards and A. Jha, "Femtosecond pulsed laser deposition of silicon thin films", Nanoscale Research Letters,* ***8****, (1) 272*

(3) *M. Murray, G. Jose, T Teddy Fernandez, B. Richards and A. Jha, "Fabrication of surface channel waveguides on a thin film of rare earth doped silicon", TMS2013 Supplemental Proceedings, 11-15*

The candidate confirms that the work submitted is his own and that appropriate credit has been given where reference has been made to the work of others.

Acknowledgements

Throughout the course of my PhD, there are many people who have offered time, effort and support to assist my research endeavours. I would therefore like to offer my most humble of thanks to them, for without their assistance, in its many forms, this work would not be possible.

Firstly, I would like to thank my supervisors for their guidance and support throughout my PhD. I must especially thank Prof. Gin Jose for his constant belief and dedication as well as offering countless words of motivation.

Although I cannot individually thank all who have assisted me during my PhD, there are those who deserve particular thanks. For repeated guidance in the practical application of electron microscopy I would like to thank all the LEMAS staff. For considerable support in X-ray diffraction, Dr. Tim Comyn has gone above and beyond the call of duty. For conducting the femtosecond laser micromachining, I owe a great deal of thanks to Dr. Toney Fernandez. Within the photonics group, Mohammed Javed is deserved of enormous thanks for his dedication to fixing just about everything. Perhaps most of all, I must thank Dr. Billy Richards, who has provided considerable assistance in experimentation as well as countless discussions on various principles regarding optics and rare earth elements.

Above all however, I must thank my family, friends and incredible partner Amanda Kaplanski who have collectively propelled me through the tough times, right up until the final hour.

Abstract

Femtosecond pulsed laser deposition (fs-PLD) has been investigated extensively over several decades, yet none have considered interactions between the intensely hot, high velocity plasma species ejected from a target material with a heated substrate. For this reason, the interaction of a femtosecond pulsed laser generated plasma with a given substrate is investigated in this thesis for the development novel functional materials.

The fabrication of Tm^{3+} and Er^{3+} doped silicon thin films is presented with room temperature photoluminescence peak emission wavelengths of 2.04 μm and 1.54 μm, respectively. Characterisation of these and undoped films however reveals a difficulty in engineering the materials. This approach to materials fabrication does however have potential to engineer multifunctional surfaces for a variety of applications.

A new approach to fs-PLD is therefore sought through the heating of a silicon substrate to 570 °C and ablating a rare earth doped tellurite glass target to deposit upon it. This is found to result in the sequential growth of ZnTe, Te, ZnO and rare earth doped crystallites in a modified surface layer. This is explained based upon thermochemical calculations and observations in literature. The structural characteristics of these materials are determined by scanning electron microscopy as well as transmission electron microscopy, while the crystallography is studied by selected area electron diffraction and X-ray diffraction.

Fluorescence characterisation of these surface materials formed upon silicon reveal emission from ZnO, ZnTe, Tm^{3+}-doped crystallites and Er^{3+}-doped crystallites. Fluorescence spectroscopy of these materials shows characteristic emission in the visible and near-infrared.

Table of Contents

List of Tables

List of Figures

List of Abbreviations

A, B, C and D	Coefficients of the heat capacity function
A.U.	Arbritrary units
Abreviation	Definintion
B_{hkl}	Broadening factor of an XRD peak corresponding to the miller (hkl)
BSE	Back-scattered electron
c_i	Weight fraction for species *i*
Cp	Constant pressure heat capacity
c-Si	crystalline silicon
D_{hkl}	Crystallite size as interpreted from an XRD peak of miller indices (hkl)
EDFA	Erbium doped fibre amplifier
EDX	Energy dispersive X-ray analysis
F	Laser fluence
FL	Flash lamp
fs	Femtosecond
FWHM	Full-width at half-maximum
G	Gas type used during the fabrication process
H	Enthalpy
K	Shape-factor asociated with the Scherrer equation
LA	Longitudinal accoustic phonon
LM	Laser micromachining
LO	Longitudinal optical phonon
MC	Monochromator
MIR	Mid-inrared
NIR	Near-infrared
ns	Nanosecon
P	Pressure
PD	Photodiode detector
PIPS	Precision ion polishing
PL	Photoluminescence
PLA	Pulsed laser ablation
PLD	Pulsed laser deposition
PLSM	Pulsed laser surface modification
PMT	Photomultiplier tube
RE	Rare earth
S	Entropy
SAED	Selected area electron diffraction
SE	Secondary electron
SEM	Scanning electron microscopy
sc	Single crystalline
T	Temperature

t	Fabrication duration, usually given in hours unless otherwise stated
TA	Transverse accoustic phonon
TEM	Transmission electron microscopy
TO	Transverse optical phonon
TPA	Two-photon absorption
TZN	Tellurium zinc sodium (Glass)
UV-Vis	Ultraviolet-visible, in reference to electromagnetic radiation
XRD	X-ray diffraction
z	Atomic number
Z	Average back-scattered emission coefficient
α	Absorption coefficient
Γ	Brillouin zone centre
Γ_A	zero-centre one-phonon mode of amorphous silicon
Γ_c	zero-centre one-phonon mode of crystalline silicon
δ	Diffusion coefficient
η	Back-scattered emission coefficient
η_i	Back-scattered emission coefficient for species *i*
θ	The Bragg angle used in relation to XRD
κ	Intensity ratio of the (0002) peak height to the (10-11) XRD peaks of ZnO
λ	Wavelength
$\bar{\eta}$	Average back-scattered emission coefficient

Chapter 1.
Introduction

There is a growing need for novel platforms for engineering multifunctional integrated photonic devices. The significant interest in silicon photonics has led to extensive investigations into its use in optoelectronics, which continues to diversify. Current methods of fabrication are still heavily routed in conventional semiconductor processing techniques and novel alternates are greatly sought after. It is therefore essential to develop new ways of engineering silicon photonic structures for current commercial and industrial interests.

1.1. Aims

The overall aim of this project is to explore the use of femtosecond pulsed laser deposition (fs-PLD) for the fabrication of silicon based optical and optoelectronic applications. The rare earth ions thulium (Tm^{3+}), erbium (Er^{3+}) and ytterbium (Yb^{3+}) shall play key roles in assessing this potential, due to their importance in the field. The first part of this study shall be directed toward the deposition of rare earth doped silicon thin films upon silica. These films shall be characterised and processed for potential application in photovoltaic and integrated optical devices. The former shall be investigated through the inclusion of Yb^{3+} in an absorber layer to enhance the efficiency of silicon based photovoltaic devices. The latter shall use femtosecond laser micromaching for mask-less processing of the thin films in order to form waveguide structures for integrated photonic applications.

The second part of this thesis shall investigate the use of silicon as a substrate for high temperature deposition of rare earth doped tellurite-based glass using fs-PLD. Specifically, this shall consider the interactions between the plasma phase and the heated substrate material; an area of considerable neglect in literature. Moreover, attempts shall be made to observe the penetration of depositing material into the substrate. This effect shall be probed by way of variations in the substrate temperature, laser fluence and gas pressure as well as its time dependence. This second part shall not necessarily be directly application driven, but a piece of

fundamental research into the plasma-substrate interactions and how this may be exploited for future endeavours.

1.2. Objectives

- To prepare silicon thin films, undoped and doped with rare earth ions by femtosecond pulsed laser deposition (fs-PLD);
- To identify experimental parameters which can achieve reduced porosity and surface roughness in these thin films;
- To process rare earth thin films using femtosecond laser micromachining for the formation of surface channel waveguides and study its applicability to the field;
- To produce *pn*-junctions of silicon thin films for use as photovoltaics, both doped and undoped with rare earth ions and electrically characterise them
- To deposit tellurite-based glass onto heated silicon substrates in a variety of experimental conditions;
- Determine if any penetration has occurred in these samples and expand on the theoretical basis for its occurrence;
- To determine links between the experimental conditions and the plasma-substrate interaction as well as how these may be utilised for applications;
- Characterise the optical properties of the rare earth dopants and any other optically active phases detected.

1.3. Thesis outline

Chapter 2 provides a detailed review of the literature related to this thesis. This includes the fundamental nature of the fs-ablation mechanism, the growth of thin films, comparisons between fs-PLD and various other techniques, discussions on all materials described in this thesis, including rare earth ions and their optical properties. Chapter 3 provides an overview of the various experimental techniques used for fabrication and characterisation of the materials produced during this thesis. A short description of their function is provided along with the procedure employed for their use.

Chapter 4 details the fabrication of silicon thin films by femtosecond pulsed laser deposition, including their doping with the rare earth ions Er^{3+} and Tm^{3+} with optical characterisation provided. The fluorescence characteristics of these ions are described as well as the structural features of the deposited films.

Chapter 5 describes the short ablation ($\leq$1 hour) of Tm^{3+}-doped tellurite glass and its modification of the surface of a single crystalline silicon substrate. These films demonstrate the formation of ZnTe and Te crystallites in the subsurface of the Si substrate. Chapter 6 builds upon the conclusions of the previous chapter where 4 hour fabrication times are used and the growth of extensive ZnO and Tm-rich silica phases are observed. Chapter 6 then offers the first insight into the engineering the ZnO crystallites by the alterations of the gas type used.

Chapter 8 characterises the various optically active materials of the surface modified samples, including Tm^{3+}, Er^{3+}, ZnTe and ZnO. The optical characterisation of Tm^{3+}-ions is also used to infer the site-symmetry within the host crystal system. Chapter 8 then concludes the work of this thesis and suggests further work in this area.

Chapter 2.
Literature Review

2.1. Light-matter interactions

The most fundamental physical aspect to this thesis is the interaction between light and matter; it is therefore paramount to adequately define this phenomenon at the outset. Light can thus be considered as a wave phenomenon composed of electrical and magnetic fields, situated perpendicular to each other and the propagating direction. This defines light as electromagnetic radiation where both fields oscillate with space and time. A quantum system in the path of such radiation will thus experience these oscillations. The wavelength of oscillations for light described as being ultraviolet (UV), visible or infrared (IR) is much larger than that of atoms, ions, molecules and nanoparticles. Collectively, these shall be referred to as quantum systems. Thus the oscillations with respect to space become negligible and light is thus experienced as spatially uniform electrical and magnetic waves oscillating with time.

Upon illumination of a quantum system with such radiation, electrons will receive energy from the incident beam. This energy is acquired primarily through interaction with the oscillations of the electric field but also, to a lesser extent, with the magnetic field. If the frequency of light is close to one of the natural frequencies of the quantum system, the interaction is defined as resonant. A band of frequencies exists around this central resonant frequency and energy transferral from one such frequency to the quantum system is termed absorption. Should these frequencies not match, they are described as non-resonant, yet small energy transferrals may still occur. This small amount of energy is often lost rapidly and isotropically, as such is defined as light scattering. For a system, micro- or macroscopic, the remaining light either unabsorbed or scattered in the same direction as the propagating direction is called transmission.

The polarizability is defined as the degree to which the systems electron cloud is influenced by the electronic component of light. Thus, polarizability is a

ratio of the induced electric dipole moment of the electron cloud and the applied electric field strength from the electric component of light. For relatively low light intensities a linear correlation between these two factors is observed, however for high intensities, such as for a laser pulse, nonlinear effects can occur.

Nonlinear optical effects are observed as a trend in which polarization of the material responds nonlinearly to the electric field component of light. Specific processes which may occur in such regard are second-harmonic generation, where two photons of the same wavelength constructively interfere. This produces a photon of half the wavelength (double the frequency and therefore energy). Such interactions are very weak for a common broadband light source, however with high intensity lasers such processes become dominate. Other effects include the bound electronic Kerr effect, in which high intensity light in the transparent region of an illuminated material experiences induced changes in the absorption coefficient and refractive index.

For an absorption event, an induced electric dipole moment is created as with polarization, however the magnitude is much greater. The release of electromagnetic radiation corresponding to the energy associated with this induced electric dipole moment is named emission or luminescence. Should the electric dipole moment have been induced by another photon, the subsequent re-emission is often called fluorescence. The excess energy may instead be delivered to the structural environment via the emission of lattice vibrations, called phonons. The emission of photons from such a system is defined as radiative relaxation. If the release of energy occurs through the emission of phonons, it is defined as non-radiative relaxation.

A third process may also occur however, whereby the energy of the induced electric dipole is transferred to that of a nearby system. Such processes are therefore described as energy transfer and the likelihood of the event occuring is very much dependent upon the resonance of the dipole energy to the natural frequency of the recipient system. As these two magnitudes deviate from one another, phonon scattering must occur in order for energy to be conserved. This may include the generation of phonons due to an excess of energy, or a scattering event, whereby single or multi-phonon absorption is required to fill the energy gap. As with the initial absorption from electromagnetic radiation, the probability of such an energy

transfer process occurring is greater when a single phonon is required. As the number of phonons required increases, this likelihood decreases further.

2.2. Femtosecond pulsed laser deposition

2.2.1. Ablation and plasma formation

The interaction of a femtosecond (10^{-15} s) laser pulse of sufficient fluence (~ 10^{10} to 10^{16} W/cm^2) [1] with matter is known to ablate a hot dense plasma from a targets surface [2–4]. This generation of plasma has thus found applications in a wide variety of materials processing and fabrication techniques. The nature of the plasma itself is found to be highly reflective of the initial ultrafast laser parameters and considerations of the target material [5]. Laser-matter interaction and how this pertains to plasma ablation is thus of great importance for a coherent understanding of deposited material.

A femtosecond laser pulse is found to interact with a target material in a manner quite dissimilar to that of other pulsed laser ablation techniques, such as for a nanosecond (ns) pulse. The primary difference between these two pulsed laser ablation (PLA) techniques is their duration relative to the relaxation mechanisms for a target material. The transferral of energy from a delocalised and highly energetic electron to a lattice is of the order of 1 ps [6]. A femtosecond laser pulse is thus classified as *ultrashort* or *ultrafast* due to it being faster than any possible relaxation mechanism for an excited electron. The major relaxation processes are listed as electron-to-lattice energy transfer, heat diffusion and hydrodynamic diffusion[7,8]. Thus during the entirety of the fs-excitation and ionisation event, atomic motion is negligible. Longer laser pulses such as nanosecond and picoseconds pulses are thus classified as thermal ablation techniques [8–10] as these interact with a surface modified by the ‘front’ of the laser pulse.

The absorption of the fs-pulse occurs in a very thin layer, defined as the skin layer, and is typically found to be a few tens of nanometres thick [1]. For a typical indirect bandgap semiconductor such as silicon, this would appear to be much too short due to its absorption coefficient [11]. The reason this is shortened to such an extreme is due to the dominant nonlinear absorption mechanisms for the extreme

laser intensities of a fs-pulse [7]. Two-photon absorption (TPA) is a major component of fs-laser absorption. For TPA, the absorption coefficient of a material is found to increase with the square of the light intensity. As with many aspects of fs-PLA, many of the mechanisms governing ablation are contested. This includes avalanche ionisation [8] which was believed to play a fundamental role in the absorption mechanism, has recently been challenged [12]. This is found to be true for many aspects of the excitation and ablation mechanisms of fs-PLA [7,13].

Nonlinear absorption provides the fundamental reasoning for the intense variety of possible target materials which can be used for fs-PLA. Such materials include semiconductors [14–16], glasses [17,18], metals [19,20], ceramics [21,22], polymers [17,23] and biological materials[24,25]. This makes fs-PLA a highly versatile physical vapour deposition technique.

Following the initial deliverance of energy to the electrons of the skin layer, the subsequent electron-to-lattice energy transfer process can occur. The effective temperature of electrons following the fs-laser energy transferral is determined to be several thousand Kelvin. As an example, Gamaly *et al* [7] determined that an 800 nm fs-laser focused onto the surface of Al at a fluence of 0.5 mJ cm^{-2} would have a maximum electron temperature of 3520 K. Note that 0.5 mJ cm^{-2} is low for deposition experiments. Laser fluence, F, can be defined for a given laser energy, E (J), focused upon an area A (cm^2) through the following relationship:

$$F = {}^{E}/_{A} \qquad \textbf{(2.1)}$$

For the ejection of atoms and ions from a surface, sufficient energy must be delivered to an atom in the lattice in excess of the binding energy. This process occurs very shortly after the electron-to-lattice energy transfer process, due to the enormity of energy contained within the skin layer. The minimum energy required to initiate this type of ablation constitutes the threshold for ablation. For silicon this has been determined to be 0.1 J cm^{-2} for an 800 nm laser [26] and as the fluence is increased from this point, the yield of ions will also increase [27]. Note also that the depth from which ablation will occur also increases with increasing fluence [28].

As the laser fluence is increased so as to approach the energy required to cause complete atomisation (i.e. a change in state to the gas phase), nanoparticles are ablated [5,20,27,29]. Nanoparticles are believed to be formed in the highly dense plasma region where the focal point of the laser was positioned [27]. The

nanoparticles form very rapidly via inelastic atomic collision [7] and do not grow during progression through a gas phase or vacuum. This is at odds with the growth of nanoparticles via ns-PLD [30] which are formed in the gas phase. The proximity of formation of nanoparticles to the surface following fs-laser excitation originally led researchers to suspect the particles formed directly from the surface [31]. Only very recently have satisfactory assessments linking numerical calculations and computer simulations to empirical data been achieved [1,7,28].

Upon further increases in the laser fluence, one may expect liquid droplets in the plasma plume [7,27]. Their formation is believed to stem from thermal interactions due to spatial non-uniformity in the incident laser intensity upon a target surface [32]. This results in low-threshold material transformations such as amorphisation [33].

2.2.2. Deposition and thin film growth

The plasma phase emanating from the target surface very much dictates the nature of the deposited material, which is directed by the fs-laser parameters. The deposited material can be made to pass through a vacuum, which is common [4,34,35], or a background gas [36]. Deposition in a dilute gaseous atmosphere however is preferable for the growth of thin films [37] in order to achieve a continuous surface layer.

Garcia *et al* [38] identified a significant variation in the stoichiometry of ablated material to that of the target. This too is reflected in the stoichiometric mismatch in the deposited material [27]. For binary systems with 1:1 composition, Garcia identified variations in the elemental ratio as high as 50:1 for ablated material. These ratios are found to vary from one system to another, yet demonstrate an independence from the laser fluence. The stoichiometric mismatch is thus attributed to the dissimilar ionisation energies of the elemental constituents of the target.

The primary interest in literature is still directed toward the fundamental understanding of the ablated material, with few groups progressing with deposition experiments [4,27,39,40]. There is still limited knowledge in the various fundamental aspects governing deposition of material upon a substrate. This includes deposition in a background gas [41], the distribution of depositing material [42] as well as interactions between the depositing material and a substrate. These

aspects of fabrication are of great importance of the progression of the technique and can be applied to the production of devices.

2.3. Alternate fabrication techniques

2.3.1. Nanosecond pulsed laser deposition (ns-PLD)

Nanosecond pulsed laser deposition (ns-PLD) operates within similar operating procedures to that of fs-PLD [43], involving the use of a vacuum chamber and described through similar laser parameters. The longer pulse duration however leads to markedly dissimilar ablation mechanics. This leads to the formation of nanoparticles at a much later stage in the plasma expansion, forming through a nucleation event, dependent upon the background gas pressure [44]. Much of this difference arises from the difference between the pulse duration and the electron cooling time [13]. For a femtosecond pulse, this is much shorter than the cooling rate. This equates to a significant disparity in the electron and lattice temperatures following the end of the pulse. A nanosecond pulse however is also considerably longer than the electron cooling rate, this leads to an electron-lattice coupling, in which equilibrium is met during laser irradiation. Ns-PLD is therefore a thermal ablation process as the ns-laser pulse is used to heat the target material so as reach the vaporisation temperature of the target.

Ns-laser intensities are considerably less than for fs-pulses thus the effect of non-linear absorption is negligible in relation [7]. For this reason, the laser wavelength used is often in the UV. For example a ArF laser, operating at 193 nm is common [45], so as to ensure ablation from materials which do not absorb longer laser wavelengths.

The ablation of metals by ns-PLD first results in a heating of the focal area to the melting point, which continues as the pulse continues, ultimately reaching the vaporisation temperature and triggering ablation [46]. Much of the energy delivered to the material is lost through thermal diffusion to the bulk during the laser pulse duration. The extent of this thermal diffusion zone is found to extend between 10 μm and 1 mm, where fs-lasers tend not to extend further than a few hundred nm [47]. This thermal expansion throughout the region surrounding the laser focal point is often sufficient to cause phase changes, this is evident as the ‘splashing’ of large micrometer sized particles [6,10,48]. This is found to be particularly common for

high energy ns-laser ablation. This not only has dire consequences for the prospects of micromachining of surface, but also in the repeated use of a singular target for ablation.

The composition of the ablated plasma is also found to be quite dissimilar to that of fs-laser generated plasma. Zhang *et al* [49] studied this extensively for various target materials. They identified that ns-laser generated plasma has a much lower concentration of high energy ions and low charge ions when compared to fs-albation. Furthermore, the fs-laser is much more efficient at initiating ablation at lower laser energies and lead to considerable less residual surface damage following ablation.

Based upon this survey, fs-LA would be more appropriate for:

(1) Encouraging the modification of a substrate surface with high energy plasma pulses

(2) Allow a more varied range of target materials for future endeavors based upon this research,

(3) The formation of waveguide structures upon a targets surface,

(4) Reducing the abundance of large microparticles caused by thermal ablation.

Fs-LA is therefore more appropriate for the objectives of this thesis.

2.3.2. Ion implantation

Ion implantation is a method doping substrates with ions accelerated using a high electric field to energies between 1 to 3,000 keV [50]. The energy selected is based upon two primary criteria: the depth of penetration required and the nature of the host material. Soft materials, such as polymers, would require a comparably lower accelerating voltage than a semiconductor for example. Ion implantation is the *de facto* industry standard for semiconductor processing. For example the doping of silicon to form *pn*-junctions [51] with boron, arsenic etc.

Ion implantation uses single elemental ion sources for implantation; meaning only one ion is implanted at a time. A noteworthy characteristic of ion implantation, relevant to this thesis, is the depth profile of dopants implanted into a substrate. The dopants implanted into a substrate by ion implantation follow a first order Gaussian

distribution, or more accurately a 4-point Pearson (IV) distribution [52]. Ultimately, this translates to a non-uniform ion distribution with respect to depth. In order to correct for this, multiple implants must be undertaken to reach a level of concentration continuity with respect to depth. These implants are done at a range of accelerating voltages so as to incorporate a spread of peak dopant concentrations at different depths [53]. This creates a more uniform dopant distribution profile and remains the only means of doing so. Ion implantation was also commonly used in the early experimentation to dope silicon with rare earth ions [54].

Following implantation, the substrate must be annealed so as to alleviate the damage to the crystal structure and relieve stresses in the doped material [55,56]. These damage centres include the formation of vacancies and dislocations [55],

Ion implantation has been intensely studied for many decades now, however many of the difficulties raised in this review may be alleviated through a method associated with fs-LA. This would allow co-implantation and the prospects of achieving a uniform implantation profile can be investigated.

2.4. Rare earth ion doped materials

Rare earth ions encompass all lanthanides and actinides as well as yttrium and scandium, however it is common to refer to only lanthanides as rare earths [57–61]. For the purposes of this thesis, only the lanthanides Er^{3+} and Tm^{3+} are considered due to their desirable optical properties. One of the defining characteristics of rare earth ions is the isolation of individual absorption and emission bands specific to each ion. When doped in a crystal or salt, these bands are composed of a group of narrow lines, while in a disordered host, such as a glass, the lines become broadened to a singular band. For a given absorption spectrum, each of the lines and bands are found to correspond to electronic transitions within the 4f-electron shell. Each line within that band corresponds to a transition between a crystal-field level of an excited state to that of a lower level, often the ground state. Such transitions are otherwise forbidden by the Laporte rule, however, when the ions are coordinated in some way (in a crystal, glass etc), a perturbation on the 4f electron cloud partially allows such transitions [62].

The transitions themselves are found to occur between two $^{2S+1}L_J$ free ion levels, or manifolds, where S is the spin quantum number, J is the total angular

momentum and L is the orbital angular momentum. The collation of these values thus describes the energy state of electrons in the 4f-electron shell.

The sharpness of the transitions and the relative independence of their frequency centre from one host to the next is due to the effective shielding of the 4f electrons by the outer 5s and 5p shells. This results in very weak variations between hosts, however spectroscopic differences are visible due to specific influences upon the electron cloud. The nature of the transitions can be interpreted in one of tree forms:

1. Induced electric dipole transition – This describes the majority of transitions within lanthanide ions and is described by Judd-Offelt theory [63]. These transitions are induced by interactions with the electronic component of light.
2. Magnetic dipole transition – Such transitions are often much weaker than induced electric dipoles, but also express much weaker sensitivities to the host material. A given transition may possess both magnetic and electric dipole character, as with the Er^{3+}: $^4I_{13/2} \rightarrow {}^4I_{15/2}$ [64].
3. Electric quadrupole transitions – These transitions have not been conclusively observed as they are much weaker than magnetic dipole transitions. Hypersensitive transitions, as will be described, have the same selection rules of quardupolar transitions [65].

Although the influence of the host upon the spectroscopic features of rare earth ions is in some ways minute, due to the effective shielding by the 5s and 5p electron clouds, it is not negligible. Significant influences from the site-symmetry (crystal field splitting) are noted upon certain transitions of lanthanide ions [66,67]. A particularly interesting transition in this regard is Tm^{3+}: $^3F_4 \rightarrow {}^3H_6$. This transition is often observed through the excitation of the $^3H_4$ level, depicted in Figure 2.1. This interaction involves an energy transfer process defined as cross-relaxation between the excited Tm^{3+}-ion and a neighbouring Tm^{3+}-ion in the ground state. The cross-relaxation mechanism thus brings both ions to the $^3F_4$ manifold. Radiative decay from both ions at the $^3F_4$ manifold thus results in the emission of two photons following the initial absorption of a single, higher energy photon. This transition is also considered to be hypersensitive, whereby an increased sensitivity to the coordinating ligands can result in dramatic increases in the relative emission intensity to other possible transitions. Hypersensitive transitions are always induced electric dipole transitions [65] and occur only within certain site-symmetries [68]. A

great deal of variability is also found in the spectral lineshape and peak position of absorption and emission of this transition [69–74].

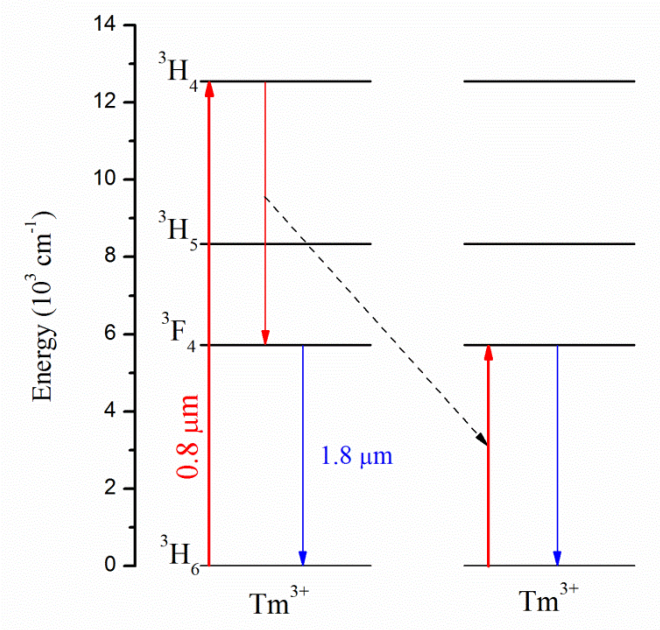

Figure 2.1. Tm^{3+} energy level diagram demonstrating the cross-relaxation mechanism and subsequent decay from the $^3F_4$ manifold. Approximate excitation and emission wavelengths are also illustrated.

2.4.1. Rare earth doped silicon

There are several reasons rare earth doped silicon materials and devices are seen as attractive. Firstly, the coupling of the infrared emission properties of rare earth ions with the transparent window in single crystalline silicon between ~1 and 7 µm makes them a suitable pair. The primary interest however is due the indirect bandgap of silicon making it a very poor emitter of light. Doping with rare earth elements is therefore viewed as a route to introduce optically active centres which may be electrically or optically pumped [54,73,75–79]. This is whilst maintaining the highly desirable material and electrical properties of silicon.

The primary applicability of rare earth doped silicon is therefore in optical and optoelectronic devices. The combination of these two fundamental aspects of modern technology: optical and electronic, is of great interest for the development of mobile and increasingly miniaturised and efficient devices. Similarly, the exceptional optical properties of rare earth ions being utilised in erbium doped fibre amplifiers (EDFA) [80]. These devices have been utilised for the deployment of

intercontinental fibre optics, minimising the degradation of the propagating signal with low power consumption [81]. The combined use of silicon and rare earth elements can be utilised in a similar manner and forms the basis of motivation for work in this field.

It has been demonstrated through numerous publications however, that although silicon does not absorb the emitted infrared light, it can quench the excited states of rare earth ions. This occurs through an energy backtransfer process in which the long lifetime of excited state manifolds within a rare earth ion can efficiently transfer energy to the silicon system. This process is defined schematically in Figure 2.2 for the common example of Er^{3+}-doped silicon [75,82]. The relevant manifolds of Er^{3+} are provided, including the $^4I_{15/2}$ ground state, the $^4I_{13/2}$ excited state of interest and the pumped $^4I_{11/2}$ manifold. There are further manifolds beyond this up to the 5d states which can be found in full alongside all other rare earth ion energy level diagrams in reference [83]. For the Er^{3+}:Si system [82], excitons are found to be trapped in states created either by the hybridisation of Si conduction band states with Er^{3+} 5d states, or due to an impurity induced level. One can therefore state that the Er^{3+}-manifolds are coupled to the band states of the Si system. Excitation of the Er^{3+} manifolds can occur via the recombination of these bound excitons in an Auger process. Er^{3+}-ions can then decay radiatively, where the 1.54 μm luminescence is observed.

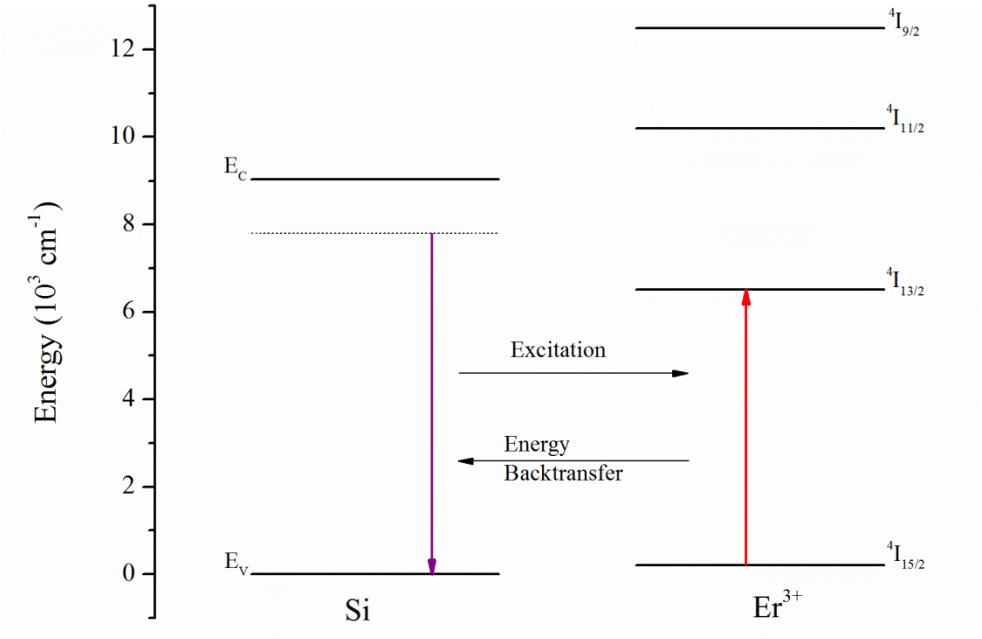

Figure 2.2. Energy level diagram depicting the excitation and energy backtransfer processes possible between Er^{3+} and trap states within the crystalline silicon bandgap. E_c and E_v represent the conduction and valence band edges of Si.

This process is found to dominate at low temperatures (<150 °C) [75] and above this, rapid quenching of the Er^{3+} excited states is identified [84]. This is spectroscopically observed as dramatic decreases in the luminescence intensity and the decay lifetime. The quenching process has been demonstrated to be a direct reversal of the earlier excitation process [82], whereby energy transfer from the excited Er^{3+}: $^4I_{13/2}$ state to a trap centre occurs. Hence the process is described as energy backtransfer. The temperature sensitivity of this process is due to the contributions of phonon absorption to the energy transfer process. Thus one observes both a decrease in the overall intensity, but also a decrease in the observed lifetime. Because the probability of this backtransfer increases over time, the longer the Er^{3+}: $^4I_{13/2}$ states remain stable (i.e. do not decay), the greater the probability of backtransfer occurring. Thus one observes an 'induced' shortening of the lifetime.

Similar energy transfer processes have been identified for other rare earth doped silicon materials, such as Tm^{3+} [73]. Although improvements on the spectroscopic properties are quoted in literature, the luminescence intensity remains heavily quenched and lifetime measurements are rarely, if ever quoted due to the difficulty in their acquisition [85].

In order to overcome these material limitations, novel concepts such as rare earth doped silicon rich silica were conceived. These materials are described as

dispersed silicon nanocrystals in a silica glass matrix doped with rare earth ions. The precise location of the rare earths is often difficult to define, however room temperature luminescence has been observed and quantified [79]. Due to the glass matrix used in these experiments however, electrical excitation is not feasible and thus is limited to optically pumped applications.

Another alternative to the crystalline silicon host system is that of amorphous silicon [78,86]. An associated increase in the solubility of the rare earth ions in amorphous silicon is also noted [78]. The first report of luminescence from Er^{3+}-doped amorphous silicon [86] suffered greatly from defect mediated quenching of the excited states as well as poor electrical properties. Subsequent work however identified improvements in both regards through the hydrogenation of the material [87]. Similarly, the inclusion of oxygen aided in the enhancement of the optical properties at room temperature at the expense of the electrical properties [88]. Masterov *et al* identified that in oxygenated Er^{3+}-doped silicon, the Er^{3+}-ions are coordinated by oxygen ligands, akin to the Er_2O_3 system.

2.5. Semiconductor materials

2.5.1. Silicon

Silicon is certainly the *de facto* standard of the semiconductor industry. Its use in virtually every aspect of modern day technology makes it the most important semiconductor materials available. Single crystalline silicon can be grown by the well-established Czochralski process [89]. The ingots which are produced can then be cut into wafers and subsequently polished to extremely high quality finishes. This produces wafers of extremely high quality and purity suitable for applications such as solar cells [90] to microelectronics.

2.5.2. Zinc oxide

Zinc oxide (ZnO) is a highly versatile material, with applicability in personal care [91], solar cells [92], piezoelectrics [93], light emitting devices [94] and for space-based devices [95]. One of the most interesting properties of ZnO is its ability

to form such a wide array of crystal structure, which can be controlled to an extremely high degree [96–98].

ZnO is a wide 3.4 eV direct bandgap group II-VI semiconductor with a large exciton binding energy of 60 meV [99]. Inherently, these semiconductors are n-type, which is believed to be due to hydrogen doping [100]. It is also noted that the formation of p-type ZnO is somewhat difficult, such as through the inclusion of Na [101].

ZnO crystallites have been fabricated by a variety of techniques, each with specific methodologies for the control of the growth mechanics [102–105]. ZnO nanocrystallites have also been fabricated via fs-PLD when grown at high temperature on a sapphire substrate [106].

An extensive body of work has been dedicated to developing ZnO crystallites for application in a variety of devices. Its true applicability is however still limited by current alternatives, such as silicon for electronics and superior alternatives such as PZT for piezoelectric materials. It is therefore an ideal material for study through novel fabrication methodologies.

2.5.1. Zinc telluride

Zinc telluride is a wide 2.26 eV direct bandgap group II-VI semiconductor. This particular compound, like other Zinc chalcogens (e.g. ZnS and ZnSe), is known to have a high iconicity of 0.49. This has made ZnTe rather difficult to fabricate through other methodologies, due to significant site vacancies and interstitials as well as a sensitivity to strain in the crystal lattice [107]. ZnTe is highly desirable for optoelectronic devices due to the visible luminescence centred at approximately 550 nm [108–110]. Similarly, ZnTe has also been studied extensively for photovoltaics [111] and is commonly used in conjunction with CdTe due to the similarity in the lattice spacings [110]. Furthermore, its use as a terahertz (THz) detector makes it particularly attractive for photonic applications [112].

Chapter 3.
Experimental Procedures

This chapter describes the various experimental procedures adopted during this thesis for both fabrication and analysis. Detailed discussion of the procedures adopted during experimentation is also given. Moreover, fundamental discussion is given to both the use of certain analytical techniques as well as their applicability

3.1. Femtosecond pulsed laser based fabrication techniques

3.1.1. Femtosecond pulsed laser deposition (fs-PLD)

Samples are fabricated inside of a vacuum chamber using a 100 fs-pulsed 800 nm Coherent Ti:sapphire LIBRA laser operating at a 1 kHz repetition rate. Before the laser enters the sample chamber, it passes through a half-waveplate and then an adjustable polarizer. Thus, as the polarizer is adjusted (rotated) the laser energy can be precisely controlled while the average laser energy is measured with a Coherent LabMax-Top laser power and energy meter. The laser is focussed into the vacuum chamber through a transparent window, whereby it is directed at a 30° angle of incidence to a targets surface. The target material is positioned on a raster table, whereby it is both rastered and rotated in accordance with a pre-programmed procedure. This ensures the laser can ablate the target surface evenly, whilst minimising excessive material removal from a singular area. The experimental set up adopted for fabrication and thus far described for fs-PLD is given schematically in Figure 3.1.

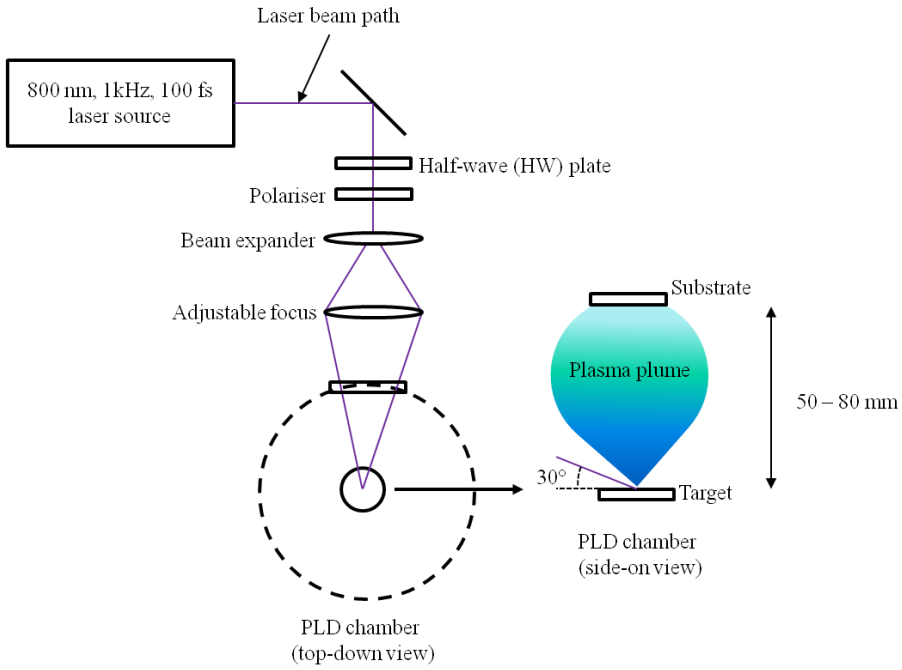

Figure 3.1. Experimental set up for fs-PLD. The purple line indicates the path of the laser.

During fabrication, the target rastering process runs continuously while a substrate is positioned directly above the target surface at a set distance of 50 to 80 mm. The substrate can be heated through a programmable heating element giving control of heating rate (up to 50 °C per minute) to a maximum temperature of 800 °C. The temperature is read through a digital output from a thermocouple fitted to the top of the substrate. Approximately 1 cm below the substrate is a shutter which can be used to block plasma ablation from contacting the substrate at any stage.

The sample chamber has 6 target holders, giving the option for multilayered thin film architectures, where separate rastering programmes can be applied to each in order to accommodate for different target dimensions.

Prior to loading the substrate into its holder, it is cleaned using a lens cleaner commercially sourced from Thorlabs™, first using distilled water, then once dry, it is cleaned with methanol and repeatedly inspected until no dust or debris is visible on its surface. After the final clean, it is immediately loaded into the PLD chamber.

If the target material is a silicon wafer, as used in chapter 4, its surface is often given a single wipe with a lens cleaner doused with methanol. When a series of consecutive samples are being produced from a single target, the target is often

left in the target holder so as to minimise any contact and possible contamination of the surface.

As described in section 2.2.1, the nature of the ablated material is heavily dependent upon the set laser fluence. For this reason, the spot size and laser energy must be as tightly controlled as possible to ensure continuity in the fabrication process from one sample to the next.

Due to the analogue control of focussing for the fs-laser beam in the PLD system, it is important to maintain stringent control mechanisms in setting up each experiment so the spot size can be approximated as best as possible. In order to do this, each target is vetted for its surface texturing, i.e. if the rastering is not controlled precisely, a considerable dip in the centre due to ablation can appear. This tends to happen after an extensive number of passes with the laser. Its onset can be delayed by optimising the rastering to ablate from the outer regions of the targets as much as possible. Should a target develop a concave centre as described, considerable fluctuations in the laser spot size and the direction of the ablating plume can occur during an experiment. This can be extremely detrimental for the continuity of the samples produced and must therefore be avoided. Should a concave centre develop on a target, it is either polished in order to smooth it out, or is disposed of. Most often the target is polished with 2500P or 1200P SiC paper as a preventative measure before such surface features can develop. This effect is particularly troublesome for targets made by pressing a powder under several tons to from a pellet. Due to the highly porous nature of the pellets, it can easily crumple and so prohibits polishing; this results in a rapid onset of a concave centre and so only one experiment can be conducted with a single pellet before a replacement is required.

For ensuring continuity with regard to the spot size at the start of every experiment, a qualitative approach is taken. Firstly, the laser is set to a very low energy (typically 20 μJ) and with the chamber open and the target rastering started, the laser shutter is opened so as to trigger ablation. The focussing is then adjusted where the laser spot will appear as a white dot, visible with laser safety goggles on. Once the dot is visible, the laser energy is lowered again through adjustment of the polarizer, usually to 10 μJ. The focussing is again adjusted until a white dot is visible. This process is repeated until the spot is no longer visible for sufficiently

low laser energies. This ensures that the spot size is set to its minimum and should be so for each material utilised. Moreover, this ensures that adjustments to the fluence can be made via alterations to the laser energy alone and is the only foreseeable way to overcome this instrumental limitation.

This of course does not correct the problem entirely as material would still be removed from the surface during fabrication and thus altering both the spot size and plume dynamics. A means of compensating for this would be continual monitoring of the ablated plasma plume via wavelength-, time- and space-resolved optical techniques with at least a 100 ns resolution [27]. In addition to this, a feedback mechanism would also be required to automatically adjust the focussing accordingly. An *in situ* optical spectroscopy technique such as this could infer the relative velocities of the ablated material as well as the relative yield of ionic ablated material, nanoparticles and microparticles. Such data can then directly feed into subsequent analysis with tremendous benefits for understanding a given experiment. It is important to note that this still does not correct for the alterations in the surface topography and possible laser induced phase changes to the target itself [113] in addition to laser-induced changes to the target surface stoichiometry . The removal or reduction in these laser-induced surface modifications is not something that can be done *in situ* and therefore must be integrated into ones understanding and expectations of the fabrication process and any given experiment.

After the initial preparation stages, the PLD chamber is evacuated to a vacuum of 5×10^{-6} Torr or higher, whilst the substrate is heated to 300 °C for 30 minutes at 50°C/min to degas it. Once the substrate has cooled to room temperature, a 400 Torr N_2 gas purge is done and the chamber is once again pumped down to its final base vacuum of 3×10^{-6} Torr or higher. Once reached, the chamber is pumped to a set pressure using the specified gas type. At this point, the substrate is once again heated to 300 °C for 30 minutes at 50 °C/min. For samples deposited onto a TEM grid, no substrate heating is carried out as this would melt the silver paint used to attach them to the substrates surface.

Once the substrate has cooled to room temperature, the deposition can then commence. Note that an additional 10 to 15 minutes is allowed following the room temperature measurement to ensure the sample is cooled sufficiently. The input duration of the deposition is entered into the computer system and final checks of

gas pressure, laser energy and temperature are conducted. The rastering processes are then initiated and the substrate shutter is engaged so as to block any plasma deposition. This allows for a short 2 to 3 minute ablation whereby the surface of the target can be cleaned of any surface contamination with the laser. This also allows for the plume dynamics to be inspected, ensuring the plume is stationary. This means that the target surface is flat and therefore suitable for ablation. The target rastering process can also be checked to a certain extent by ensuring the plume does not flicker. If the plume was found to flicker, or 'blink', it would indicate that the laser was no longer focused upon the target surface and would therefore require adjustment. Should any of these final checks fail, the chamber would be reopened and the experiment restarted after correcting them.

Once satisfied with the plume dynamics and an adequate clean of the surface was completed by the laser, the laser shutter is closed, the substrate raster started with the substrate shutter cleared and finally the laser shutter is reopened to start the experiment. This will run for the duration of the experiment, whereby multiple checks are conducted throughout the experiment. Approximately every hour, measurements are made of the laser energy, the gas pressure, the plume dynamics etc. Should the plume begin to blink, or the gas pressure drop (or the gas flow stop) or any other problem which would affect the results of the experiment, the experiment is stopped and restarted.

Upon completion of a successful experiment, the PLD chamber is vented to room pressure using N_2 gas. If the sample was heated, this is done after it has cooled to room temperature. The sample can then be removed, inspected and characterised.

3.1.2. Femtosecond pulsed laser surface modification (fs-PLSM)

The name applied to this method of fabrication, fs-PLSM, is used to distinguish between conventional fs-PLD applied in chapter 4, and that used in later chapters. Samples produced through this technique begin with a silicon substrate heated to 570 °C and TZN glass target (80 mol% TeO_2, 10 mol% ZnO, 10 mol% Na_2O and the addition of 3 wt% Tm_2O_3).

Silicon substrates are first cut to the appropriate dimensions so as to fit in the substrate holder, using a diamond scribe. This is best achieved by making a single inscription along a set line with a plastic ruler. One side of the inscription is then sandwiched between two silica glass slides and the opposite side is gently and repeatedly tapped across the surface. This eventually causes a very clean break along the inscribed line. The substrate sizes produced for this work are measured as 1 x 2 cm. The silicon wafers are undoped, single side polished, 0.5 mm thick and cut slightly off-axis to the {100} plane.

From this stage on, the preparation procedure is very much the same as that described in section 3.1.1, where a low energy laser raster check is done to adjust the beam path to only cover the target surface. The laser energy can then be lowered so the minimum spot size can be found and set. Furthermore, all samples have a set target to substrate distance of 70 mm and a pressure of 70 mTorr. This is used to standardise the plume dynamics.

Once this second 30 minute degassing stage is completed, the sample is heated to the desired temperature, whereby a set heating regime such as the one depicted in Figure 3.2 is followed for the entirety of the fabrication process.

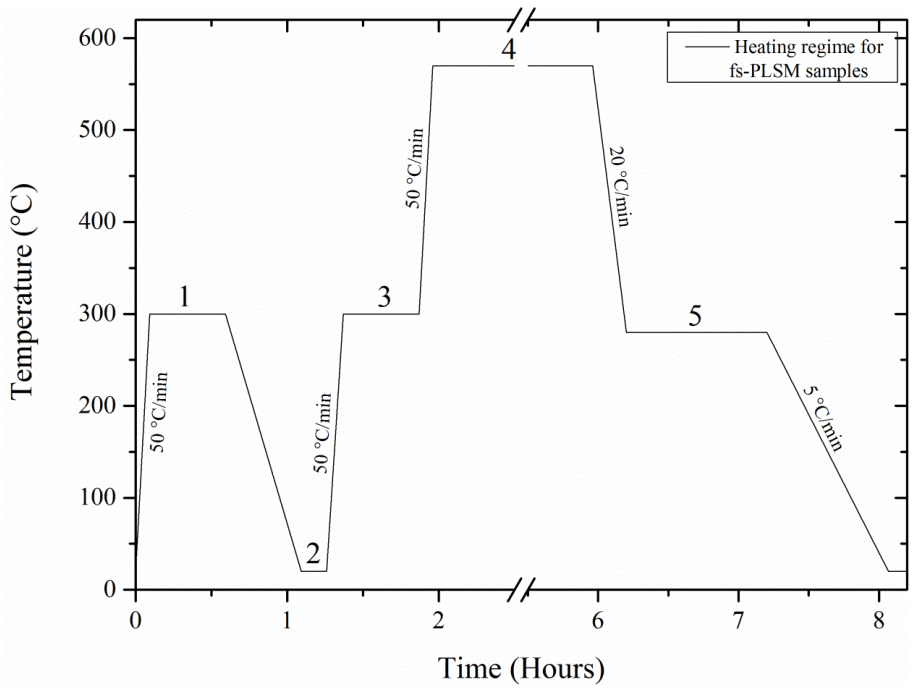

Figure 3.2. Heating regime for the femtosecond pulsed laser surface modified samples. The temperatures refer to those applied to the substrate: (1) 300°C, first degassing stage; (2) desired gas introduced into the chamber; (3) 300°C second degassing stage; (4) set fabrication temperature; (5) 280 °C hold temperature relieve stresses in the sample

The heating regime in Figure 3.2 may be modified depending on the sample, for example if the fabrication is only to last 1 hour, stage 4 will be reduced accordingly. The temperature of each stage is read off the digital output of a thermocouple, whereby the thermocouple is fixed in close proximity to the substrate itself. Due to the thermocouples location, an additional 10 to 15 minutes is given at the start of stage 4, prior to deposition so to ensure thermal equilibrium across the substrate at the start of the fabrication.

At stage 4, prior to the fabrication process commencing, the same target cleaning procedure described in section 3.1.1 using the fs-laser is adopted. The desired fabrication duration is set and the experiment is begun. The same regular checks of all experimental parameters is carried out throughout the experiment, at least once every hour until the fabrication is completed. The cooling process at the end of stage 4 down to room temperature generally extends into the evening and so a fabricated sample is often collected the next day.

3.1.2.1. Target glass preparation

The samples fabricated in the manner described in section 3.1.2 were fabricated by the ablation of a tellurite glass with composition 80 TeO_2 – 10 ZnO – 10 Na_2O (mol%) and 3 wt% Tm_2O_3. The glass target was prepared from high purity (>99.99%) starting chemicals in powder form. These powders were first weighed out accordingly, ground up with a marble mortar and pestle and then transferred to a gold crucible. The mixture was then heated to 800 °C in an electric furnace where it is molten and held at this temperature for 1 hour. The mixture was then cooled to 750 °C and homogenised for 2 hours in an atmosphere of dried O_2 gas. The melt was then cast into a 265 °C pre-heated brass mould and subsequently annealed at 285°C for 3 hours. Following this, a slow cooling rate of <1 °C/min was followed until at room temperature. The resulting glass was then polished on both sides to a finish of 2500 grade SiC. Great care was given to ensure a uniform finish was achieved, thus avoiding the formation of a wedge-shape.

3.1.3. Femtosecond laser micromachining (fs-LM)

Femtosecond laser micromaching (fs-LM) employs the use of an ultrafast laser, ordinarily operating at a very low fluence, to machine the surface or subsurface of a material. Surface channel waveguides are produced in this thesis using the laser system described in section 3.1.1. The laser beam is orientated so as to focus upon the surface of a thin film sample. A schematic of the experimental set up is presented in Figure 3.3. This laser processing system is highly advantageous for the fabrication of waveguide structures. Structures can be produced without the need for a clean room or mask, reducing costs and increasing flexibility in the design process.

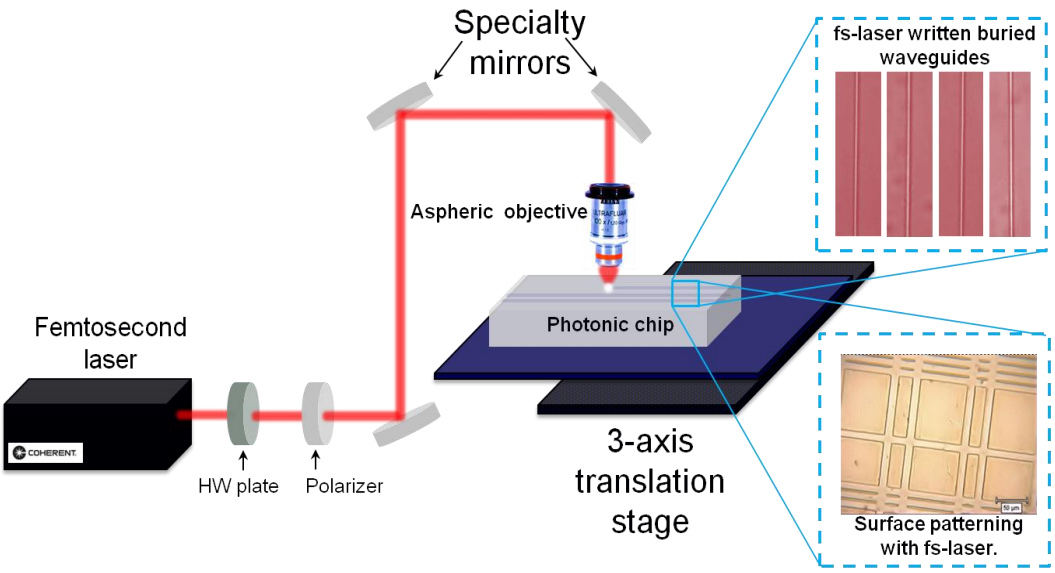

Figure 3.3. Illustration of the instrumental set up used for femtosecond pulsed laser micromachining

Figure 3.3 illustrates the ability to produce surface patterning as well as buried waveguide structure. Only surface patterning is used in this work as the materials are all surface deposited or surface modified. Prior to performing the surface patterning, the stage is aligned so that it is focused precisely upon the surface of the sample. The focussing is done on all four corners of the material so as to ensure the focusing is continuous across the surface. For performing surface patterning, a 2 μm translation in the z-axis is done (i.e. elevating the sample), so that the focal point is just below the surface and will therefore remove the thin film. For

carrying out sub-surface patterning however, the specimen would be lowered to a depth of approximately 20 μm.

The surface channel waveguides are produced via inputting the desired speed of translation as well as the specific path to take. The path taken extends across a 1 cm surface with the laser extending beyond the edges of the sample. This ensures the channels are made cleanly, from edge to edge with no interruptions.

3.2. Optical characterisation

3.2.1. Photoluminescence spectroscopy

It is common to use the terms photoluminescence spectroscopy and fluorescence spectroscopy interchangeably, as used in this thesis. Photoluminescence encompasses both fluorescence and phosphorescence, which are themselves defined simply by the duration taken for emission to occur following an initial excitation with another photon.

Emission spectra in the range 200 to 2100 nm were acquired using an Edinburgh Instruments FLS920 steady state and time resolved fluorescence spectrometer. This houses a thermoelectrically cooled visible photomultiplier tube (PMT) (200-900 nm), liquid nitrogen cooled near-infrared (NIR) PMT (700-1700 nm) and InGaAs (1000-2100 nm) detectors. A schematic representation of the spectrometer is provided in Figure 3.4, where the three 'arms' are shown (MC1, MC2 and MC3). The first branch, passing through the first monochromator (MC1) is used for the isolation of a specified wavelength (in the range 200-900 nm) from the broadband μs flash lamp source. MC2 has two gratings, one optimised for the visible region with 1800 grooves/mm (the same as MC1) and one for the NIR with 600 grooves/mm. MC3 also has two gratings, one for the NIR region and another for the MIR region where both have the same 300 grooves/mm. For fluorescence measurements with the InGaAs detector, a mechanical chopper and lock-in amplifier is used, as shown in Figure 3.4

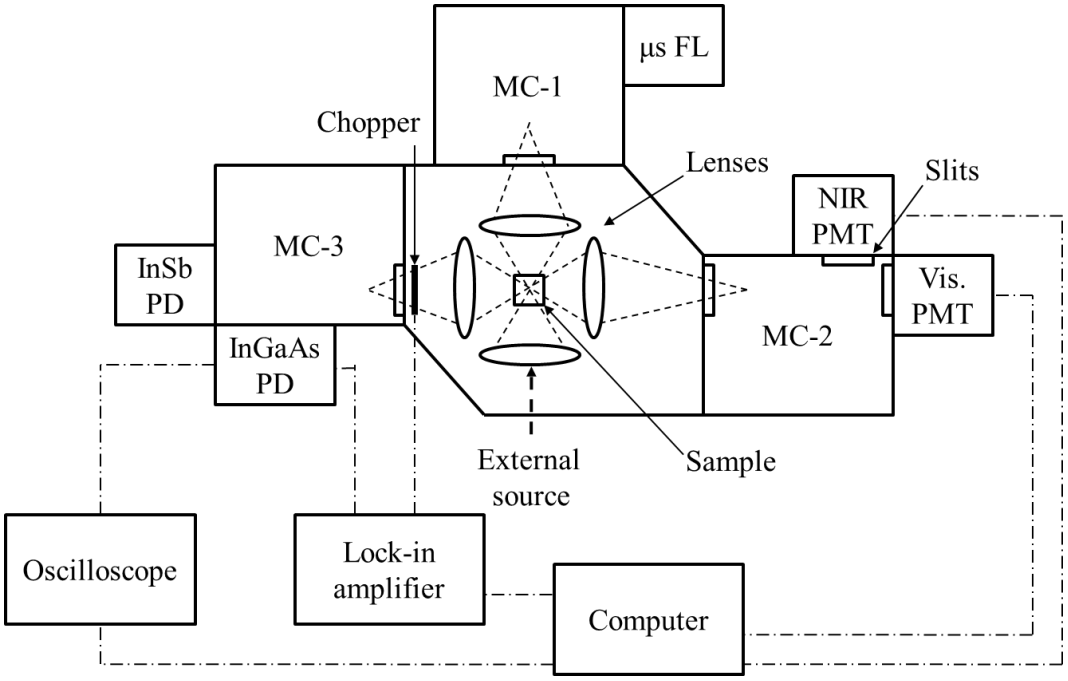

Figure 3.4. Schematic diagram of the experimental set up used for conducting steady-state fluorescence and lifetime measurements. Notation used is as follows: MC = monochromator, FL = flash lamp, PD = photodiode detector, PMT = photomultiplier tube

The sensitivity of the detectors deteriorates as the wavelength range extends, i.e. InSb is considerable less sensitive in comparison to the visible PMT. This is particularly true for the cross-over detection range for the InGaAs and NIR PMT detectors. For this reason, the 1540 nm Er^{3+} emission, which both detectors are able to detect, is investigated using the NIR PMT.

Excitation sources used for samples include the internal µs-flash lamp source (200-900 nm) and a series of external laser sources. This includes two external laser diodes operating at 808 and 974 nm, where the output is given from a fibre-optic cable which can be fixed in position on the outer casing of the spectrometer. Twin Ar-ion lasers (514 nm main line [114]) which can be either directed into the spectrometer individually, or combined to pump a tunable Ti:Sappire laser (peak power output at ~800 nm).

3.2.2. UV/Visible/NIR transmission spectroscopy

Absorption measurements were carried out using a Perkin Elmer Lambda 19 UV/Visible/NIR spectrometer. Due to the fundamental nature of this work

directed toward the fabrication of rare earth doped thin films, the concentrations of the ions are found to be below the detection capabilities of this system. This is compounded by the strong visible absorption of Si, thus obscuring any indication of absorption from any such ions. Following the upgrade of this equipment to a Perkin-Elmer Lambda 950, repeated attempts were made to characterise the rare earth ions, however no discernable absorption peaks could be identified. Further attempts to characterise the absorption properties of rare earth doped materials discussed in this work, including Fourier-transform infrared spectroscopy (FTIR) (both in transmission and reflection mode) as well as reflectivity measurements of the films using the new UV-Visible-NIR spectrometer. Another attempt was made through the mechanical removal of several thin films which were then mixed with KBr and again characterised using the new spectrometer, however absorption data remained allusive.

The absorption properties of silicon thin films could however be characterised. The primary interest in the transmission spectra of fabricated Si thin films is the determination of their optical bandgap. The optical bandgap, as opposed to the electronic bandgap, is defined as the minimum photon energy required to generate an electron hole pair (exciton). The electronic bandgap in comparison is the minimum required energy to both create and separate an exciton. One can characterise the optical bandgap of a material by manipulation of the following relationship [115]:

$$\boldsymbol{\alpha = (E - E_0)^2 \, A/E} \qquad \textbf{(3.1.)}$$

Where α is the absorption coefficient, E is the energy of a photon, A is a constant and E_0 is the optical bandgap. Plotting $(\alpha E)^{1/2}$ against the photon energy (in eV), commonly referred to as a Tauc plot [115] after its discoverer, can thus be used to acquire the optical bandgap. This is found by applying a linear fit to the linear region of the curve, where the x-intercept is found to be the optical bandgap. This is highly beneficial for understanding the material properties of the deposited silicon thin films as it allows for interpretation of the particle size. As the particle size decreases, the bandgap raises which is evident through the formation of a Tauc plot.

Prior to performing a transmission scan on a deposited Si thin film, as in chapter 4, a reference scan is taken using a clean, blank silica substrate of matching

thickness. Thus the resulting measurement is only due to contributions from the thin film.

3.3. Structural characterisation

3.3.1. X-ray diffraction (XRD)

For the characterisation of crystallites within a material, the quintessential form of analysis is X-ray diffraction (XRD). This technique utilises a beam of monochromatic X-rays to study the crystallography of a given material. Interaction between the incident X-rays and a crystal plane produce constructive interference and a diffracted ray when Bragg's Law is satisfied:

$$n\lambda = 2d \sin\theta \qquad (3.2)$$

This relates the wavelength, λ, to that of the angle of diffraction, θ, and the lattice spacing, d, in a crystalline sample. Note that this law extends to other wave-like phenomena, such as electrons and neutrons. Thus, by observing the angle at which the X-rays diffract, one can interpret the crystal phase that is interacting with the X-rays. This process is depicted in Figure 3.5 for the interaction of X-rays with an arbitrary crystal plane.

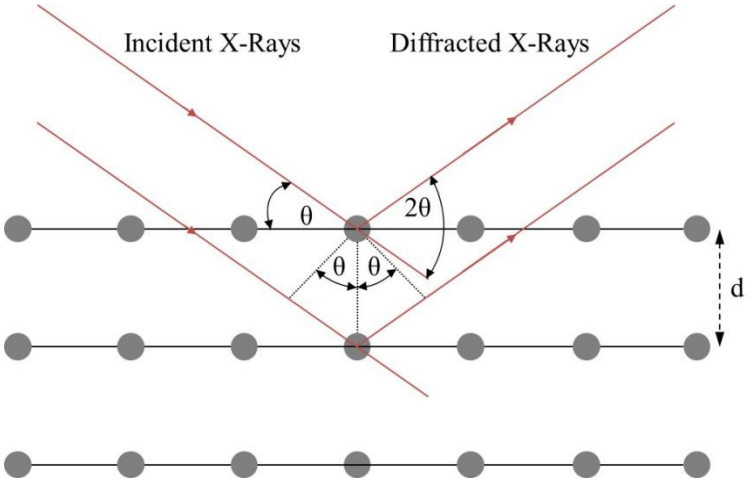

Figure 3.5. Schematic representation of the diffraction of X-rays from a set of crystal planes

XRD is a particularly powerful technique for describing unknown crystal structures. The resulting pattern of diffracted X-rays recorded by the instrument can

be used to define the average spacing between layers of atoms, known as d-spacings. These d-spacings can be then compared to that of thousands of standard reference patterns supplied in the international centre for diffraction data's (ICCD) PDF-4+ 2013 database. This can be used to identify what material and crystal phase they may correspond to. This in turn can then be used to deconvolute a pattern to isolate one crystal phase from the next as more are defined.

XRD is not, however, a compositional analysis technique, as other crystals can have similar diffraction patterns (including variations of the same chemical composition). With adequate knowledge of the material composition as well as complementary analysis with other techniques, accurate interpretation of the data can be made to determine the crystallite composition.

XRD measurements are taken by positioning the sample on a glass slide, where a blank silicon wafer is used to ensure the height of the sample is set to that calibrated for the instrument. The holder used focusses the X-rays to a certain height, thus it is essential to position the sample accordingly. Once done, the instrument can be sealed up and a pre-programmed scan can be initiated.

3.3.1.1. The Scherrer equation

A well-established methodology for calculating the average particle size from an XRD pattern is with the Scherrer equation. P Scherrer [116] identified this equation as:

$$\boldsymbol{D_{hkl} = \frac{K\lambda}{(B_{hkl}\cos\theta)}} \qquad \textbf{(3.3)}$$

Where D_{hkl} is the crystallite size determined in the direction perpendicular to the lattice planes, hkl are the Miller indices of the plane in question, K is a numerical factor often referred to as the crystallite-shape factor, λ is the X-ray wavelength, B_{hkl} is the broadening factor (full-width at half maximum) of the XRD peak at the Bragg angle θ, in radians.

The Scherrer equation has known limitations in its application [117], so one cannot simply apply it to all systems to define the crystallite size. There are a multitude of factors effecting the observed broadening of an XRD peak [118]. Firstly, the instrumentation in use will result in a degree of broadening, often called the instrumental profile; this can be accounted for by scanning a highly ordered and

stress-free material and taking the FWHM of a peak and deducting that from further observations. The crystallite size, which the Scherrer equation pertains to, also contributes. Another important factor is that of microstrain on the crystal phase being analysed. It should be noted that strain factors can vary from one crystal plane to the next and can be in the form of non-uniform lattice distortions, faulting, dislocations and grain surface relaxations. Additionally, if the crystal shape (on average) does not match that deduced for selection of the appropriate shape factor to be applied to the Scherrer equation, additional miscalculations can occur. In general, it is found that the application of the Scherrer equation is best applied to peaks within the range 30 to 50 º2θ. Below this, peak asymmetry can affect the profile analysis, while above it the instrumental profile and various microstrain broadening factors have a larger effect. In addition, peak intensity is generally weaker at higher angles.

The application of the Scherrer equation is however extremely useful in particle size analysis. When used with a full complement of analysis regarding the aforementioned considerations, it can provide rapid particle size analysis. For the purposes of analysing the samples presented here, stress-induced factors are not considered, however they are acknowledged and therefore the size measurements shall not be considered with a high degree of certainty.

3.3.2. Raman Spectroscopy

Raman spectroscopy entails the characterisation of the inelastic scattering of laser light to determine vibrational, rotational and other low-frequency modes of a specimen. The corresponding change in the frequency of the laser light following a scattering event is found to precisely correspond to the energy of these quantised phenomena. Thus with sufficient supporting data, chemical composition and structural subtleties, such as the grain size of a nanocrystal, can be inferred.

The specific changes in frequency of the scattered light are comprehended through Figure 3.6. Figure 3.6 illustrates that the shift may be through the gain or loss in energy of a scattered photon via interaction with the hosts quantised vibrational modes, i.e. phonons.

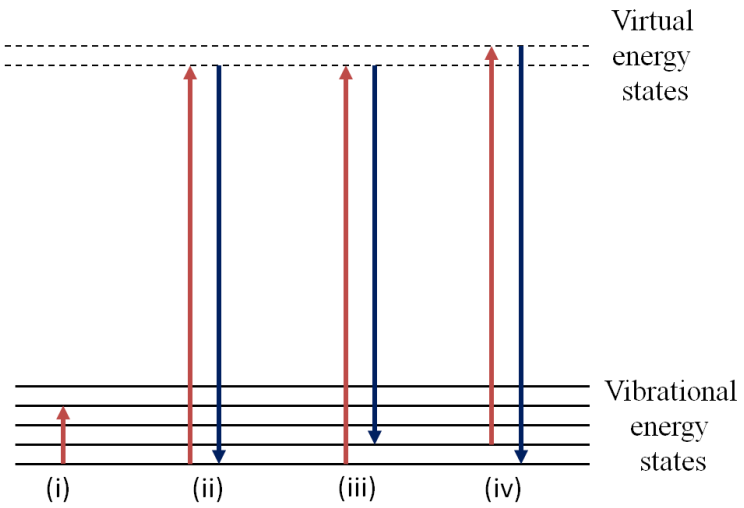

Figure 3.6. Energy level diagram of the various transitions possible following laser excitation for Raman spectroscopy: (i) Infrared absorption, (ii) Rayleigh scattering, (iii) Stokes Raman scattering, (iv) Antistokes Raman scattering

The theory of Raman spectroscopy thus corresponds to data which may be acquired via infrared absorption. A distinctive advantage over infrared absorption for Raman spectroscopy is that water in addition to many atmospheric gasses do not interfere with the spectrum. Interference due to absorption of a mid-infrared source can thus be avoided through this technique.

A Renishaw inVia micro (μ-) Raman spectrometer is used for this work. The 50x objective lens used in this instrumentation offers the ability to focus the laser upon a desired section of the material. In addition to this, the laser may be focussed to a fine spot size, thus maximising the observed scattering. Furthermore, the ability to migrate the stage offers the ability to investigate differences between one region and another. For example if one area of a silicon thin film is more crystalline than one a few micons away.

Due to the non-destructive nature of this technique and lack of sample preparation requirements, thin films samples can be immediately analysed. Each sample is individually loaded onto the sample stage and a very low power (< 1 μW) laser is used to focus onto a given surface feature observed through the optical microscope. Refinements to the focussing are made so as to minimise the spot size as much as possible.

Data collection is typically conducted over the course of a 5 minute period involving at least 2 accumulations. Samples scattering very weakly (i.e. low signal intensity) are typically analysed for longer with several accumulations. Fluorescent samples, such as where ZnTe is observed, are analysed at extremely low laser powers and for much shorter periods of time. Multiple areas may be studied for a single sample, often 4 or 5 in order to characterise the material. This is done in order to ensure the observed features are not artefacts, to find an area with decreased fluorescence and thus observe the spectral features, or simply to probe different regions of a sample.

3.3.3. Scanning electron microscopy (SEM)

For the preparation of thin films for SEM analysis, two routes can be taken. For a face-on perspective of the surface, the sample is simply attached to a standard SEM stub (stainless steel) using conductive graphite paint. This both secures the sample to the stub and provides a conductive pathway for charge to dissipate. For a nonconductive substrate however, the graphite paint is applied generously to all exposed regions, i.e. no area of the substrate is left uncovered and a connection is made to the thin film under analysis.

For a cross sectional view of the material, the sample must be snapped. This is done in a controlled way so as to maximise the quality of the exposed area following the snap. In order to do this, the underside of the substrate is marked in a clean line using a diamond scribe. For Si substrates a singular inscription is made and the same process as described in section 3.1.2 is carried out. For a glass substrate, a considerably more vigorous approach is taken, whereby inscriptions are made to a greater depth.

For each preparation method the sample has a 3 nm Pt/Pd layer applied using a sputter coater. This reduces charging of the surface in addition to not altering the surface features of the material being analysed. SEM is conducted using a LEO 1530 FEG-SEM for high resolution imaging and EDX measurements, while a Carl Zeiss EVO MA15 is used for backscattered electron characterisation. The Carl Zeiss SEM uses a tungsten filament and as a result the image resolution is not as high in comparison. Descriptions of the two primary imaging modes are provided below as well as for energy dispersive X-ray (EDX) analysis.

3.3.3.1. Secondary electron imaging

Secondary electron (SE) imaging is the most common imaging technique for SEM. It detects the inelastically scattered, low energy electrons ejected from the upper surface of a sample. This imaging technique therefore offers a topographical view of the surface of a material.

Several key factors must be accounted for when interpreting an SE image. These are elaborated in the next section but are also discussed progressively throughout the experimental chapters.

The use of SE imaging of the samples described in this thesis is extremely useful for determining the microstructure of the fabricated material. It both reveals the porosity of the deposited thin films, whilst indicating the degree of roughness upon the surface. For the surface modified samples, it allows a clear view of the subsurface when a cross section is taken. This information is invaluable in understanding the manner in which these materials are forming. Additionally, it provides sufficient data to make an informed decision on what aspects of the fabrication process require altering or if further analysis, for example with the TEM, is needed.

3.3.3.2. Backscattered electron imaging

Backscattered electrons (BSE) originate from elastic interactions between incident electrons from the primary electron beam with the atomic nuclei of a constituent atom in a given interaction volume. A fundamental principle of this interaction is the strong correlation between the probability of its occurrence and the atomic number of that nuclei, z. That is to say that with a larger atomic nuclei, there is an increased chance of a backscattering event occurring. Hence the resulting image will have a strong contrast ratio related to the average atomic number of that region, a *Z-contrast* as it is often called [119]. For a system with many elements to be considered, in various quantities, the calculation of an average atomic number, Z, for a given region is required. Analytically, one must consider the BSE emission coefficient, η, when discussing the contrast ratio of a given BSE image. This quantity, η, relates to the number of beam electrons being scattered elastically backward, i.e. an angle greater than 90° from the scattering event. This is found through the following equation [120] for samples orientated normal to the incident electron beam direction:

$$\eta = 2^{-9/\sqrt{Z}} \quad \textbf{(3.4.)}$$

A great deal of uncertainty is associated with the calculation of BSE emission coefficients for low atomic numbers [121], i.e. Z≤10. Equation (3.4 however has been cited [122] as effective for this purpose in relation to other proposed equations. Following calculations of individual η values, one can then proceed to an average BSE emission coefficient, $\bar{\eta}$, through the following relationship [123]:

$$\bar{\eta} = \sum_{i=1}^{n} c_i \eta_i \quad \textbf{(3.5.)}$$

Where c_i is the weight fraction of the specified element in the composition and η_i is its respective BSE emission coefficient.

When used correctly, BSE imaging can be extremely powerful. The surface penetration allows one to identify subsurface features of a different chemical makeup. This is used to great effect with the surface modified samples, allowing the identification of the distribution, abundance and the spread of subsurface particle sizes.

3.3.3.3. Energy dispersive X-ray analysis

Energy dispersive X-ray (EDX) spectroscopy is an analytical tool used in conjunction with an electron microscope for compositional analysis. Electrons of a sufficient energy are used to excite a bound electron of a given element to a higher electron shell. The hole this excitation produces is quickly filled by the decay of an electron from a higher energy shell. This decay releases a photon with a characteristic energy in the form of an X-ray. These X-rays can thus be recorded and mapped to known spectrums of each element. The data is computationally fitted to describe both the existence of certain elements within a spectrum and to calculate their composition. Due to overlaps of certain peaks and inherent resolution difficulties, such analysis can be somewhat prone to inaccuracies, thus it is described as semi-quantitative.

This technique is used both for SEM and TEM analysis. Its use in SEM analysis can be somewhat prone to errors, very much akin to BSE-SEM imaging. The interaction zone for electrons generating these characteristic X-rays is located below the BSE region. This means that the observed spectrum is not necessarily representative of the composition of the surface features, but more likely the

subsurface. The penetration depth of the electrons can be accounted for by Monte Carlo simulations based upon an estimate of their composition and density. Thus one can apply a lower accelerating voltage to reduce the depth of these electrons, however the trade-off is that lower accelerating voltages may not be sufficient to observe characteristic X-rays from elements of interest. Furthermore, this too does not guarantee knowledge of the interaction volume, thus errors persist. Interactions with surface texturing can also imbue additional inaccuracies in the compositional analysis. This shall be elaborated upon in subsequent chapters.

EDX analysis is however extremely useful for compositional analysis and the ability to determine the area of effect allows one to map certain features. Although this is more accurately conducted using TEM, the considerably shorter sample preparation times leads to a higher throughput of analysis.

3.3.4. Transmission electron microscopy (TEM)

A transmission electron microscope (TEM) operates very much like a light microscope, except electrons are used instead of visible light. The reason for using electrons is due, in part, to their considerably shorter wavelength which enables the resolution of objects in the order of angstroms (10^{-10} m). Such high resolutions are able to be met due to the ability to focus the electron beam to a very fine point. An associated maximum sample thickness of approximately 100 nm must also be adhered to due to the interaction of electrons with matter. Samples thicker than this will result in significant degradation of the intensity of the beam electrons, thus compromising the image.

For the description of a TEM system, it is convenient to describe the equipment used for this work. This includes two TEM microscopes: an FEI Technai TF20 and a Phillips CM200. The former is a field-emission gun TEM (FEG-TEM) using a high-angle annular dark-field (HAADF) detector and is also used for acquiring energy dispersive X-ray (EDX) analysis. The latter is also a FEG-TEM, capable of acquiring EDX mapping as well as point EDX analysis. Both TEMs are also able to acquire selected area electron diffraction (SAED) patterns.

The use of TEM for this work is fundamental to gaining adequate understanding of the samples produced. For the deposited silicon samples, TEM

allows for particle size analysis, where experimental limitations precluded the use of other analytical techniques. The additional features of a TEM (EDX, SAED etc.) allow for the acquisition of an enormous wealth of data, making this any invaluable resource.

3.3.4.1. Sample preparation by the mechanical removal of thin films

Some thin films, described in chapter 4, were mechanically removed from their substrate and dispersed in methanol. The dispersion was homogenised using a sonicator which also assisted in the further breakdown of dispersed particles. A small drop was extracted from this solution and deposited onto either a standard copper TEM grid or a SiN grid for high temperature studies. This technique is useful for particle size analysis, however the destruction of the sample structure precludes any gain of information regarding the film structure.

3.3.4.2. Standard cross-sectional preparation methodology

The standard methodology for the preparation of a thin film cross-section for TEM analysis involves many steps. Firstly, two sections of a sample are removed using an ultrasonic cutter and subsequently cleaned in acetone. Following this, the two film faces are bound together using an epoxy resin. Additional silicon wafers then sandwich the bound sample, providing adequate depth for subsequent processing. The same ultrasonic cutter is then used to bore through a cross section of the sandwiched layers, centred upon the sample wafers producing a tube shaped core. This core is then coated in epoxy resin and inserted into a copper tube. The core is then cut into individual sections of approximately 1 mm thickness using a diamond blade saw. The resulting sample grids are ground down to a thickness of 250 μm with a high finish on either side. From here, the wafer must then be thinned at its centre using a dimple grinder, positioned at the centre of the interface between the two sample wafers. An approximate thickness of 2-4 μm is achieved and verified by its transparency using an optical microscope. An equal amount of material is removed from both faces of the sample, as this produces the best results in the following step. Through the use of precision ion polishing (PIPS) two Ar-ion guns are used to further remove material from the dimple until a minute hole is visible at the centre of the sample interface. Upon completion of this stage, the sample is therefore ready for analysis with TEM.

This technique is extremely useful for cross-sectional imaging. The ability to dissect a sample in this way allows one to preserve the structural characteristics, which is paramount for the surface modified samples. Although the viewable area is much larger than samples prepared by FIB, there is no way to accurately determine which area is being studied. This will be discussed in greater detail in chapter 6. Additionally, some features may be lost during the abrasive thinning process.

3.3.4.3. Focused ion beam (FIB) lithography for the preparation cross-sections for TEM analysis

Focused ion beam (FIB) lithography is a more precise sample preparation tool than that described in section 3.3.4.2, where a specific area of a surface can be extracted. This however produces a considerably smaller sample size than what can be achieved by the standard methodology. The FEI Nova 200 NanoLab used for the sample preparation described in this work uses a high resolution FEG-SEM for imaging and a focused Ga-ion beam for etching. Prior to etching, the instrument also deposits a layer of platinum on the surface in order to protect the surface features from the Ga-ions. The sample can then be mechanically removed and positioned upon a grid ready for TEM analysis.

FIB is a far more refined manner of cross-sectional TEM sample preparation. It offers the ability to specifically isolate areas of interest for extraction and analysis. This is impossible with the standard technique, however FIB is considerably more expensive in comparison, thus extensive studies are unfortunately undoable.

3.3.4.4. Energy-dispersive X-ray (EDX) analysis through TEM

EDX spectroscopy acquired during TEM analysis is found to be inherently more accurate, this is due not only to the lack of surface texturing, but also because much higher electron voltages can be applied, thus enhancing the spectral resolution of higher energy characteristic X-rays.

3.3.4.5. Selected area electron diffraction (SAED)

Selected area electron diffraction (SAED) utilises high energy electrons during TEM analysis to characterise the crystallography of a material. This is achieved by observing the resulting diffraction pattern made by electrons following their interaction with a crystallite (or lack thereof). The diffraction events occur due to the wave-like nature of these high energy electrons and their wavelength being

orders of magnitude smaller than the spacings between atoms. This process thus follows the same theoretical basis as described for XRD in section 3.3.1. The long-range order of small crystallites (i.e. <100 nm) thus causes a spot pattern to become apparent and is recorded using a detector. Due to the angular sensitivity of crystal planes, the angle of incidence of the electron beam thus affects the observed spot patterning. Thus a sample is often tilted in order to align with a particular crystal plane.

Should the specimen be composed of a collection of nanocrystallites, the diffraction pattern appears much more as a 'ring' pattern, where the rings, as with the patterned spots, correspond to electron diffraction down a particular crystal plane. Note also that an amorphous material will simply appear as a diffuse glow protruding from the centre due to the lack of long-range order in the material.

SAED is an excellent complementary technique to XRD, and vice versa. Where XRD provides an overall view of the samples diffraction pattern, SAED is able to pinpoint the crystal structures at the nanoscale. In turn, this allows one to build a complete image of the material under investigation. As the surface modified samples were completely unexplored prior to this work, this kind of investigative technique is highly advantageous.

3.3.5. Atomic force microscopy (AFM)

Atomic force microscopy (AFM) studies were conducted using an Agilent Technologies 5420 in tapping mode. This produces high resolution surface images of a specimen by the interaction of a tapping cantilever and detecting the dampening of the oscillations due to interactions with the surface. The image is therefore recorded as the tip scans across the surface. The 3-dimensional profile that is generated is particularly useful for characterising fs-LM samples.

AFM can provide very high resolution surface topography images, which can be used to make a number of quantitative interpretations, such as surface roughness. Additionally, specific AFM tips can be used to measure a wide range of material characteristics, such as magnetism, conductivity etc.

3.3.6. Thermochemical calculations using HSC Chemistry™ 6.0

As will be seen in chapter 5 to 8, extensive crystallisation occurs during the fabrication of the surface modified samples. To use an example, the formation of ZnTe in the subsurface, i.e. embedded in SiO_2, poses many questions regarding the formation mechanisms involved. As part of the investigation to probe this, much discussion is given toward the extent of diffusion in the material *in situ*; however the absence of oxides from the original glass requires special consideration. Diffusion is tackled within the relevant chapter, however, to best understand the chemical behaviour during the experiment, thermochemical calculations are required. Thermochemical calculations allow one to query the likelihood of formation for one phase over another. Manually, this is a rather laborious process, hence the software package HSC Chemistry™ 6.0 is employed. This package contains an exhaustive database of thermochemical data for over 20,000 chemical species. Each species in the database contains the enthalpy (H), entropy (S) and the constant pressure heat capacity (C_p) as well as a variety of other information. Other key values associated with each species include A, B, C and D which are coefficients of the heat capacity function predicted from experimental data. These are unimportant for room temperature calculations, however they are essential at elevated temperatures.

As the plasma phase is not continuously in contact with the substrate, due to the pulsed nature of the laser (1 kHz repetition rate, i.e. 1 pulse per ms), the prevailing influence upon the substrate is the applied heat to the substrate. This is also true during the extensive cooling process depicted in Figure 3.2. Thus it is reasonable to assume that chemical interactions occurring *in situ* are predominantly driven by the substrate temperature. For this reason, thermochemical calculations can assist in determining the likely route a considered reaction may take and therefore aid in the understanding of the surface modification process.

The software can thus calculate the Gibbs free energy, ΔG, value for a given interaction for a set of temperatures. ΔG is a standard chemical quantity which is used to infer the direction a reaction may take. If it is negative, the product of a reaction is favoured, if it is positive, the reactants will likely remain isolated. Due to the complexity of many of the interactions possible in the aforementioned chapters, the calculations are used more as a guide.

A typical example of how the software would calculate a reaction is provided for the reduction reaction of 1 mole of TeO_2 and ZnO by 1.5 moles of Si at 500 °C:

$$TeO_2 + ZnO + 1.5Si = 1.5SiO_2 + ZnTe$$

For this reaction, the HSC software first calculates C_p at the set temperature. Because this cannot be predicted through thermodynamics at elevated temperatures, the Kelly equation is adopted:

$$\boldsymbol{C_p = A + B.10^{-3}.T + C.10^{5}.T^{-2} + D.10^{-6}.T^{2}} \quad \textbf{(3.6)}$$

The individual enthalpies (H), entropies (S) and Gibbs energies (G) for the reactants and products are then calculated through:

$$\boldsymbol{H(T) = H_f(298.15) + \int_{298.15}^{T} C_p.dT + \sum H_{tr}} \quad \textbf{(3.7)}$$

$$\boldsymbol{S = S(298.15) + \int_{298.15}^{T} (C_p/T).dT + \sum H_{tr}/T_{tr}} \quad \textbf{(3.8)}$$

$$\boldsymbol{G = H - T.S} \quad \textbf{(3.9)}$$

Where H(298.15) and S(298.15) are the enthalpy and entropy of formation at room temperature (in Kelvin), T is temperature and H_{tr} is the enthalpy of phase transformation at temperature T_{tr}. This then allows for the various components of the reactions to be calculated, and then finally the Gibbs energy of the reaction. These are as follows:

$$\boldsymbol{\Delta H_r = \left(1 \times H_{TeO_2} + 1 \times H_{ZnO} + 1.5 \times H_{Si}\right) - \left(1.5 \times H_{SiO_2} + 1 \times H_{ZnTe}\right)} \quad \textbf{(3.10)}$$

$$\boldsymbol{\Delta S_r = \left(1 \times S_{TeO_2} + 1 \times S_{ZnO} + 1.5 \times S_{Si}\right) - (1.5 \times S_{SiO_2} + 1 \times S_{ZnTe})} \quad \textbf{(3.11)}$$

$$\boldsymbol{\Delta G_r = \left(1 \times G_{TeO_2} + 1 \times G_{ZnO} + 1.5 \times G_{Si}\right) - (1.5 \times G_{SiO_2} + 1 \times G_{ZnTe})} \quad \textbf{(3.12)}$$

Note the integers in front of each quantity represent the stoichiometric ratio for that compound. As can be seen, this calculation would become extremely laborious for several hundred individual temperatures across dozens of possible reactions. The use of HSC Chemistry™ is therefore necessary.

Chapter 4.
Fabrication and characterisation of silicon and rare earth doped silicon thin films

This chapter describes the experimental exploration of femtosecond (10^{-15} s) pulsed laser deposition (fs-PLD) of silicon and rare earth doped silicon onto low cost silica substrates. The fabrication process is studied relative to variations in pressure, background gas type, laser energy and substrate temperature as well as studies into the fabrication of multilayer p-i-n structures. Trivalent thulium (Tm^{3+}) and erbium (Er^{3+}) doped silicon thin films were also studied for their mid-infrared and near-infrared fluorescence characteristics, respectively. Tm^{3+} doped samples were also processed via femtosecond pulsed laser micromachining for the fabrication of surface channel waveguides.

4.1. Introduction

With regard to the doping of silicon based materials with rare earths, considerable efforts have previously been made to effectively incorporate the lanthanide erbium (Er^{3+}) into a silicon host for optical applications [78,82]. The optical characteristics of Er^{3+}-ions make it highly desirable for communications [86]. Similarly, fluorescence from the $^3F_4 \rightarrow {}^3H_6$ manifolds of Tm^{3+}-ions are in the eye-safe region around 1800 nm [73].

Investigations for the doping of silicon with rare earth elements have confirmed an energy transfer mechanism from the long-lived excited states of the ions to silicon [54,78,82]. This transfer process demonstrates a temperature dependency as phonon scattering is required [82]. Thus a single crystalline silicon host demonstrates very poor room temperature fluorescence characteristics [84]. Amorphous silicon however has been found to demonstrate room temperature fluorescence from rare earth dopants [86,88,124], yet expresses very poor conductivity [78]. This however can be improved via hydrogenating the sample [88].

The interaction of an ultrafast laser pulse with a pressed powder pellet may enable the formation of nanoparticles composed of both silicon and a rare earth. This may enable an effective doping scheme in which to introduce rare earth ions to silicon nanostructures which may be exploited for light harvesting applications.

4.2. Experimental parameters

The experimental parameters for samples described in this chapter have been segmented into different tables for corresponding subsections. The nomenclature applied to each sample has been set so as to convey the relevant experimental variables used. Each sample name follows the same pattern:

[Duration – hours] [key variable] [quantity of that variable – J cm^{-2}, mol%, mTorr or °C] [Gas type used] – [sample version if parameters match]

Where the duration is set to 2 minutes, as in the samples described in Table 4.1, an s is used to denote 'short'. The variables used for these samples are given as F for fluence, T for temperature, P for pressure, Tm for thulium content (this may be in a fluoride or a sesquioxide form) and Er for erbium content. The gas type used is defined as H = 4%H in Ar and Ar = Ar gas. Where possible, these variables are simplified only to key variables in order to shorten the names. This chapter has been broken in several subsections, into which different sample sets are discussed. Sample tables related to each subsection are provided to simplify the array of samples discussed.

The experimental variables used for the fabrication of sub-monolayer samples discussed in section 4.3.1 are provided in Table 4.1, while the fixed parameters for these samples are provided in Table 4.2. The experimental variables for undoped silicon thin films studied by SEM as described in section 4.3.2.1 are provided in Table 4.3. The samples studied by Raman spectroscopy in section 4.3.2.2 are described in Table 4.4 and the optically characterised samples of section 4.3.2.3 are provided in Table 4.5. Each of these sample sets used fixed variables which were kept so for reasons that will be become clear during analysis and are defined in Table 4.6. The experimental parameters for rare earth doped samples are discussed in section 4.3.3 for Tm doped samples and 4.3.4 for Er doped samples are provided in Table 4.7 and their fixed parameters are defined in Table 4.8.

Table 4.1. Experimental variables used for the fabrication of sub-monolayer samples described in this chapter

Sample ID	Laser energy (mJ)	Laser fluence (J cm^{-2})	Pressure (mTorr)
sF0.9P40H	0.150	0.9	40
sF1.3P40H	0.220	1.3	40
sF1.9P40H-1	0.315	1.9	40
sF1.9P20H	0.315	1.9	20
sF1.9P40H-2	0.315	1.9	40
sF1.9P60H	0.315	1.9	60

Table 4.2. Fixed experimental parameters used in the fabrication of the sub-monolayer samples

Target	Single crystalline silicon wafer (5 inch diameter)
Gas type	4% hydrogen in argon
Target to substrate distance	70 mm
Spot size, cm^2	1.7×10^{-4}
Substrate	Cu TEM grid attached to SiO_2 glass
Substrate temperature, °C	20
Deposition time	2 minutes

Table 4.3 Table of the experimental parameters for samples fabricated from the ablation of a single crystalline silicon wafer. Column headings have been abbreviated as: F: Fluence, P: pressure during deposition, T: Temperature during deposition, t: duration of deposition, g: Gas type used during deposition

Sample ID	**F (J cm^{-2})**	**P (mTorr)**	**T (°C)**	**t (hours)**	**G**
1P0	2.0	None	20	1	None
1P70Ar	2.0	70	20	1	Ar
1P120Ar	2.0	120	20	1	Ar
3T20Ar-1	2.0	20	20	3	Ar
3T100Ar	2.0	20	100	3	Ar
3T200Ar	2.0	20	200	3	Ar
3T20Ar-2	2.0	20	20	3	Ar
3T20H	2.0	20	20	3	4%H_2 in Ar
3T100H	2.0	20	100	3	4%H_2 in Ar
3T200H	2.0	20	200	3	4%H_2 in Ar

Table 4.4. Table defining the fabrication variables of samples used for Raman spectroscopy in section 4.3.2.2

Sample ID	**F (J cm^{-2})**	**P (mTorr)**	**T (°C)**	**t (hours)**	**G**
1T20H	1.47	50	20	1	4%H_2 in Ar
1T50H	1.47	50	50	1	4%H_2 in Ar
1T100H	1.47	50	100	1	4%H_2 in Ar
1T200H	1.47	50	200	1	4%H_2 in Ar
1T300H	1.47	50	300	1	4%H_2 in Ar
1T400H	1.47	50	400	1	4%H_2 in Ar

Table 4.5. Table defining the experimental variables for the fabrication of samples characterised for their optical bandgap in section 4.3.2.3

Sample ID	**F (Jcm^{-2})**	**T (°C)**	**P (mTorr)**	**t (hours)**	**G**
1F1.7P5H	1.7	20	5	1	4%H_2 in Ar
1F1.7P20H	1.7	20	20	1	4%H_2 in Ar
1F2.3P5H	2.3	20	5	1	4%H_2 in Ar
1F2.3P20H	2.3	20	20	1	4%H_2 in Ar
1F2.9P5H	2.9	20	5	1	4%H_2 in Ar
1F2.9P20H	2.9	20	20	1	4%H_2 in Ar

Table 4.6. Fixed experimental parameters applied to all samples described in Table 4.3 (SEM), Table 4.4 (Raman) and Table 4.5 (optical)

Target to substrate distance (mm)	70
Laser spot size (cm^2)	1.7×10^{-4}
Target	Single-crystalline silicon wafer (5 inch diameter)
Substrate	Fused silicate glass

Table 4.7. Table of the experimental parameters used for the fabrication of rare earth doped silicon thin films. The rare earth composition is provided in mol%, intermixed with electronic grade silicon as a pressed powder pellet. The specific experimental procedure of 6Tm10Ar is provided in the text

Sample ID	**F (Jcm^{-2})**	**t (hours)**	**G**	**Target**
6Tm10Ar	2.40	6	Ar	10% Tm_2O_3 and c-Si
4Tm1Ar	1.47	4	Ar	1% TmF_3 in Si
4Tm2Ar	1.47	4	Ar	2% TmF_3 in Si
4Tm3Ar	1.47	4	Ar	3% TmF_3 in Si
4Tm3H	1.47	4	4% H_2 in Ar	3% TmF_3 in Si
4Tm0Ar	1.47	4	Ar	Si pressed powder pellet
4F0.59Er1Ar	0.59	4	Ar	1% Er_2O_3 in Si
4F1.47Er1Ar	1.47	4	Ar	1% Er_2O_3 in Si

Table 4.8. Table of the fixed experimental parameters used for the fabrication of rare earth doped silicon thin films

Pressure (mTorr)	20
Target to substrate distance (mm)	70
Laser spot size (cm^2)	1.7×10^{-4}
Substrate	Fused silicate glass
Substrate temperature (°C)	20

4.3. Results and discussion

4.3.1. Sub-monolayer fabrication

A series of samples were fabricated in order to define the laser fluence regime for the ablation of single crystalline silicon wafer targets. This also allows better comparison to observations in literature to better define the thin film samples fabricated. The samples are deposited directly onto standard copper grids designed for transmission electron microscopy (TEM). This was achieved by attaching the grids onto the underside (i.e. the side exposed to the plasma plume) of a silica substrate using conductive silver paint supplied from Agar Scientific. A study of this kind was also done by Eliezer *et al* [125] for the ablation of aluminium by fs-PLD. All copper grids are positioned in the centre of individual glass slides so to only collect material propagating directly upward. In order to prevent possible contamination of the grid surfaces, immediately after the sample is removed from the PLD chamber, it is put into a sample tub, sealed and then put into a vacuum desiccator.

TEM was used to image several areas across the samples, whereby no microparticles could be identified, however a large abundance of nanoparticles was found and a selection of these are provided in Figure 4.1

.

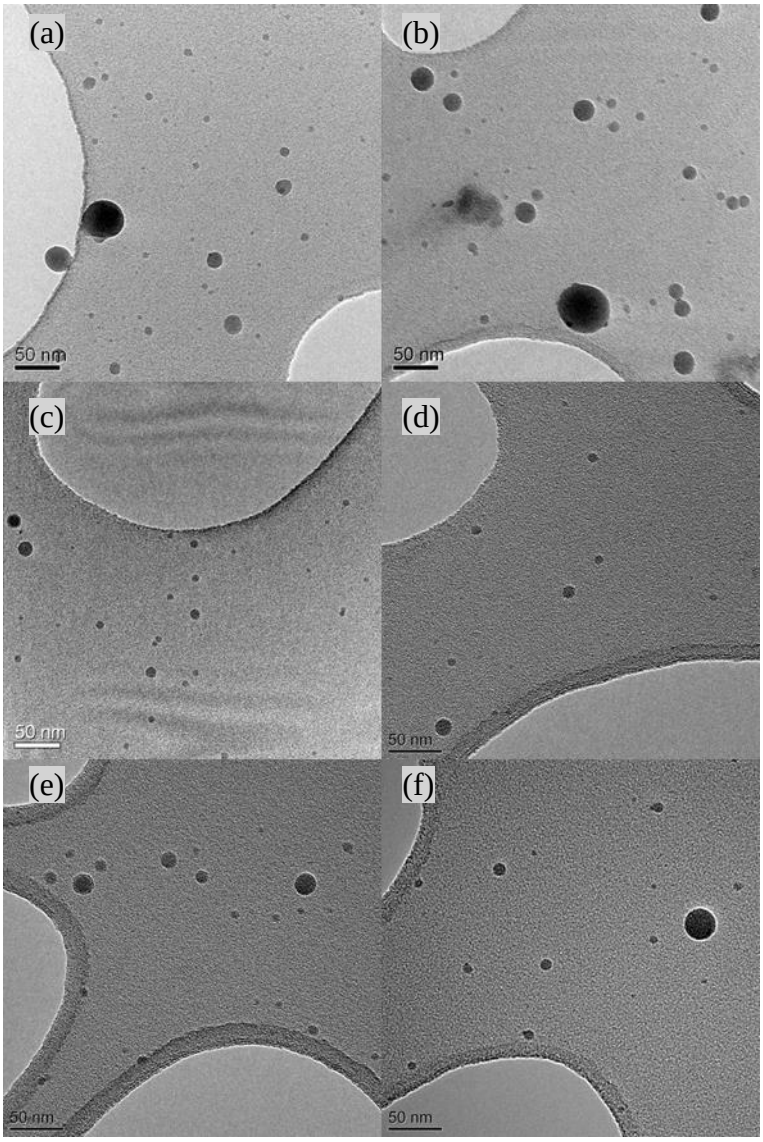

Figure 4.1. TEM images of sub-monolayer samples (a) SF0.9P40H; (b) T2; (c) sF1.9P40H-1; (d) sF1.9P20H; (e) SF1.9P40H-2 and (f) T6

With reference to Figure 4.1, the minimum particle size measurements have been limited to 5 nm because of the low contrast ratio of such particles against the copper grid. To confirm that the observed particles are in fact silicon, energy dispersive x-ray (EDX) analysis was performed on a selection of particles. Examples of two EDX patterns are presented in Figure 4.2. For convenience, the matching elemental X-ray signatures of the respective peaks have been marked on.

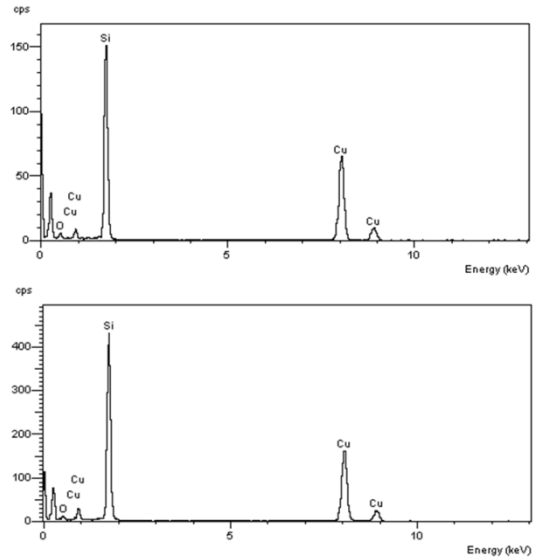

Figure 4.2. Energy dispersive X-ray (EDX) analysis of two example particles observed during TEM analysis of the samples presented in Figure 4.1

EDX analysis was conducted on several particles across the surface of each sample. The two EDX spectrums provided in Figure 4.2 best reflect the observations made. One should note that the detection of copper is unavoidable due to the grid in use. Deducting this from the compositional analysis is thus considered to be acceptable. Upon doing so, one acquires an average Si atomic percentage (at%) for all EDX scans acquired of approximately 95 at%. The remaining contribution is invariably oxygen which can be ascribed to contamination and the existence of an oxide layer on the surface of the Si particles. An accurate determination of the oxygen content of these samples by EDX is highly dubious due to the low atomic number of oxygen. The observed oxygen composition can be influenced by factors such as contamination in the form of ice formed on vacuum traps within the TEM instrument as well as on the surface of the sample itself. For example if a 'pure' SiO_2 sample were analysed by EDX (i.e. with a stoichiometric match and no contamination) the ratio observed would likely deviate from the real due to the factors listed as well as others. Due to these considerations, direct interpretation of the oxygen composition is discounted and it is simply understood as being 'low' in the particles.

Note that due to the particle sizes, observation of crystal planes is found to be difficult to identify. This is due to the amorphous Cu grid obscuring their observation. The ideal way to observe crystal planes is to identify a particle which

is positioned over the edge of a hole in the copper grid. One such example of this is presented in Figure 4.3. Note that no crystal planes are observed for this particle, nor any other during TEM analysis. The particle in Figure 4.3 is therefore interpreted as being amorphous. It should be noted that due to the minute sample size studied by TEM, it is not possible to generalise such observations. Thus, the interpretation of levels of crystallinity shall be investigated in subsequent sections of this chapter.

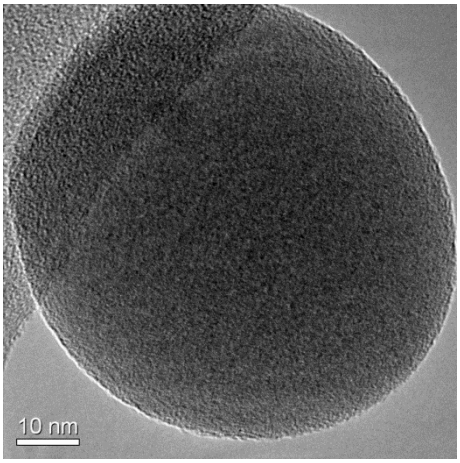

Figure 4.3. TEM image of a deposited particle where part of it protrudes over a hole in the copper grid showing no crystal planes

Histograms of the particle size distribution for each sub-monolayer sample are provided. Comparisons of samples where laser fluence is varied are presented in Figure 4.4 and variations in gas pressure are presented in Figure 4.5

.

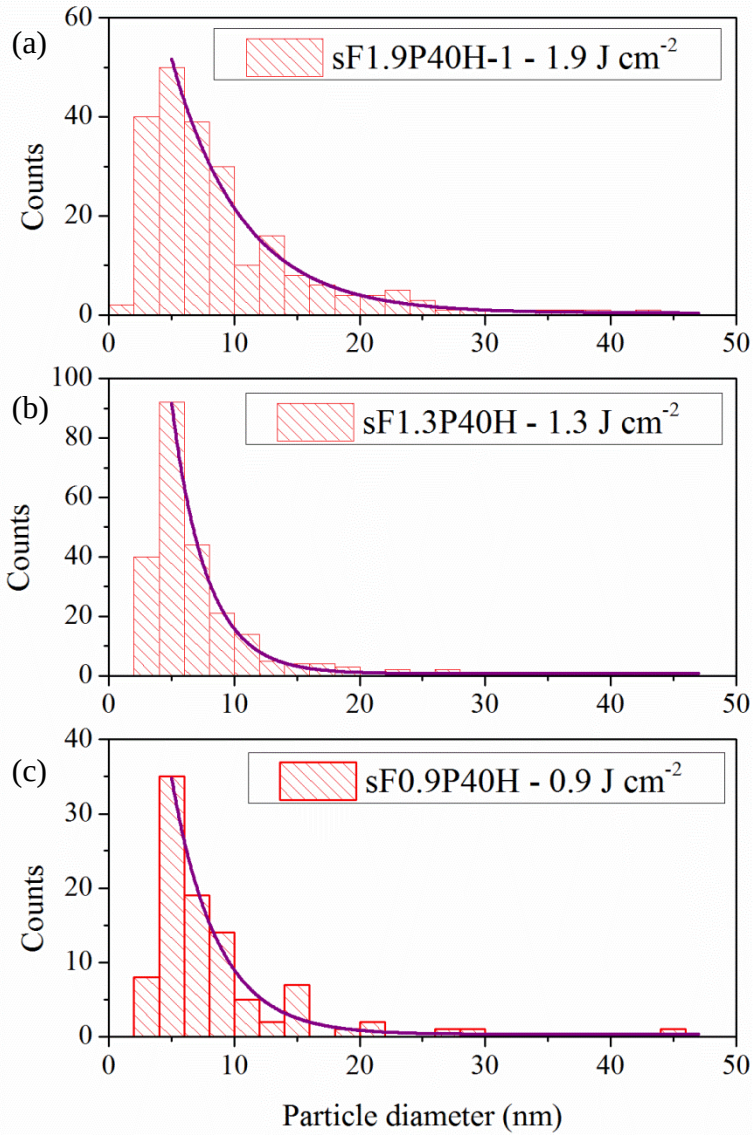

Figure 4.4. Histograms of the particle size distribution for samples deposited at different laser fluences at a fixed 4% hydrogen in Ar gas pressure of 40 mTorr: (a) sF1.9P40H-1 – 1.9 Jcm^{-2}; (b) sF1.3P40 - 1.3 Jcm^{-2} and (c) sF0.9P40 - 0.9 Jcm^{-2}

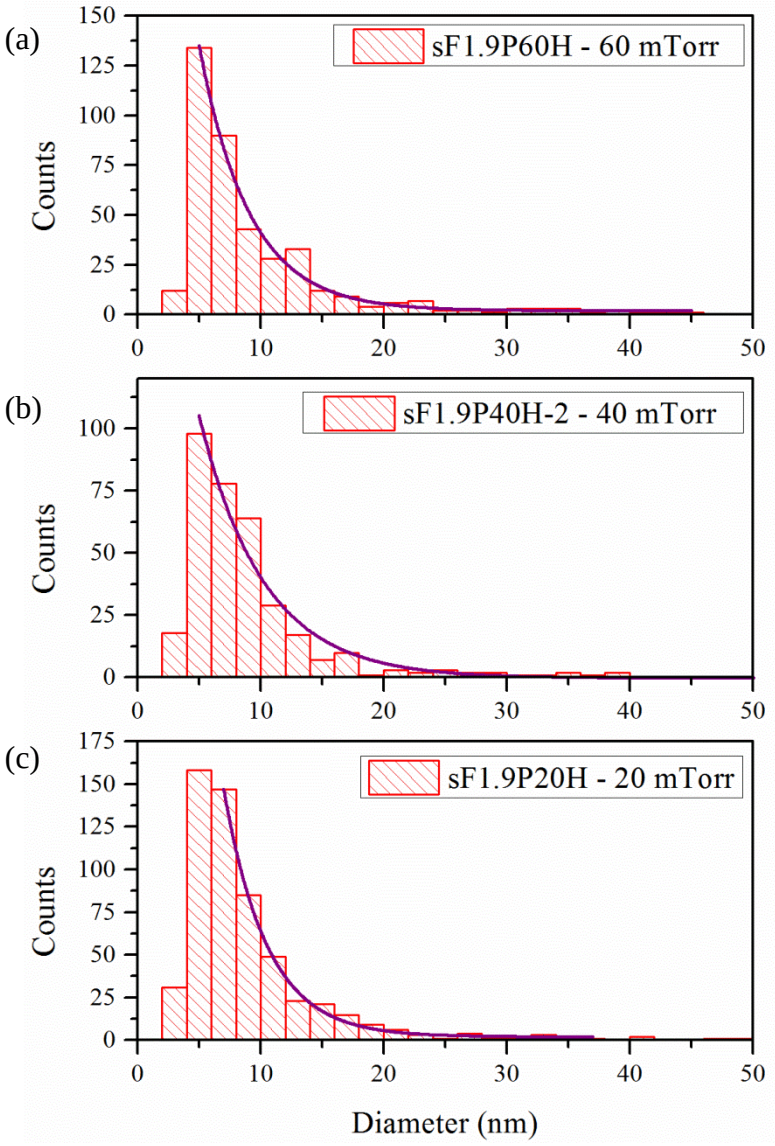

Figure 4.5. Histograms of the particle size distribution for samples deposited at different 4% hydrogen in Ar gas pressures at a fixed laser fluence of 1.9 Jcm^{-2}: (a) sF1.9P60H – 60 mTorr; (b) sF1.9P20H – 40 mTorr and (c) sF1.9P40H-2 – 20 mTorr

The exponential decays applied to the histograms of Figure 4.4 and Figure 4.5 are found to be consistent, aside from that of sF1.3P40H. The discrepancy between the exponential fit for sF1.3P40H and the other samples is ascribed to inconsistencies in the resolution of certain TEM images. This results in miscounts for the smaller particle sizes. For this reason, a minimum particle size for this characterisation was set at 5 nm, so as to avoid gross miscalculations.

The yield of nanoparticles of a larger size than that of the most abundant decreases exponentially as the particle size becomes larger [28]. The exponential

fits therefore convey this relationship, suggesting continuity with that of literature [4].

It is worth noting that the particle size distribution identified in literature, which matches the distribution profile depicted in Figure 4.4 and Figure 4.5 appears to resemble that of a log normal distribution. Fitting this to the current data however has not been attempted for the reasons already mentioned. A log normal distribution in particle size has been linked to particle growth by coalescence [126–128]. This meets with the current theory [7] describing the formation of particles at or just above the skin layer, following ablation.

Detailed understanding of the ablation mechanism cannot be acquired through the use of this system, as explained in section 3.1.1. In order to gain greater insight, specific diagnostic tools are required. Thus one can simply state that the observed particle size distribution reflects that reported in literature and is found to be consistent across this narrow range of laser energy and pressure regime described in Table 4.1. Amoruso *et al* [4] identified a mean particle size of 8 nm and was also able to identify the sub-5 nm particles, the particle size distribution identified alos found to fit to a log normal.

Note also that significant particle size variations with these experimental parameters is also not expected, as defined by Gamaly *et al* [28]. Gamaly identified that in order to generate a particle size distribution skewed to larger sizes, considerably higher pressures are required. For example to increase the average nanoparticle size from that found here by approximately 2 nm requires a pressure of approximately 50 Torr. Such pressures are not experimentally viable as the expansion of the plasma would be severely hindered. Similarly, in order to achieve smaller particle sizes, lower pressures would be required. At lower pressures however, the plume does not broaden sufficiently and thus a significant disparity in the thin film thickness occurs across the surface. This will be evident as a thick film in the centre (i.e. directly in line with the plume centre), thinning rapidly toward the edges. This is an experimental limitation of fs-PLD and must therefore be accounted for in order to fabricate continuous films across a substrate.

4.3.2. Thin film analysis of deposited silicon

The fundamental nature of ablation and the mechanisms involved [6–8,13,26,31,34,38,129,130] have been intensely studied by others. Additionally, the study of a targets surface following ablation [131–135] and short depositions of a sparsely distribution array of particles upon a surface [4,20,27,136] are also well documented. The resulting growth of a thin film via fs-PLD upon a substrate is however not as common in literature [37,39,137–140]. The study of thin film surface morphologies and influencing factors in their formation is therefore of interest to this developing field.

4.3.2.1. SEM characterisation of silicon thin films

Cross sectional secondary electron (SE)-SEM imaging of the samples described in Table 4.3 are presented in Figure 4.6. These samples were prepared for SEM in the manner described in chapter 3. Each image is acquired from the centre of the respective thin film by snapping the film through the centre of the substrate and then directing the microscope accordingly. The samples presented in Figure 4.6 represent the observed differences in the material cross section at a fixed laser fluence of 2.0 Jcm^{-2}, but varying substrate temperature and the gaseous environment. The observations of sample 1P0 in Figure 4.6 (a) in relation to the discussions in section 2.2.2 pertaining to fabrication in a vacuum are of importance for thin film fabrication by fs-PLD [4,34,35]. The surface features identified for this sample suggests a tremendous increase in the amount of material delivered to the centre of the substrate. This is due to the lack of lateral expansion for the plasma plume. This is plainly seen in comparison to 1P70Ar in Figure 4.6 (b) fabricated under identical conditions but for a dilute 70 mTorr Ar atmosphere.

It is also noticeable that the surface of 1P70Ar in Figure 4.6 (b) has a rather cauliflower-like topography. This is undesirable in a thin film due to the incompatibility with electrical contacts in addition to significant losses for photonic applications. It is found that these features can be significantly reduced by the inclusion of a small concentration of H_2 in the gaseous environment during fabrication. Similarly, fabrication in a 20 mTorr atmosphere is also found to reduce the clustering of depositing material. A reduction in the pressure is understood to decrease the number of collisions during the propagation of the plasma phase from the target surface. The increase in collisions thus reduces the kinetic energy of the

propagating plasma phase. With increased pressure (>100 mTorr) as with 1P120Ar in Figure 4.6 (i) a significant reduction in the amount of material deposited upon the surface is observed at the 70 mm target to substrate distance. This is due to the confinement of the plasma phase to a much smaller volume and subsequent redeposition upon the target. Thus if the target to substrate distance was lowered, a greater film growth rate would be observed. The deposited area would also shrink however, in a similar manner to fabrication at very low pressures. From these observations, it is therefore clear that the control of the particle size via the adjustment of the gas pressure, as proposed by Gamaly [28] is unrealistic for the fabrication of thin films.

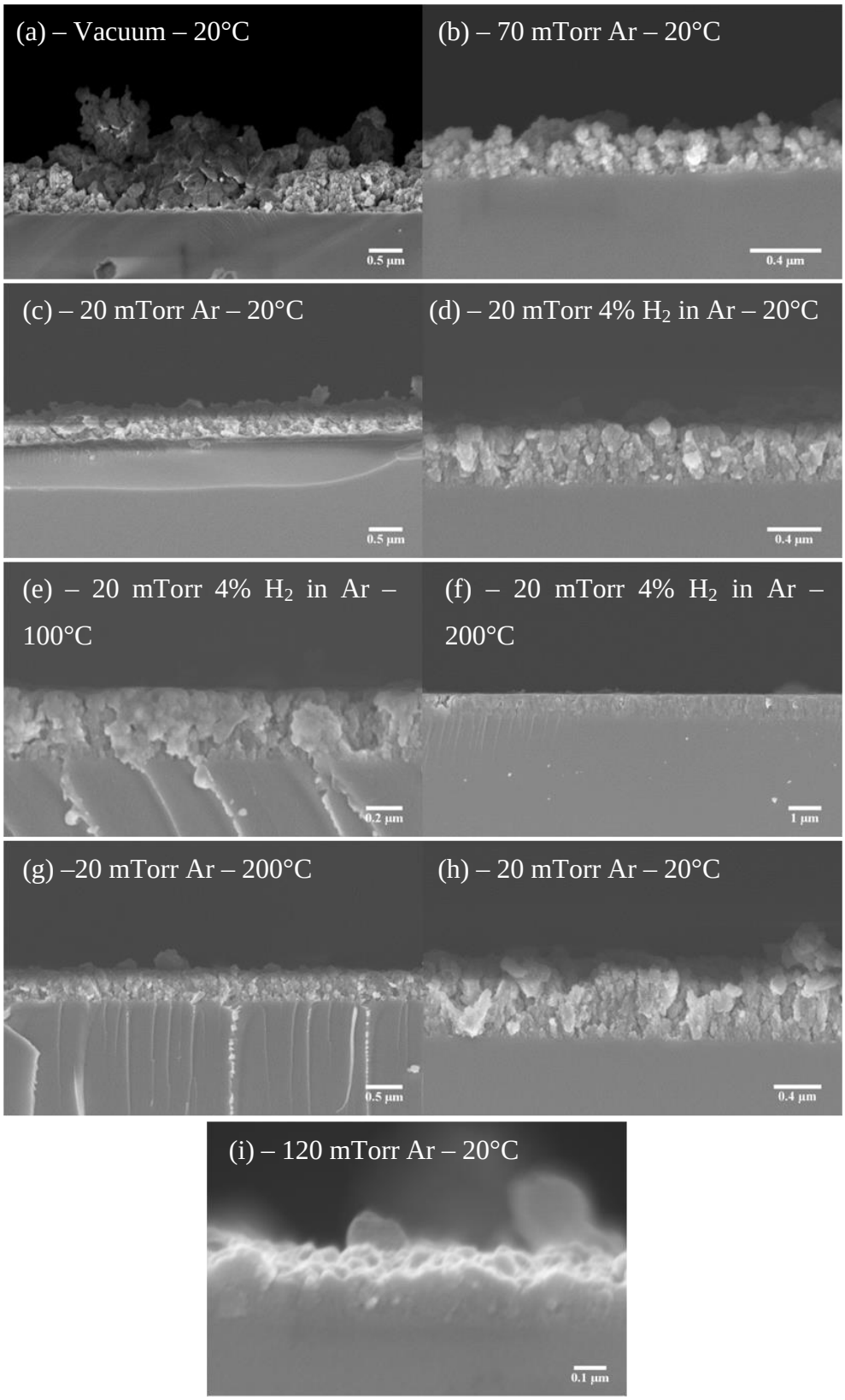

Figure 4.6. SE- SEM cross sectional images of (a) 1P0, (b) 1P70Ar, (c) 3T20Ar-1, (d) 3T20H, (e) 3T100H, (f) 3T200H, (g) 3T200Ar, (h) 3T20Ar-2 and (i) 1P120Ar

The inclusion of small concentrations of H_2 in the background gas is also found to reduce the clustering of the depositing particles, although this only becomes apparent at higher temperatures. Notice the distinct similarities between the cross sectional image of 3T20Ar-1 and 3T20H in Figure 4.6 (c) and (d), where a similar level of clustering and porosity is visible. As the temperature is increased to 100 °C in (e) then to 200 °C for (f), a distinct reduction in porosity and surface roughness is visible for fabrication in a 4% H_2 in Ar gas environment. Fabrication under identical conditions at 200 °C for 3T200Ar in Ar gas is depicted in Figure 4.6 (g), significant porosity is however still clear.

Alternate fabrication techniques, such as variants of CVD demonstrate considerable less porosity for the fabrication of silicon thin films for optoelectronic applications [141]. The well-established manufacturing processes associated with CVD offer considerable advantage over fs-PLD in this regard.

The effect of temperature in creating more favourable deposition conditions for thin film growth can be plainly understood. At higher temperatures, the depositing particles are given sufficient energy to reform upon the surface, thus the surface appears smoother and the porosity decreases to reduce surface energy.

4.3.2.2. Raman spectroscopy of amorphous and crystalline silicon material

As discussed in relation to the TEM analysis of the sub-monolayer samples, electron microscopy may not always convey a representative view of a given samples microstructure. μ-Raman spectroscopy can provide additional data to better describe a material. The Raman characterisation made for a selection of samples fabricated in 4% H_2 in Ar described in Table 4.4 are provided in Figure 4.7. These samples were fabricated due to the greater applicability to photonic and electronic applications based upon observations in section 4.3.2.1.

Figure 4.7 outlines several key features related to the deposition of silicon material by fs-PLD, but also with regard to the characterisation of silicon by Raman spectroscopy. Additionally, Figure 4.8 and Figure 4.9 provide the Raman spectra of multiple areas of samples 3T100Ar and 3T200Ar; recall that these samples are fabricated in an Ar atmosphere at elevated temperatures.

Silicon materials produce very distinctive Raman shifts in a given spectrum. The Raman spectrum of single-crystalline silicon, for example, is often used as a reference for calibration. The zero-centre one-phonon mode of silicon, denoted Γ_c,

is the lattice vibration corresponding to the Brillouin zone centre, also denoted Γ. In bulk single crystalline silicon, this is centred at 521 cm^{-1} and has an intense characteristic Lorentzian lineshape [142]. If the silicon should be in an amorphous state, this mode will have a Gaussian lineshape, centred at approximately 480 cm^{-1} [143]. This allows one to define the silicon being either in an amorphous, crystalline or mixed phase.

For silicon in a crystalline or mixed phase, where the crystallite size is below the Bohr exciton radius of silicon (i.e. 9.5 nm diameter), a characteristic red-shift in the Γ_c peak is be observed [144]. Measurements of these shifts can be used to infer the average particle size of the material [145]. One must however have detailed knowledge of the stresses upon the material [146], specifically the nanocrystallites. Much like the Scherrer equation used for XRD analysis, stresses upon nanocrystallites can induce additional changes in the characteristic Raman peak centre. Without prior knowledge of such factors, considerable errors can occur in the interpretation of the results [147]. A similar principle applies to the interpretation of a ratio of the amorphous and crystalline fraction in a given spectrum [148].

Due to the lack of knowledge regarding stresses on the Si particles, it is impossible to accurately interpret the amorphous to crystalline ratio or average particle size through Raman spectroscopy. One can however disregard these factors simply to provide a qualitative interpretation of crystalline and amorphous phases in a given spectrum. This is unfortunate, however direct interpretation is not necessary due to an incomplete view of the nature of the plasma plume. Alterations to the plasma plume, evident through *in situ* analysis of the plume fluorescence, would provide a greater insight into the defining factors influencing crystallisation. This would include the temperature of the depositing particles [3] which currently cannot be defined, as well as their velocity [149]. As noted in section 2.2.1, the intense temperatures that the plasma plume is likely to be at [3] upon impacting onto the silica substrate would result in an extremely rapid thermal quenching process. Such events are found to favour the formation of amorphous phases, however others have observed nanocrystalline material under a similar process [150].

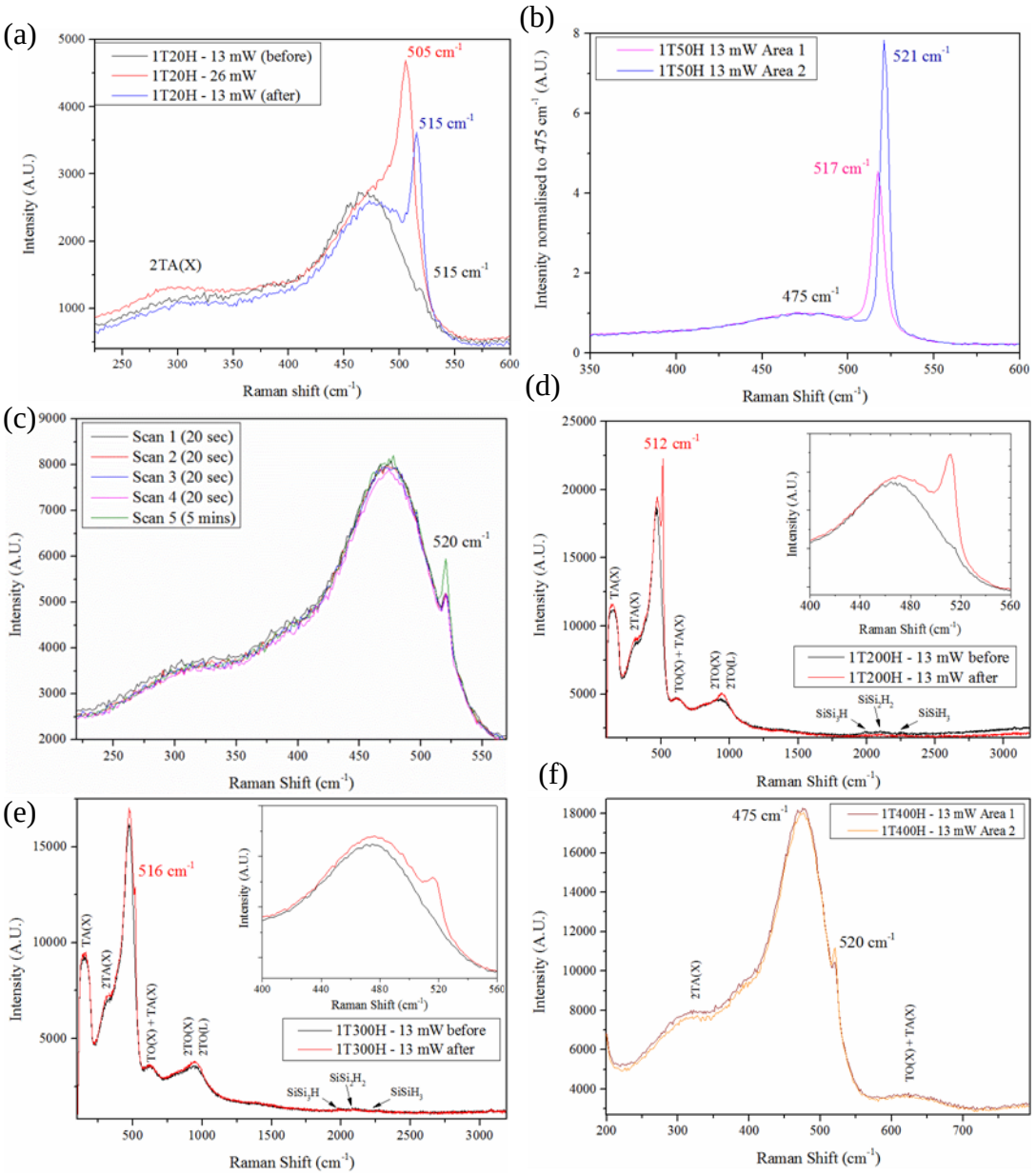

Figure 4.7. Raman spectroscopy of multiple areas or scans for samples (a) 1T20H, (b) 1T50H, (c) 1T100H, (d) 1T200H, (e) 1T300H and (f) 1T400H. The Γ_c of each spectra are illustrated upon the graph. The TO mode related to amorphous silicon is found to remain at 475 cm^{-1} for each spectra. A detailed description of each spectrum is provided in the text.

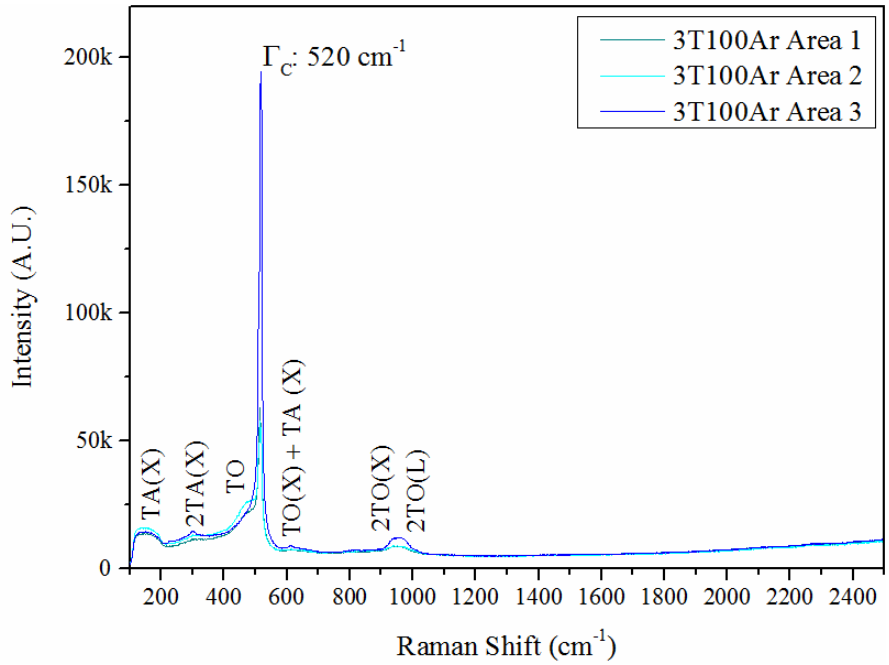

Figure 4.8. μ-Raman spectroscopy of 3 different areas of sample 3T100Ar with the zero-centre one-phonon mode for crystalline silicon (Γ_C) and the TO mode associated with amorphous silicon as well as other associated modes of crystalline silicon

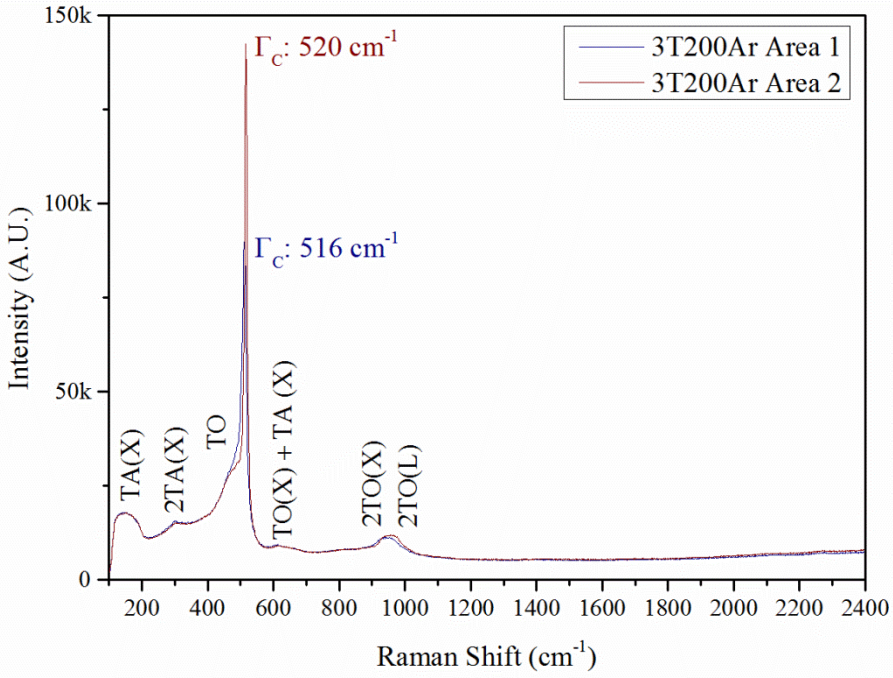

Figure 4.9. μ-Raman spectroscopy of 2 different areas of sample 3T200Ar with the zero centre one-phonon mode for crystalline silicon (Γ_C) and the TO mode associated with amorphous silicon as well as other associated modes of crystalline silicon. The shift in the peak position of the Γ_C mode has been illustrated.

The overall indication from the Raman spectra presented in Figure 4.7 is that the majority of the material is found in an amorphous state. Occasionally the Γ_c is observed when analysing multiple areas of a sample, however these appear to be random in nature. There is however a general trend to increased amorphisation with increases in the fabrication temperature as well as deposition in an dilute hydrogen atmosphere. The logical approach to quantify such factors is to conduct X-ray diffraction (XRD) studies. Following several long (>8 hours) scans however, no crystalline peaks could be identified. This indicates that the crystalline fraction is below the threshold for detection by XRD.

Evidence of laser induced crystallisation during Raman spectroscopy is also identified. Figure 4.7 (a) demonstrates an increase in the relative intensity of the Γ_c peak when 26 mW of laser power is used relative to a scan at the 'safe' 13 mW. This peak is then found to be more intense relative to the initial scan when conducted on the same spot at 13 mW laser power. 13 mW was identified as safe as it does not cause any alterations to the Raman spectra compared to observations at lower laser energies. This was determined by conducting several scans of the same area at different laser powers. 13 mW was determined to be the highest laser power before the onset of laser induced crystallisation. Figure 4.7 (c) of 1T50H demonstrates that this effect is not always as severe as with 1T20H. Repeated acquisitions following 20 second exposure times to 26 mW of laser power is found to result in negligible crystallisation. However, long exposure times are sufficient to induce crystallisation. The 5 minute exposure time used prior to acquiring scan 5 of Figure 4.7 (c) is typical of a short scan using Raman spectroscopy. A similar trend in laser-induced crystallinity is also identified for 1T200H and 1T300H in Figure 4.7 (d) and (e).

Evidence of H-bonding in the silicon thin films is also evidenced by the small cluster of weak peaks between 2000 and 2250 cm^{-1} [151]. This suggests that there is an interaction between the deposited material and the background gas. What remains uncertain is whether these interactions occur after deposition or in the plasma phase. Due to the extreme temperatures of the plasma phase [3] (>1000°C), the formation of H-bonds would be highly unlikely. Chemical interactions between the plasma phase and the background gas is also contested by others [28]. Thus hydrogen bonding likely occurs on the deposited material. Notice the absence of these peaks in the spectra for 3T100Ar and 3T200Ar in Figure 4.8, Figure 4.9. The

relative intensity of these hydrogen related peaks are however very low, this suggests that H-bonding is not as extensive compared to other fabrication techniques [152].

Observations of crystallinity are evidenced through example spectra of 1T50H in Figure 4.7 (b) and for 3T100Ar and 3T200Ar in Figure 4.8 and Figure 4.9. Due to the random distribution of this crystallinity, no clear mechanism to induce crystallisation has yet been identified. This would suggest that achieving high levels of crystallinity for a sample requires either high substrate temperatures, or another, as yet unidentified mechanism. This reduces the applicability of this fabrication technique for electronic devices [153]. The low conductivity of amorphous silicon has hindered the applicability of devices based upon this material, regardless of other favourable attributes, such as rare earth doping [78]. The low H-bonding in the samples presented in Figure 4.7 may be improved by higher H_2 concentrations, however this was not pursued.

4.3.2.3. Characterisation of the optical bandgap of deposited silicon thin films

Due to the nanoparticulate and relative mixed phase nature of the thin films, transmission spectroscopy can be of use to quantify the optical bandgap of these materials. As described in section 3.2.2, a Tauc plot of the absorption spectrum [154] for a silicon thin film can provide its optical bandgap, E_{opt}. This quantity is of great interest for defining the particulate nature a given material and its electronic states. Moreover, the observation of shifts in E_{opt} from that of bulk crystalline or amorphous silicon correspond to associated quantum confinement and other associated mechanisms [154–160].

Samples described in Table 4.5 were characterised by transmission spectroscopy. The resulting transmission spectrum was then related to their observed thicknesses in the manner described in section 3.2.2 so as to form a Tauc plot. The resulting data is presented in Figure 4.10 for the samples deposited at 5mTorr and Figure 4.11 for those deposited at 20 mTorr, both in 4% H_2 in Ar. These figures include the linear fits which have been continued to the x-intercept where the precise E_{opt} can be recorded.

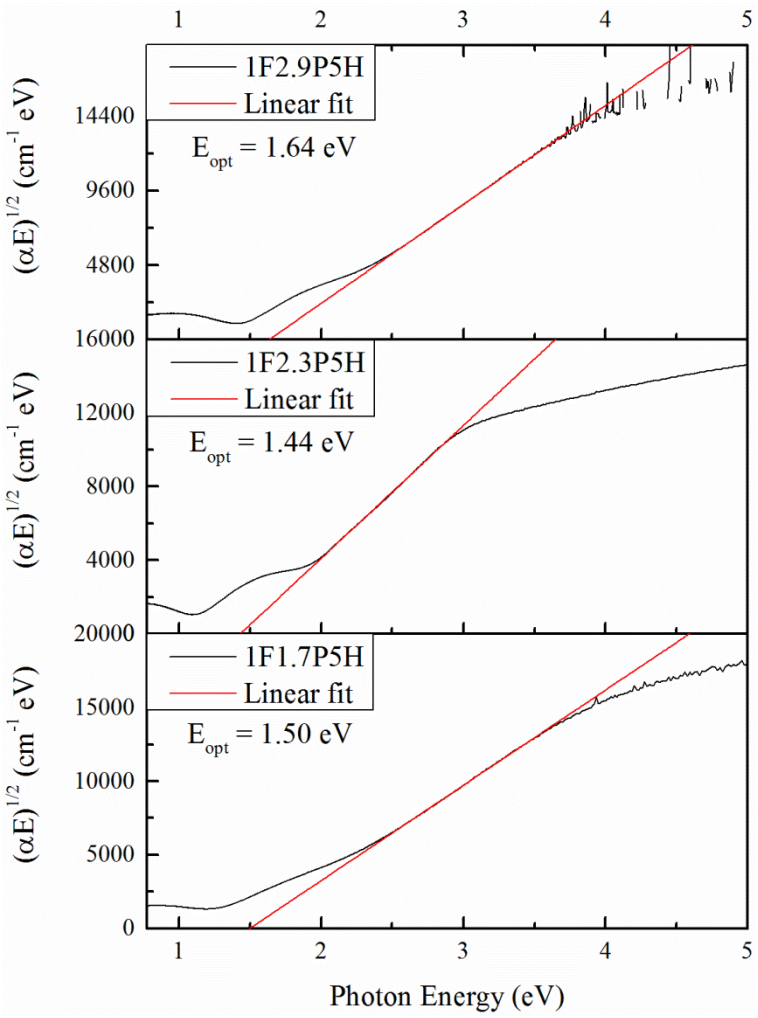

Figure 4.10. Tauc plots of samples fabricated at different laser energies in 5 mTorr of 4% H_2 in Ar: (a) 1F1.7P5H, (b) 1F2.3P5H. (c) 1F2.9P5H

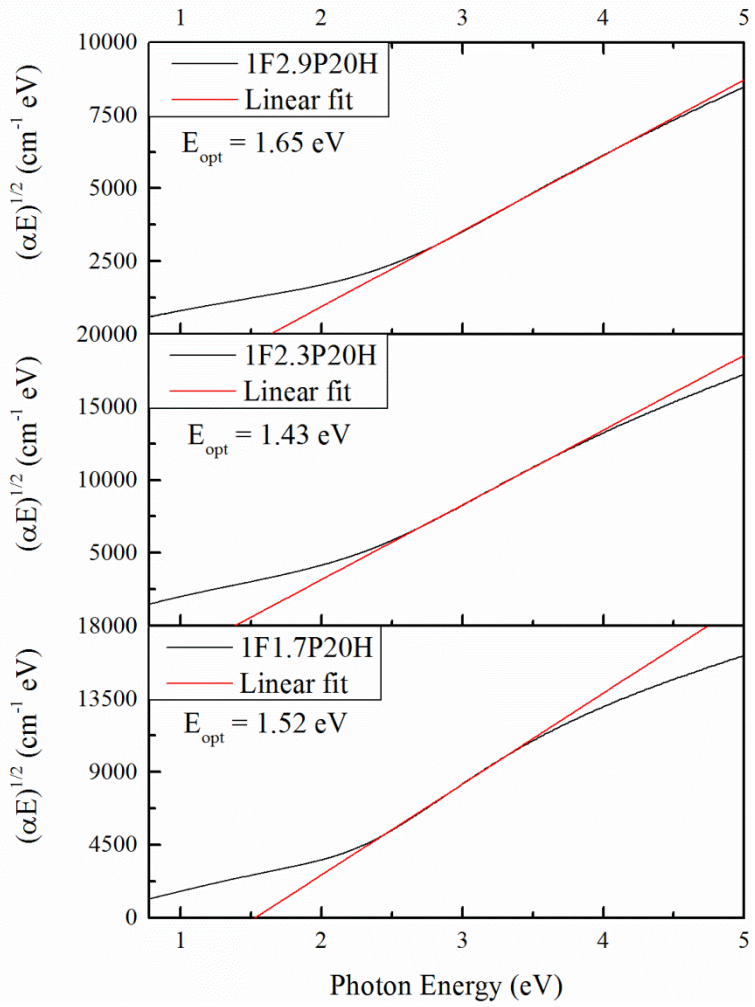

Figure 4.11. Tauc plots of samples fabricated at different laser energies in 20 mTorr of 4% H_2 in Ar: (a) 1F1.7P20H, (b) 1F2.3P20H. (c) 1F2.9P20H

A clear continuity is observed for the samples deposited at either 5 or 20 mTorr in a H_2/Ar atmosphere with respect to laser energy. This is in agreement with literature in that the laser fluence is the primary means of dictating the nature of the deposited material [3,27,129]. Similarly, no alteration is expected for the average particle size, as identified in section 4.3.1. The observed Tauc plot lineshape for these samples is the culmination of the effects of the amorphous phase as well as any crystalline material. Crystalline silicon at particle sizes below the Bohr exciton radius experience quantum confinement effects which results in an associated increase in the bandgap of the material [155,158,161]. This expansion in the bandgap is interpreted through the E_{opt}. Amorphous silicon is known to have a wide bandgap between 1.7 and 2.1 eV [162], thus the E_{opt} recorded for these spectra are primarily attributed to nc-Si.

The correlation between the observed E_{opt} and the laser fluence suggests the fluence may be utilised to engineer the nanocrystallite size. From previous sections however, this may not be significant, because without the ability to create a continuous coverage of the crystallites across the surface, this cannot be used for device fabrication. For application into photovoltaics for example, these materials would demonstrate poor electrical activity, thus reducing their applicability. The high concentration of amorphous silicon nanoparticles also creates large numbers of scattering centres as well as defect states which also have negative impacts upon a materials photoconductivity.

4.3.2.4. Attempts to electrically characterise multilayered thin films device architectures

The original goal of this thesis was the fabrication of multilayered silicon p-i-n structures aimed at photovoltaic devices. Attempts were made in this pursuit by the fabrication of a number of samples to be tested as part of a newly developed collaboration with a photovoltaic research group at Sheffield Hallam University. An example of the sample architecture is depicted in Figure 4.12. The samples fabricated included a range of different architectures involving thickness of each layer as well as those doped or undoped with the rare earth element Yb^{3+}. Yb^{3+} was used as a means to study possible energy transfer processes between the rare earth ion and Si, thus expanding the absorption window of a possible silicon photovoltaic device. Additionally, samples fabricated at varying temperature were also produced in accordance with the observations made in section 4.3.2.1.

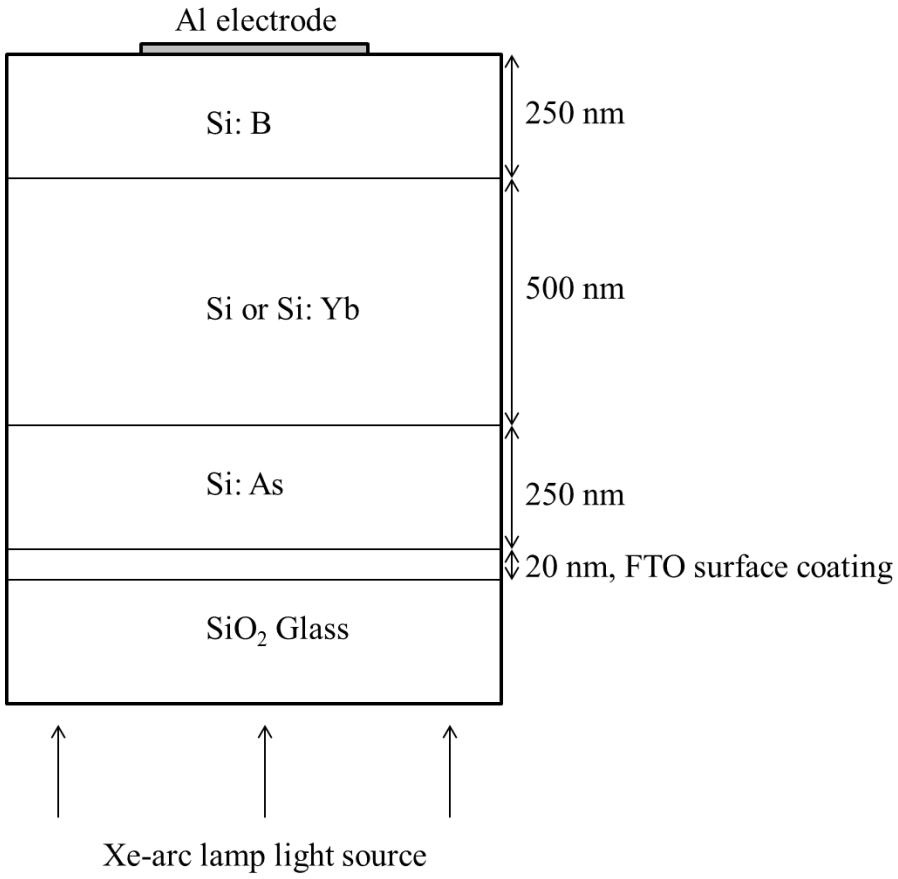

Figure 4.12. Device architecture for photovoltaic samples

Following fabrication, the surface of each sample was sputter coated with aluminium electrodes and electrically characterised. No measurable electrical activity could be detected from any sample tested. This included testing to see if the the material was conductive from an Al-electrode to exposed FTO. This was identified for each sample on multiple electrode spots. As will become clear in the ensuing chapters of this thesis, the likely cause of this effect is the modification of the FTO surface coating to one of increased resistivity. For room temperature experiments, this most likely occurred via subplantation of the FTO by the depositing silicon [163]. Upon acquisition of these results, the direction of this thesis was altered to its current state. This section is therefore included for completeness, but also to highlight the redirection of the thesis.

In comparison to other more established techniques for the production of thin film silicon photovoltaics, such as CVD, fs-PLD cannot compete [164–167]. Although the inclusion of rare earths is novel and would not be possible through

CVD, the lack of electrical activity negates this advantage, confining it to purely optical applications.

4.3.3. Characterisation of Tm^{3+}-doped silicon thin films

As defined in literature, an increase in the laser fluence for a femtosecond laser pulse will increase the depth at which ablation occurs from [28]. An increase in the depth of vaporisation, coupled with the inherently porous nature of a pressed powder pellet could encourage the formation of lanthanide-doped silicon particles to be ablated from the surface. Due to the distinct chemical similarity between lanthanide ions [168–172] this can be generalised to encompass all rare earth ions. It should be noted however that rare earth dopants amorphise the silicon lattice, thus are not expected to exist in crystalline particles [54]. The only incidence where the rare earth doped silicon may crystallise is upon the formation of rare earth silicides which are not favourable for fluorescence characteristics [54,173].

The samples which were fabricated for discussion in this section are defined in Table 4.7. All except one sample was fabricated from pressed powder pellet targets over the course of a 4 hour deposition. Sample 6Tm10Ar was fabricated over a 6 hour period by alternating 1 minute ablations from a two target arrangement. This included a mixed pressed powder pellet of 10 mol% Tm_2O_3 in Si and a single crystalline Si wafer, as used in previous sections. This sample is labelled 6Tm10Ar and was fabricated to assess any differences in the spectral features resulting from an increased probability of energy transfer from neighbouring silicon nanoparticulates. Nanoparticles of Si are found to absorb 808 nm very strongly, thus energy transfer is considered a possibility. The sample is deposited at room temperature to maximise the crystallinity of the sample and thus favour energy transfer.

As described in section 3.1.1, the modifications to the pressed powder pellet target surfaces strongly deters the fabrication of samples in excess of 4 hours in duration.

As expected, the fabricated thin films are found to be structurally identical to undoped silicon thin films shown for 6Tm10Ar in Figure 4.13. From this figure, the thickness of 6Tm10Ar was determined to be 0.8 μm thick. The refinements for decreased porosity and surface roughness described in the previous section are not implemented for these samples as repeated attempts at elevated substrate

temperatures produced no rare earth fluorescence. This is likely because sufficient energy is available for the lanthanide ions to cluster once deposited, thus quenching the fluorescence.

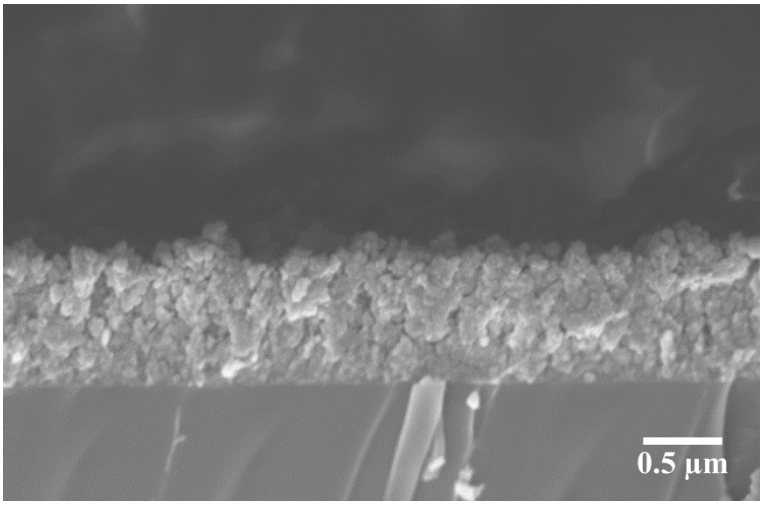

Figure 4.13. Cross sectional SE-SEM image of sample 6Tm10Ar. The thickness is determined to be 0.8 µm

The thin films were intensely analysed for their absorption spectra, as described in section 3.2.2, however no characteristic peaks could be detected. This is to be expected due to the significantly low lanthanide composition by volume in the submicron-thick films. Due to a lack of absorption data, full characterisation of the lanthanides by way of standard Judd-Offelt calculations cannot be conducted. Due to the only possible fluorescence from silicon between 700 to 800 nm [174] and no absorption in the mid-infrared region, no interference is expected for the Tm^{3+}: $^3F_4 \rightarrow {}^3H_6$ fluorescence. As noted in the introduction, this transparency region is one of the desirable characteristics of silicon as a host material.

Room temperature fluorescence spectroscopy of sample 6Tm10Ar for the $^3F_4 \rightarrow {}^3H_6$ transition of Tm^{3+}-dopants when excited with an 808 nm laser diode is presented in Figure 4.14. The peak emission, as depicted in the figure, is found to be 2043 nm with a FWHM of 164 nm and associated lifetime of 250 µs, determined from the decay profile in the inset of Figure 4.14 [137].

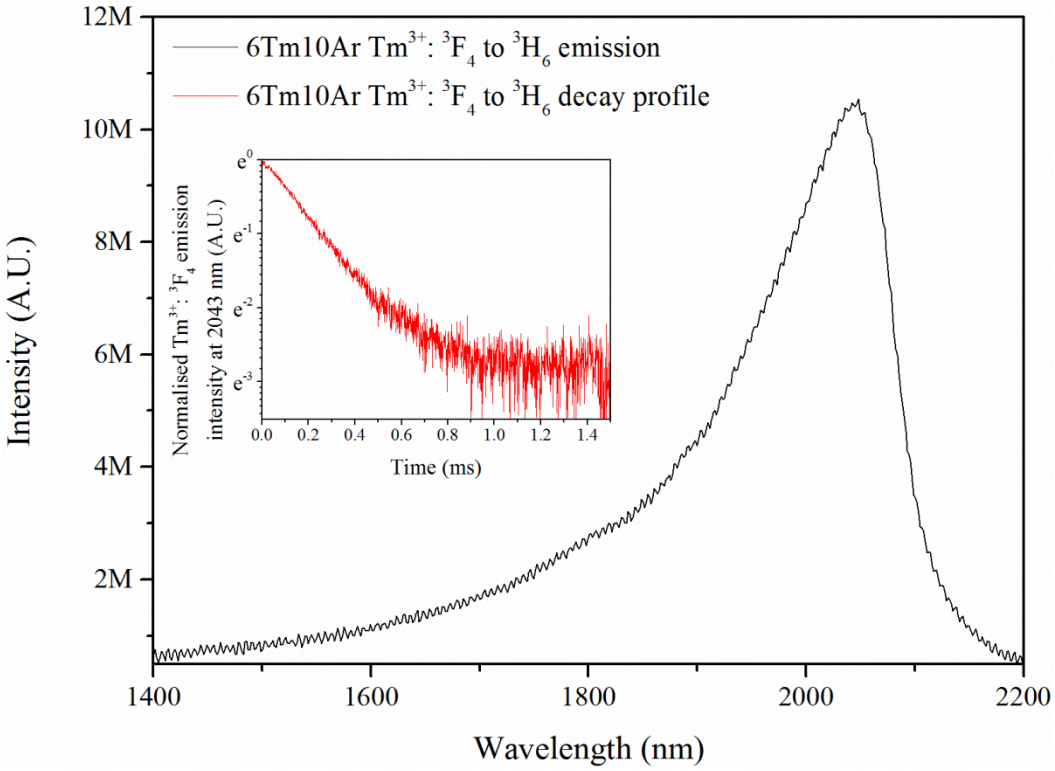

Figure 4.14. Room temperature photoluminescence spectrum of Tm^{3+}: $^3F_4 \rightarrow {}^3H_6$ transition from sample 6Tm10Ar composed of a 50-50 mix of Si and 10 mol% Tm_2O_3 in Si (further described in the text). Inset shows the fluorescence decay profile of this transition at 2043 nm.

Sample 4Tm1Ar, 4Tm2Ar, 4Tm3Ar and an undoped sample matching the fabrication parameters, 4Tm0Ar, were also characterised for room temperature fluorescence spectroscopy and are presented in Figure 4.15. The spectral features of these samples including the peak position, FWHM and the room temperature lifetimes are presented in Table 4.9.

Table 4.9. Table comparing the spectral features of the Tm^{3+}: $^3F_4 \rightarrow {}^3H_6$ transition in samples 6Tm10Ar, 4Tm1Ar, 4Tm2Ar and 4Tm3Ar

Sample ID	Peak position (nm)	FWHM (nm)	Lifetime (μs)
6Tm10Ar	2043	164	250
4Tm1Ar	2034	210	260
4Tm2Ar	2033	211	255
4Tm3Ar	2034	198	254

The observed photoluminescence lineshape for all samples thus far presented for Tm^{3+} doping appear inhomogenously broadened. There are however slight shoulders on the lower wavelength region of these spectra. Specifically they appear around 1800 and 1900 nm. The nature of these sub-peaks may be elucidated through a repeat observation at lower temperatures. A reduction in the temperature of the material would thus reduce the Stark level splitting of a given energy level. For a crystalline or polycrystalline material, this is seen as a reduction in the FWHM of the photoluminescence spectral lines. In disordered materials, observations at lower temperatures simply results in a reduction of the FWHM of the inhomogeneously broadened fluorescence. Thus if greater clarity emerges for these emission shoulders, it would suggests some of the Tm^{3+}-ions are in crystalline sites.

To study this, the samples 4Tm1Ar and 4Tm3Ar were cooled to 77 K using liquid nitrogen and studied for their photoluminescence properties. Incremental temperature photoluminescence measurements then acquired, with corresponding fluorescence lifetime measurements. Collective photoluminescence spectrums at these incremental temperatures for 4Tm1Ar are presented in Figure 4.16, while those for 4Tm3Ar are in Figure 4.17. The intensity of the 1855 nm peak for both samples became too weak at 250 K to acquire a clear decay profile, thus measurements are only reported up to here. There are associated losses due to the additional windows of the cryostat-housing. This reduces the intensity of the already weak emission signal. Reductions in the signal intensity relative to those made in ambient conditions in Figure 4.15 are therefore expected. The recorded fluorescence decay profiles of 4Tm1Ar and 4Tm3Ar at 77 and 250 K are provided in Figure 4.18. All fluorescence lifetime measurements are then presented in the Figure 4.19 to demonstrate its consistency over the temperature range.

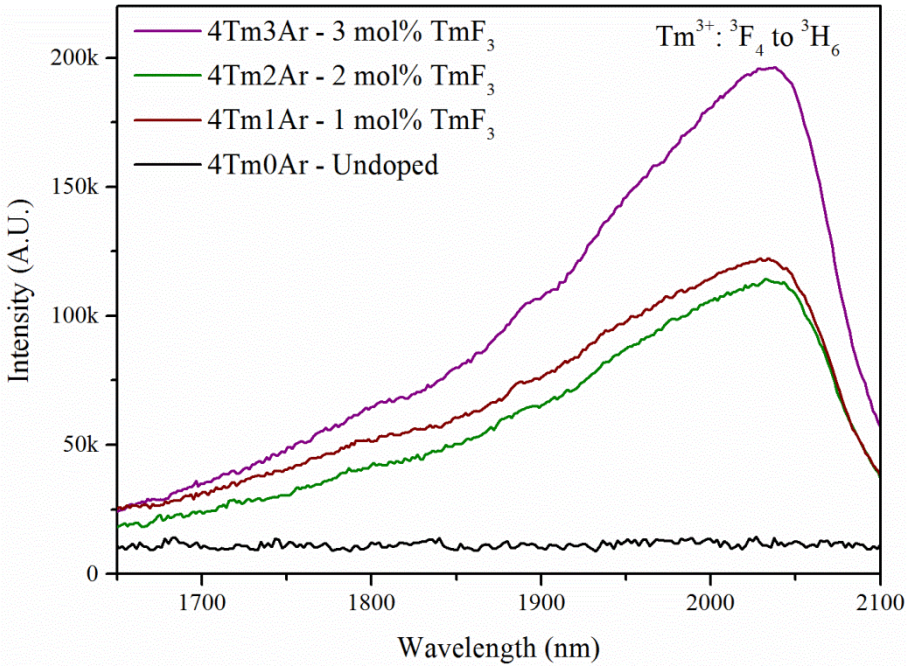

Figure 4.15. Room temperature photoluminescence spectrum of the Tm^{3+}: $^3F_4 \rightarrow$ $^3H_6$ transition for 0, 1, 2, 3 mol% TmF_3 doped Si thin films when excited with an 808 nm laser diode.

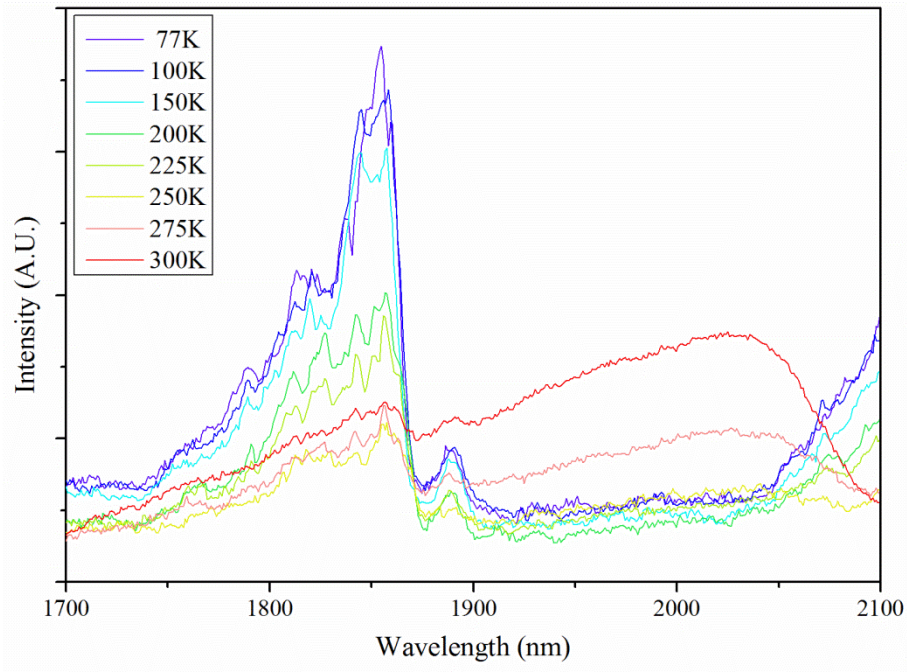

Figure 4.16. Photoluminescence spectrum of the Tm^{3+}: $^3F_4 \rightarrow$ $^3H_6$ transition in 4Tm1Ar (1 mol% TmF_3 in Si) at incremental temperatures from 77 K to 300 K when excited with an 808 nm laser diode.

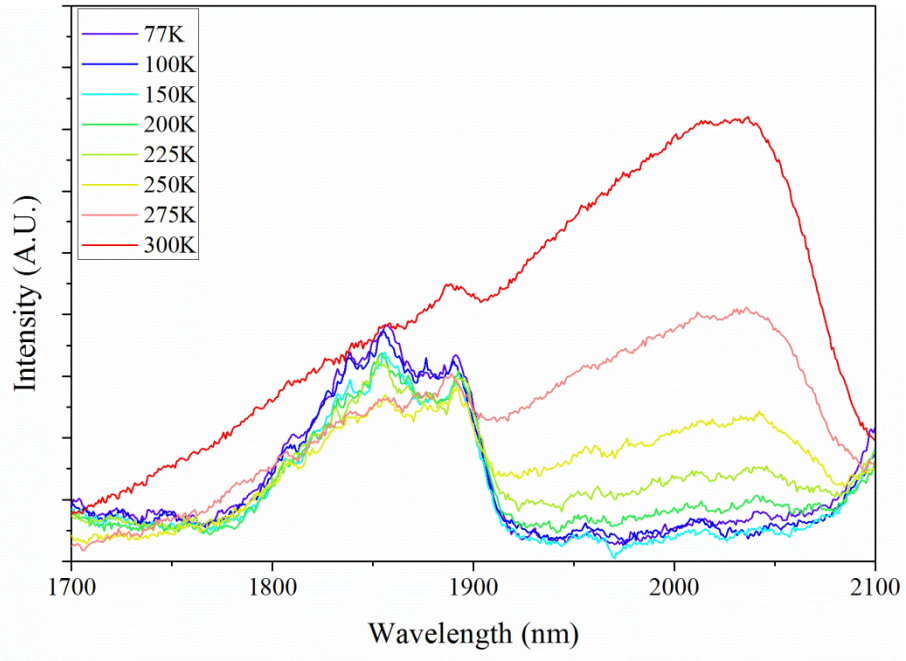

Figure 4.17. Photoluminescence spectrum of the Tm^{3+}: $^3F_4 \rightarrow {}^3H_6$ transition in 4Tm3Ar (3 mol% TmF_3 in Si) at incremental temperatures from 77 K to 300 K when excited with an 808 nm laser diode.

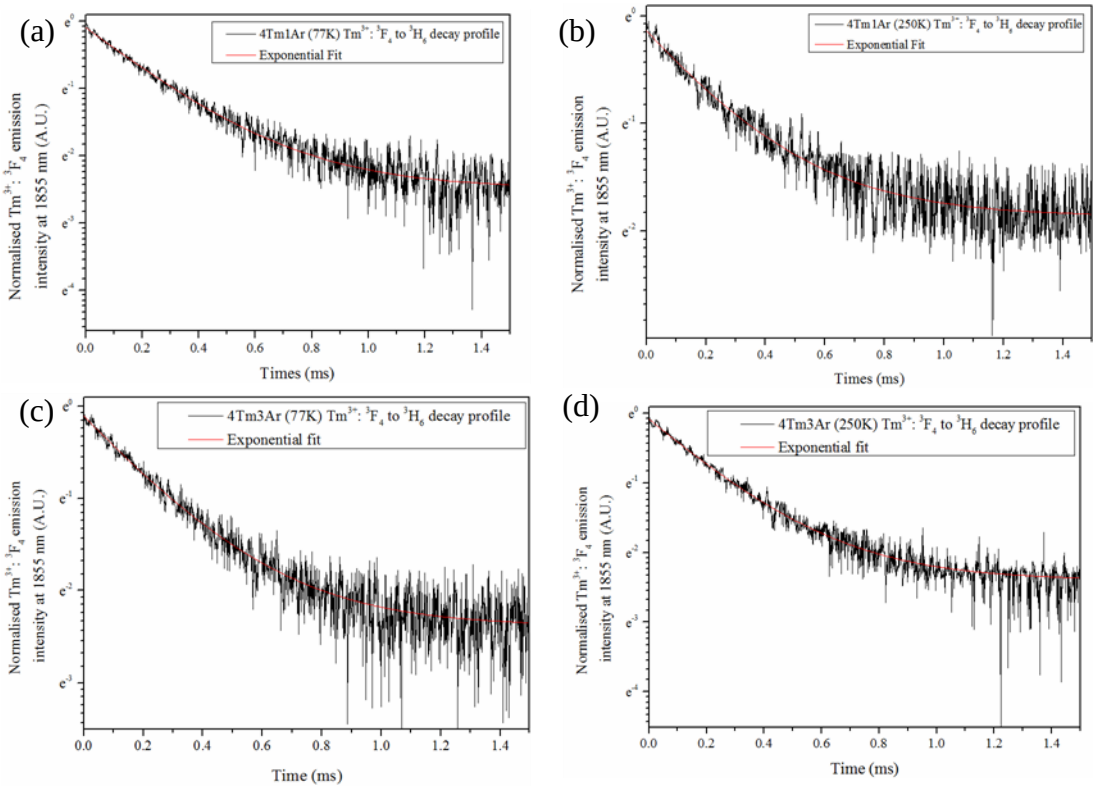

Figure 4.18. Fluorescence decay profiles for the Tm^{3+}: $^3F_4 \rightarrow {}^3H_6$ transition for 4Tm1Ar at (a) 77K and (b) 250 K; then for 4Tm3Ar at (c) 77 K and (d) 250 K.

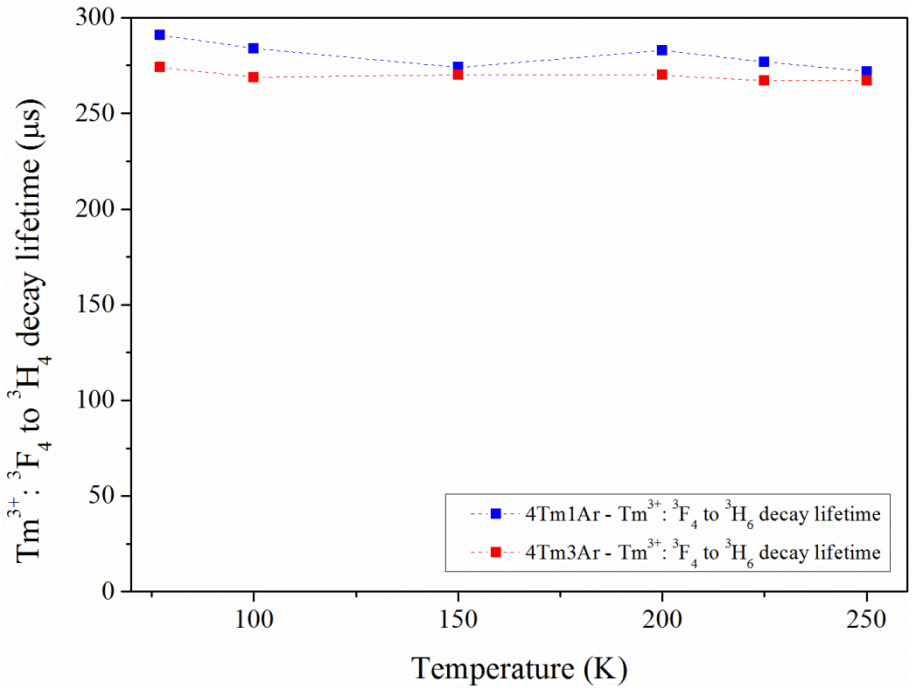

Figure 4.19. Collected fluorescence lifetime measurements at 1855 nm for the Tm^{3+}: $^3F_4 \rightarrow {}^3H_6$ transition in 4Tm1Ar and 4Tm3Ar between 77 K and 250 K

Figure 4.16 and Figure 4.17 for the incremental temperature photoluminescence of 4Tm1Ar and 4Tm3Ar, respectively, demonstrates a distinctive change in the emission characteristics with respect to temperature. There is also an increase in the emission intensity beyond 2050 nm for observations at lower temperatures. This is interpreted as instrumental interference as the sensitivity of the detector depreciates from here. This was the topic of much debate during analysis as the spectral features for this region very closely resembled what one would expect for vibronic transitions [59,175,176]. For this reason, extensive work was done to describe the observed photoluminescence as such, where a manuscript was prepared for submission. This was unfortunate, however it remains that the emergence of the peak fluorescence centred at 2034 nm has a clear temperature dependence. This may be understood as a temperature dependent energy transfer mechanism, such as for Er^3-doped crystalline silicon materials studied by others [75,177]. These materials, as described in section 2.4.1, suffer greatly from a temperature dependent energy backtransfer mechanism between states within silicons bandgap and the $^4I_{13/2}$ manifold of Er^{3+}-dopants [178]. For the current system, the bandgap of silicon can be expected to be larger than that of single crystalline silicon based upon the Tauc plots presented in section 4.3.2.3. Expected

defect states however could result in this energy backtransfer process, especially if the lanthanides 5d-states are hybridized with that of silicons conduction electrons [179].

As defined in section 4.3.2.3, the E_{opt} of the deposited silicon material is near resonance with 808 nm (1.53 eV), thus an efficient energy transfer process may occur between the Si host and the Tm^{3+}-dopants. This can be visualized from Figure 2.1. The available energy due to temperature at 77 K equates to 6.6 meV, up to 25.8 meV at 300 K which could be used to facilitate an energy transfer process between the host and the rare earth. This is suggestive of an energy transfer process resulting in a significant red-shift in the luminescence spectrum of Tm^{3+}-ions. This may be quantified by electron paramagnetic resonance as well as deep-level transient spectroscopy [82].

4.3.3.1. Determination of Tm^{3+} composition through TEM analysis

In order to quantify the concentration of Tm^{3+}-dopants in the deposited silicon thin films, the sample 6Tm10Ar was mechanically removed from its substrate and analysed by TEM as described in section 3.3.4.1. A series of images were collected of the samples and are presented in Figure 4.20. EDX analysis of the illustrated areas of Figure 4.20 are also quantified in Table 4.10.

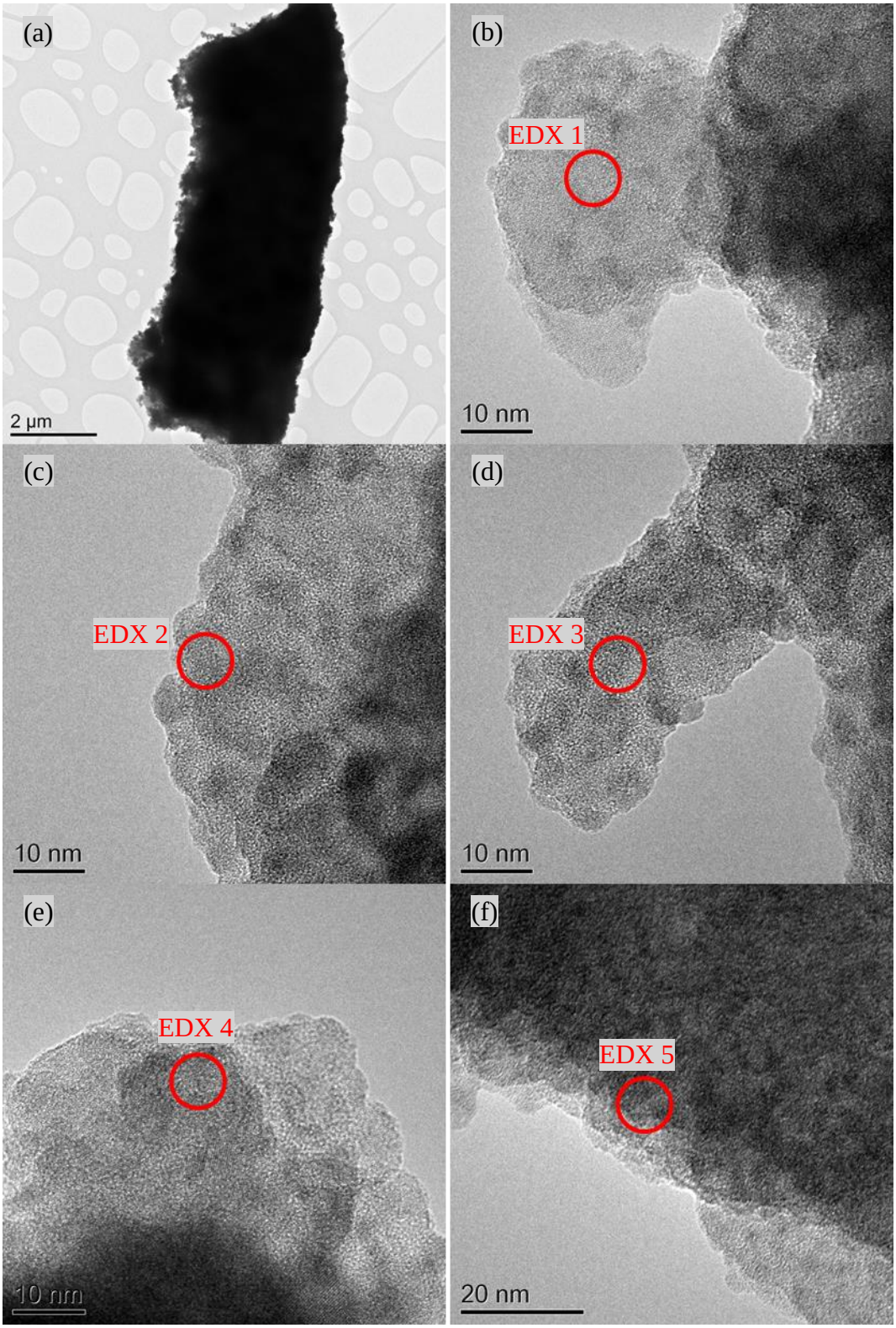

Figure 4.20. TEM images of sample 6Tm10Ar after it was mechanically removed from its substrate. (a) Image of a large section of the material from which (b) to (f) were acquired. Corresponding compositional EDX measurements are provided in Table 4.10

Table 4.10. Table of the compositional EDX data acquired from points across the surface of 6Tm10Ar, illustrated in Figure 4.20.

Element ID	EDX 1 (at%)	EDX 2 (at%)	EDX 3 (at%)	EDX 4 (at%)	EDX 5 (at%)
Si	92.0	77.0	85.2	90.9	91.3
Tm	8.0	23.0	14.8	9.1	8.7

The compositional analysis acquired through EDX spectroscopy provided in Table 4.10 demonstrates considerable local fluctuations across the material. This is particularly clear for the point EDX 2. The data described in Table 4.10 was acquired from areas approximately 5 nm wide, in order to test larger areas, this collection region was then expanded to approximately 50 nm wide. Over 10 separate areas from different clusters distributed across the TEM grid, an average composition of 92.1 at% and 7.9 at% ± 0.6 at% was identified for Si and Tm respectively. Therefore, a localised clustering of Tm^{3+}-dopants is apparent on the nanoscale, however on a larger scale, the actual concentration can be approximated to 8 at%.

Concentration quenching due to this high concentration and localised clustering can therefore explain the shortening of the fluorescence decay lifetime relative to similar systems and weak emission signal.

4.3.3.2. Laser micromachining of surface channel waveguides

The fabrication of surface channel waveguides was conducted using a re-orientation of the femtosecond pulsed laser beam normal to the surface, as described in section 3.1.3. Using a variety of laser powers and translation speeds, one can thus deduce the optimum working conditions for the fabrication of surface channel waveguides. This technique was applied to a section of the sample 6Tm10Ar to optimise the machining parameters and thus produce a surface channel waveguide structure. The primary advantages to using fs-LM is that it is a maskless technique which does not require the use of a clean room to operate. As described in section 2.2.1, the ablation process occurs non-thermally, thus resulting in very little damage to material outside of the focal point. This principle has been observed and

quantified by others, demonstrating a very limited influence upon surrounding Si material so long as certain laser thresholds are not exceeded [180].

Figure 4.21 provides 4 examples of differing laser energies applied to the surface and at different sample translation speeds. This provides a qualitative assessment of the side-wall quality of each channel.

At laser fluences below the threshold for ablation, a sintering process occurs, as with Figure 4.21 (a), thus showing only surface modification. It is interesting to note that the direction of the 'ripples' observed for this line correspond to the direction of polarisation of the laser [181]. The side walls of Figure 4.21 (c) and (d) appear extremely rough. This can be understood through the Gaussian profile of the laser pulse. The intensity of the extremities of the beam profile are considerably lower than at the centre, thus at high laser energies, or slower translation speeds sufficient energy is delivered to the edges to induce phase changes in the material. These effects can cause significant alterations to the side walls, as seen in the figure. Such features are highly undesirable as they would result in significant losses in the propagating light.

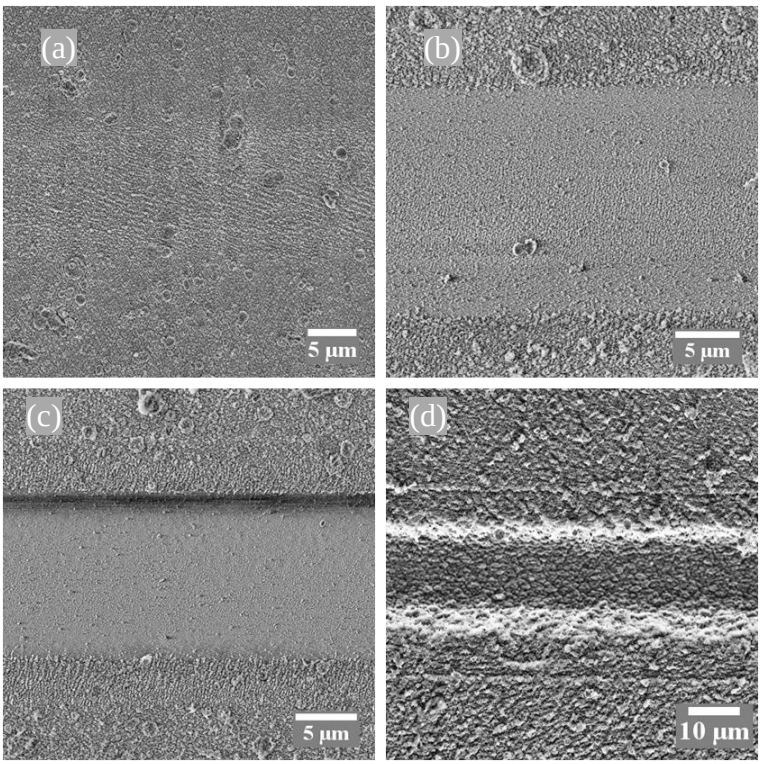

Figure 4.21. SE-SEM images of channels inscribed using (a) 0.5 µJ of laser energy and 2 mm/s translation speed; (b) 1.0 µJ of laser energy and 2 mm/s translation speed; (c) 2.0 µJ laser energy and 2 mm/s translation speed; (d) 3 µJ laser energy and 1 mm/s translation speed

Figure 4.21 (b) demonstrates a considerable reduction in the sintering of the side wall material, whilst a clear channel has been ablated from the surface of 6Tm10Ar. Based upon these observations, this channel was characterised by atomic force microscopy (AFM) using an Agilent Technologies 5420 AFM. Additionally, a fibre coupled 1550 nm laser (Agilent 81640A) was used to characterise the waveguides mode propagation. These are depicted in Figure 4.22 and Figure 4.23.

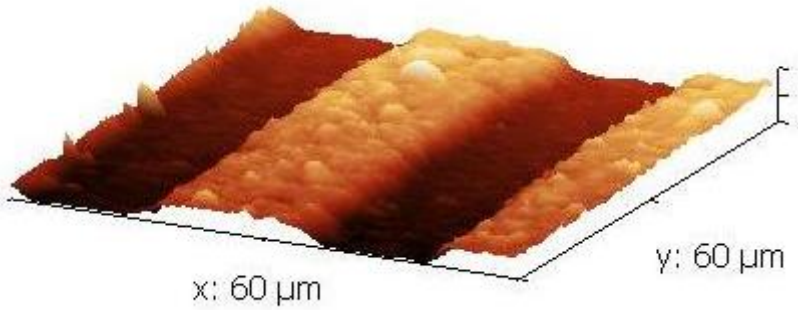

Figure 4.22. 3D-AFM image of the waveguide depicted in Figure 4.21(b), measuring 15 µm across (the z-axis reads 1 µm/division)

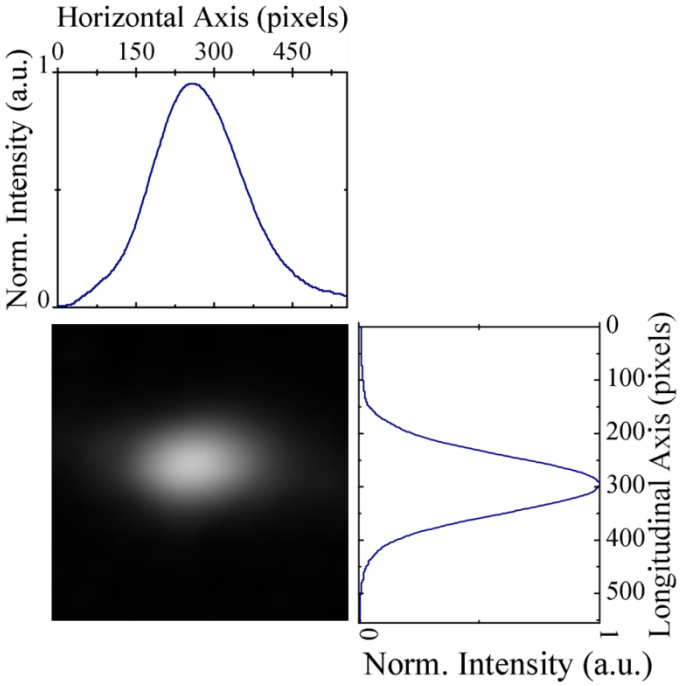

Figure 4.23. 1550 nm output mode profile observed from the waveguide. The Gaussian line shape of the x- and y-axis are representative of intensity.

The observation of a Gaussian mode profile demonstrates the applicability of fs-LM to films produced by fs-PLD. This was the first time these two techniques

had been combined, and thus demonstrates that an all fs-laser fabricated waveguide structure is possible. Due to the high degree of porosity evidenced in Figure 4.13 in addition to the end facets not being properly processed, significant losses are expected. These may be reduced however by refining the initial deposition technique, as in section 4.3.2.1. Recall, deposition at higher temperatures and in a dilute 4%H in Ar gas was found to reduce both surface roughness and porosity.

The highly undesirable material properties observed for these samples however suggests that an all-fs-laser fabricated waveguide system would not offer advantage over more established techniques [182]. As identified in earlier sections, the quality of the silicon thin films could not be improved beyond that achievable through alternate fabrication techniques. This is also true for waveguide fabrication, whereby far more functionality can be incorporated to better suited fabrication techniques [183].

4.3.4. Optical characterisation of Er^{3+}-doped silicon thin films

Er^{3+}-dopants are used to further explore the fluorescence characteristics of lanthanide doped silicon thin films fabricated by fs-PLD. The observed red-shifting of the Tm^{3+}: $^3F_4 \rightarrow {}^3H_6$ fluorescence spectrum suggested significant influences from the ligand environment and a possible energy transfer mechanism. Influences from the ligand environment can be attributed to a perturbation on the 4f-electron orbitals. The Tm^{3+}: $^3F_4 \rightarrow {}^3H_6$ transition is however defined as an induced electric dipole transition and hypersensitive, i.e. subject to discernible influences in the 4f-manifolds Stark levels and relative 4f-4f transition intensities. The Er^{3+}: $^4I_{13/2} \rightarrow {}^4I_{15/2}$ decay however has a mainly magnetic dipole transition character. Such transitions are far less sensitive to their environment and thus the lineshape and spectral intensity are often found to be invariant for a variety of hosts. The minor electric-dipole character however demonstrates some sensitivity to the environment which has been observed under certain conditions [184].

In the current fabrication regime, the Er^{3+}-ions would thus be subject to quantum confinement in nanoparticulate silicon as well as inhomogeneous broadening due to the range of dipole environments. Two samples, 4F0.59Er1Ar and 4F1.47Er1Ar, were deposited onto fused-silica substrates using 0.59 and 1.47 Jcm^{-2} laser fluence, respectively, from individual pressed powder pellet targets of Si mixed with 1 mol% Er_2O_3. Er^{3+}-ions are known to suffer from concentration

quenching [185] and there is no associated cross-relaxation mechanism, thus a lower concentration was utilised in reference to the Tm^{3+} study. The samples were characterised by fluorescence spectroscopy when excited to the $^4I_{11/2}$ manifold with a fibre coupled 974 nm laser diode. The $^4I_{11/2}$ manifold has a very short associated lifetime and thus decays rapidly to the $^4I_{13/2}$ state before decaying to the $^4I_{15/2}$ state. The observed fluorescence was studied in the 1400 to 1700 nm range using the NIR PMT detector. The observed fluorescence and fluorescence lifetime data associated with these samples is presented in Figure 4.24 and Figure 4.25 respectively. As indicated by the inset of Figure 4.24, the spectral lineshape of this transition is found to be near-identical for both samples. This suggests that Er^{3+}-dopants are in very similar local environments for both samples. The distinctive difference in the spectral features of this emission profile to the same in other host materials such as oxidised silicon fabricated by ns-PLD [186] or indeed amorphous silicon [153] is however compelling.

This suggests that there may be additional perturbations upon the 4f-electron cloud which are not observed in similar systems. The unusual fluorescence spectra of Tm^{3+}: $^3F_4 \rightarrow {}^3H_6$ reported in section 4.3.3 which is considerably more sensitive to the local environment agrees with this assertion. The decreased spectral intensity for sample 4F0.59Er1Ar relative to 4F1.47er1Ar may be suggestive of either a greater abundance of deposited material or a higher yield of optically active centres.

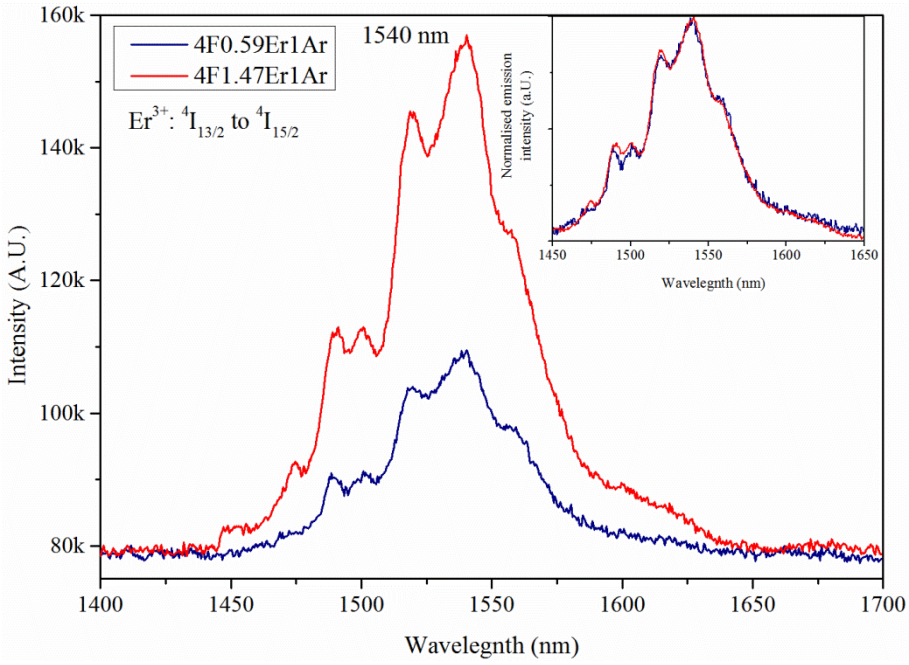

Figure 4.24. Room temperature photoluminescence of the Er^{3+}: $^4I_{13/2} \rightarrow {}^4I_{15/2}$ transition for samples 4F0.59Er1Ar and 4F1.47Er1Ar fabricated from individual pressed powder pellets of 1 mol% Er_2O_3 in Si. Inset shows an intensity normalised spectrum of the same emission spectra.

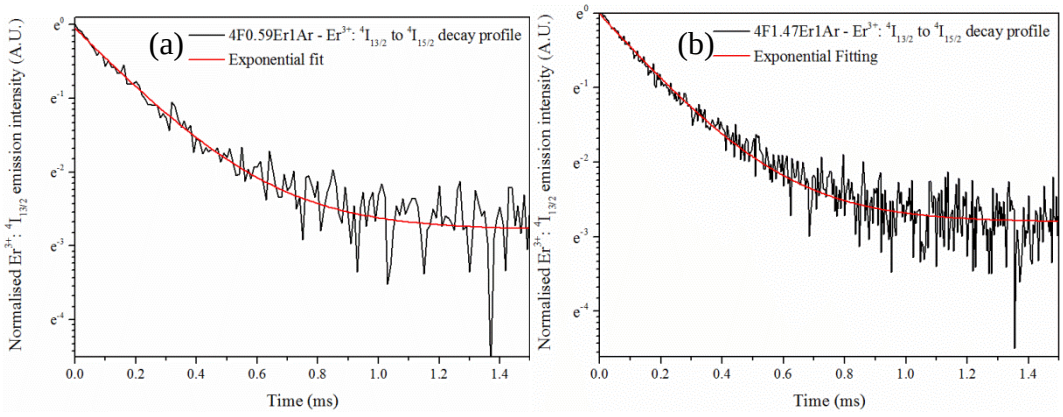

Figure 4.25. Fluorescence decay profiles for the Er^{3+}: $^4I_{13/2} \rightarrow {}^4I_{15/2}$ transition for samples (a) 4F0.59Er1Ar and (b) 4F1.47Er1Ar at room temperature

In order to better resolve the spectral features of this transition, low temperature photoluminescence measurements were conducted on 4F1.47Er1Ar and are reported in Figure 4.26.

The reduction in the FWHM of the spectral lines at 77 K is observed, due to the narrowing of the Stark levels of the Er^{3+}-manifolds. This is accompanied by a slight shift in the primary peak centre as the temperature is raised. This shift is due

to the increased number of transitions occurring from lower Stark levels in the excited state to the ground level.

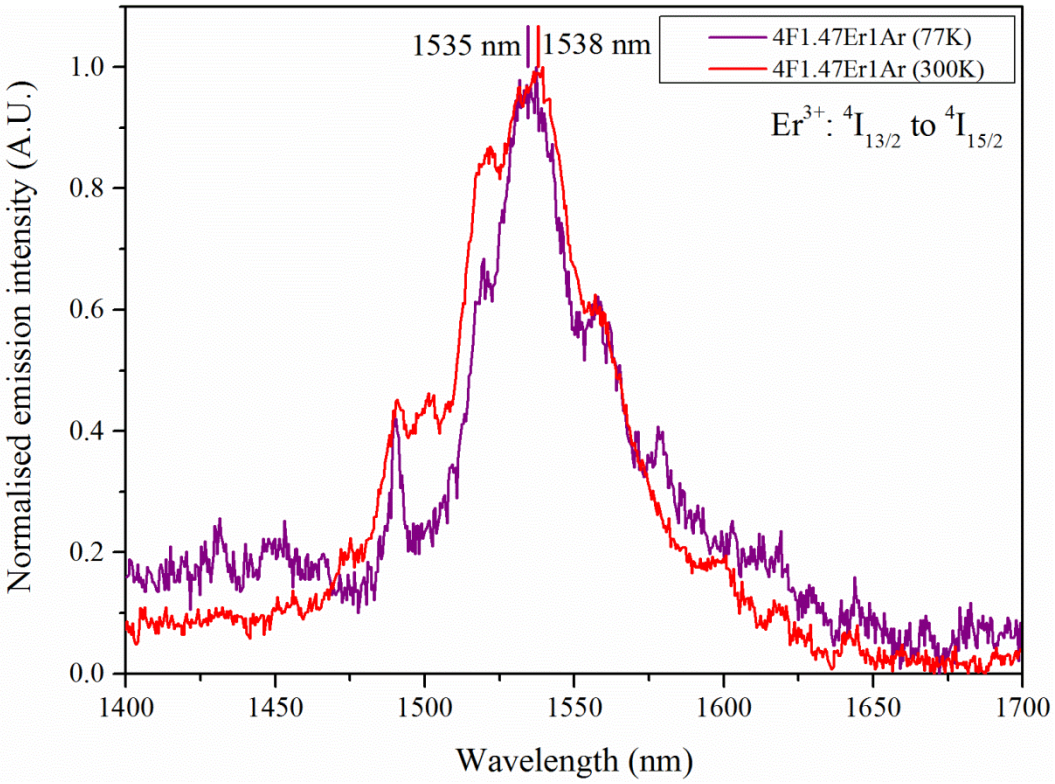

Figure 4.26. Room temperature (red) and 77 K (purple) photoluminescence spectrums for the Er^{3+}: $^4I_{13/2} \rightarrow {}^4I_{15/2}$ for sample 4F1.47Er1Ar. The peak centres are marked to indicate the red-shift due increased temperature.

There are two primary influences upon the fluorescence spectra of the Er^{3+}-ions and thus why they do not match with that of Er^{3+}-doped amorphous silicon. One is that the coordinating ligands may be oxygen, thus the perturbation upon the 4f-manifolds of Er^{3+} are different. Alternatively, quantum confinement of the dopants within an amorphous silicon nanoparticle may be resulting in additional perturbations upon the various manifolds.

4.4. Conclusions

The fabrication of silicon thin films and rare earth (Tm^{3+} and Er^{3+}) doped silicon thin films upon inexpensive fused silica substrates by femtosecond pulsed laser deposition is demonstrated. These materials are characterised both optically and structurally. It is found that the thin film morphology can be influenced by raising the substrate temperature to 200 °C in a dilute 4% H_2 in Ar gas atmosphere. The degree of crystallinity within these materials however is found to be randomly distributed, as identified through Raman spectroscopy. This severely limits their applicability for devices as has been experienced by amorphous silicon thin films fabricated by other means.

Photovoltaic devices were also fabricated, however the electrical properties were found to be severely hindered by a subplantation process occurring during the initial stages of the fabrication. This resulted in a loss of electrical activity due to the extensive damage to the transparent conductive FTO layer.

Rare earth doped silicon thin films have been fabricated for the first time by femtosecond pulsed laser deposition. Photoluminescence of the Tm^{3+}: $^3F_4 \rightarrow {}^3H_6$ and the Er^{3+}: $^4I_{13/2} \rightarrow {}^4I_{11/2}$ transitions are observed across a range of temperatures. Tm^{3+}-emission is found to have a distinct temperature dependency, indicative of an energy transfer process. The local environment of these dopants however remains unclear as standard Judd-Offelt calculations are not possible due to the lack of absorption data.

Surface channel waveguides have also been fabricated from a Tm^{3+}: doped silicon thin film. The machining parameters have been refined so as to optimise the side wall quality of the waveguide structures. These were found to be 1 μJ of laser energy with a 2 mm/s translation speed. A 1550 nm laser was launched through the optimised waveguide and an output was detected. This was deemed to have a high loss factor due to the porosity and abundance of grain boundaries which act as scattering centres. Direction to improve this has been provided, yet it is not believed this methodology would be competitive with conventional routes. Higher temperatures during fs-PLD would likely cause undesirable interactions with the silica substrate. As will be seen in subsequent chapters, this would likely result in a graded refractive index, leading to further losses.

Chapter 5.
Femtosecond pulsed laser assisted surface modification of silicon substrates I: 30 to 60 minute ablations

This chapter describes the use of femtosecond pulsed laser generated plasma from a TZN glass for the rapid growth of surface and subsurface crystallites on a silicon substrate. X-ray diffraction in conjunction with Raman spectroscopy reveals both ZnTe and Te nanocrystallites in the subsurface of the substrates. Combined with cross-sectional SEM and top-down backscattered SEM analysis, it is therefore concluded that these crystallites are found in a sedimentary layer in the subsurface of the silicon substrate.

5.1. Introduction

Femtosecond pulsed laser deposition (fs-PLD) technique has long been studied for the ablation of a target material [1,2,32,36]. Similarly, the ablated material is studied for its composition and particle nature [27,38], and occasionally the growth of thin films [39,140,187]. This current direction of research has discovered some of the key aspects of the ablation mechanisms as well as the nature of the plasma phase [28]. It would appear however that no studies have been dedicated toward the interaction of the plasma phase with a substrate material.

The applicability of fs-PLD to the fabrication of devices and applications of interest to industry is severely lacking, primarily due to more established alternatives. For nano- and micro-fabrication techniques upon a surface, chemical vapour deposition (CVD) has been widely used for decades to produce thin film materials and surface coatings [188,189]. This technique however can require the use of highly dangerous precursor gasses as well as being limited to singular reactions for the gasses employed [190]. The vast array of possible target materials and background gasses available to fs-PLD alleviate such constraints. Through the combination of an appropriate set of precursor materials in the form of the target, substrate and gaseous environment, one can thus explore the possibility inducing surface modification and complex chemical interactions in a high temperature environment. Thus, it may be possible to drive reactions and therefore develop a

novel direction for femtosecond pulsed laser based fabrication and materials engineering techniques.

This chapter thus introduces the concept of modifying the surface of a silicon substrate through the use of a tellurite glass target [63]. This glass is selected due to the array of semiconductor materials which may form through such interactions, such as ZnTe, ZnO and Si_2Te_3 [96,191,192].

5.2. Fabrication parameters

A full description of the experimental procedure adopted for these samples is provided in section 3.1.2. In order to study the proposed surface modification of a silicon substrate by femtosecond pulsed laser generated plasma a series of samples based on 30, 60 and 240 minute fabrication times were chosen. This does not include the length of time required during the cooling process described in section 3.1.2. This section is dedicated to the study of the 30 minute fabrication times, while 60 minutes is discussed in the next section and 240 minutes in subsequent chapters. In this manner, the evolution of the materials can be characterised and discussed and a greater understanding of the layer growth can be gained as a result. For this purpose, a series of samples were fabricated for short durations; these are D30-1, D30-2, D60-1 and D60-2.

As detailed in Table 5.1, the deposition times are the only variables in these samples. The fixed experimental parameters are defined in Table 5.2 while the different target materials used for experimentation are provided in Table 5.3. The selection of the experimental parameters used for the samples in Table 5.1 is based upon experimental observations not provided here. As will be discussed in chapter 5, high substrate temperatures are required in order to initiate implantation. At lower temperatures, implantation into the substrate decreases and appears as deposition. 50 μJ of laser energy was selected due to preliminary investigations at higher and lower energies. High laser energies (>100 μJ) can cause the newly formed film to delaminate from the surface, too low and the plasma phase will have insufficient energy to penetrate the surface. The Ar gas is used to drive oxygen deprivation in the vacuum chamber which has interesting consequences for the material interactions, as will be seen in section 5.3.3.4.

Table 5.1. Table of the key variables in the fabrication of samples discussed in this chapter.

Sample ID	**Laser energy (μJ)**	**Temperature (°C)**	**Gas type**	**Duration (minutes)**	**Target material**	**Substrate**
D30-2	50	570	Ar	30	G0	Silicon
D30-1	50	570	Ar	30	G0	Silicon
D60-1	50	570	Ar	60	G0	Silicon
D60-2	50	570	Ar	60	G2	Silicon
G0-4	50	20	Ar	30	G0	Fused silicate

Table 5.2. Table of the fixed experimental paramters applied to all samples in this chapter

Pressure	70 mTorr
Target to substrate distance	70 mm
Target and substrate rotations	20 rpm

Table 5.3 Table of the target materials used in the fabrication process, including key composition data

Target ID	**Fabrication Process**	**Composition**
G0	Standard glass making procedure	TZN (77:10:10): 3 wt% Tm_2O_3
G2	Powder pressed	TeO_2

5.3. Results and Discussion

5.3.1. Characterisation of starting silicon substrate

For the purposes of a concise discussion, it is prudent to begin with basic observations of the starting silicon substrate. A sample was prepared whereby the substrate itself was exposed to all the same treatments as a 4 hour fabricated sample in Ar gas, except the laser was never used. Henceforth, this sample shall be referred to as the 'dry run' sample. Such a sample therefore alleviates concerns as to the effects of the processing treatments on the substrate. For this purpose, cross sectional and top-down SEM images were acquired as well as cross-sectional TEM analysis to study the extent of the oxide layer and for general observations of the topography itself. This is presented in Figure 5.1 and Figure 5.2 respectively. In the TEM analysis provided in Figure 5.2, the epoxy from the processing stage is still visible on the image. This is left in view intentionally so as to ensure the 'true' surface can be seen, and not a region exposed from the grinding process, i.e. one in which the oxide layer may have been ground away. In addition to this, Raman spectroscopy and X-ray diffraction are used to reaffirm both the chemical composition as well as the crystallinity of the silicon substrate in Figure 5.3 and Figure 5.4, respectively.

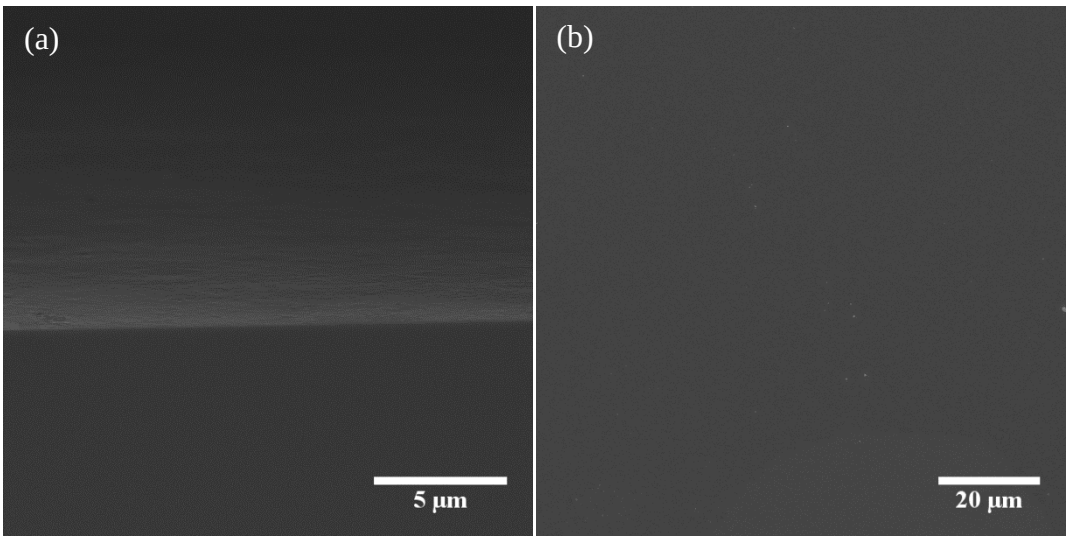

Figure 5.1. SE-SEM images of (a) a cross section of the dry run sample and (b) a top down image of its surface

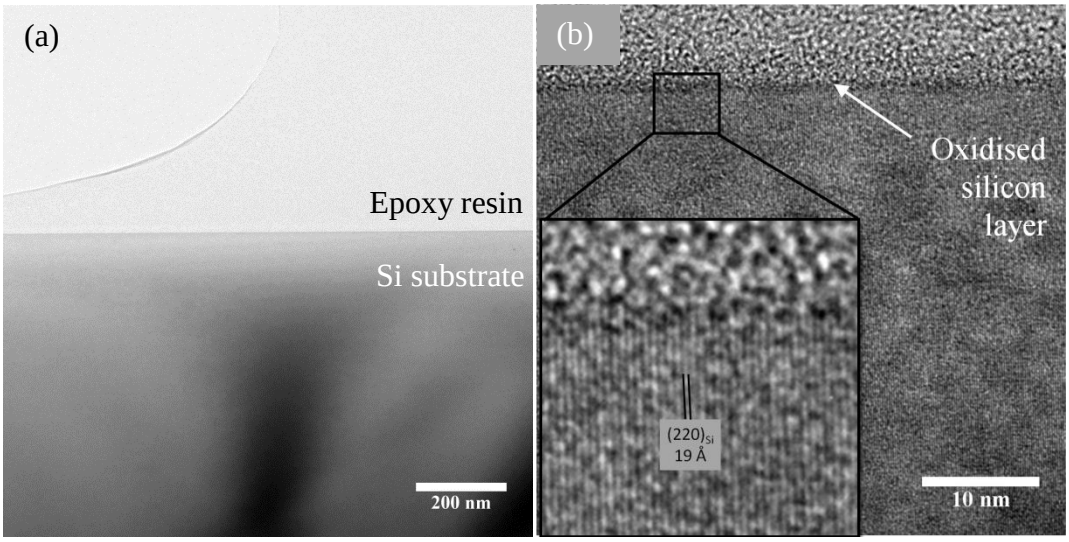

Figure 5.2. Cross sectional TEM images the dry run sample, (a) low magnification image revealing the interface between the residual epoxy layer and the silicon wafer, (b) high magnification image if the interface as well as an inset of the crystal planes in which the (220) Si plane is visible, as well as the 90 Å thick oxide layer.

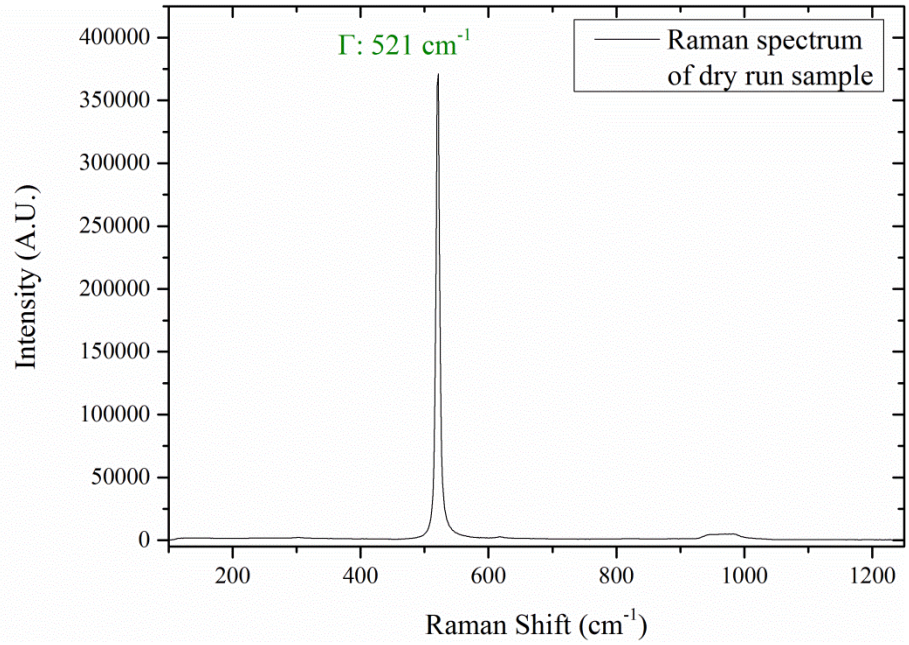

Figure 5.3. Raman spectroscopy of the dry run sample, including the peak position of the zero-centre one-phonon mode (Γ) of single crystalline silicon

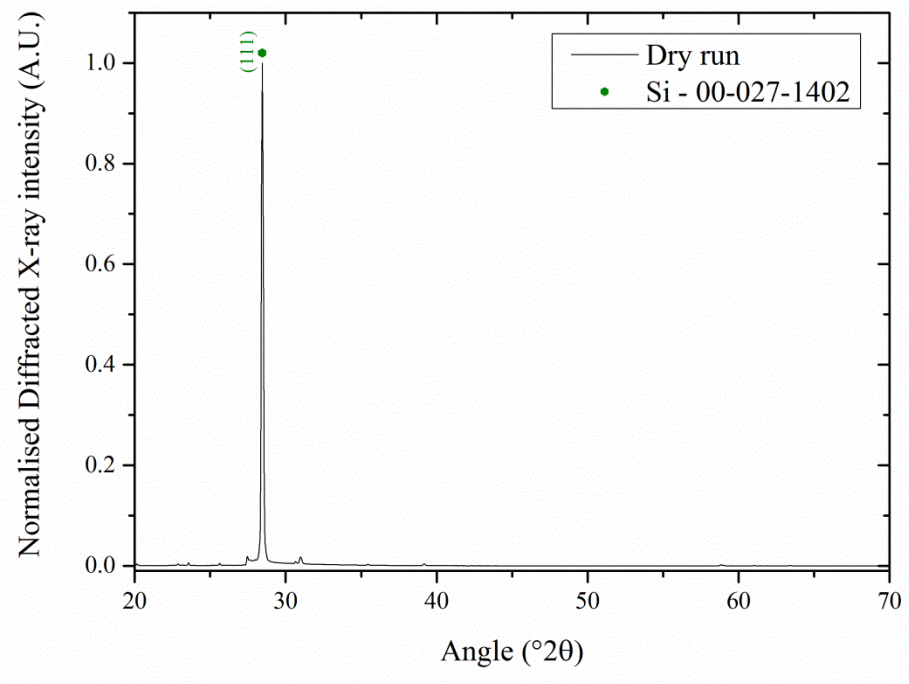

Figure 5.4. XRD spectrum of dry run sample, corresponding to single crystalline silicon (ICCD ref: 00-027-1402). The sample was analysed with a slight off-set in order to acquire the crystal peaks as the wafer is cut at an off-axis

From the cross sectional SE-SEM image in Figure 5.1 (a), a continuous and flat surface is visible with no discernible debris, this too is reflected in the top-down SE-SEM image in Figure 5.1 (b), indicating an ideal surface in which to experiment with for surface modification. In addition to this, both cross sectional TEM images reveal the surface layer to be extremely flat and crystalline up to where a thin oxide layer is identified, measured as approximately 90 Å thick. In the inset of Figure 5.2 (b), the (220) crystal plane is identified via the spacings between the lattice. The (220) plane is orientated perpendicular to the surface of the substrate, i.e. where it is cut, suggesting the wafer itself had been cut along the (100) plane, which is typical for Si processing. This is also indicated by the singular notch cut perpendicular to the [011] direction on the starting Si wafer.

Raman and X-ray diffraction analysis also suggest a single crystalline Si material. The absence of additional peaks in the XRD data is suggestive of a single crystalline material, where only the (111) plane is observed. Raman spectroscopy is used as a means of complementing this assessment with the observation of an intense peak at the precise location of single crystalline silicon [193].

The acquisition of this data provides a useful insight into the starting substrate which will become invaluable throughout this chapter as well as those to

follow. Using this knowledge, a more accurate and informed assessment of the fabricated samples can commence.

5.3.2. Characterisation of surface modification following 30 minutes of laser ablation

5.3.2.1. Surface topography characterisation

Secondary-electron scanning electron microscopy (SE-SEM) images of the surface of sample D30-1 are provided in Figure 5.5. These images were acquired using the LEO 1530 FEG-SEM with a 15.0 kV accelerating voltage in the inLens orientation for high resolution imaging of secondary electrons.

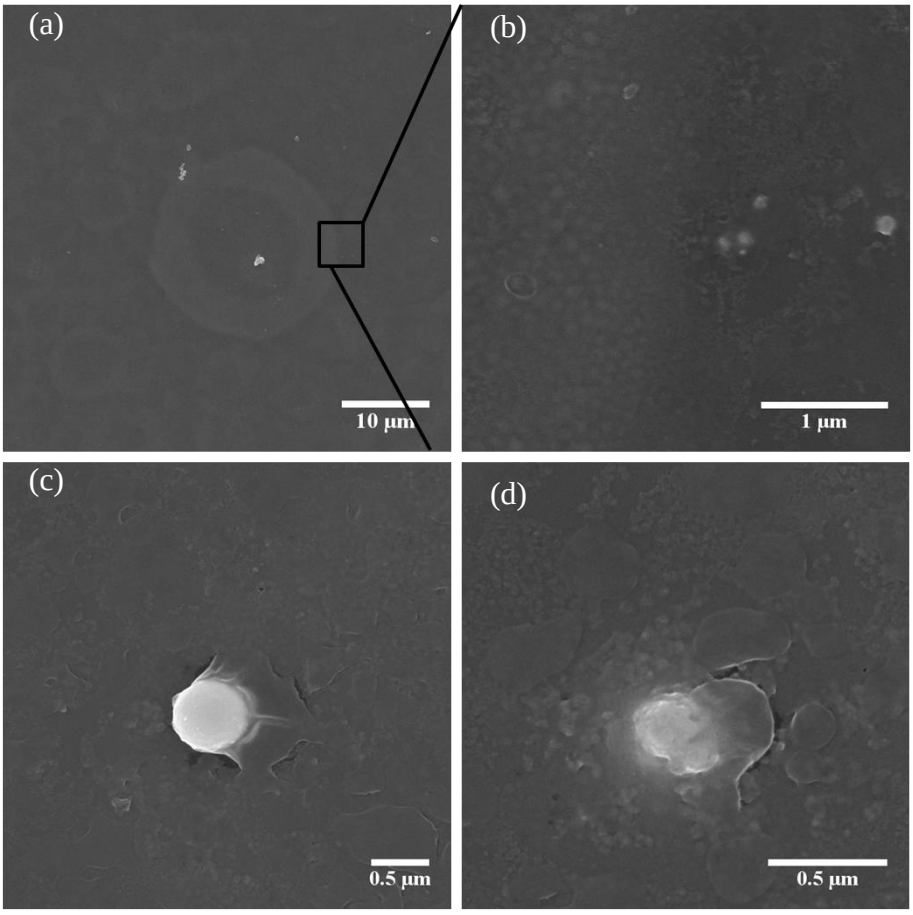

Figure 5.5. Top-down SE-SEM images of areas of interest from the surface material of sample D30-1, including: (a) a toroid formation, (b) a higher magnification of the edge of one the toroid depicted in (a), (c) and (d) unknown material propagating upward

The toroid formations in Figure 5.5 (a) appear somewhat similar to those identified by Volkov *et at* [194] for femtosecond laser generated Ge ions implanted into Si substrates. In Volkov's findings however, the toroid deposits appear to be a continuous surface layer, as opposed to the collage of smaller particulates which make up those observed for D30-1, as indicated by SEM analysis in Figure 5.5 (b). It is probable that this is due to the surface tension between the surface deposits and the underlying substrate. As identified earlier in Figure 5.2, a thin SiO_x layer on the surface of the silicon substrate has been identified and for describing surface tension, and hence wettability, one need only consider the uppermost surface atoms of a substrate [195]. With this in mind, the surface of the substrate can be considered as a silica layer for discussing interfacial interactions. Observations by Da *et al* [196] identified complete wetting of a silica surface by TZN glass (75:10:15) above 500 °C. This was studied in great detail with respect to variations in the contact angle between the TZN deposit and the silica surface, where the contact angle is found to increase with temperature from approximately 375 ºC. Due to its significance in this work, it has been reproduced in Figure 5.6 [196].

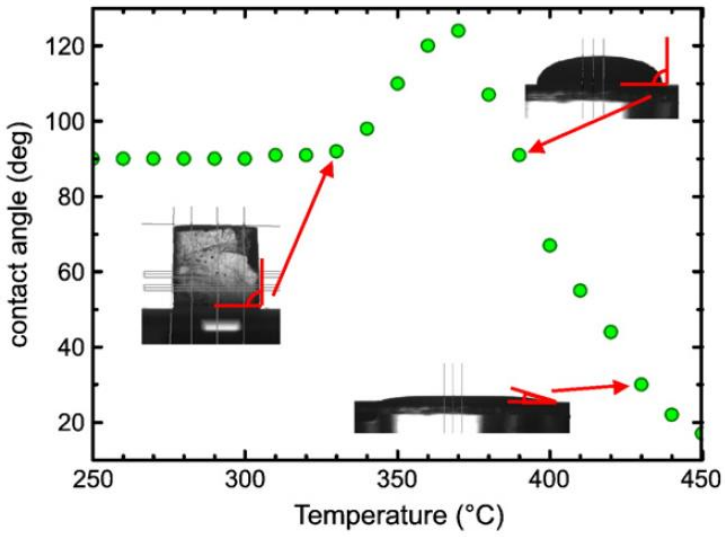

Figure 5.6. Optical dilatometry study of the wetting angle made by TZN on a silica surface for a heating rate of 3 K/min. Reproduced from reference [196]

Although no scale is provided for the particle size in Figure 5.6, they are quoted as being part of a macroscopic study, suggesting a larger particle size to the micron and sub-micron sized particles observed for D30-1.

If one considers a TZN microparticle on a silica surface, the difference between its internal pressure and the 70 mTorr external pressure, Δp, should be quite substantial, relative to that of a macroscopic system. This is expressed in relation to the surface tension,γ, using the well-known Young-Laplace equation [197,198]:

$$\Delta \boldsymbol{p} = \boldsymbol{\gamma}\left(\frac{\mathbf{1}}{\boldsymbol{R_x}} + \frac{\mathbf{1}}{\boldsymbol{R_y}}\right) \qquad \textbf{(5.1.)}$$

Where R_x and R_y are the radii components of curvature for the respective axes of a particle on a surface.

The relationship expressed in equation 4.1 accounts for differences in pressure between a particle and its surroundings, which is convenient for the present system, however another highly influential component to be considered is that of temperature. Temperature is known to have a significant impact on the surface tension, where increases in temperature will result in a decrease in surface tension This is expressed in the following relationship [198]:

$$\boldsymbol{\gamma} = \boldsymbol{\gamma_0}\left(\mathbf{1} - \frac{\boldsymbol{T}}{\boldsymbol{T_c}}\right)^{\boldsymbol{n}} \qquad \textbf{(5.2.)}$$

Where γ_0 is a constant, T_c is the critical temperature and n is an empirical factor. Equation 4.2 suggests that the 'hot' impacting particles, found during fabrication, are likely to have the required temperature to induce wetting of the silica surface, as was found by Da *et* al [196]. Based upon the aforementioned principles, one can envisage two possible reasons for the formation of these nanoparticle toroid collages:

(1) *A result of the cooling process at the end of the experiment*. The cooling process is relatively gentle and should therefore allow ample time for the surface structures to relax;
(2) *Rapid thermal quenching of recently deposited material*. As has been stated previously, the effective temperature of particles in the plasma phase close to a substrate can be in excess of 1000°C, but would rapidly cool to meet the surface equilibrium temperature of approximately 570 °C.

To better understand this process in relation to temperature, a comparison to sample G0-4 is considered. G0-4 was fabricated under the same experimental parameters as D30-1 except the substrate was silica and was kept at room temperature throughout. The different substrate for the samples described in Table

5.1 (i.e. silica) is not prohibitive for comparison in this regard, with reference to the upper oxidised silicon layer indicated in Figure 5.2 (b).

20x magnification optical images at of the surfaces of D30-1 and G0-4 are provided in Figure 5.7 (a) and (b) respectively. Figure 5.7 (a) reveals an extensive surface coating of overlapping toroid deposits, illustrating complete coverage by these structures. By comparison, the surface of G0-4 appears to be made up of whole particles, many of which can be seen overlapping and thus not interacting so as to coalesce. This does not necessarily rule out either of the earlier proposed hypotheses as to how these toroid structures may be forming. With regards to (2), the relatively low substrate temperature of G0-4 would rapidly cool the depositing particles at the same rate as D30-1; however it would have done so to room temperature instead of 570 ºC. This may suggest that the material on the surface of D30-1 is molten at 570 ºC, a curious observation as tellurite glass becomes molten at much higher temperatures [63].

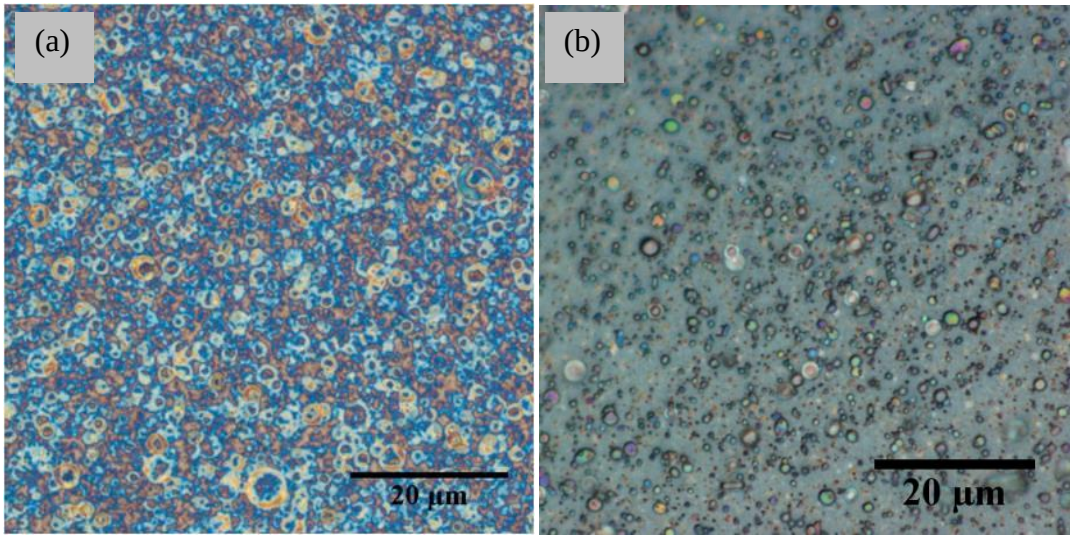

Figure 5.7. Optical microscope images of samples magnified 20x (a) D30-1 and (b) G0-4

The existence of toroid particulates is somewhat perplexing, where no supporting examples can be found in the literature for femtosecond laser ablation. There are however examples from other fabrication methodologies. Taking spray drying as an example, donut-like toroid microparticles are known to form out of an agglomeration of silica nanoparticles [199]. This fabrication technique results in a mixture of toroid and mixed shape microparticles based specifically on the

experimental parameters. As indicated in the images discussed for D30-1 thus far, only toroid like surface formations are visible, suggesting that either the conditions are ideal for complete toroid formation in the present experimental conditions or that these structures are forming on the surface in response to an interaction between the depositing material and the heated substrate. Another possibility which must be ruled out is the influence of the rotations of the substrate *in situ*. If one considers the rotation of a droplet on a surface at high angular velocities [200], that droplet could only form an axisymmetric torus if the droplet were over the centre of rotation, as the name suggests. Those far from the centre of rotation would likely form elongated allantois. This is contradicted in the current system by the observation of toroids across the surface of the substrate and therefore cannot be applied.

To ensure that the observation of toroids is not an anomaly, a second sample to precisely match the fabrication parameters of D30-1 was produced. A 20x magnified optical image of D30-2 was taken and is presented in Figure 5.8, revealing identical toroid formations to those observed for D30-1. This suggests that the toroid formations are not anomalous but are a feature of the deposition process under these experimental parameters.

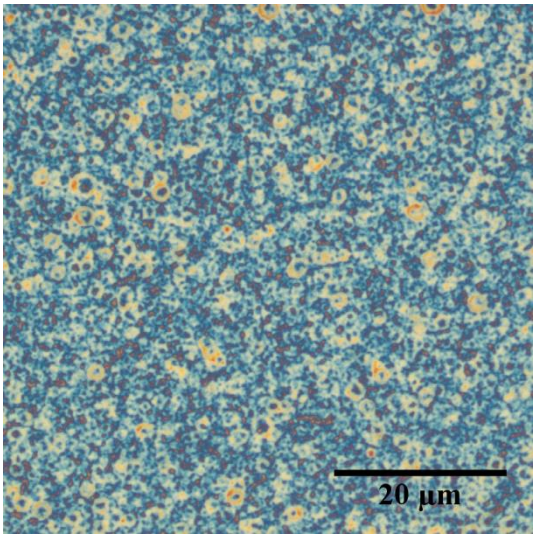

Figure 5.8. 20x magnified optical microscope image of the surface of D30-2, revealing extensive coverage with toroid structures

In addition to the toroid formations on the surface of D30-1, there is also evidence of particulates propagating from the surface, as indicated in Figure 5.5 (c). These formations are quite sparsely and randomly distributed across the sample

surface, however the distinction between these structures and surface contamination is found where they appear to be integral to not only the surface deposited layer, but also the subsurface. This is apparent in the disruption to the surrounding material, where cracks around the clusters have appeared. These formations can also be seen in various stages of development as indicated in Figure 5.5 (d). These may be early indications of crystal growth from the substrate but unfortunately cannot be conclusively linked to longer depositions.

5.3.2.2. Characterisation of ZnTe and Te crystallites

XRD spectrums of D30-1 and D30-2 are provided in Figure 5.9 and Figure 5.10 respectively, whereby cubic ZnTe (ICCD reference code: 04-012-6469, star quality) and hexagonal Te are fitted to the diffraction peaks (with corresponding ICCD reference code: 00-036-1452; star quality). The observation of Si, also labelled (ICCD reference code: 00-027-1402, star quality), is expected as the substrate is slightly off axis, but not far enough to entirely remove all traces of the c-Si substrate from the XRD pattern. Note that the marked phases are positioned in accordance with the reference spectra to convey the likeness to the observed diffraction peaks to the respective phases. Ball and stick models for cubic ZnTe and hexagonal Te crystallites produced using the software CrystalMaker are provided in Figure 5.11 and Figure 5.12 respectively, to assist in discussions. It should be noted that the atomic structure of hexagonal Te is comprised of chains of covalently bonded Te atoms along the c-axis, loosely bound to adjacent chains by van der Waals forces [201]. Knowledge of this structure will become important in subsequent Raman analysis.

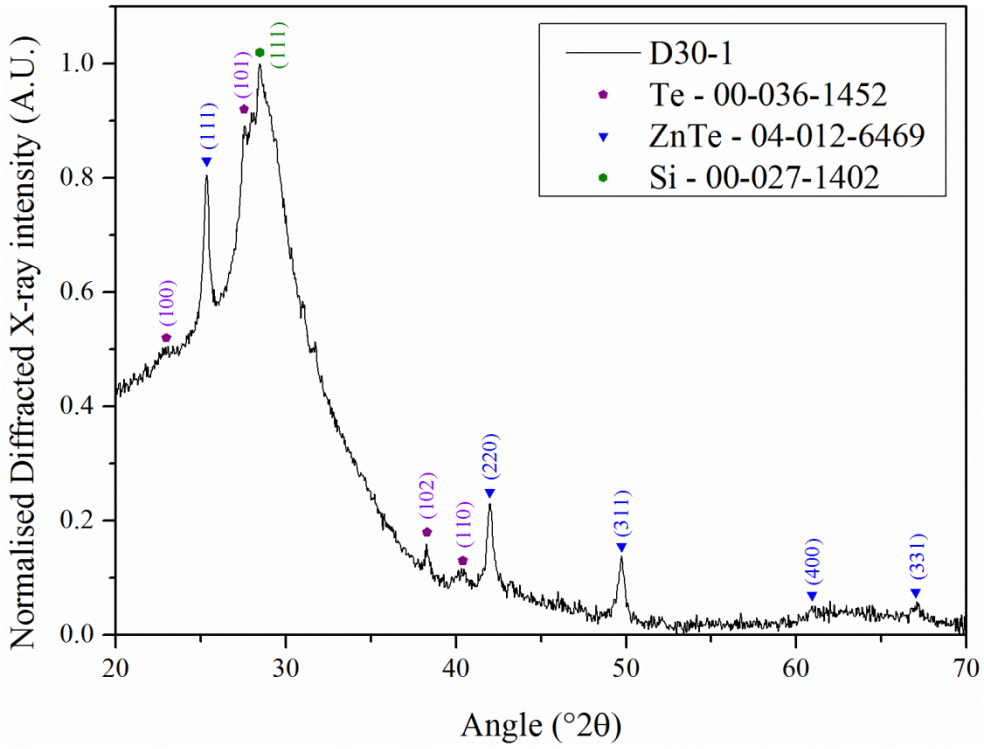

Figure 5.9. X-ray diffraction pattern of D30-1, including the reference patterns for cubic ZnTe (▼) (ICCD ref: 04-012-6469), hexagonal Te (⬟) (ICCD ref: 00-036-1452) and Si (⬢) (ICCD ref: 00-027-1402)

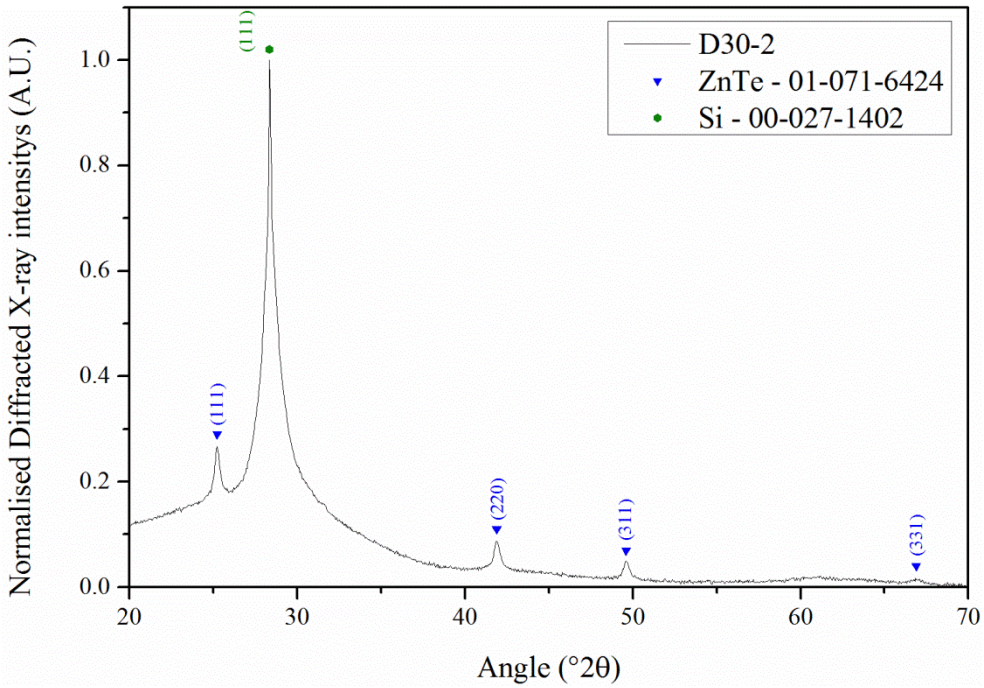

Figure 5.10. X-ray diffraction pattern of D30-2, including the reference patterns for cubic ZnTe (▼) (ICCD ref: 04-012-6469) and Si (⬢) (ICCD ref: 00-027-1402)

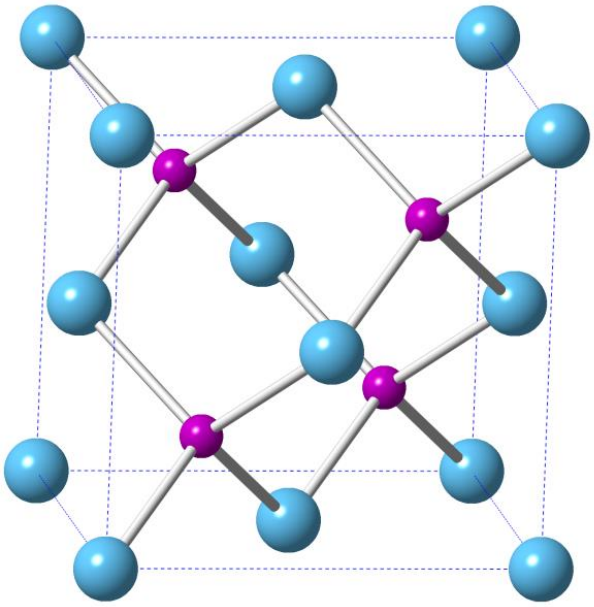

Figure 5.11. Crystal models of the unit cells of cubic ZnTe (ICCD reference code: 04-012-6469); Zn is represented by the purple spheres and Te by the light blue spheres

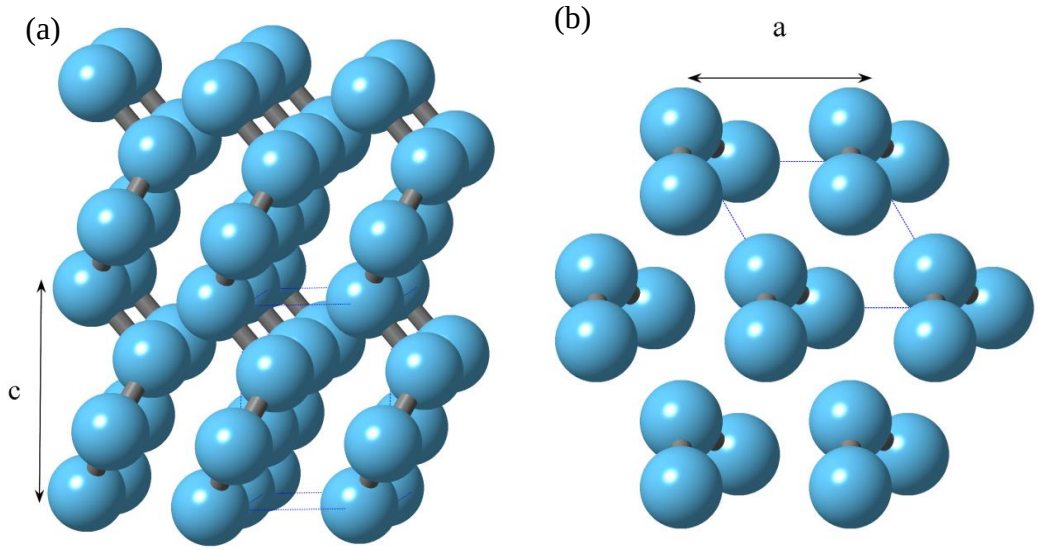

Figure 5.12 Ball and stick diagram of hexagonal Te (ICCD reference code: 00-036-1452) (a) view of the c-axis from close to the [111] direction, (b) view of the a-axis in the [001] direction.

The XRD spectrums of both samples in Figure 5.9 and Figure 5.10 possess a broad background which cannot be ascribed to crystalline silicon. Although disordered materials are rarely analysed by X-ray diffraction due to the intense broadening of the spectrum, it is possible to infer what the broad background may be

indicative of by comparing its centre to the primary peak location of a crystalline equivalent [202]. In this regard, it can be suggested that the broad background of D30-1 and D60-1 in Figure 5.9 and Figure 5.10, peaked at approximately 26.6º is indicative of SiO_2. The primary peak in an XRD spectrum of crystalline quartz is at 26.64º according to a star quality reference pattern in the ICCD database (ICCD Ref: 00-046-1045). Note that polymorphs of quartz may vary around this point, but not by a great deal. The significance of this broad background in the XRD spectrum also indicates a distinct increase in the oxide layer of the Si substrate from that defined in Figure 5.2 for the dry run sample. This strongly suggests a growth of the oxide layer during the fabrication process.

ZnTe, which is indicated in the XRD spectrum, is a known wide direct bandgap semiconductor and following excitation of electrons to the conduction band, emission of photons in the visible region can be expected through their subsequent decay. Based upon this principle, a useful technique for the analysis of these samples is Raman spectroscopy, whereby one can observe not only the photoluminescence, following excitation with the 514 nm laser, but also the phonon modes for both Te and ZnTe simultaneously. Combined with supporting XRD data, Raman spectroscopy therefore acts as a powerful fingerprinting tool for materials, particularly in confirming the allocation of phases to the XRD pattern.

Raman spectrums of both D30-2 and D30-1 are presented in Figure 5.13 and Figure 5.14, respectively. Illustrated on these spectrums are the zero-centre one-phonon (Γ) mode for crystalline Si [203] in green, multiphonon longitudinal optical (LO) phonon modes (*n*LO) for ZnTe in blue [204] and the A_1 and doubly degenerate E phonon modes (composed of both the LO and TO modes) of hexagonal Te marked in purple [205]. The various peak positions for these phonon modes in the Raman spectra have been noted and compared to those found in literature in Table 5.4. In addition to the comparison to literature, a schematic representation of the atomic motions of Te crystallites are given in relation to their identified phonon modes in Figure 5.15.

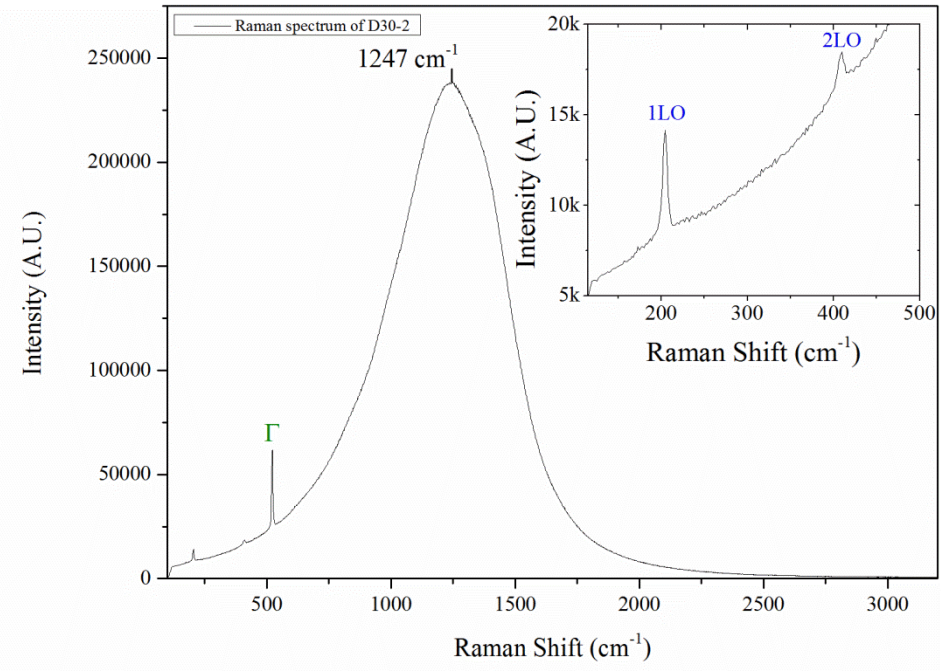

Figure 5.13. Raman spectrum for D30-2; the zero-centre one-phonon mode (Γ) for c-Si is marked in green and those corresponding to cubic ZnTe in blue

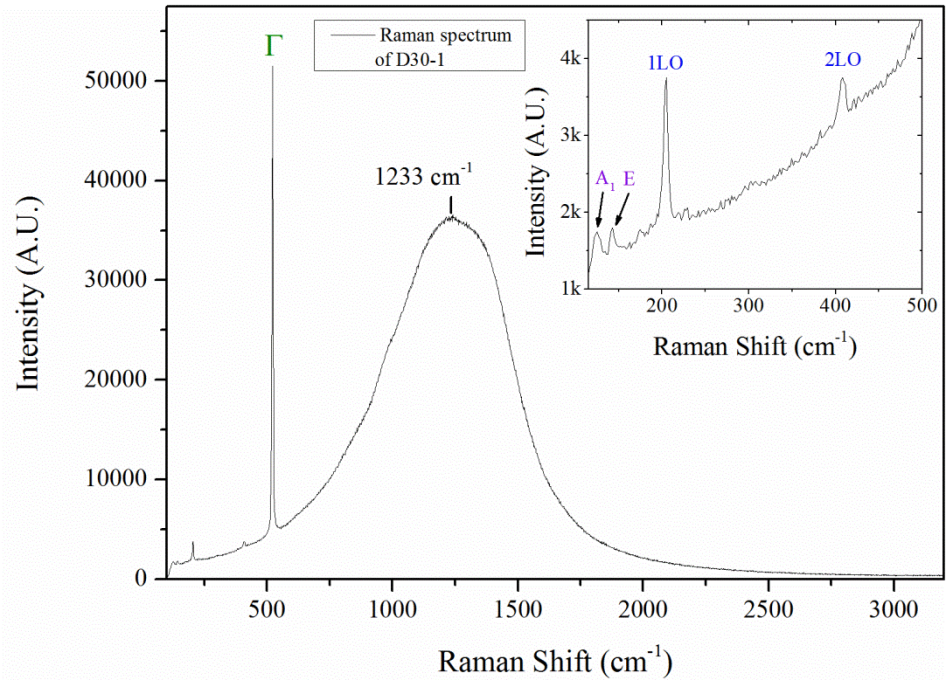

Figure 5.14. Raman spectrum for D30-1; the zero-centre one-phonon mode (Γ) for c-Si is marked in green and those corresponding to hexagonal Te in purple and cubic ZnTe in blue

Table 5.4. Comparison of the Raman peak positions related to various phonon modes for D30-1 and D30-2 to that reported in literature. Peak phonon mode positions have been measured following the removal of the photoluminescence baseline

Phonon mode	**D30-1**	**D30-2**	**Literature**	**Reference**
Si: Γ	521.2	521.4	521.1	[142]
ZnTe: 1LO	205.0	204.4	205.0	[204]
ZnTe: 2LO	408.0	408.7	409.5	[206]
Te: A_1	125.2	-	122	[207]
Te: E_{TO}	142.7	-	142	[207]

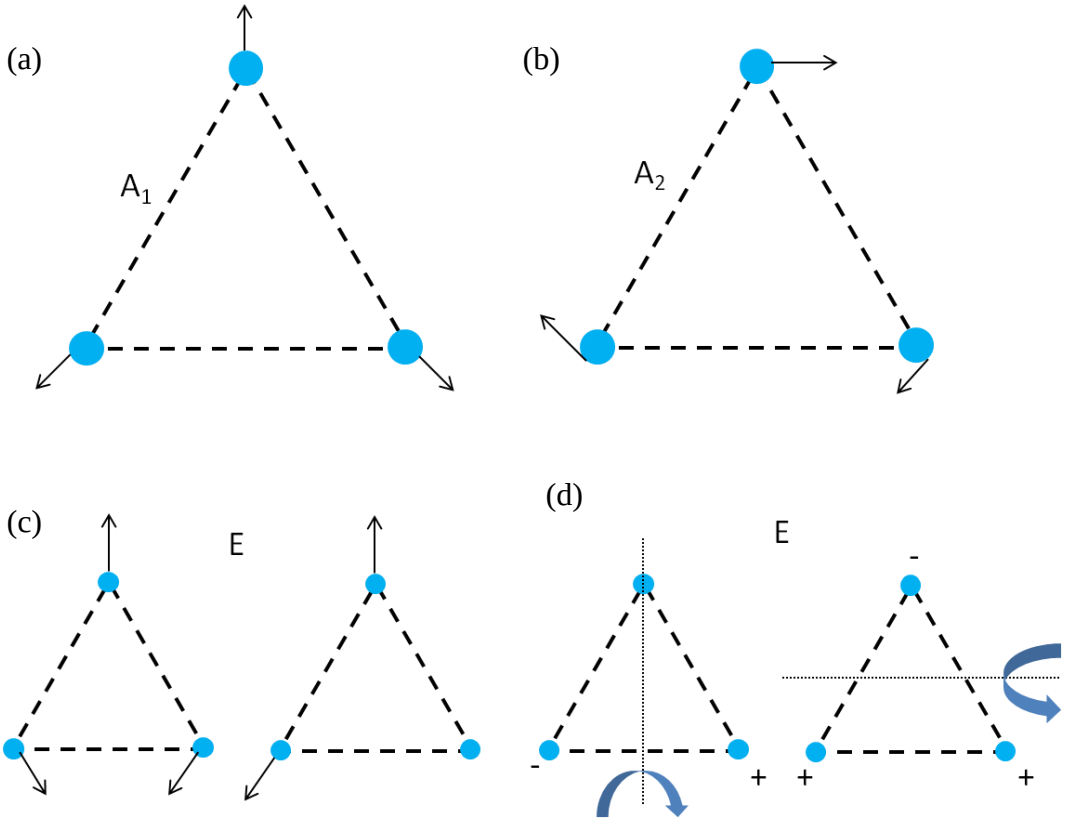

Figure 5.15. Schematic representation of identified hexagonal Te atomic motions viewed in the [001] direction with corresponding optical modes (a) symmetric breathing mode, (b) rigid chain rotation, (c) asymmetric stretching and (d) intra-chain rotation

The Raman spectra for both D30-1 and D30-2 correspond to cubic ZnTe and in combination with their respective XRD spectra, thus confirming the existence of ZnTe crystallites. Furthermore, the observation of ZnTe phonon modes in the Raman spectrum is rather useful for approximating the particle size. Hayashi *et al* [208] has previously identified a correlation between their average particle size and the relative heights of the 1LO and 2LO phonon modes of ZnTe in a Raman spectrum, expressed as:

$$\boldsymbol{E_{ex} = E_i - 2E_{LO} + (C/A)^{1/2}} \qquad \textbf{(5.3)}$$

E_{ex} is the exciton energy, E_i is the energy of the incident light (i.e. 2.41 eV), E_{LO} is the energy of the LO phonon (26 meV), A is the ratio of the 2LO intensity to the 1LO intensity and C is a constant. The exciton energy is found to conform to an exponential relationship with grain size.

Equation 4.3 has a temperature dependence associated with it, where increases in temperature results in an increase in the overall energy of the valence electrons, thus red-shifting the excitation energy. Experimentally, this red-shifts the relative intensity of the multiphonon Raman peaks for ZnTe from a greater intensity in higher-order *n*LO phonons at lower energies/ temperatures to higher intensities of the 1LO phonon mode at higher energies/temperatures. This principle was effectively demonstrated by Feng *et al* [209], where temperature was maintained at 80 K and three different laser excitation wavelengths were used to record the Raman spectra of a sample of ZnTe nanocrystallites.

Unfortunately, the Raman instrumentation in use for this work does not have temperature control functionality and therefore 80 K measurements could not be attempted. Equally, the wavelength is fixed at 514 nm. A qualitative interpretation of equation 4.3 can however be attempted as the fundamental principle it employs can be extrapolated to higher temperatures. As equation 4.3 suggests, a decrease in the average particle size would also blue-shift the spectrum through an associated increase in the bandgap via quantum confinement. The associated blue shift is relative to the operating temperature and thus temperature can be somewhat negated, provided the first two phonon modes can be resolved. This would therefore result in *n+1*LO/*n*LO phonon mode ratios which would be self-consistent with the samples discussed in this work and therefore relative increases or decreases in ZnTe average particle size can be inferred.

With this principle established, the peak height of the 2LO to 1LO phonon modes of ZnTe for samples D30-1 and D30-2 were measured, following the subtraction of the fluorescence baseline. The ratio of the 2LO to 1LO peaks were calculated, giving a ratio of 0.28 and 0.34 for samples D30-1 and D30-2, respectively. These are very small ratio variations and are within a reasonable degree of error for this calculation; see figure 2 in reference [208]. The likeness of these ratios suggests the average grain size for ZnTe crystallites in these two samples is rather similar.

The absence of Te in the Raman spectrum of D30-2 can be attributed to inhomogeneities in the starting glass target. This could be due to a local increase in the Zn content in the target region ablated for the fabrication of D30-2 relative to D30-1, thus favouring ZnTe crystal growth. Alternatively, a relative increase in Te when D30-1 was being fabricated would shift the stoichiometry from that of a closely matched ZnTe (i.e. 1:1), to one with an excess of Te, thus promoting Te crystal growth. What this does suggest however is that the formation of ZnTe crystallites are more favourable than that of pure Te crystallites in the presence of Zn. This shall be discussed in greater detail in section 5.3.3.4.

Both the A_1 and E modes from Te are zone centre optical phonons [205]. The A_1 mode corresponds to the symmetric breathing of a given chain (Figure 5.15 (a)) while the E mode is a doubly degenerate mode comprised of an asymmetric stretching and intra-chain rotation (Figure 5.15 (c) and (d)). These are depicted in Figure 5.15, where the blue dots represent Te atoms as viewed from the [001] direction, i.e. down a chain of Te atoms, such as that depicted in Figure 5.12 (b). Unfortunately, two lower frequency modes [205] (A_2 and a second doubly degenerate E mode) are not able to be characterised as they are below the Raman instruments minimum detection limit. This, however, is not detrimental to the work at hand, as the other modes are sufficient to identify the Te phase and therefore corroborate the XRD data, thus confirming the existence of Te in the sample D30-1. The characterisation of the Te modes not included here are predominantly used for single crystalline materials, i.e. with a preferred orientation of the chains [205].

5.3.2.3. Back scattered electron characterisation of toroid features

A series of secondary electron (SE) images and corresponding back-scattered electron (BSE) images of the surface of D30-1 at different magnifications are presented in Figure 5.16. What is most distinctive about the BSE images is that the toroid formations are still entirely visible relative to the corresponding SE images. From this, two key observations can be made about the tori:

(1) The high contrast ratio of the toroids in the BSE images (thus, high Z-contrast) implies they are composed of high atomic number elements (e.g. containing Zn, Te and/or Tm).

(2) The distinct similarities of the toroid structures between the SE and BSE images suggest the toroids may be embedded in the substrate due to the expected penetration depth of BS electrons at 20.0 kV.

The depth at which BSEs should be expected when working at a 20.0 kV accelerating voltage varies depending upon the sample composition and texture, however, they would almost certainly penetrate the nanoparticles identified in Figure 5.5 (b). This effect is made quite clear by some of the particulates scattered across the surface of the sample in Figure 5.16 (c) (most likely contamination), where they can be seen with SEs, but they have disappeared in the BSE image in Figure 5.16 (d) because of the depth at which the BSEs are emanating from. This suggests that the toroids at least extend under the surface of the substrate, perhaps even completely submerged. Furthermore, it suggests the SE images have a BSE contribution to them.

Based upon the previous observations, the formation mechanism of the toroids remains unclear. It is evident however that they are formed from the high temperature/velocity plasma particles. Based on this, one may speculate the toroids are firstly composed predominantly of Te in a molten state. This is due to the melting temperature of Te (449.5 °C) being below the experimental temperature (570 °C). As a result, the molten Te may be 'dripping' from the substrate surface as it is not able to diffuse into the SiO_2 fast enough and therefore coalesces on the surface. As the excess Te drips from the surface, one may postulate that it leaves behind a shape akin to a coffee stain.

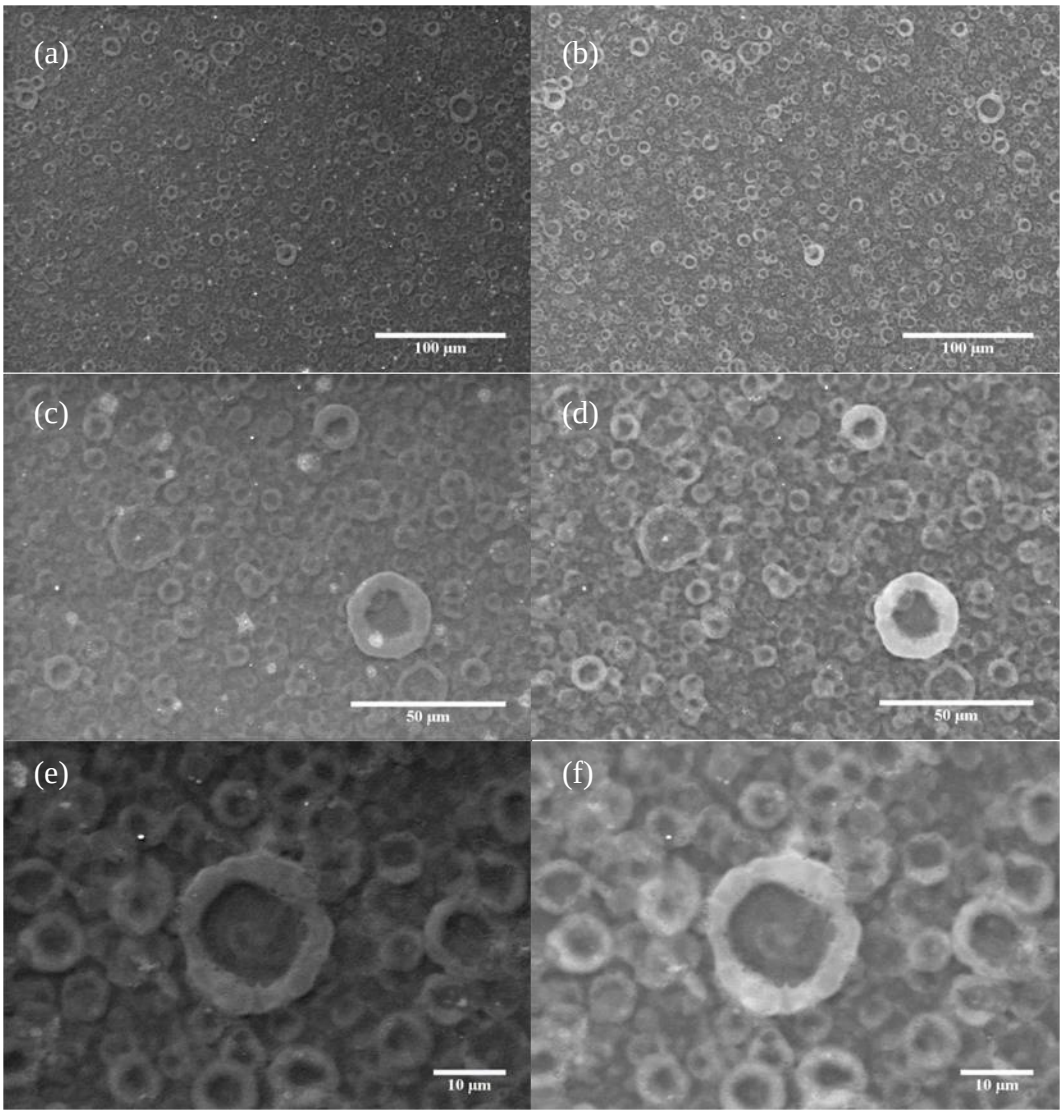

Figure 5.16. SE-SEM images (a, c and e) of the surface of sample D30-1 and their corresponding back scattered electron images (b, d and f, respectively)

5.3.3. Characterisation of surface modification following 60 minutes of laser ablation

5.3.3.1. Topography characterisation

Following the study of samples fabricated for 30 minutes, a 1-hour sample was fabricated with all other experimental parameters fixed, named D60-1. One of the most distinctive features to be identified in this sample in relation to the previous samples studied is demonstrated in the secondary electron (SE) SEM images of Figure 5.17. Not only have distinctly different surface features begun to appear at this magnification and orientation, but sub-surface nanoparticulates are also clearly

visible in the cross section. For convenience, these two features shall be discussed separately, beginning with the surface topography.

Based on a comparison to the previous toroid formations on the surface of D30-1 in Figure 5.5, an initial assessment in relation to the findings by Da *et al* [196] would suggest these new features are a result of an alteration to the substrate surface. This would thus alter the interfacial characteristics between the depositing TZN plasma and the upper oxidised silicon substrate (see equation (5.1 - Young-Laplace). Based upon this assertion, it may be postulated that the nanoparticles identified in Figure 5.5 (b) have coalesced in response to the additional time and the increased abundance of deposited material, thus forming considerably larger particles. Such a hypothesis could also explain the absence of surface material surrounding the disk-like formations identified in Figure 5.17.

Figure 5.17 (a) and (b) were acquired from two different areas of the D60-1 approximately 500 μm apart. This distance should not be large enough to expect extensive alterations to the nature of the incoming plasma [27]; however significant differences in the average disk size for these regions are noted. Figure 5.18 presents histograms for the disk size distribution, whereby an overall graph for the aforementioned regions (and others not presented here) is provided. In addition to this, Figure 5.18 (b) and (c) also provides disk size distribution histograms for the regions identified in Figure 5.17 (a) and (b), respectively, to highlight some of the key features of the overall size distribution.

The distinct difference in disk size distribution in Figure 5.18 for these two regions suggests discontinuities in the interactions between the surface deposits and the substrate from one area to the next. This may be a result of variability in the surface kinetics across the sample, or perhaps a difference in chemical composition leading to alterations in the interfacial energies.

Observation of the smaller disks depicted in Figure 5.17 (b) and quantified in Figure 5.18 (b) are reminiscent of observations made for G0-4, presented in Figure 5.7 (b). Comparison of the particle size distribution for the sample G0-4, fabricated under the same experimental parameters as D30-1 but at room temperature, to that of the smaller disks of D60-1 identified in Figure 5.17 (b) reveals an interesting trend. This comparison is given as overlapping histograms in Figure 5.19, acquired by optical microscopy and SE-SEM for G0-4 and D60-1 respectively. The primary

interest in this comparison is to discuss the possibility that the substrate may have changed somewhat from the original SiO_x/Si, to one more favourable to depositing particles at this temperature. It is acknowledged that the absolute minimum resolution for a light microscope is approximately 0.25 μm; to compensate for this, particles measuring less than 0.5 μm are discounted; however associated errors in measurements are still to be expected.

An additional SE-SEM image is provided in Figure 5.20 whereby the only toroid structures identified on the surface of D60-1 are included. It is interesting to note that not only were they the only to be identified, but they are also clustered together. This has interesting links to the clustering effects of distinct surface features across these samples and shall be discussed in greater detail in subsequent chapters.

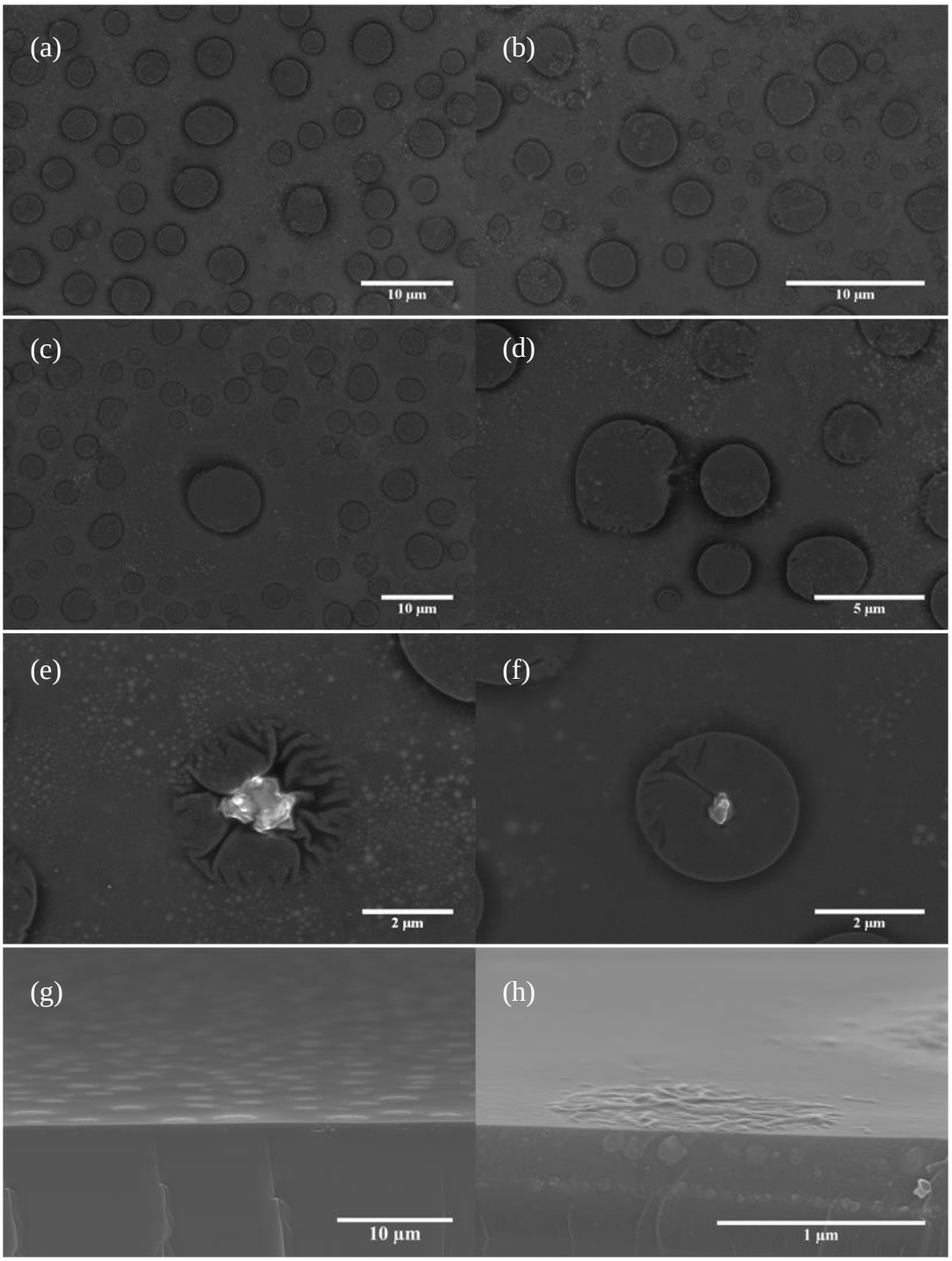

Figure 5.17. SE-SEM images of sample D60-1, including its surface (a-f) and cross section (g-h)

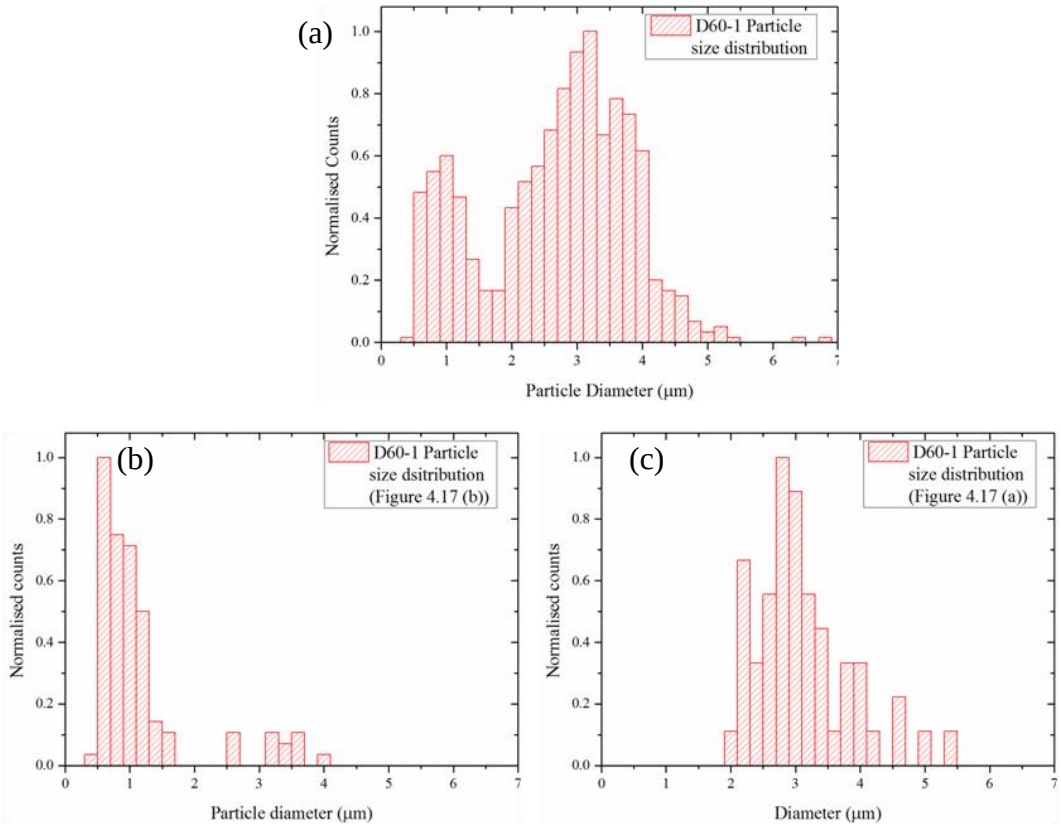

Figure 5.18. Histograms of (a) all particles observed through SE-SEM imaging, including the top down images of Figure 5.17 and others no presented here; (b) particle size measurements from Figure 5.17 (a); (c) particle size measurements from Figure 5.17 (b)

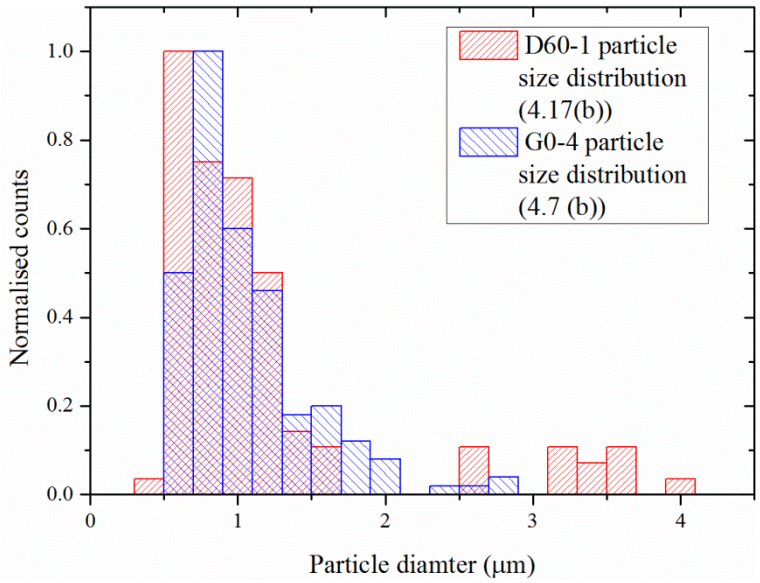

Figure 5.19. Histograms of the particle size distribution for D60-1 from Figure 5.17 (b) and those of G0-4 in Figure 5.7(b)

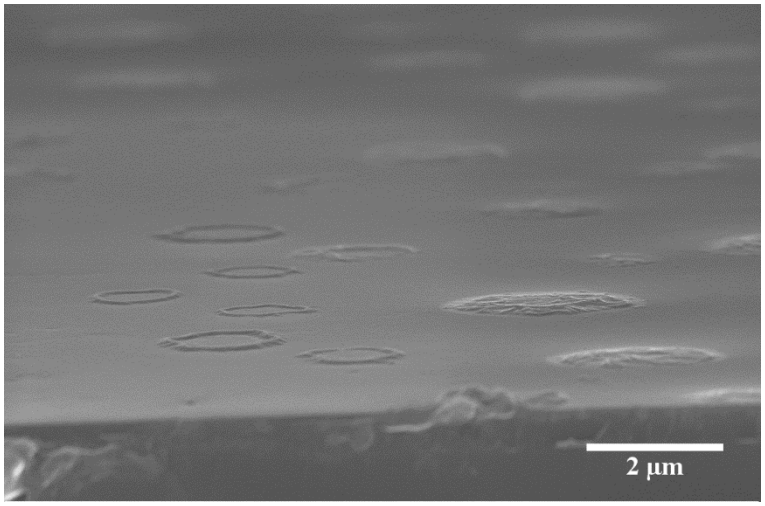

Figure 5.20. Cross-sectional SE-SEM image of the only confirmed toroid formations on the surface of sample D60-1

The similar trend identified in Figure 5.19 between the particle size distribution of the surface of D60-1 and G0-4 is quite compelling. This may indicate that following extensive surface modification by the incoming plasma, recently deposited microparticles are more stable on its surface and therefore are apparent upon the surface of the sample, as found in Figure 5.17 (b). Alternatively, these observations suggest particle growth by coalescence [128] may be the main driver for the disk particles on D60-1.

In order to coherently discuss the way these surface disk formations have emerged based on the aforementioned observations, it is prudent to asses a theory on its own merits, before coming to a conclusion.

Perhaps the most feasible mechanism in which these surface structures have come about is due to an increasing abundance of deposited material. This in turn may lead to a local densification and subsequent nucleation and growth of the observed disk-like surface formations. It is likely that such structure would contract somewhat in response to the cooling process, in accordance with the principles expressed in equation 4.2 governing surface tension. The disk-like formations, in this regard, could therefore grow further via coalescence, whereby large particles grow at the expense of smaller particles with larger radial pressures. This physical phenomena stems from the consequences of the Young-Laplace relationship in equation 4.1. The proposed hypothesis is based on several key observations for the system studied:

(1) The distinct growth in particle size, i.e. from the small nanoparticles observed for D30-1, suggests the associated increase in deposited material over time has thus encouraged a growth in particle size via coalescence. The average particle size D_A for a given interaction can be found via [210]:

$$\boldsymbol{D_A = 6V/A} \quad \textbf{(5.4)}$$

Where V is the total volume of the material and A is the associated surface area. One can therefore deduce that as the volume of material increases, the systems inherent tendency to reduce surface energy will thus reduce in area via coalescence of a similar process as inferred by Figure 5.17.

(2) Larger particles, such as the one in the centre of Figure 5.17 (c) appear to have a more significant boundary between itself and surrounding particles. This is indicative of Ostwald ripening, whereby the surrounding particles have been absorbed by this larger central particle. It should be noted that this is not an isolated observation, others have been made but at not included here.

(3) No particles are observed to be in contact throughout the entirety of the regions studied on sample D60-1, suggesting coalescence would ensue as a result and thus form a singular particle. Note that if particles were found to be in contact, it may not necessarily rule out Ostwald ripening as it may suggest a slow dissolution of the smaller, neighbouring particle. The closest example of contact between disks of any size yet identified is given in Figure 5.17 (d), where an interaction appears to be taking place between them. The exact nature of this interaction is unclear, however the scarcity of its occurrence suggests either a hastened process or a gradual decrease in such activity during the cooling stage.

(4) Observations by Da *et al* [196] support this hypothesis, in that the gradual decrease in temperature from 570 °C to room temperature would cause a decrease in the wetting of the surface. This would encourage the contraction of surface material into condensed circular deposits. In order to further reduce the surface energy of these formations, condensed material would preferentially form circular particles.

(5) The particle size distribution appears very similar to a log-normal distribution, indicative of particle growth by coalescence [128].

A major consequence of this hypothesis is that it suggests mobility of the particles on the surface. If the particles were assumed to be immobile, this would still not rule out Ostwald ripening as the primary growth mechanism; one would however expect to see a number of deformed particles from the predominantly disk-like ensembles presented in Figure 5.17, implying the disks formed from a liquid state.

In addition to the occurrence of disk-like deposits, the existence of material propagating from the centre of some is also noted. With all SE-SEM images in Figure 5.17 being acquired via an InLens detector orientation, the saturation of the image over these particles could be due to multiple effects. The difference in SE emission from a protrusion or an edge is generally greater than that from a flat surface, this is known as edge contrast. In addition to this, high atomic number elements also produce a higher contrast when viewing backscattered electrons. Contributions from backscattered electrons must also be considered, whereby Z-contrast may be responsible. Another effect which may be contributing to this image is charging, whereby the particle may be nonconductive, and therefore prevent normal SE emission. This effect can be observed as localised increases in the contrast ratio without other associated effects, such as drifting and image deformation. It is conceivable that Figure 5.17(e) could have contributions from each effect; however the particle in view for Figure 5.17 (f) appears much too low in the substrate and therefore is rather unlikely to have significant contributions to its brightness from edge/protrusion contrast. This would suggest that there is considerable segregation of relatively high atomic number elements in these isolated regions and/or the material is nonconductive. Both explanations however strongly suggest a difference in chemical composition from the various surface features. It still remains however, that these particulates may simply be contamination on the substrate from when it was put into the PLD chamber and the disk-like particle simply formed around it. Without more detailed analysis, this cannot be known with certainty.

In order to further investigate the growth mechanisms involved in the formation of D60-1 and how they may have manifested, another sample was fabricated under identical conditions as D60-1, but using a pressed powder pellet of TeO_2 as a target, this target is labelled G2 in Table 5.3. This sample was also

deposited onto a silicon substrate at 570 °C for 1 hour. Initial analysis using SE-SEM imaging, provided in Figure 5.21, reveals very similar surface structures, as found with D60-1, however subsurface particles could not be identified during cross-sectional SEM analysis. A histogram of the particle size is also provided in Figure 5.22 so as to compare to that of D60-1.

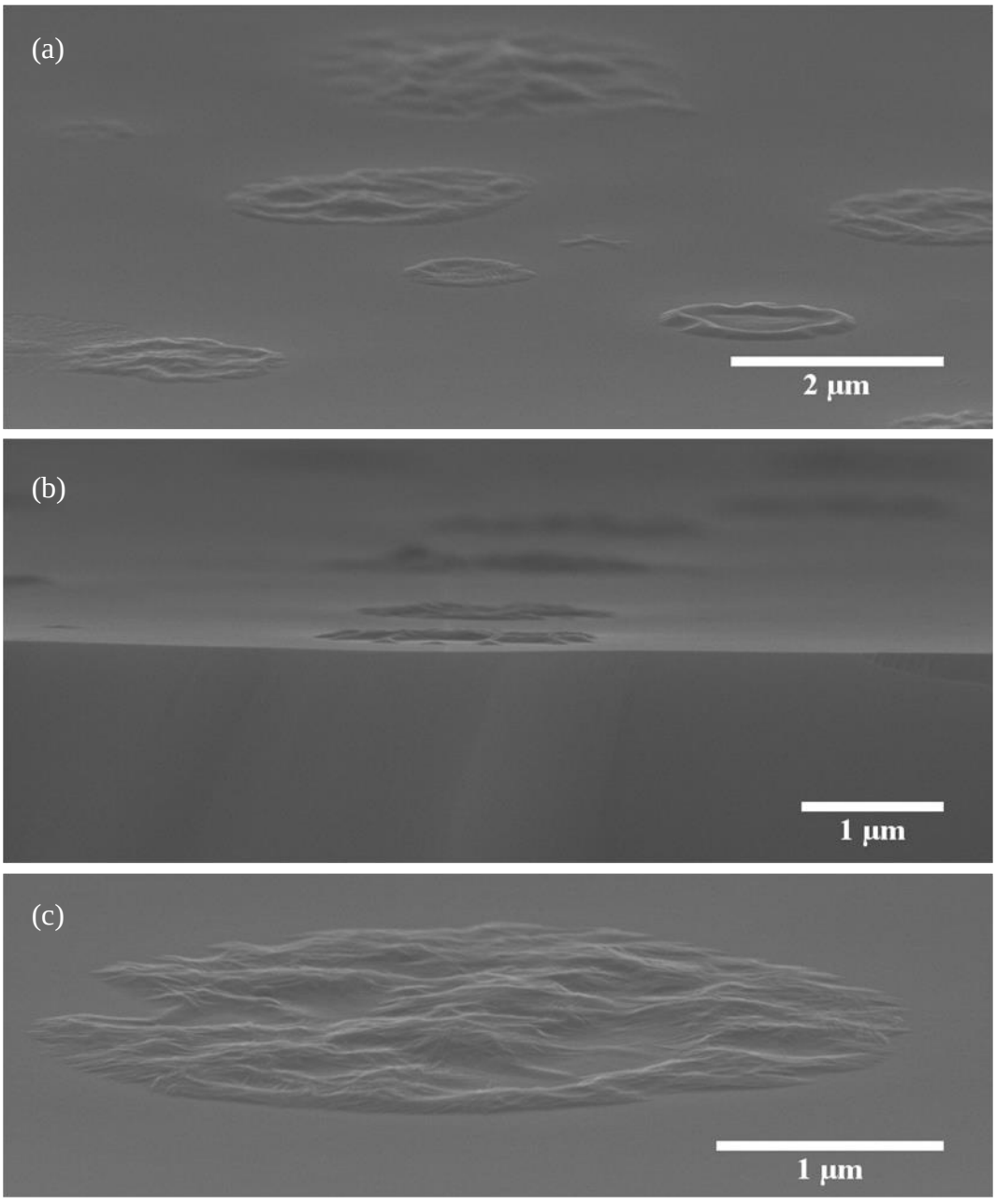

Figure 5.21. Cross sectional SE-SEM images of sample D60-2

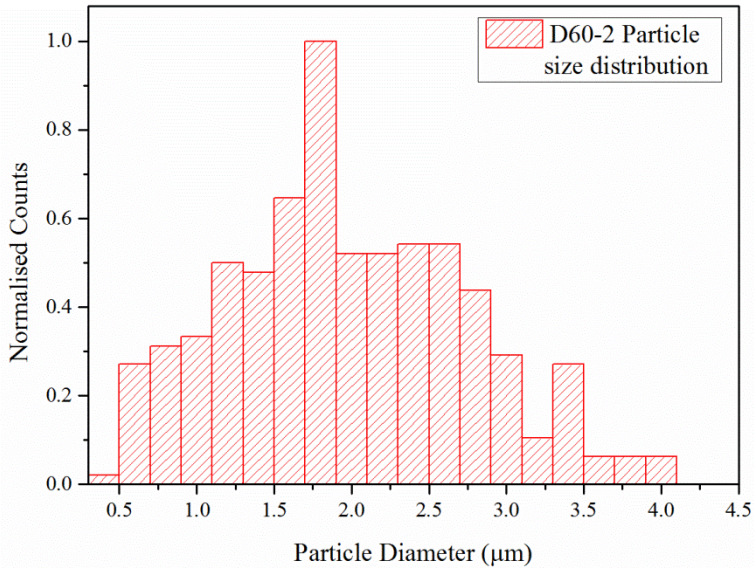

Figure 5.22. Histogram of the surface disk size distribution identified across the surface of D60-2 using SE-SEM images such as those in Figure 5.21 and others not presented here

The disk-like particles of D60-2 appear to correspond to those of D60-1 in both shape and distribution, implying they have both formed via a similar mechanism. Furthermore, it suggests that the surface material in D60-1 is likely to have a high concentration of Te, while the subsurface particles are either not Te or additional dopants are required to enable Te penetration of the surface. The average disk size for D60-2 is measured as 1.9 μm, while that of D60-1 is 2.6 μm, so although similar, there are differences. A particularly noteworthy distinction in the surface disks of D60-2 in relation to D60-1 is the abundance of toroid formations, protruding from the surface of the substrate. A clear example of this is found in Figure 5.21 (a), where the bottom right particle appears to be a toroid structure. Qualitatively, these are noticeably more common in D60-2 than D60-1.

It seems reasonable however that based upon the size distribution of these surface features, that coalescence is the key driver in their growth. The log-normal distribution of particle sizes is indicative of this, and the boundaries between particles upon the substrate also strongly suggest coalescence as a main influence. This would suggest that not all material is able to penetrate the surface, in particular Te. Furthermore, it would suggest a depletion of Te, particularly with longer fabrication times.

5.3.3.2. Characterisation of crystallites for 1 hour fabricated samples

The absence of Zn in the target G2 for sample D60-2 removes the possibility of observing ZnTe, however, based on observations from the samples discussed in section 5.3.2, an excess of Te may lead to the formation of hexagonal Te crystallites. In order to study this, analysis using both Raman spectroscopy and XRD data was used to define the materials structure. These are presented in Figure 5.23 and Figure 5.24 respectively for sample D60-2. From these figures, it is clear that the previously observed hexagonal Te crystal phase is not found in D60-2. This suggests that the conditions required for the formation of hexagonal Te crystallites requires the addition of other elements to the SiO_x matrix, such as Na. The existence of an extended amorphous silica layer is inferred once again from the broad background at approximately 26 º2θ in Figure 5.24. This is an important observation for the purposes of designing an experiment to encourage the growth of a specific crystal phase.

The minor peaks identified in the XRD spectrum of D60-2 unfortunately could not be found to correspond to a known XRD pattern. It should be noted that these peaks do not correspond to that of a Te phase and are thus ascribed to a different crystallite.

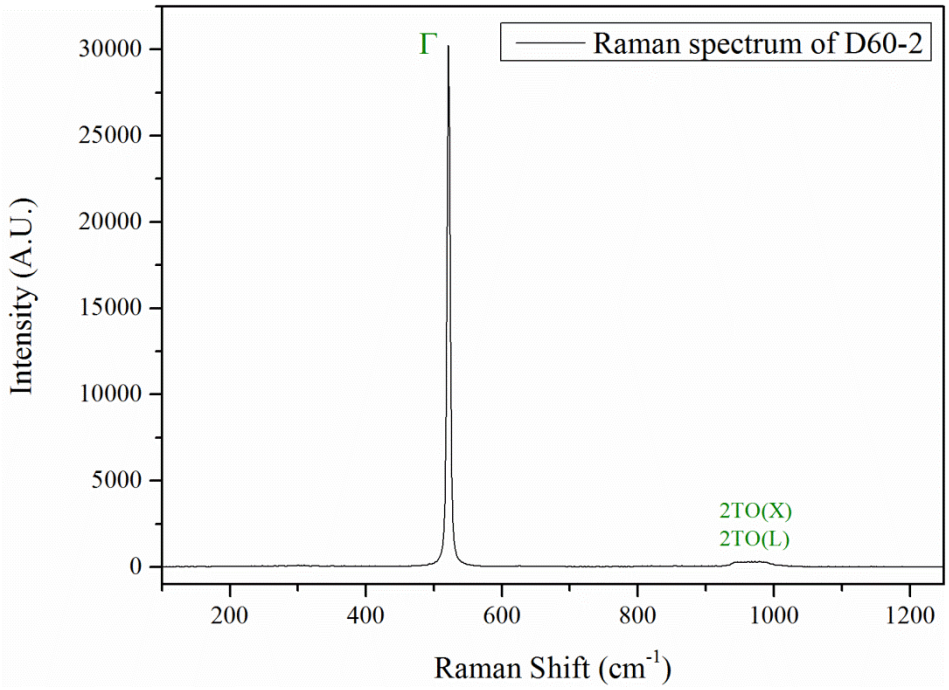

Figure 5.23. Raman spectroscopy of sample D60-2 with the zero-centre (Γ) mode and other associated peaks of c-Si labeled in green

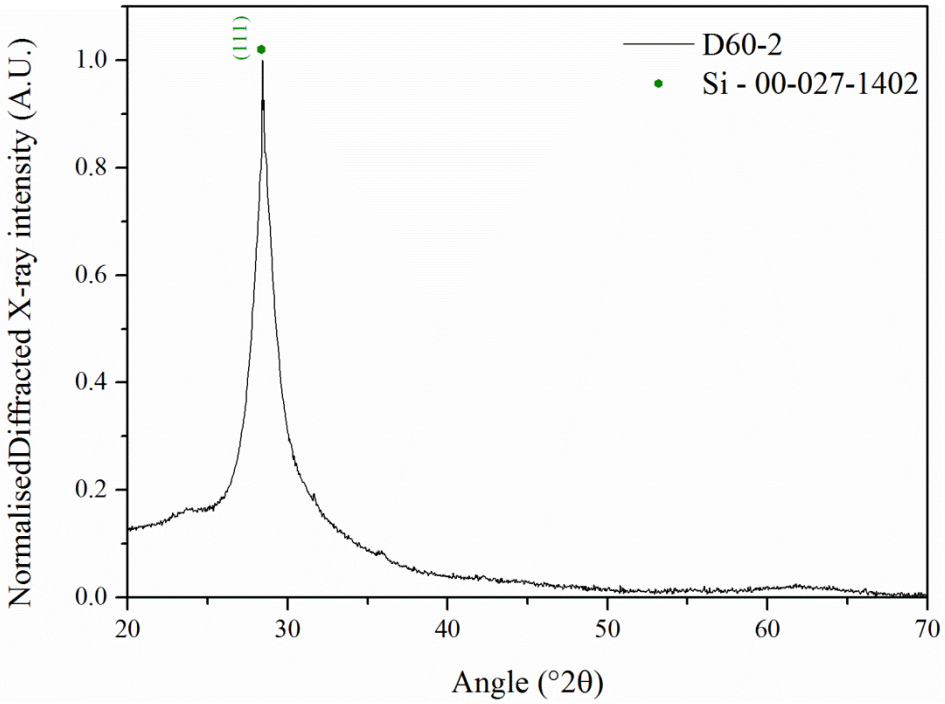

Figure 5.24. X-ray diffraction pattern of sample D60-2, including the peak position of Si (⬢) (ICD ref: 00-027-1402)

For adequate comparison to the previously studied samples, D60-1 was also characterised by Raman spectroscopy in Figure 5.25, and XRD in Figure 5.26. Beginning with the XRD spectrum, the previously observed ZnTe phase (ICCD Ref: 04-012-6469) is again found, but with additional peaks to those previously observed in D30-1 and D30-2 as well as some other key features.

In addition to the observed ZnTe crystallites in the XRD spectrum of D60-1, a number of reasonably intense peaks remain unassigned. Although no reference patterns from the ICCD database directly match the remaining peaks the closest match to it in peak intensity as well as position is an SiO_2 crystalline polymorph known as α-cristobalite (ICCD ref: 04-008-7642). This allocation is also in good agreement with observations in literature [211]. To illustrate this match, the remaining unassigned peaks have been simulated from the spectrum in Figure 5.26 and are provided in Figure 5.27 with identical broadening and intensity ratios, but with the baseline removed for clarity. Furthermore, Table 5.5 details the peak position and relative intensities of the peaks to those of various ICCD reference patterns for α-cristobalite.

The simulated XRD pattern of Figure 5.27 in combination with the example patterns of α-cristobalite suggest that SiO_2 is beginning to crystallise following 1 hour of fabrication time. The formation of α-cristobalite begins through the formation [212,213] of metastable β-cristobalite between 1470ºC and 1728ºC (the melting point) where this phase remains stable down to approximately 275 ºC, whereby it undergoes a first order transition from the cubic ($Fd\bar{3}m$) β-phase to the tetragonal ($P4_32_12$ or $P4_12_12$) α-phase, which is also metastable. This transition is believed to be brought about due to simultaneous translation and rotation of the silicate tetrahedra along <110> [213]. This indicates that the plasma phase is heating the substrate substantially, causing the formation of a high temperature polymorph of the silica layer. What is key in this assessment is that the β-phase would be stable *in-situ*, but the α-phase is stable *ex-situ*, i.e. after the cooling process. A ball-and-stick diagram of the α-cristobalite unit cell and a view along the [100] plane is depicted in Figure 5.28.

Shifts in diffraction peak position for a given phase can be representative of uniform strain on that particular plane. Physically, this is interpreted as an expansion of the plane (an increase in the d-spacing) if it shifts to lower angles, or a contraction if it shifts to higher angles. As indicated in the numerical comparisons in Table 5.5, the observed peaks appear to be slightly shifted to lower angles, thus suggesting an expansion of the unit cell. Unfortunately this assertion cannot be corroborated with supporting data, however the XRD data is found to be rather compelling and is therefore worthy of discussion.

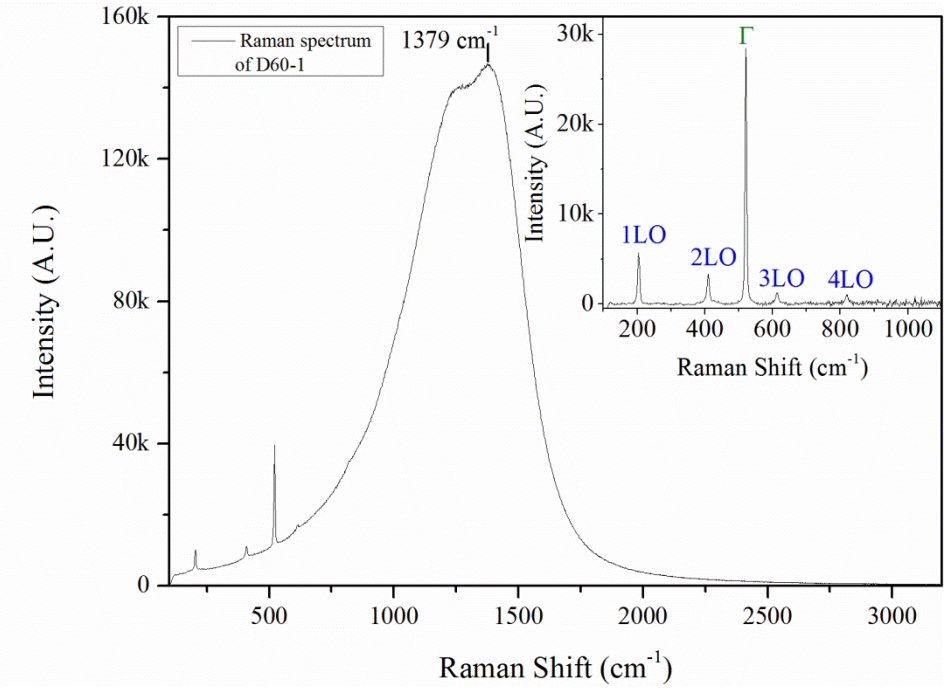

Figure 5.25. Raman spectroscopy of sample D60-1. Inset shows the multiphonon LO modes of ZnTe (blue) and the Γ mode of the crystalline silicon substrate (green) with the ZnTe photoluminescence deducted for clarity.

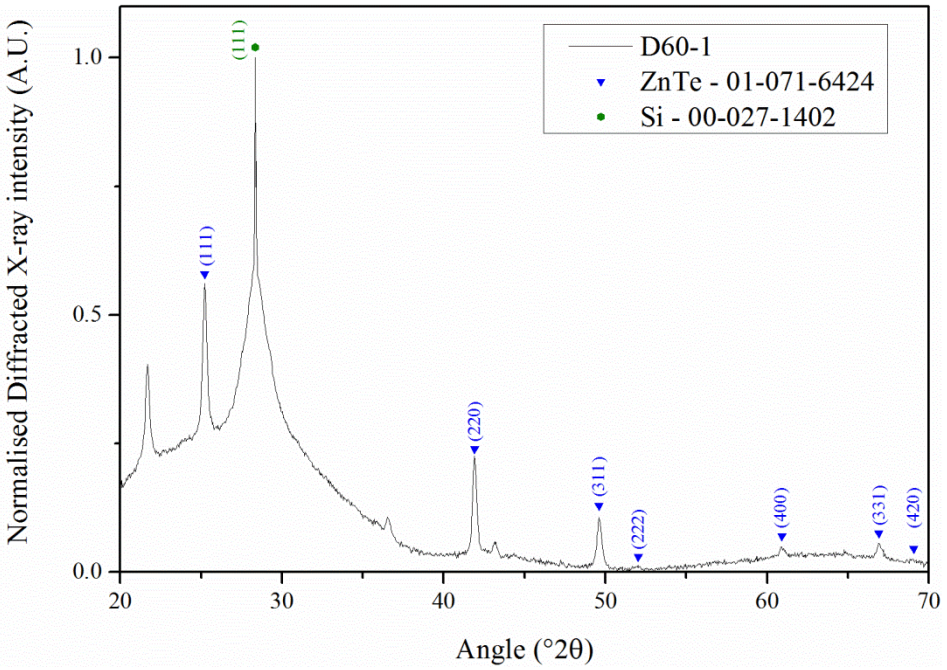

Figure 5.26. XRD pattern of sample D60-1, including peaks corresponding to cubic ZnTe (▼) (ICCD Ref: 04-012-6469) and silicon (⬢) (ICCD Ref: 00-027-1402). Remaining peaks are evaluated in Figure 5.27 and Table 5.5.

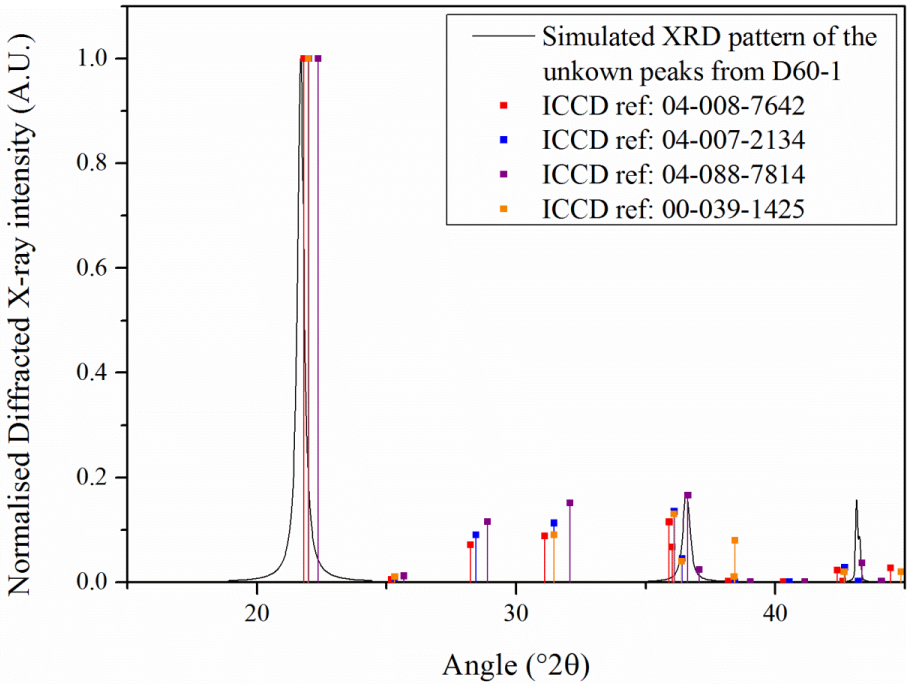

Figure 5.27. Simulated XRD pattern of the remaining, unassigned peaks from sample D60-1 where the spectrum appear to mimic that of α-cristobalite, a crystalline polymorph of SiO_2. The ICCD reference patterns included of α-cristobalite are 04-008-7642 (red), 04-007-2134 (blue), 04-008-7814 (purple) and 00-039-1425 (orange).

Table 5.5 Table comparing the unassigned peak from the XRD spectrum of D60-1 to four different diffraction patterns from α-cristobalite; columns marked with a *P* signify the peak positions, while those with an *I* refer to the relative intensity of that peak.

α-cristobalite Crystalphase (hkl)	**D60-1**		**04-008-7642**		**04-007-2134**		**04-008-7814**		**00-039-1425**	
	P	**I**	**P**	**I**	**P**	**I**	**P**	**I**	**P**	**I**
(101)	21.68	100	21.81	100	21.99	100	22.36	100	21.98	100
(200)	36.57	16.9	35.90	11.5	36.10	13.5	36.63	16.6	36.08	13.0
(211)	4.15	15.8	42.40	2.3	42.68	2.8	43.34	3.7	42.66	2.0
(202)			44.45	2.7	44.85	2.5	45.64	1.5	44.84	2.0

(a)

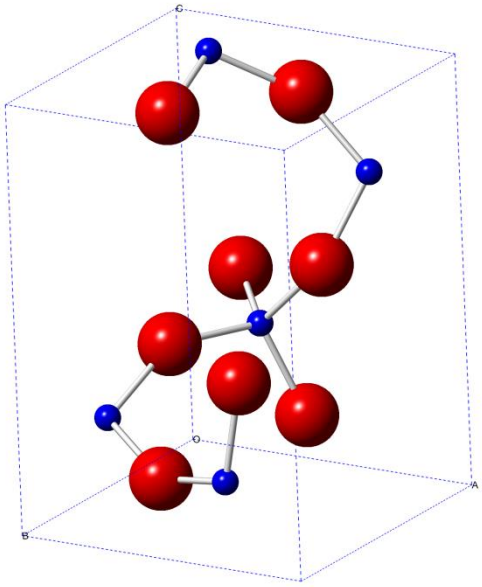

(b)

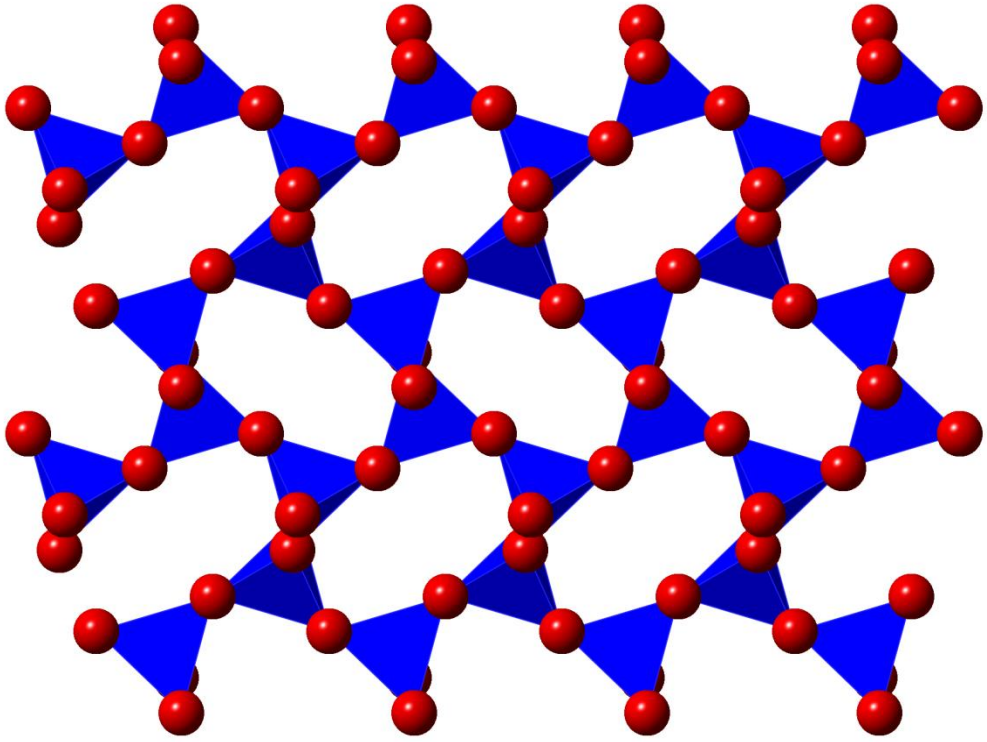

Figure 5.28. Ball and stick diagram of α-cristobalite, (a) the unit cell (ICCD ref: 00-039-1425), (b) view along the [100] direction of a crystallite. Red balls represent Si and blue represent O.

The average crystallite sizes were calculated from the respective XRD spectrums of sample D30-1, D30-2 and D60-1 using the Scherrer equation, presented in Table 5.6. The results of these calculations indicate an increase in average particle size for ZnTe with respect to time. It should be noted that the crystal sizes of Te crystallites are not included as the signal to noise ratio is deemed too high for accurate analysis.

Table 5.6. Table of the calculated average particle sizes in nm of different phases of crystallites, as calculated from the XRD spectrum of samples D30-1, D30-2 and D60-1 using the Scherrer equation on different peaks

Sample ID	**Peak position**	**Crystal size (nm)**	**Corresponding material**	**Miller indices (hkl)**
D30-1	25.29	105	ZnTe	(111)
	41.96	109	ZnTe	(220)
	49.68	116	ZnTe	(311)
D30-2	25.22	114	ZnTe	(111)
	41.88	115	ZnTe	(220)
	49.58	126	ZnTe	(311)
D60-1	21.67	147	α-cristobalite	(101)
	25.21	149	ZnTe	(111)
	41.88	189	ZnTe	(220)
	49.58	162	ZnTe	(311)

The K factor used in the Scherrer calculations of Table 5.6 was 0.89, i.e. one relating to a spherical particle shape, is based upon the cross sectional SE-SEM observations of subsurface spherical particles in D60-1.

The analysis of the XRD and Raman data pertaining to the samples discussed thus far indicates a significant presence of ZnTe and Te crystallites in differing quantities. Significantly however, the present XRD data also suggests the existence of a silicate phase forming. This has interesting consequences for understanding the

nature in which the materials are forming and suggests considerable alterations to the original surface material. Furthermore, it indicates an evolution of the surface material with time, one dependent upon both the amount of material delivered to the surface and the time at 570 °C.

5.3.3.3. Backscattered electron characterization of subsurface particles after 1 hour of fabrication

In order to evaluate the nature of the subsurface particles further, backscattered electron imaging was carried out on D60-1 and is presented in Figure 5.29. This figure presents three areas located across the sample at different magnifications, whereby the previously observed circular formations in SE-mode (left hand side figures – a, c and e) are clearly visible. The disks are found to be too thin (i.e. above the BSE interaction volume) to be viewed by BS electrons and thus only the subsurface features are visible. The high Z-contrast of the subsurface particulates in relation to their surroundings indicates they possess a much higher average atomic number.

The confirmation of ZnTe crystallites using XRD and Raman spectroscopy as well as their size calculated using the Scherrer equation leads to a plausible assumption that the high contrast particles, most noticeable in Figure 5.14 (f) due to their size, are ZnTe. This would therefore indicate that the ZnTe has crystallised below the surface of the substrate and are the subsurface particulates in view in the cross-sectional SE-SEM image in Figure 5.17 (h).

The 300 nm depth at which these crystallites have been identified is too deep to be accounted for by the diffusion of Zn and Te metal ions [214]. Based upon the observations in XRD of the existence of a broad peak in the corresponding region for amorphous SiO_x, as well as indicators of a modified SiO_2 crystallite, it is therefore reasonable to suggest that the Te and Zn have diffused into an expanded oxide layer from that found in the original substrate and crystallised. Findings by Espiau de Lamaestre *et al* [215] are of great import in this current context. It was found that Te precipitates into nanocrystallites when implanted into a silica matrix via ion implantation with negligible diffusion, even at annealing temperatures as high 950 ºC. This is a significant observation as is suggests that Te ions may be implanting into the silica surface layer and hence precipitating and crystallising. It

is known that Te ions remain isolated in a silicon lattice and do not precipitate, even in high doses and high annealing temperatures [216]. Therefore if Te ions were to be found in a silicon lattice, the nucleation and growth of crystallites would be highly unlikely.

Returning to the present sample, D60-1, ZnTe would follow suit with this principle, whereby subsurface crystallites of ZnTe would require mobility within the lattice structure in order to nucleate and thus crystallise and grow. This strongly suggests that if implantation is occurring, it is certainly occurring into the silica matrix; however its occurrence in an underlying crystalline silicon structure is as yet unclear.

An alternate hypothesis, supported by observations from Da *et al* [196], where rapid diffusion of all major oxides of TZN (TeO_2, ZnO and Na_2O) in SiO_2 was observed. Furthermore, Si was observed diffusing into the TZN material. This may suggests that instead of the singular ions (recall the fast ions in the plasma phase) implanting directly into the substrate, they are instead diffusing as oxides into a newly formed SiO_2 layer and subsequently reducing, nucleating, crystallising and thus growing.

Both hypotheses appear equally valid at present and shall be considered in greater detail in section 5.3.3.4 and subsequent chapters.

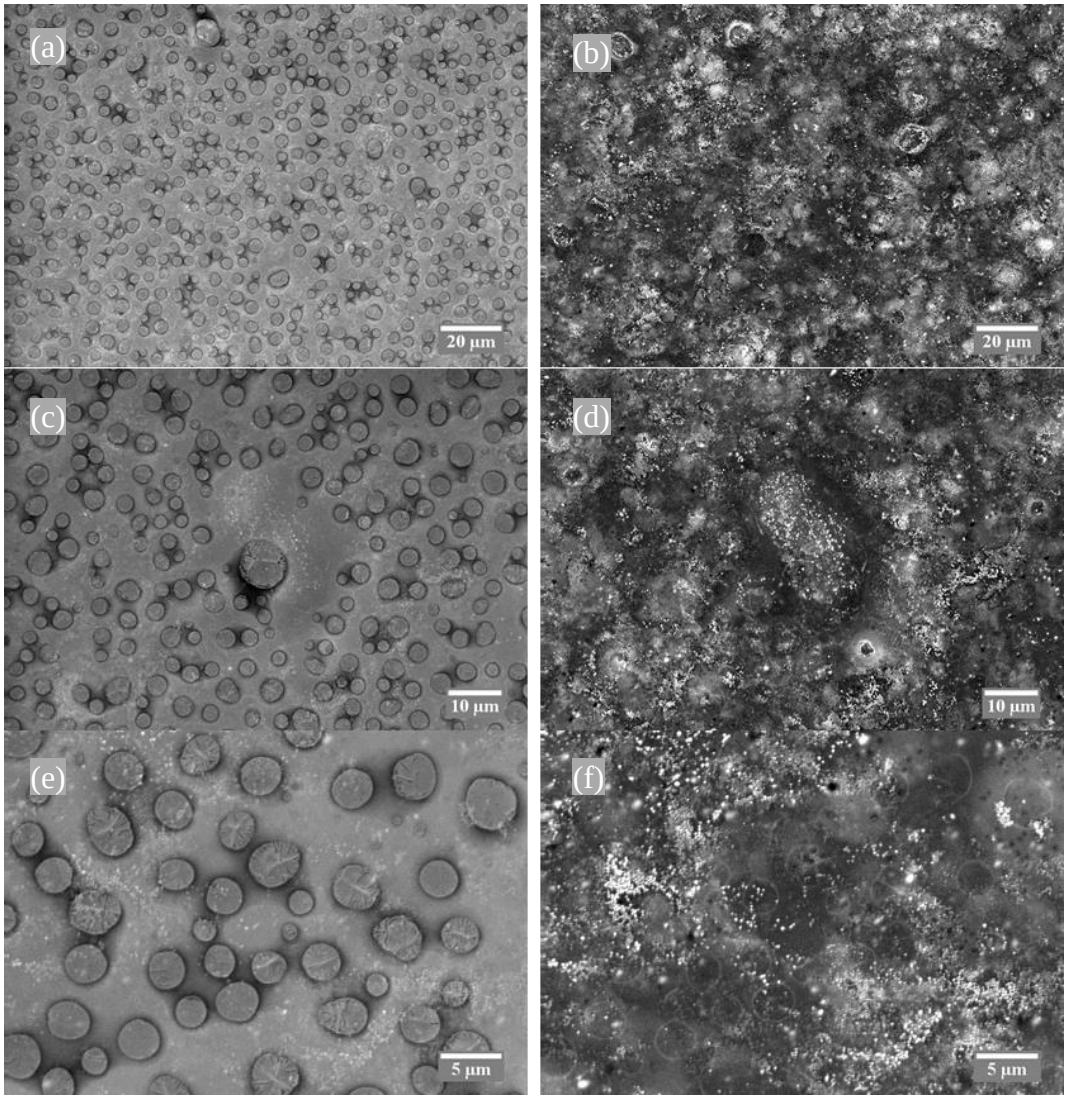

Figure 5.29. SE-SEM images (a, c and e) of the surface of D60-1 and their corresponding back scattered electron images (b, d and f, respectively)

The BSE images in Figure 5.29 (right hand side – b, d and f) appear to suggest a discontinuity in the distribution of the subsurface crystallites across the sample surface. The localised clustering of ZnTe/Te crystallites in the subsurface is somewhat contradictory to the idea of ion implantation. For ion implantation, one would expect to observe a continuous distribution of crystallites due to the plume dynamics, particularly over the course of 1 hour of fabrication. As noted earlier, the negligible diffusion of Te ions in SiO_2 would inhibit such distinctive migration throughout the subsurface.

As discussed earlier, the wetting of the substrate surface by the disks would likely be more extensive than that visible at present. This suggests their linkage to

the distribution of subsurface crystallites and hence their role as sources for diffusion cannot be ruled out.

What is clear from the observations in Figure 5.29 is that the irregular distribution of subsurface crystallites appears somewhat clustered. This would suggest that they have formed in response to certain conditions pertaining to the substrate and surface material, i.e. encouraging diffusion of Zn and Te or inhibiting it. In this case, one may postulate that with further study, a level of control may be achievable, whereby the diffusion of Zn and Te could be guided and thus made to be entirely continuous across a surface or perhaps inhibited entirely.

5.3.3.4. Thermochemical calculations for the formation of an oxide layer, ZnTe and Te crystallites

In order to comprehend the possible ways in which the identified phases may have formed in the samples discussed in this chapter, a series of calculations were performed using the software package *HSC Chemistry 6.0*. The key questions which this software can directly aid in includes:

(1) the possible ways in which an oxide layer (if any) may form, and what is the most probable route

(2) The results of (1) can then assist in the question of how Te and ZnTe crystallites may have formed. Including the most likely mechanism for this process and its ramifications

Beginning with question 1, the logical approach is to propose the following reactions for the reduction of all possible target oxides in favour of the formation of SiO_2:

(1) $Si + TeO_2 = SiO_2 + Te$

(2) $Si + 2ZnO = SiO_2 + 2Zn$

(3) $Si + 2Na_2O = SiO_2 + 4Na$

(4) $1.5Si + Tm_2O_3 = 1.5SiO_2 + 2Tm$

Between the boundaries of 400 and 1500 ºC, these reactions were calculated and have been plotted in Figure 5.30. It should be noted that the software used to calculate these values is limited in that pressure is kept at the standard 1 bar and

therefore cannot be adjusted to reflect the pressure of the PLD chamber. The results of this study can however be used as an indicator. The large temperature range adopted is used to reflect the effective temperature of the plasma in contact with the substrate surface.

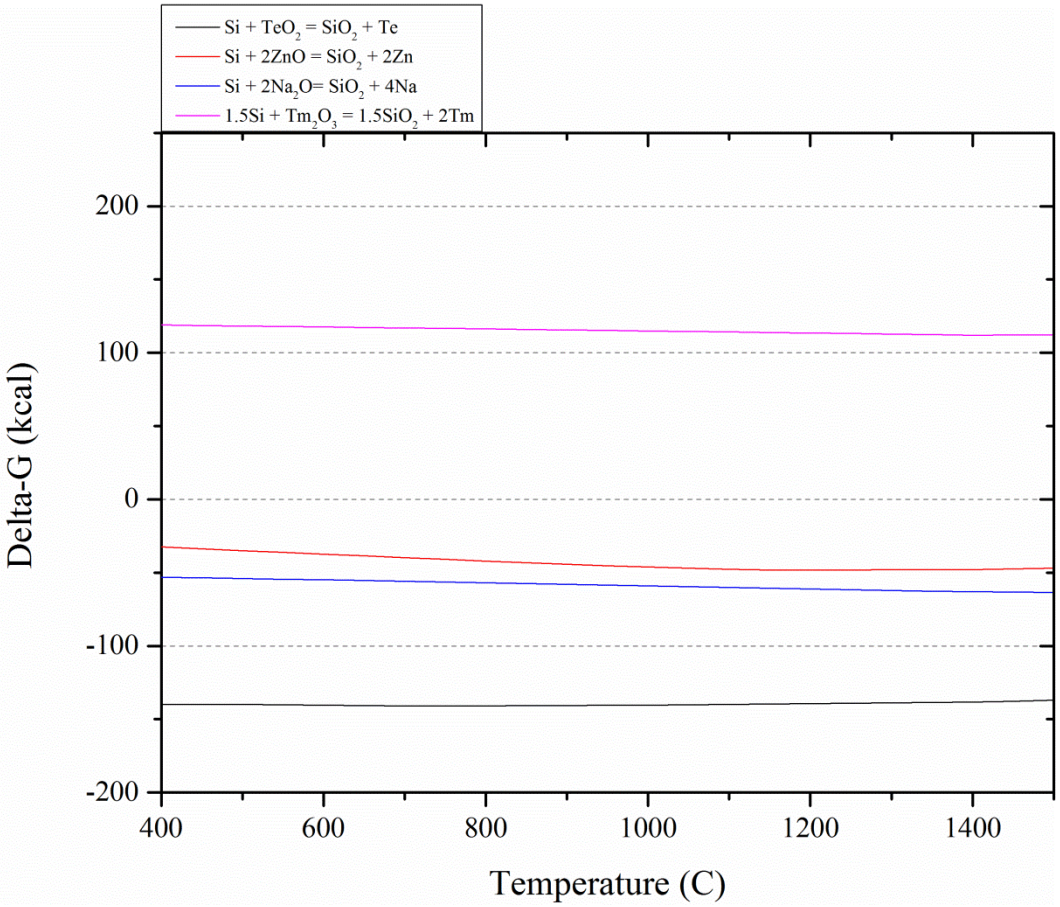

Figure 5.30. Graph of ΔG vs. temperature for the oxidation of Si by the reduction of incoming oxides from the plasma phase.

It is clear from Figure 5.30 that the oxidation of Si is favourable with all but Tm_2O_3 from the target material. This therefore conveys a thermodynamic pathway for the growth of an oxidised silicon surface, one considerably greater than that of the starting Si substrate depicted in Figure 5.2. The oxidation of Si in response to material from the plasma plume can now be considered to be certain; however the question for diffusion (and thus expansion) of this oxide material still remains. Fortunately, this process is relatively well understood due to its importance in the semiconductor processing industry. As noted earlier, the surface of crystalline silicon oxidises in ambient conditions, for that oxidation layer to diffuse deeper into the substrate, bond-breaking energy is required.

Oxygen occupies bond-centred interstitial sites (O_i) in the Si crystal lattice [217] and thus requires energy to jump to a neighbouring site and therefore continue to diffuse through the lattice structure. At high temperatures, this process is relatively well understood, i.e. akin to the processing temperatures of Czochralski

grown Si crystallites. It is found that the diffusion coefficient of O, δ_O, in Si follows the relationship [89]:

$$\boldsymbol{\delta_O = 0.13 exp\left(\frac{-2.53\ [eV]}{kT}\right)} \quad \textbf{(5.5)}$$

Where *k* is Boltzmanns constant and T is the temperature. At 570 ºC (843 K), a diffusion coefficient of 9.8 x 10^{-17} cm^2 s^{-1} is found. This can therefore be related to the observed depths at which surface modification appears to of taken place by applying it to the equation for the depth, *x*, in µm:

$$\boldsymbol{x = \delta_O t 10^4} \quad \textbf{(5.6)}$$

Where t is time in seconds. This equation will be of greater use in the next chapters, however, when applied to a 1 hour deposition, i.e. D60-1, one could expect to observe a maximum oxygen diffusion depth of 0.36 µm. If this is related to the cross sectional SEM image in Figure 5.17 (h) and others like it (not included here) an average depth of the subsurface particles is found to be 0.30 µm ± 0.1 µm. This would suggest that the underlying ZnTe or Te crystallites have precipitated just behind the extent of the oxidized Si material.

Question 2 is somewhat more complex as it develops into the mechanisms for nucleation and growth of crystallites. Before approaching this question, it is prudent to assess the ramifications of the results of the previous question. Firstly, the reduction of Te and Zn can act as a pathway for the formation of ZnTe nucleation sites. Furthermore, the substrate temperature of 570 ºC is well above the melting temperature of Zn and Te (419.5 and 449.5 ºC respectively), one may expect a degree of intermixing between the molten Zn and Te. Reynolds *et al* [218] however identified particularly low solubilities of Te in Zn at 580 ºC, where the molar fraction of Te in Zn was identifies as approximately 1×10^{-6} at this temperature, equivalent to 1 ppm. Following the expected heating from the plasma phase, this only extends to approximately 71 ppm at 910 ºC (the maximum temperature of the study). This suggests that the reduction of Zn and Te on the surface would thus result in significant segregation of the two liquid phases and therefore making it unlikely that ZnTe would form on the surface.

Based upon these considerations for the existence of molten Zn and Te on the samples following their reduction in the presence of Si, the following reactions are considered and the results of which are plotted in Figure 5.31:

(5) 1.5Si + ZnO + TeO2 = 1.5SiO2 + ZnTe

(6) Zn + Te = ZnTe

The calculations plotted in Figure 5.31 suggest a distinct tendency of ZnO and TeO_2 to form ZnTe through a reduction reaction with Si. Note that ΔG across the full temperature range is lower for this reaction than for the individual reduction reactions presented in Figure 5.30. This is in agreement with the XRD and Raman characterisation where ZnTe was found to form for each sample, but only small amounts of Te were confirmed in D30-1, suggesting ZnTe forms preferentially.

The small likelihood of ZnTe formation via a direct reaction between Zn and Te may suggest an explanation as to why the ZnTe crystallites are located in the subsurface. As noted earlier, Da *et al* identified diffusion of TZN oxides into SiO_2, as proposed for the current system. Should one consider an extended oxide layer on the surface of the silicon substrate, as suggested in these materials, whereby oxygen is saturated in the very upper layer, the depositing TZN oxides can thus begin to diffuse. This would be made possible as the SiO_2 matrix can be considered to be effectively saturated with oxygen and thus no longer reactive with the TZN oxides. Note that the reduced liquid Te and Zn products on the surface would not be able to diffuse into the SiO_2, as discussed earlier. This would therefore suggest the upper surface material in D60-1 is primarily composed of Te and Zn. Na would likely diffuse readily into SiO_2 as it is a known network modifier in glassy silica as well as being mobile and highly soluble [219].

Due to the progressive diffusion of all such dopants, the likelihood of Te or Zn oxides encountering a Si atom with a dangling bond increases with depth, particularly when in proximity to the oxide boundary, where an oxygen deficiency may be expected. This in turn could result in reaction (4), thus forming ZnTe. As the number of these events increases in a given volume over time, it would thus encourage the formation of stable ZnTe nuclei, upon which nanocrystallites could grow. Of course in the absence of ZnO, Te nuclei may form and grow, as suggested in the characterisation of D30-1. Furthermore, such an explanation would explain

the proximity between the observed ZnTe crystallites of D60-1 and the calculated oxide boundary.

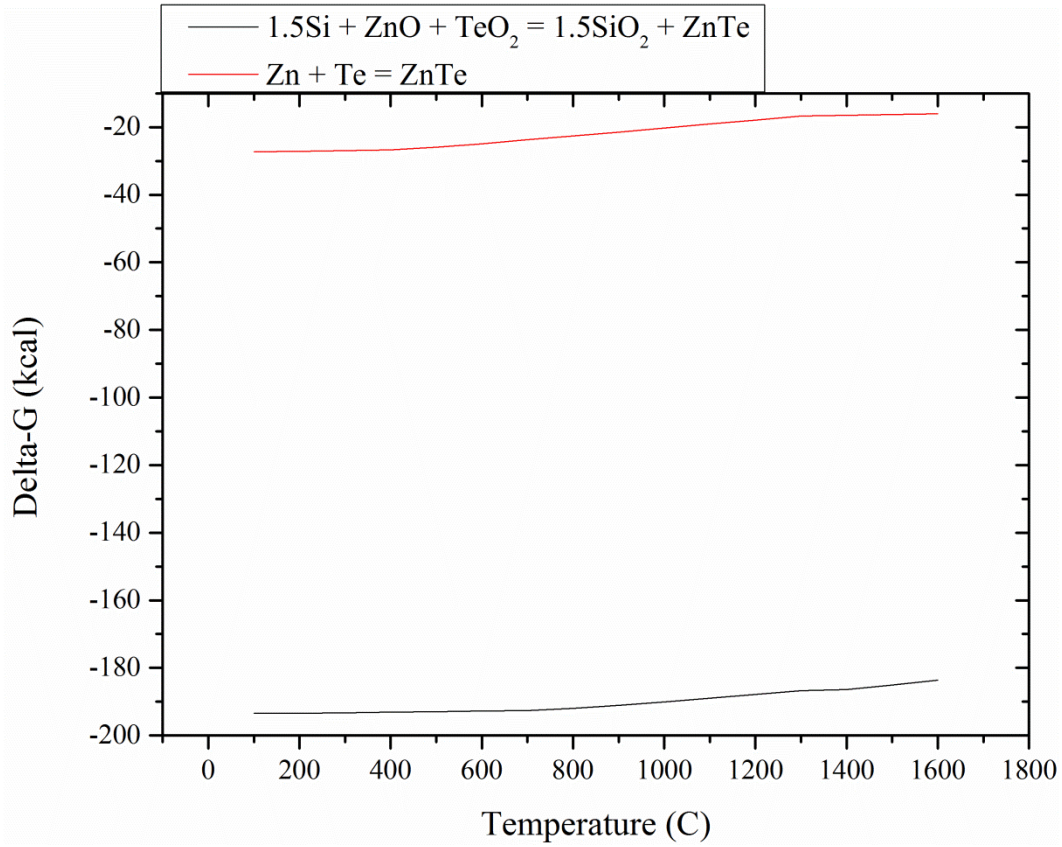

Figure 5.31. Graph of ΔG vs. temperature for the formation of ZnTe both in the presence of Si as oxides, and alone as individual ions

It is likely that the degree of wetting observed on the sample surface through SE-SEM and with regards to findings in literature [196] that heterogeneous nucleation is the formation mechanism responsible. The interface created by a material wetting a surface can act as a nucleation site for crystallites and precipitates into that material. Nucleation of this kind into a crystalline silicon material would be energetically unfavourable due to the strong bonding between sp^3-hybridized Si creating a considerable energy barrier. The disruption of that lattice by the expansion of an oxide layer, as suggested by the earlier calculations, would be much more accommodating to nucleation. Furthermore, the simultaneous reduction of ZnO and TeO_2 by Si, thus favouring the formation of ZnTe, is already expected in this energy regime and hence the supersaturation of such a crystallite can be expected.

5.4. Conclusion

The rapid fabrication of ZnTe and Te nanocrystallites and perhaps α-cristobalite is demonstrated through short ablations (up to 1 hour) of Tm^{3+} doped tellurite glass by femtosecond pulsed laser deposition onto a heated silicon substrate. This novel fabrication procedure is yet to be reported in literature and can be described on the basis of a complex diffusion and chemistry between the depositing plasma with the silicon substrate. It is found that oxygen readily diffuses into silicon, thus favouring the diffusion of stable oxides from the TZN phase. As the dopant oxides diffuse through the silica, it is postulated that an encounter with silicon dangling bonds reduces them. As these events increase in a given volume, stable nuclei of Te or more favourable ZnTe can develop. These then proceed to grow into the observed nanocrystallites. The distribution of ZnTe crystallites is found to be somewhat clustered laterally, while having a well-defined depth profile, suggesting that a greater understanding of the formation mechanics may offer a route to masked or continuous subsurface crystal formation.

Disk-like formations on the surface of the substrate after a 1 hour fabrication time are linked to Te. These features are determined to form through coalescence of deposited material. Through thermochemical calculations, this is found to be evidence of TeO_2 reduction by silicon for the growth of an oxide layer.

An amorphous SiO_2 layer, identified with XRD, forms in response to the oxygen-rich plasma on the silicon substrate in the early stages (up to 30 minutes) begins to crystallise in response to heating from the plasma. It is supposed that metastable β-cristobalite, a high temperature polymorph forms *in situ* and undergoes a first-order phase transition to α-cristobalite in response to the cooling procedure. The strain associated with α-cristobalite is determined to be due to the inclusion of some of the heavier elements, such as Tm^{3+} ions, into the crystal lattice and the subsequent expansion of the unit cell to accommodate these dopants.

The material change from 30 minutes to 1 hour is found to be rather extensive, thus continuing to longer fabrication times may provide further insights.

Chapter 6.
Femtosecond pulsed laser assisted surface modification of silicon substrates II: Effects of laser energy after 4 hours of ablations

This chapter describes the structural characterisation and formation mechanisms of crystallites formed after 4 hours of femtosecond pulsed laser assisted surface modification of silicon substrates. The surface material has now evolved into a complex rare earth doped silicate crystallite as well as isolated ZnO crystal clusters distributed across the surface. These are characterised by SEM, TEM, XRD, SAED and Raman spectroscopy as well as discussion given to describe the formation mechanisms of these materials. A laser fluence threshold is also identified for inducing surface modification.

6.1. Introduction

As found in chapter 5, the formation of ZnTe and Te crystallites is observed through fs-PLSM. A clear evolution of the surface and subsurface material was demonstrated with respect to time. This represents an interaction between the substrate and the plasma phase, whereby the silicon is reducing the deposited material. This is a key principle in defining this technique as mere deposition would not interact with the substrate in this way.

PLD is a physical vapour deposition technique which does not, by definition, involve chemical reactions between the depositing material and the substrate [220]. Such fabrication techniques are however ideal for the growth of thin films and surface coatings [221]. As described in chapter 4 this in itself may form a limitation, in that engineering of these materials can be difficult.

The variety of experimental parameters available to the newly proposed technique is however considerably more varied. The depositing material is considered to be altering the substrate composition and structural state constantly, thus can be described as evolving with respect to the progression of the experiment. Time therefore acts as a primary influence upon how the material ultimately forms and thus alterations at the outset of a given experiment may have dramatic effects in

the completed sample. This therefore offers an avenue for engineering the materials to a greater degree than is possible with the previously considered fs-PLD technique.

The present chapter thus considers this effect with respect to laser energy, whilst investigating the evolution of the material after a 4 hour fabrication time.

6.2. Experimental

Table 6.1 lists the experimental variables used for the primary samples discussed in this chapter, additional samples to aid in discussion are defined in Table 6.2. Table 6.3 details the fixed experimental parameters applied to both sample sets. The experimental parameters used for the samples described in this chapter are based upon the observations of the previous chapter. The laser fluence is varied to investigate the effect it may have upon the resulting layers. Specifically, it is to test the existence of a fluence threshold for surface modification to occur. Temperature is also varied here, so as to investigate how sensitive the surface modification is to reductions from 570 °C, as used in the previous chapter. The time fabrication time is also extended for each of the samples listed in Table 6.1 to 4 hours. In doing so, an expansion of the evolution of the surface modification can be studied with a greater emphasis on the factors effecting surface modification.

Table 6.2 provides the experimental parameters for a brief discussion on the nature of the ablated material and its appearance at room temperature. Ablating with the substrate at room temperature ensures that only PLD occurs. A view of the approximate volume and nature of the deposited material can therefore be ascertained. These samples thus serve as a guide to interpret the nature of the surface modified samples. These samples are deposited onto a silica substrate as surface modification would not occur at room temperature and they are much cheaper than single crystalline silicon. Justification for this change shall be provided in section 6.3.1.

Table 6.1. Table of the experimental variables in the fabrication of samples analysed and discussed in this chapter. Sc-Silicon refers to single crystalline silicon.

Sample ID	**Temperature (°C)**	**Laser energy (μJ)**	**Laser fluence (J cm^{-2})**	**Substrate**	**Duration (hours)**
I50A	570	50	0.30	Sc-Silicon	4
C570	570	30	0.18	Sc-Silicon	4
C300	300	30	0.18	Sc-Silicon	4
C400	400	30	0.18	Sc-Silicon	4
I100A	570	100	0.60	Sc-Silicon	4

Table 6.2. Table of the laser energy parameters and substrate used for for G0 samples.

Sample ID	**Laser energy (μJ)**	**Substrate**	**Duration (mins)**
G0-1	125	Fused silica	30
G0-2	80	Fused silica	30
G0-3	60	Fused silica	30
G0-4	50	Fused silica	30
G0-5	40	Fused silica	30
G0-6	30	Fused silica	30
G0-7	20	Fused silica	30
Blank	0	Fused silica	30

Table 6.3. Table of the variables which are fixed for each experiment in this chapter, unless otherwise stated.

Pressure	70 mTorr
Target to substrate distance	70 mm
Laser spot size	1.7×10^{-4} cm^2
Target	G0 (Tm^{3+}:TZN, 3:77:10:10)
Gas type	Ar

6.3. Results and discussion

6.3.1. Dependency of ablated TZN material upon the laser energy

To demonstrate the variability of the ablated material with regards to laser energy adjustments, a series of minor samples were fabricated. Note sample G0-4 has already been discussed in relation to the short duration depositions. These samples were all fabricated under identical experimental parameters aside from varying laser energy which is outlined in Table 6.2. All samples for this study were fabricated from the same target, G0, in 70 mTorr of Ar background gas and a 30 minute deposition onto fused silica substrates at room temperature. It is important to note that all samples, including the dry run sample, were put through the same preparation processes described in section 3.1.2 for the samples in Table 6.2.

Following deposition, optical microscopy was used to examine the relative abundance of deposited material on the surface of the substrate; images taken during this are presented in Figure 6.1.

Figure 6.1 shows a qualitative decrease in the relative abundance of deposited material with respect to laser energy, particularly in the droplet yields. This demonstrates good agreement with the observations made by others where a well-controlled and quantified laser fluence is used. Based on this, a study of the relative effect of variations in laser energy can therefore be conducted to study its effects on the resulting modified surface layer of the substrate.

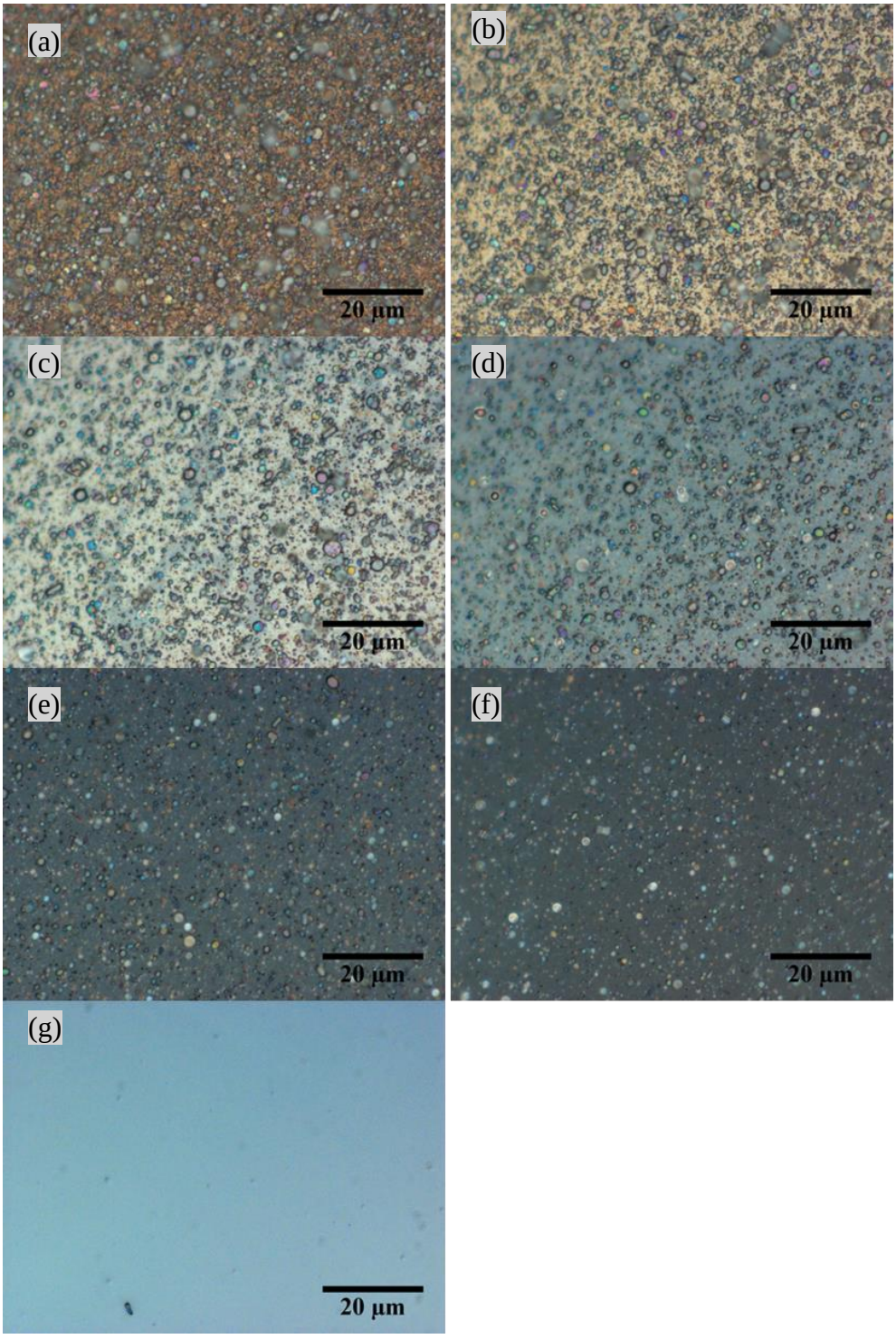

Figure 6.1. Optical microscopy at 100 x magnification of G0 samples, (a) G0-1, (b) G0-2, (c) G0-3, (d) G0-4, (e) G0-5, (f) G0-6, (g) G0-7, (h) blank silica glass substrate

6.3.2. Topographical and compositional characterisation of surface modified material

In order to build upon the analysis conducted in the previous section, a series of samples were fabricated to study the effects of laser energy on the surface modification induced over a 4 hour period of TZN plasma-Si surface interactions. This includes an equivalent sample for those discussed in chapter 5, labelled I50A. The conditions in which these samples were fabricated are detailed in Table 6.1, where certain experimental parameters are kept identical to ensure continuity, as described in Table 6.2. Of the samples detailed in Table 6.1, those of primary interest in this section include C570, I50A and I100A.

The primary samples were characterised by cross sectional secondary electron-scanning electron microscopy (SE-SEM) in Figure 6.2. This revealed extensive alterations to the surface and subsurface in comparison to the samples of chapter 5. The transition of surface features from 30 to 60 minutes revealed surface features atop a smooth, seemingly unaltered substrate; the addition of a further 3 hours to the fabrication has understandably altered that substantially, with significant texturing of the surface. What is also of note is that the subsurface particles again appear to have grown and remain in a sedimentary line below the surface.

With regard to the upper surfaces of each sample in Figure 6.2, extensive crystallisation has occurred, particularly for sample I100A, fabricated at 100 μJ, the highest laser energy studied.

In order to view the surface crystallites of I100A in greater detail, top-down SE-SEM images were acquired of various different types of crystal formations on the its surface and are presented in Figure 6.3, Figure 6.4 and Figure 6.5. Chemical composition of the surface depicted in Figure 6.6 is obtained via energy-dispersive X-ray (EDX) mapping in Figure 6.7 as well as four supporting point EDX measurements marked on Figure 6.6 and tabulated in Table 6.4.

In addition to this, a number of spot EDX measurements were taken of marked areas on the surface of I50A in Figure 6.8 where the semi-quantitative compositions were calculated; these are tabulated in Table 6.5.

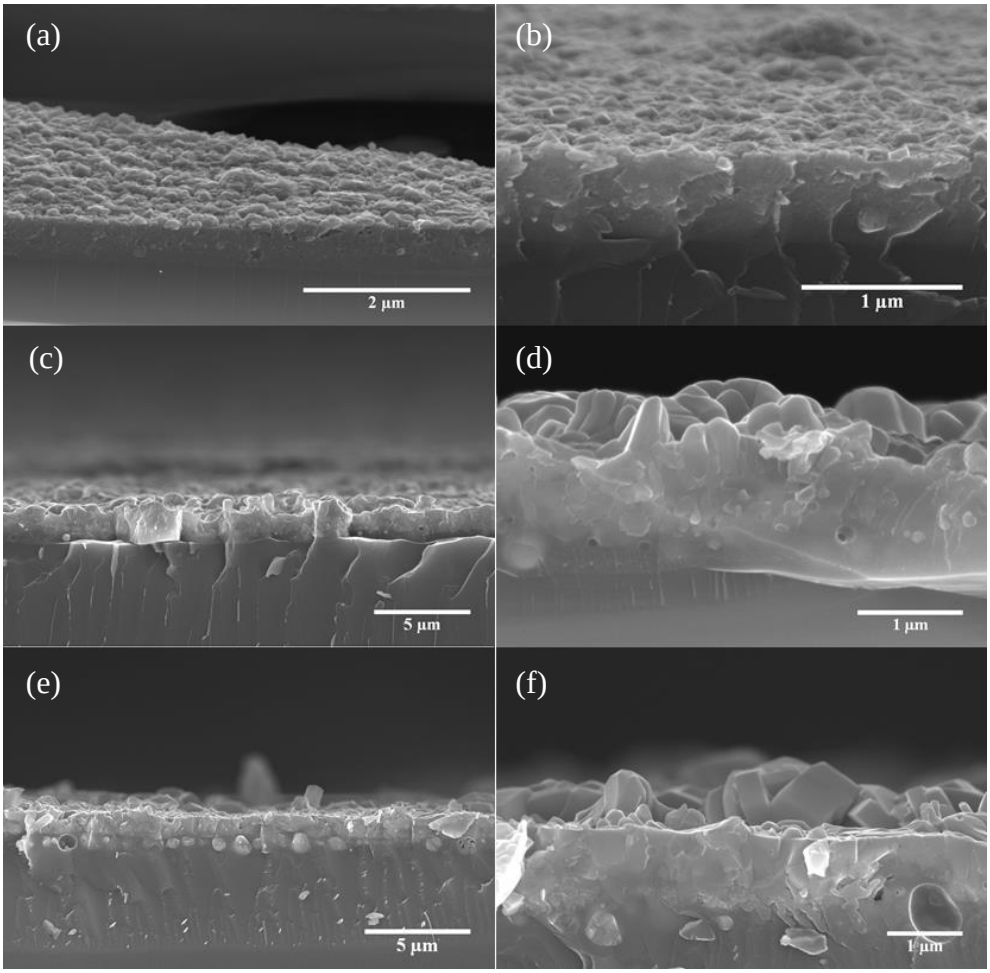

Figure 6.2. Cross-sectional SE-SEM images of samples (a, b) C570; (c, d) I50A and (e,f) I100A

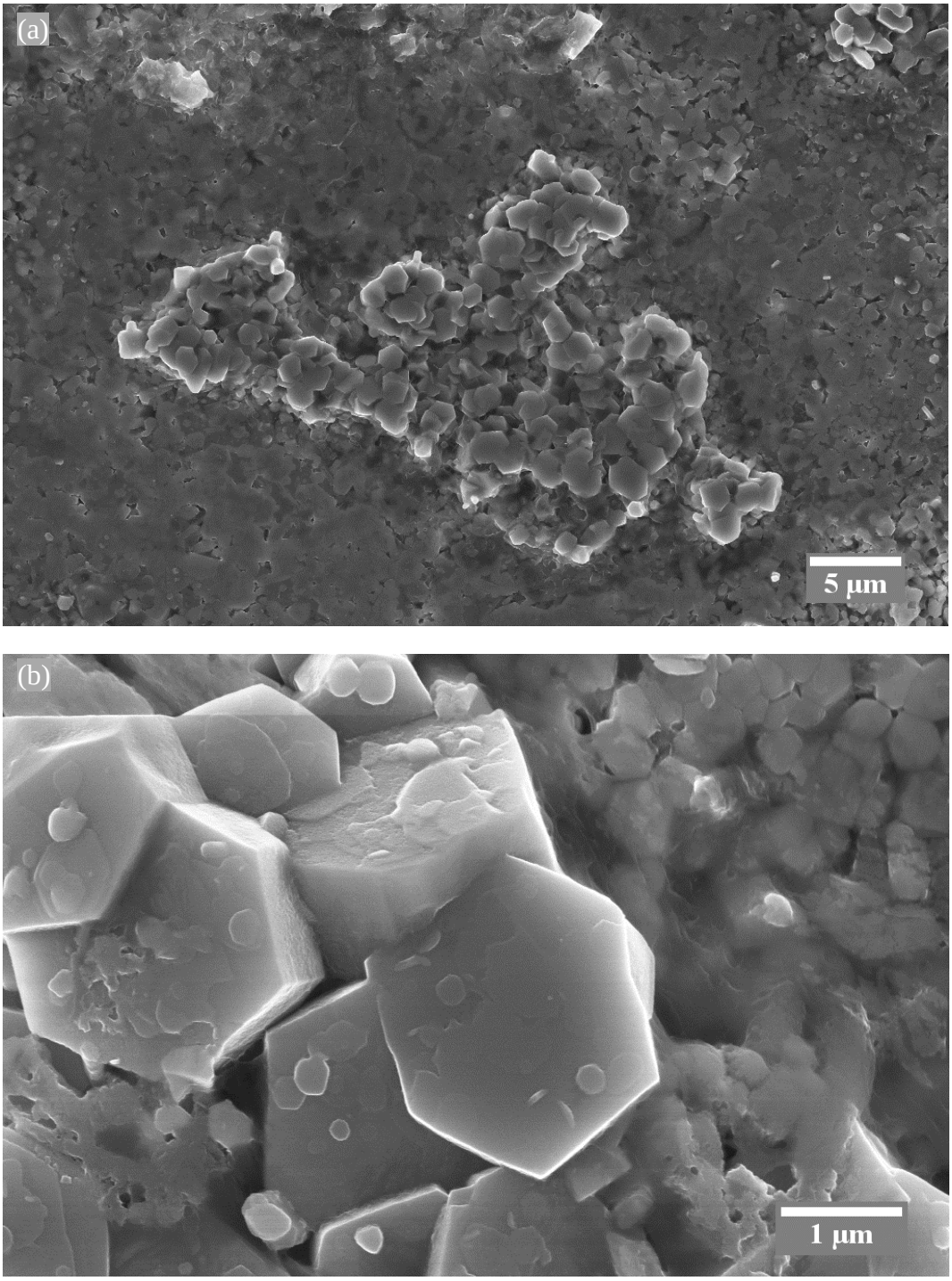

Figure 6.3. Top down SE-SEM images of I100A, (a) isolated cluster of hexagonal crystal facets protuding upward from the substrate, (b) High magnification of a small cluster of hexagonal shaped crystals revealing texturing of one of the facets

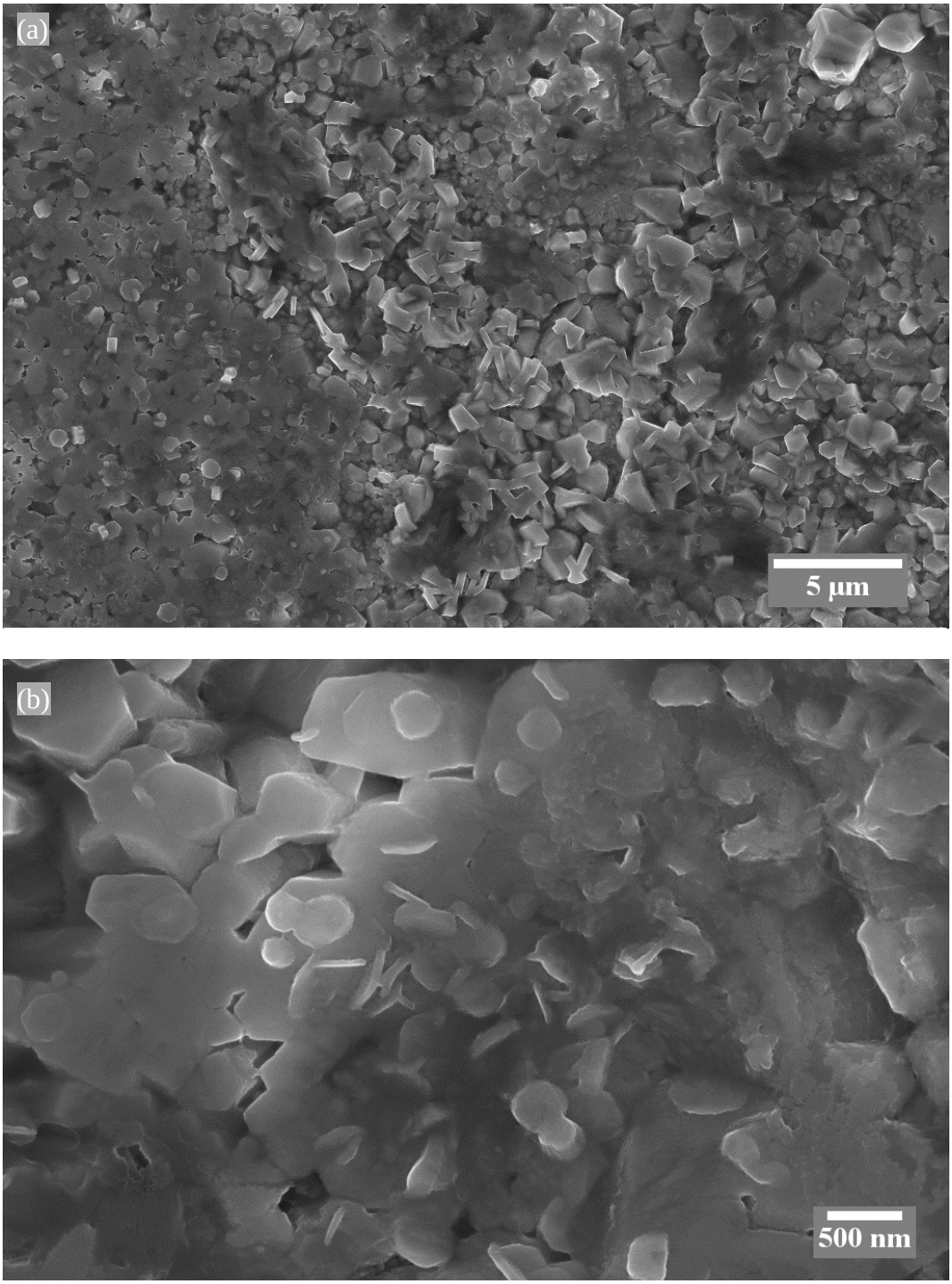

Figure 6.4. Top-down SE-SEM image of the surface of I100A, (a) clustering of microplatelets, predominantly orientated on their side (b) clustering of nanoplatelets atop some of the surface crystallites.

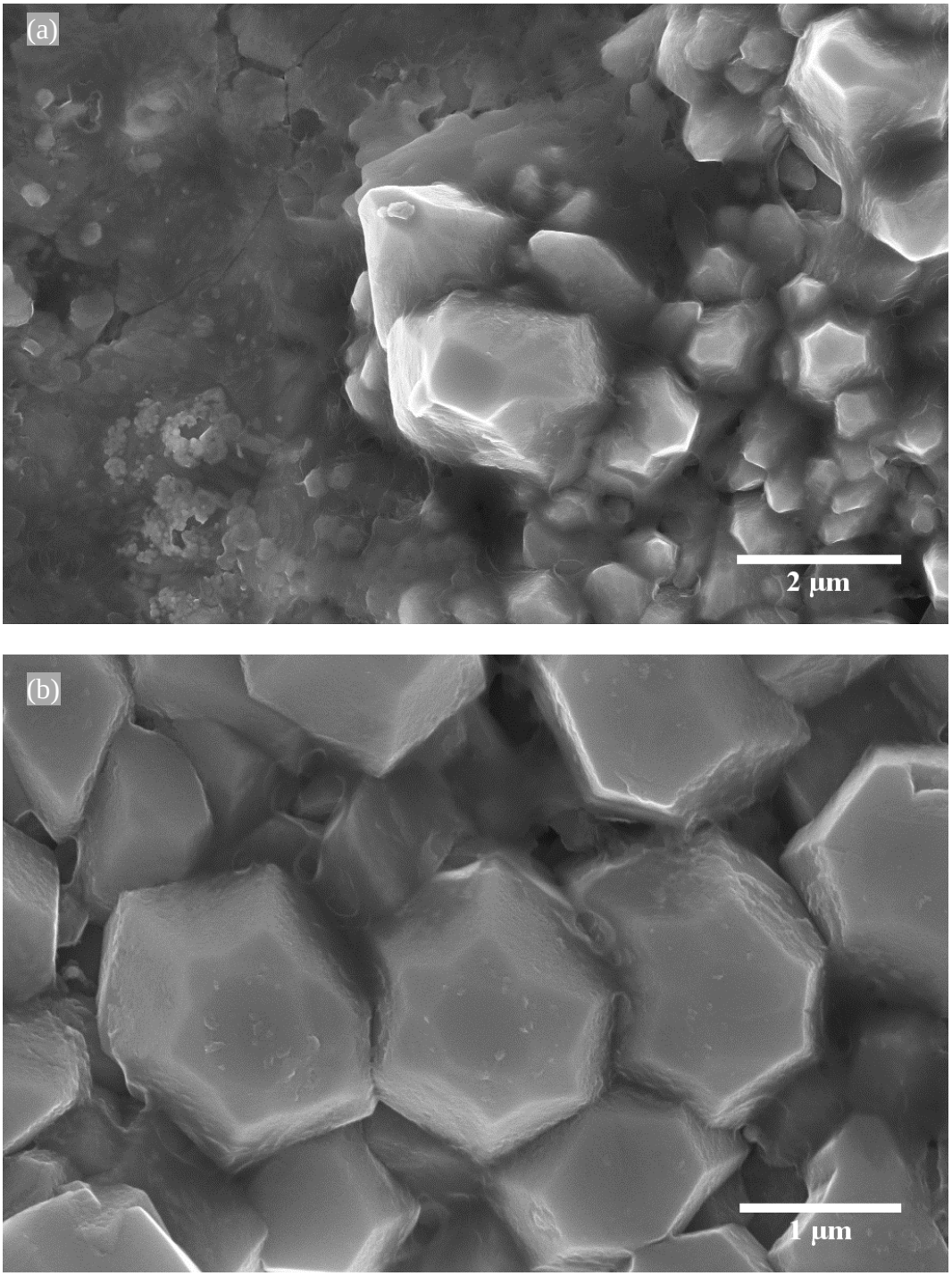

Figure 6.5. Top down SE-SEM images of I100A, (a) isolated cluster of capped hexagonal pyramid structures protruding from the surface, (b) A variation from of the capped hexagonal pyramid structures, this time in the shape of stars

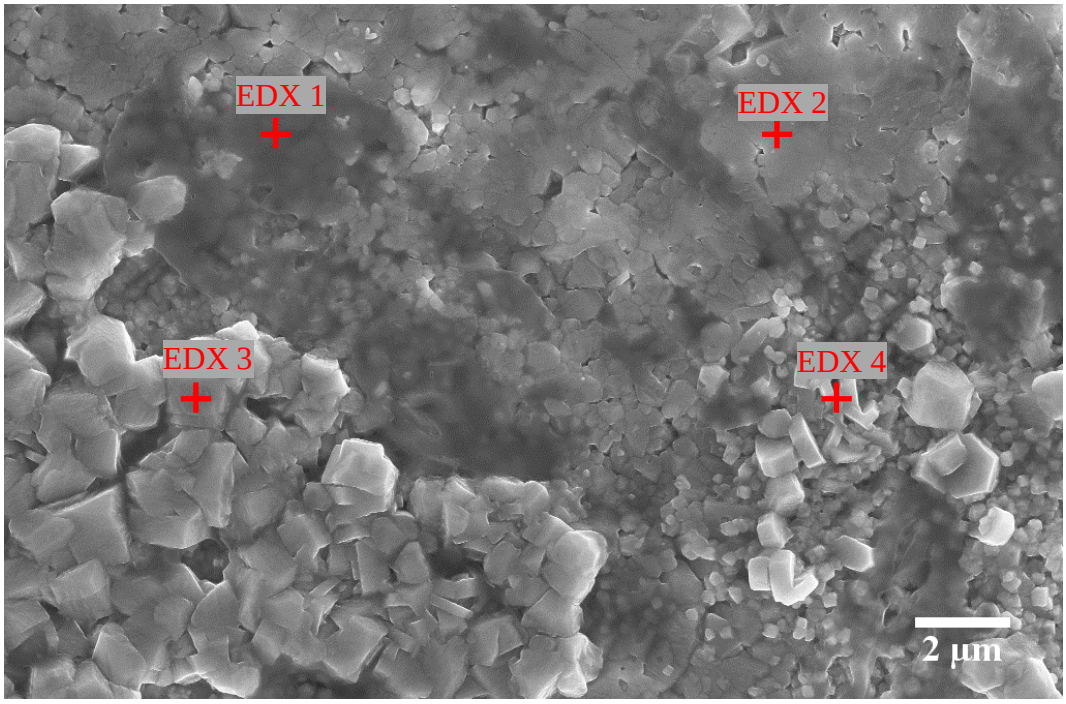

Figure 6.6. SE-SEM image of the surface of I100A which was selected for EDX mapping (see Figure 6.7). Regions from which point point EDX measurements are marked on and their semi-quantative elemental composition is provided in Table 6.4.

Table 6.4. Table of the semi-quantitative calculated chemical compositions in at% for the regions marked on the surface of the SE-SEM image in Figure 6.6

Element ID	EDX 1 (at%)	EDX 2 (at%)	EDX 3 (at%)	EDX 4 (at%)
Si	10.8	11.3	Trace	5.3
O	55.7	58.2	44.9	36.1
Te	3.5	4.3	Trace	2.9
Zn	Trace	Trace	44.3	42.8
Na	19.5	13.4	10.3	6.0
Tm	9.8	12.5	Trace	5.8

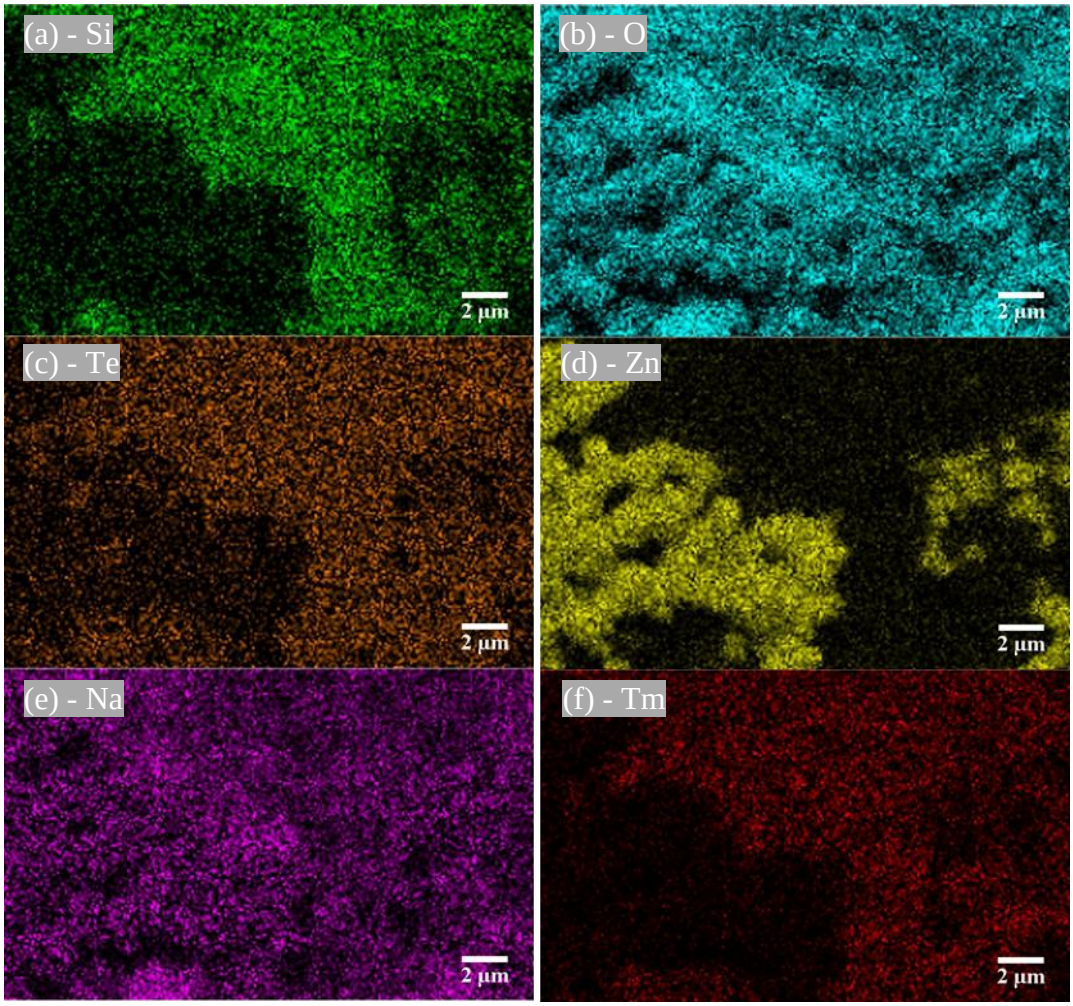

Figure 6.7. Elemental maps constructed from the characteristic EDX lines of the respective elements, resolved over successive scans of the surface of sample I100A depicted in Figure 6.6. The corresponding elements and the characteristic EDX lines selected include: (a) Si (K series); (b) O (K series); (c) Te (L series); (d) Zn (L series); (e) Na (K series) and (f) Tm (M series).

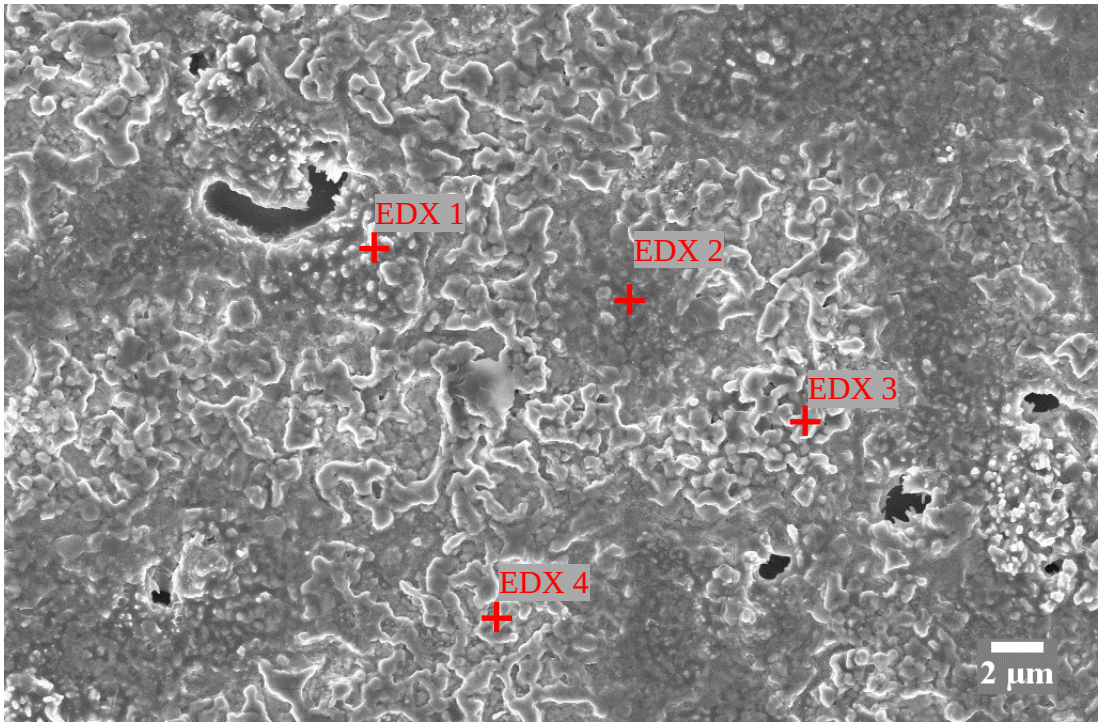

Figure 6.8. Top-down SE-SEM images of the surface of I50A with the location from which point EDX measurements were acquired. Chemical compositions acquired in this figure are provided in Table 6.5.

Table 6.5. Table of EDX point measurements of I50A acquired from the regions illustrated in Figure 6.8. Data is presented as an atomic percentage (at%) of the overall composition. Concentrations of less than 1 at% have been marked 'trace', there were no incidences of 0 at% measurements for the elements of interest.

Element ID	EDX 1 (at%)	EDX 2 (at%)	EDX 3 (at%)	EDX 4 (at%)
Si	30.9	16.4	Trace	1.0
O	40.4	55.4	44.72	38.1
Te	6.6	3.2	Trace	1.0
Zn	3.6	3.4	39.7	46.5
Na	6.2	8.3	14.0	10.5
Tm	12.2	13.4	Trace	3.0

Many of the crystal formations visible in Figure 6.3 and Figure 6.4 of I100A appear particularly well developed. In order to better understand these crystal formations, it is essential to comprehend the EDX analysis. Firstly, it is clear that an isolated Zn-rich phase exists on the sample; this is found most clearly in the EDX mapping of I100A in Figure 6.7, as well as in the semi-quantitative chemical compositions in Table 6.4 and Table 6.5 for I100A and I50A. Furthermore, the distinctive crystal formations analysed through both of these methods are repeated across both sample surfaces in differing sizes. Although EDX measurements are to a certain extent semiquantitative, it seems particularly unlikely that the Zn-rich phases are ZnTe due to the depletion of Te; this early indication strongly suggests they are ZnO.

The EDX point measurements were acquired from regions which appear best suited to detect the resulting X-ray signal from the areas of interest, i.e. a relatively flat and continuous surface. It is important to recognise however, that these measurements may or may not have a significant inclusion of characteristic X-rays from the underlying material. This shall be returned to with greater clarity in the subsequent TEM analysis.

As can be seen in Figure 6.3 (a), there is a distinct variation in the height of these Zn-rich crystallites in relation to the surrounding material; this is interpreted via the visible edge and protrusion contrast on these clustered crystallites. The surrounding crystallites from this central cluster appear to be relatively flat in comparison. The difference in contrast between these two crystal types also suggests a phase difference. Furthermore, the distinct clustering of crystallites is visible as a collective of distinct shapes and sizes, whereby microplatelets are visible in Figure 6.4 (a) while nanoplatelets are visibly clustered together in (b). As depicted in the EDX elemental mapping from the region depicted in Figure 6.6 in Figure 6.7. Based upon these observations, it is reasonable to assume at this stage of the discussion, that the microplatelets are also Zn-rich, due to the significant Zn Lα signal detected for this region.

The EDX measurements acquired for I50A from Figure 6.8 in Table 6.5 suggest an agreement in the compositional segregation for both I50A and I100A. It is important to recall however the principles governing EDX spectroscopy via SEM. The depth at which the X-rays will be emanating as well as the various

considerations with regard to phase boundaries, material densities and edges of crystallites etc. will instil additional, unaccountable influences on the quantisation of the composition. The results therefore are simply used to convey a degree of variability over small areas, where certain elements appear to be clustered. Supporting evidence for the observations made thus far shall be provided throughout this chapter before a conclusive assessment of the material can be made.

What is also of note on the surface of I50A is the existence of holes penetrating the sample. Such features were not observed on the surface of the dry run sample, nor any of the other samples as seen in Figure 5.1 (b), and therefore one must assume they stem from the extended fabrication processing. The holes depicted on the surface of I50A in Figure 6.3 (a) are identified on the surfaces of many samples deposited for 4 hours, not presented in this chapter. They are invariably located in the Tm-rich regions and therefore are associated with their formation, however conclusive evidence for their formation is unfortunately lacking.

6.3.3. Cross sectional TEM analysis of samples fabricated for 4 hours

In order to understand the structure of these materials thoroughly as well as probe some of the queries regarding chemical composition, raised in the previous section, cross-sectional TEM analysis was carried out. This is also used as a means to better understand the evolution of the surface material identified in section 6.3.2, enable this to be related to samples from the previous chapter and aid in future discussions.

6.3.3.1. TEM analysis of a cross section prepared by the standard preparation procedure

To relate the observations of chapter 5 to the current work, sample I50A was prepared for cross-sectional TEM analysis via the standard preparation methodology, as described in section 3.3.4.2. Key observations of this sample are presented in Figure 6.9. In addition to this, accompanying selected area electron diffraction (SAED) acquired from regions of Figure 6.9 (b) and (c) marked in green are provided in Figure 6.10, including d-spacing measurements from Figure 6.10 (a) provided in Table 6.6. The d-spacings calculated from the SAED pattern in Figure 6.10 (b) are compared to some of I100A in Table 6.9. In order to

qualitatively assess the cross sections chemical composition , EDX mapping was also carried out. Elemental maps acquired from this section are provided in Figure 6.12 corresponding to the TEM image in Figure 6.11. Finally, a table of the EDX analysis measurements of selected areas indicated in Figure 6.9 (b) and (c) in red, lists the varying atomic percentage (at%) concentrations of the different constituent elements in this sample. Note that TEM based EDX analysis, as with SEM, is not an entirely quantitative measurement as large errors can be associated with the precise calculation of concentrations as well as the measured response.

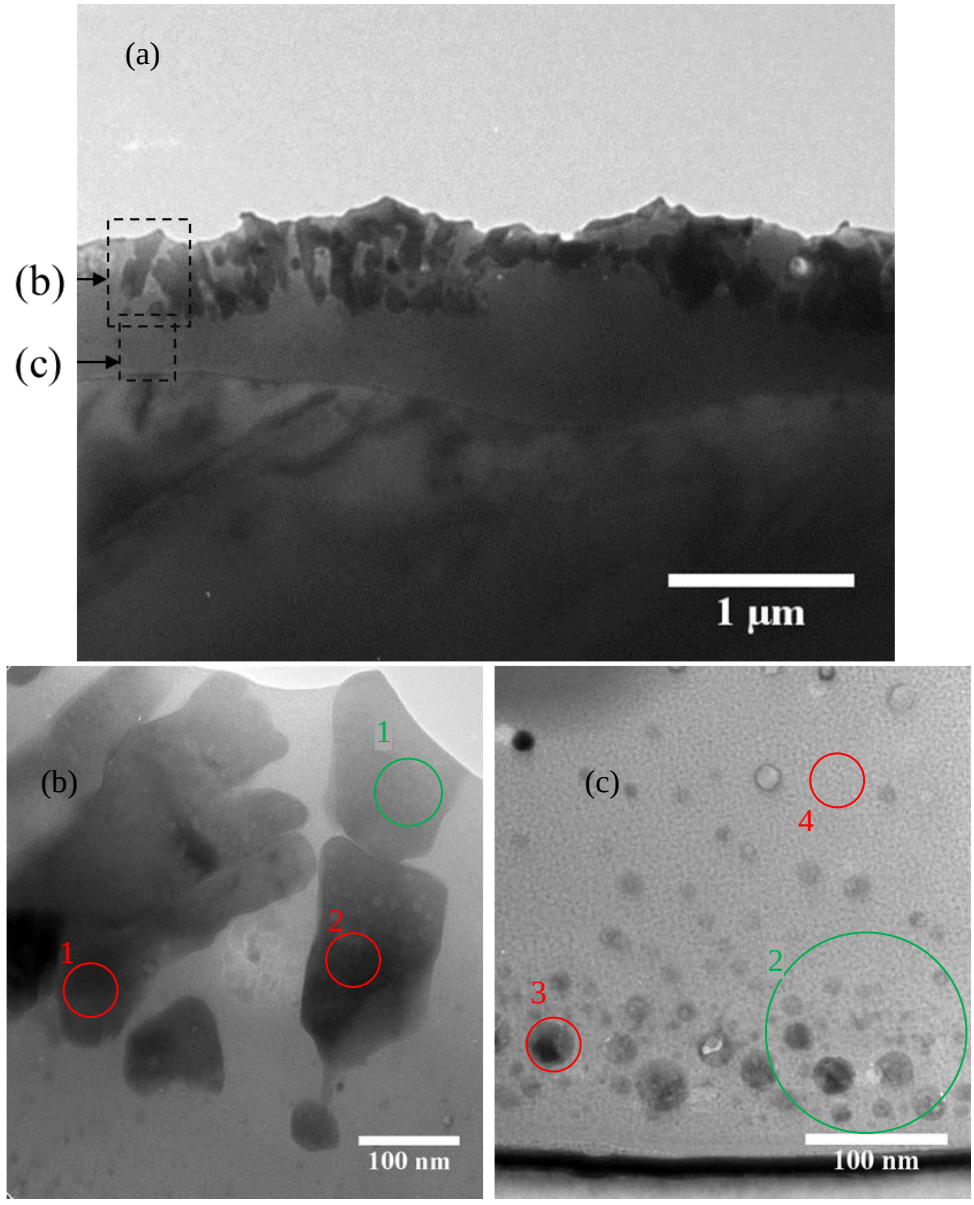

Figure 6.9. I50A cross sectional TEM images of (a) a large cross-sectional area; (b) high magnification of the upper crystallites exposed on the surface including areas from which EDX (red) and SAED (green) measurements were acquired (highlighted in (a)); (c) high magnification of the subsurface nanocrystallites and the interface including areas from which EDX (red) and SAED (green) measurements were acquired (highlighted in (a))

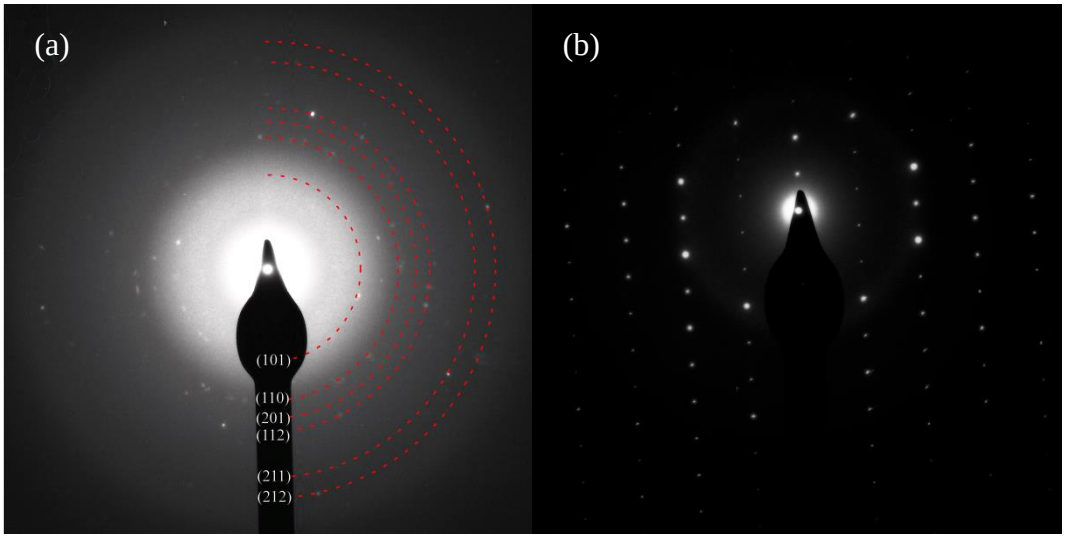

Figure 6.10. Selected area electron diffraction patterns from regions illustrated in Figure 6.9corresponding to (a) SAED 1 identifed as ZnTe and (b) SAED 2 of an unkown Tm-rich silica crystal phase

Table 6.6. Table of the calculated d-spacings from the SAED pattern in Figure 6.10 (a) compared to hexagonal Te (ICCD ref: 00-036-1452)**.**

Measured d-spacing, Å	**Reference d-spacings, Å**	**h k l**
3.22	3.23	101
2.62	-	-
2.25	2.23	110
2.03	2.08	111
1.85	1.84	201
1.77	1.78 or 1.76	112 or 103
1.44	1.46 or 1.42	210 or 211
1.31	1.31	212

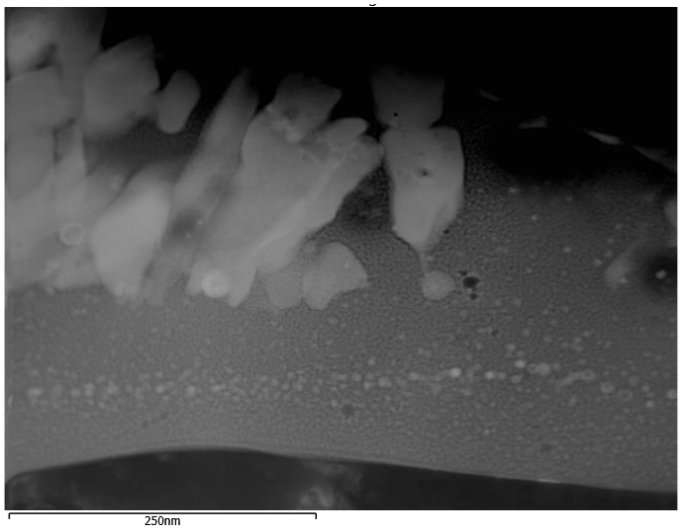

Figure 6.11. TEM cross-sectional image used for EDX mapping of sample I50A

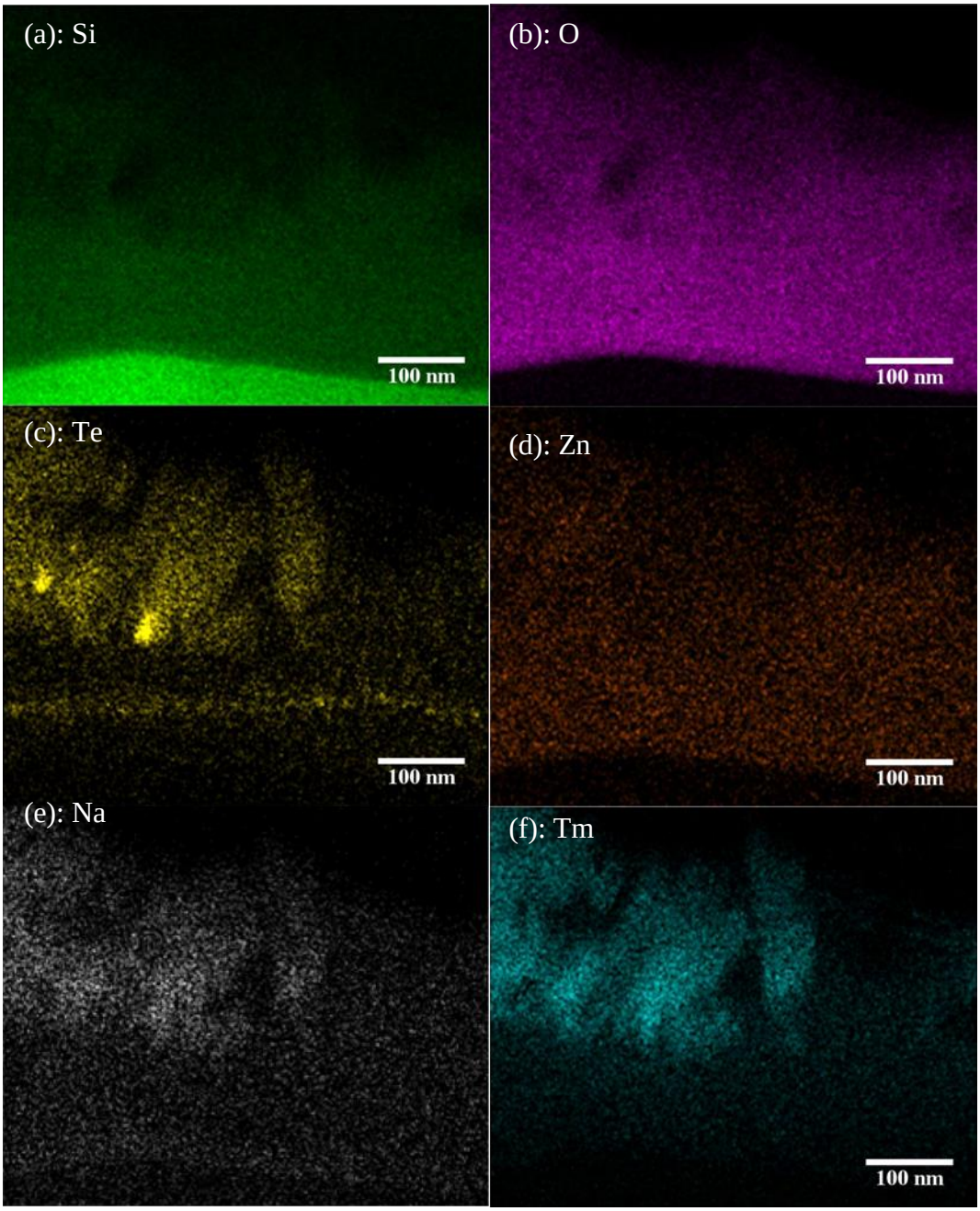

Figure 6.12. EDX maps of the area identified in Figure 6.11 for sample I50A; elemental maps include: (a) Si (K series); (b) O (K series); (c) Te (L series); (d) Zn (K series); (e) Na (K series); Tm (L series)

Table 6.7. Table of the atomic percentages (at%) calculated from the EDX measurements of the regions illustrated in red in the cross sectional TEM analysis of I50A in Figure 6.9. Concentrations of less than 1 at% have been marked 'trace', there were no incidences of 0 at% measurements.

Element	**EDX 1 (at%)**	**EDX 2 (at%)**	**EDX 3 (at%)**	**EDX 4 (at%)**
O	75.5	76.3	80.8	84.0
Si	12.8	12.8	17.3	15.6
Te	Trace	Trace	Trace	Trace
Zn	Trace	Trace	Trace	Trace
Na	11.1	9.9	1.3	Trace
Tm	1.9	2.0	Trace	Trace
Total	100	100	100	100

Due to the extensive modification observed for sample I100A in relation to others, this too was prepared via the standard preparation methodology for TEM analysis. Key data pertaining to the TEM analysis of sample I100A includes cross sectional TEM images in Figure 6.13 with areas marked in green for SAED patterns in Figure 6.14. The SAED pattern in (a) was measured in order to calculate the d-spacings and thus compare to the SAED pattern of a similar crystal from I50A in Table 6.9 while the calculated d-spacings of (b) are provided in Table 6.8 and is compared to that of a standard ZnTe pattern (ICCD ref: 04-012-6469**)**. Elemental maps of Figure 6.13 (a) assembled from an EDX area scan is provided in Figure 6.15 while calculated at% concentrations from point EDX measurements of regions indicated in red on Figure 6.13 are provided in Table 6.10.

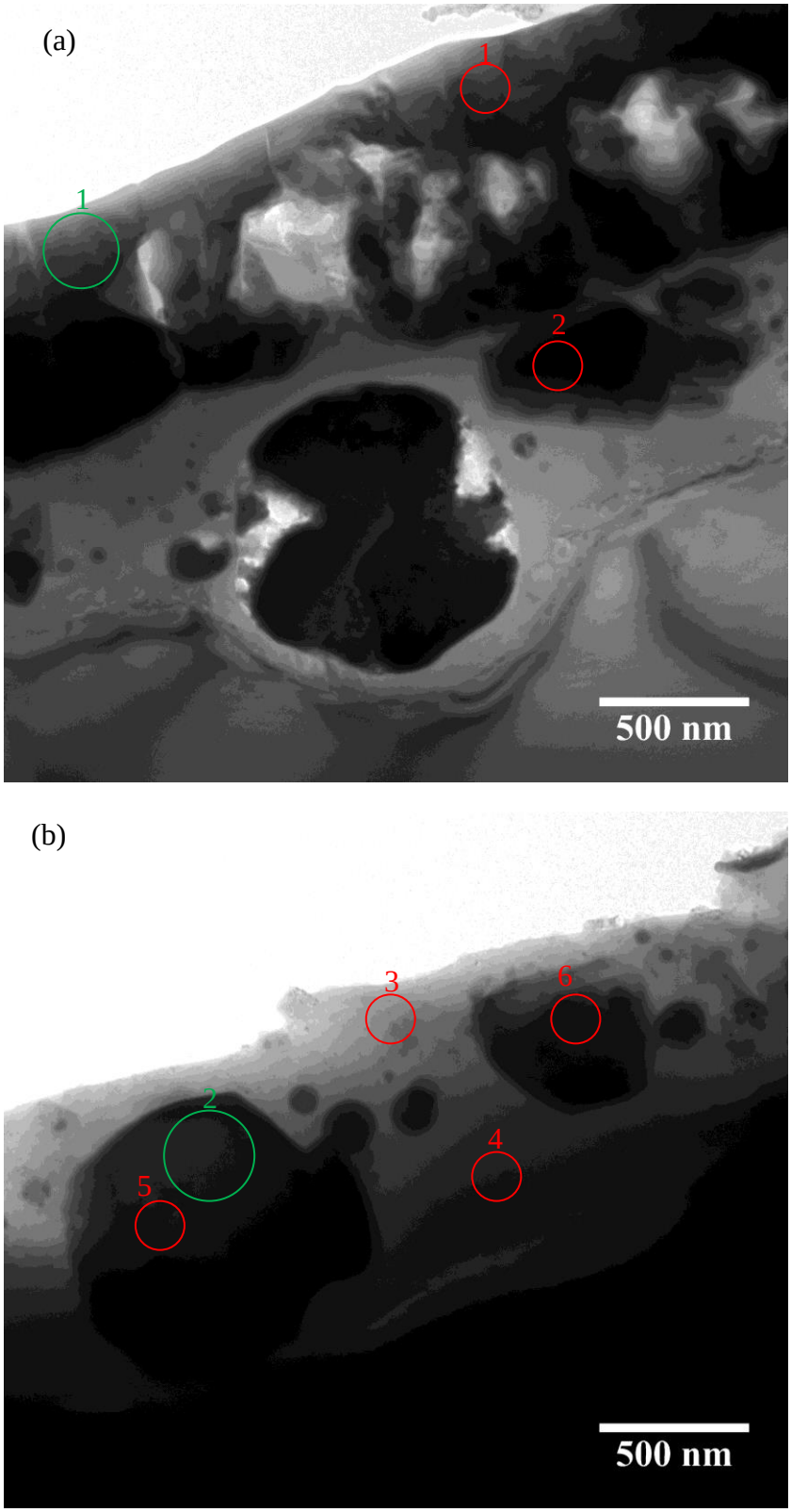

Figure 6.13. Cross-sectional TEM images of sample I100A including areas from which EDX (red) and SAED (green) measurements are taken; (a) full section, (b) subsurface with upper crystallites removed through damage during processing.

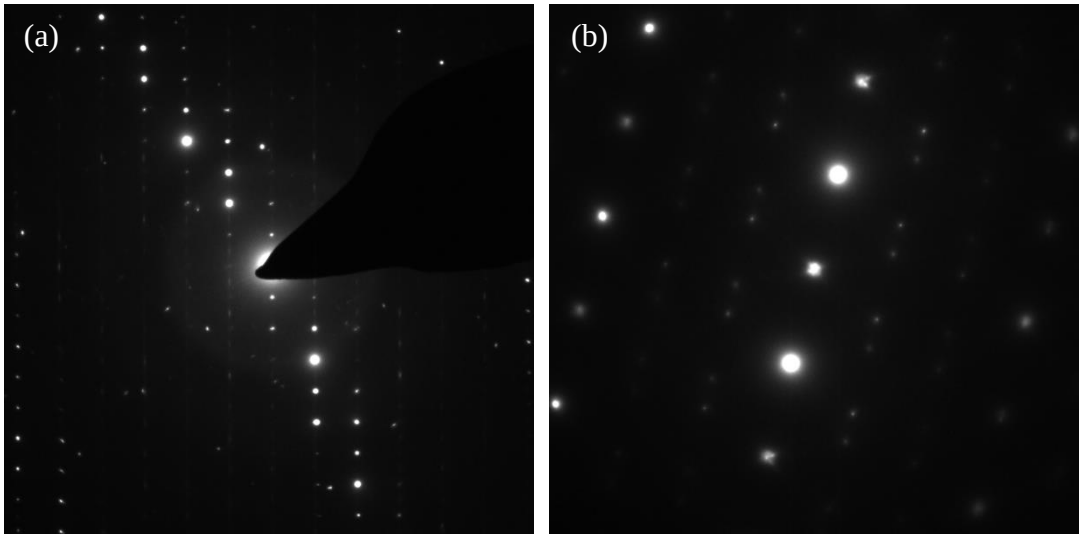

Figure 6.14. Selected area electron diffraction (SAED) patterns for areas identified in Figure 6.13 in green as: (a) 1 and (b) 2.

Table 6.8. Table of calculated d-spacings from the SAED pattern in Figure 6.14 (b) and is compared to cubic zinc telluride (ZnTe) (ICCD ref: 04-012-6469).

Measured d-spacing, Å	**Reference d-spacings, Å**	**h k l**
3.54	3.51	111
3.02	3.04	200
1.97	2.15	220
1.66	1.75	222
1.83	1.83	311
1.51	1.52	400
1.34	1.36	420
1.22	1.24	422
1.00	1.01	600

Table 6.9. Table of the calculated d-spacings from the SAED pattern in Figure 6.10(b) and Figure 6.14 (a).

Measured d-spacing, Å, from Figure 6.10 (b)	**Measured d-spacing, Å, from Figure 6.14 (a)**
9.11	8.81
5.50	5.32
4.65	-
4.60	4.49
4.19	-
3.11	-
3.03	-
2.89	-
2.74	2.73
2.45	-
2.39	2.33
2.11	2.12
1.92	-
1.84	1.85
1.71	1.73
1.61	-
1.55	1.57
1.45	-
1.43	-
1.41	-
1.39	1.36

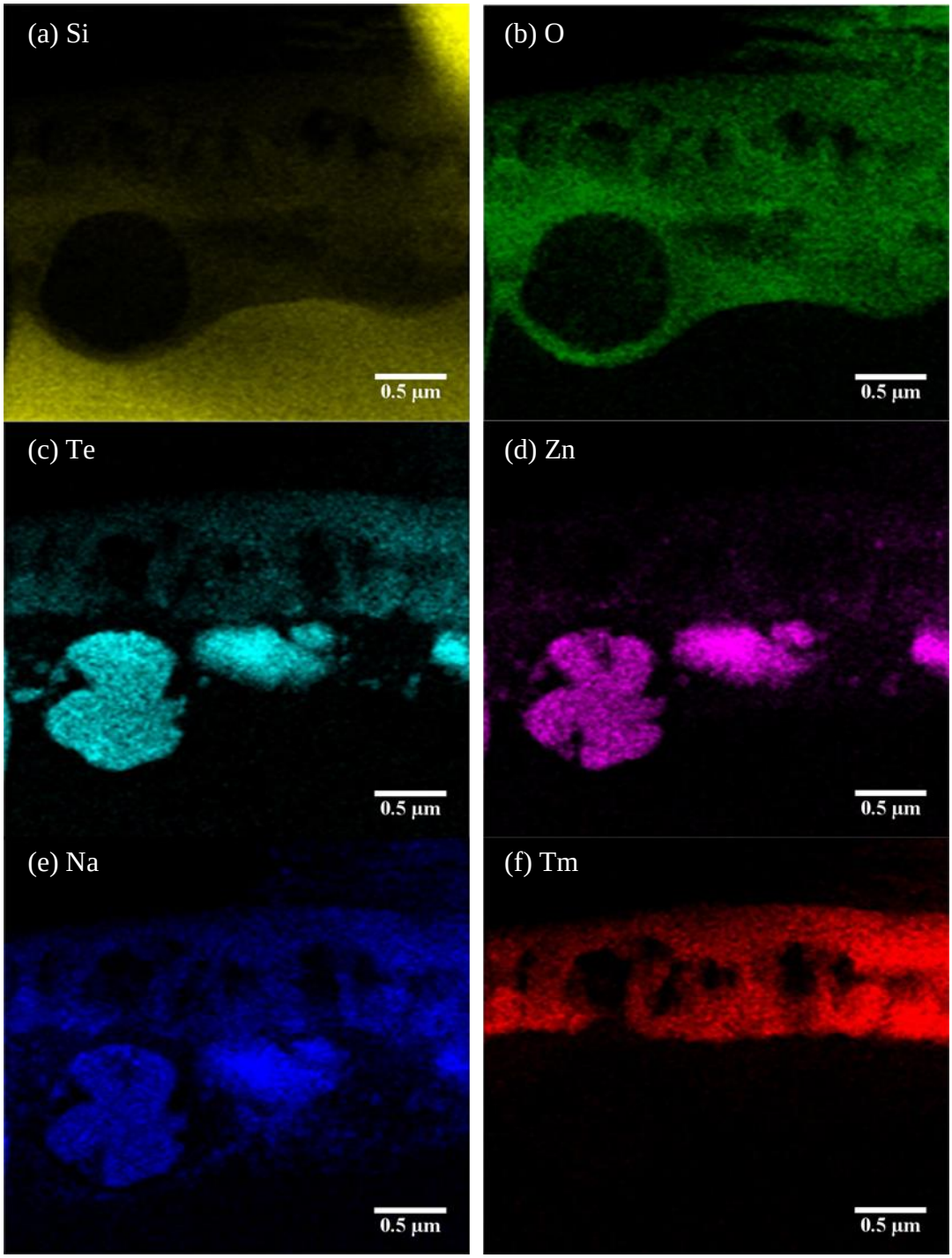

Figure 6.15. EDX maps of the region depicted in Figure 6.13 (a) of sample I100A, elemental maps include: (a) Si (K series); (b) O (K series); (c) Te (L series); (d) Zn (K series); (e) Na (K series); (f) Tm (L series).

Table 6.10. Table of the atomic percentages (at%) calculated from the EDX measurements of the regions illustrated in red in the cross sectional TEM images of I100A in Figure 6.13. Concentrations of less than 1 at% have been marked as 'trace', while those with 0 at% detected are marked as nil.

Element ID	EDX 1 (at%)	EDX 2 (at%)	EDX 3 (at%)	EDX 4 (at%)	EDX 5 (at%)	EDX 6 (at%)
O	69.9	27.8	84.2	82.1	19.3	4.4
Si	13.3	21.9	14.3	16.9	30.8	34.2
Te	Trace	6.8	Nil	Trace	10.1	13.1
Zn	Trace	26.8	Nil	Nil	36.9	30.6
Na	7.3	15.1	1.4	Nil	2.9	16.9
Tm	8.6	1.0	Nil	Nil	Trace	Trace
Total	100.0	100.0	100.0	100.0	100.0	100.0

The chemical composition of these two samples is well described by the presented point EDX and mapping techniques in combination with matched SAED patterns to known phases. EDX mapping of I50A in Figure 6.12 indicates the subsurface particulates to be composed of Te, where the respective SAED pattern in Figure 6.10 (a) corroborates this assertion. Similar subsurface crystallites in I100A instead reveal ZnTe, identified through point EDX analysis in Table 6.10 (column EDX 2) as well as the respective SAED pattern in Figure 6.14 (b). The EDX map of sample I100A in Figure 6.15 identifies high concentrations of Na in what SAED analysis in Figure 6.14 (b) indicates to be a ZnTe crystallite. This can be explained as Na is a known dopant in the ZnTe lattice structure [222], creating shallow acceptor states [223]; the abundance of Na in the plasma phase as well as its occurrence in the surrounding amorphous silica matrix should facilitate this doping. The inclusion of Na into the ZnTe lattice therefore makes this wide-bandgap semiconductor p-type.

Differences in the chemical composition of subsurface particles observed between I50A and I100A is similar to that observed in chapter 5. Chapter 5 identified the existence of hexagonal Te as well as cubic ZnTe in samples fabricated over a shorter period. This same effect appears to be present in the current samples:

I50A and I100A, and shall be fully characterised using XRD in the following section. Furthermore, there is a considerable difference in the scale of these subsurface particles. I50A for example has a considerably smaller average particle size than I100A, yet a larger yield. This may be indicative of the effects of laser energy, or perhaps a manifestation of the formation mechanisms of the specific crystallites.

The suggestion of the surface crystallites in Figure 6.9 and Figure 6.13 being the developed form of the disk-like particles previously observed on the surface of D60-1 in Figure 5.17 can also be understood in relation to the analysis of D60-1s XRD data. This suggested the existence of α-cristobalite, a high temperature polymorph of silica; although corroborating evidence could not be acquired for a more conclusive identification, observations within the present system support this assertion. EDX analysis of these surface crystallites suggests a heavily modified silicate, doped with Na, Te and Tm, indicating that the modification of the crystal network via such a doping regime has altered the d-spacing of the crystal system.

The similarities in the chemical composition of the surface crystallites for samples I50A and I100A, evidenced through EDX analysis via SEM and TEM, also extends to the d-spacing measurements acquired from their respective SAED patterns in Figure 6.10 (b) and Figure 6.14 (a). This strongly suggests the phases of these crystalline structures are very similar. The SAED pattern of I100A in Figure 6.14 (b) shows diffraction spots from the higher order Laue zones (HOLZ). Unfortunately due to a malfunction in the FEI Technai TF20, rotation of the sample was only possible in one axis, hence the usual alignment of the electron beam down the zero order Laue zone (ZOLZ) was not possible. As a result, some of the diffraction points are not visible in this orientation, this is also suggested by the lack of addition diffraction points which may (or may not) correspond with that of the d-spacing measurements from Figure 6.10 (b).

6.3.3.2. TEM analysis of a cross section prepared by FIB

In order to resolve an electron diffraction pattern from the ZOLZ as well as alleviate some of the queries raised thus far in this section, a section of I100A was extracted using focused ion beam (FIB) lithography, illustrated in Figure 6.16. The extracted region was thinned to 75 nm, as seen in Figure 6.17, so it could be imaged by TEM. An overall TEM image of a key area of interest from the FIB section is

provided in Figure 6.18 (a), while (b) includes a higher magnification of the right hand side of this area, where a large number of crystallites are located. Four areas were selected for SAED measurements, including different crystal formations; these are provided in Figure 6.19, while the d-spacing measurements from (a) and (c) are given in Table 6.11 and Table 6.12. The SAED pattern in Figure 6.19 (d) is found to be composed of at least two different spot patterns, one which is clearly single crystalline and mimics that of the SAED patterns described in Table 6.9 and another which appears to be polycrystalline. Table 6.14 contains the semi-quantitative EDX point measurements illustrated on Figure 6.18 (b). As with previous TEM cross sections, an EDX map was acquired of the area in view in Figure 6.18 (b) where the individual elemental maps are provided in Figure 6.21.

The area of I100A selected for TEM analysis in Figure 6.16 by FIB was chosen for a number of key reasons. Firstly, the Tm-rich crystallites identified in Figure 6.13 (a) are likely to be the same phase as those surrounding the Zn-rich crystallites in Figure 6.3 (a). The large Tm concentration identified during TEM analysis is also reflective of the EDX measurements acquired during SEM analysis of I100A in Figure 6.7. This can therefore be corroborated via selecting a similar region using FIB.

It would be particularly difficult to acquire a section by isolating some of the larger Zn rich crystallites, due to the risk of shadowing of the Pt coating. The Pt coating is used to protect the surface material from the beam of Ga ions used for the lithography process. This would severely compromise or even prohibit subsequent analysis and was therefore avoided. Beam damage of some of the Si substrate occurred during the final thinning stage regardless and is visible as holes at and below the interface with the modified layer. This is unfortunate, however it does not inhibit the acquisition of accurate data from the areas of interest as the modified layer/Si interface are well characterised in the previous TEM cross sections.

Finally, the area selected in Figure 6.16 has two nanoplatelets atop the surface on the right hand side of the area selected as well as a darker region on the left hand side. As noted earlier, this darker region is indicative of a different phase and can thus be identified. The nanoplatelets and similar structures have previously been linked to high Zn concentrations, thus detailed analysis of these structures is of

great interest. In summary, this area provides multiple opportunities to study different features of interest on I100A which can then be extended to other samples.

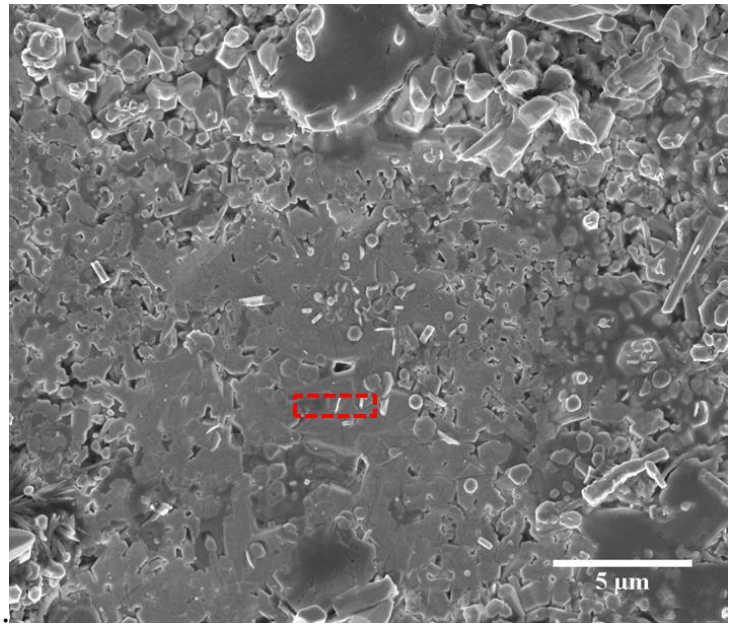

Figure 6.16. SE-SEM image of the surface of I100A, marking the selected area for extraction via focused ion beam lithography.

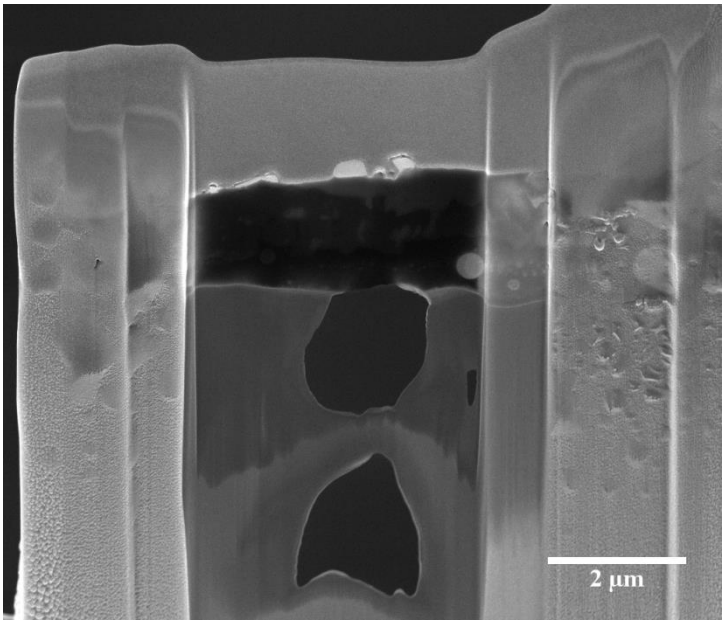

Figure 6.17. SE-SEM image of the area extracted from I100A by FIB, following the final thinning stage just prior to TEM analysis.

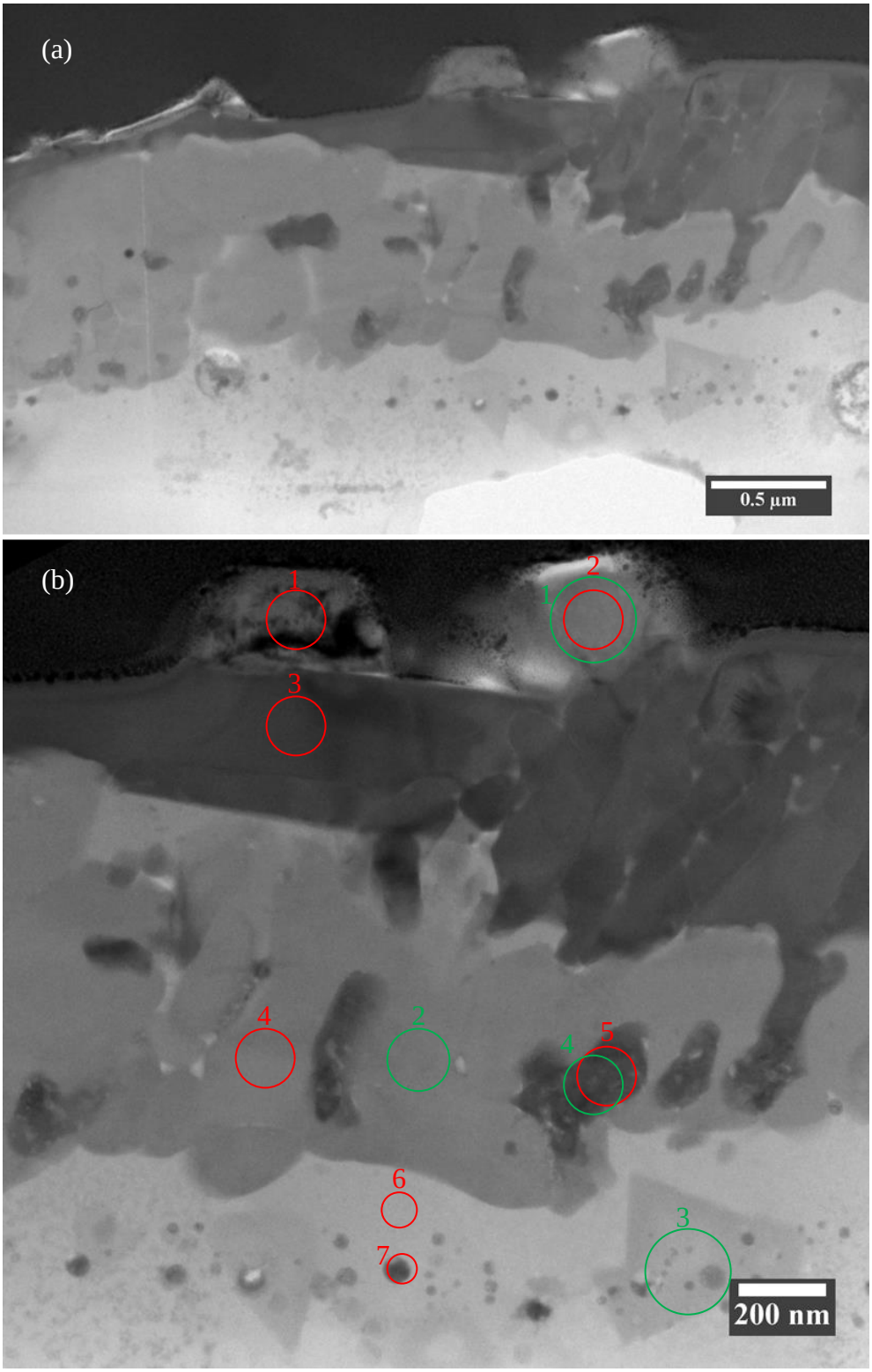

Figure 6.18. TEM cross section of I100A prepared by FIB, (a) overall view of the area, (b) higher magnification of the right hand side of (a). Regions from which EDX was acquired are marked in red, while SAED patterns are marked in green.

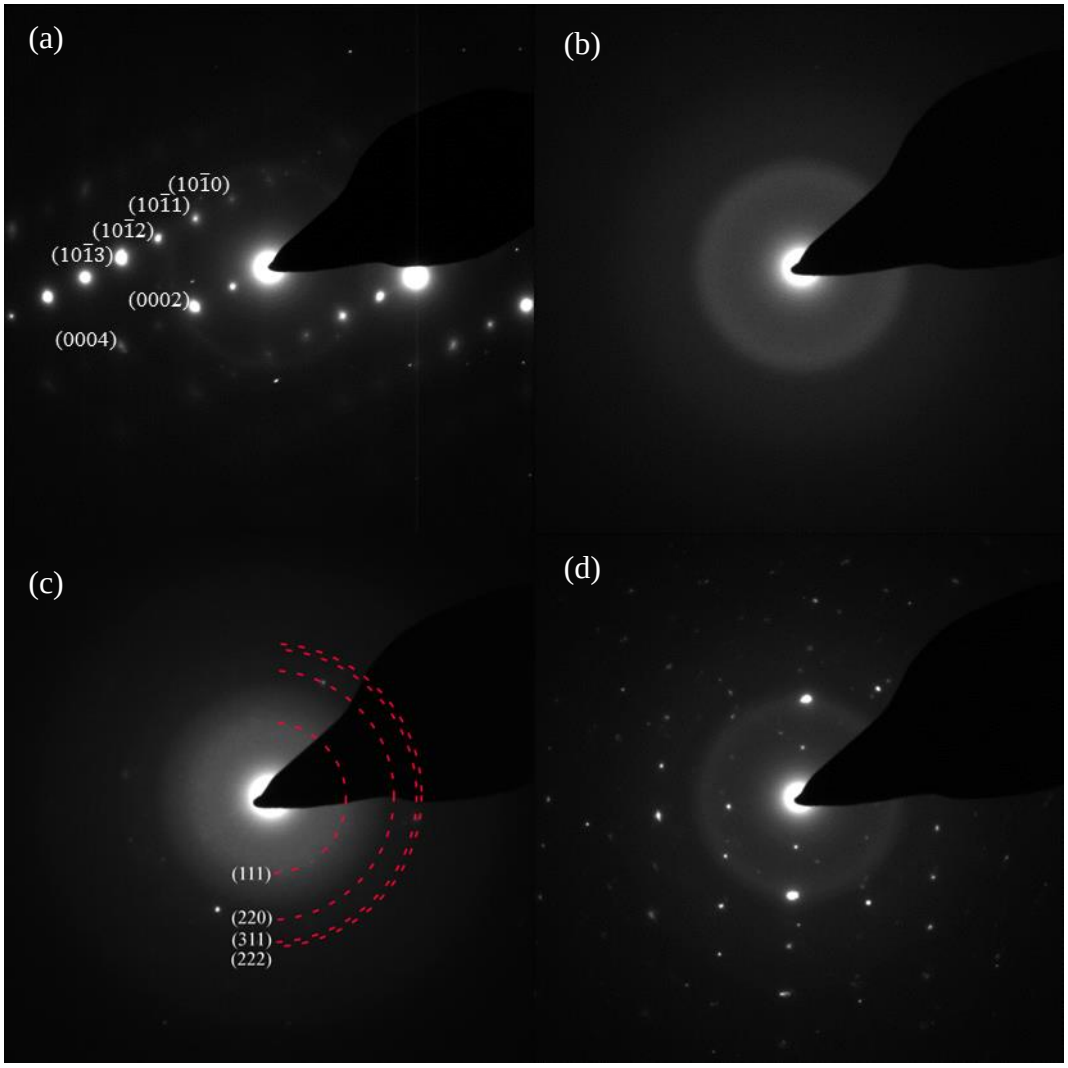

Figure 6.19. Selected area electron diffraction patterns taken of the areas depicted in Figure 6.18 (b): (a) SAED 1: ZnO; (b) SAED 2: amorphous silica; (c) SAED 3: ZnTe; (d) SAED 4: Tm^{3+} rich silicate

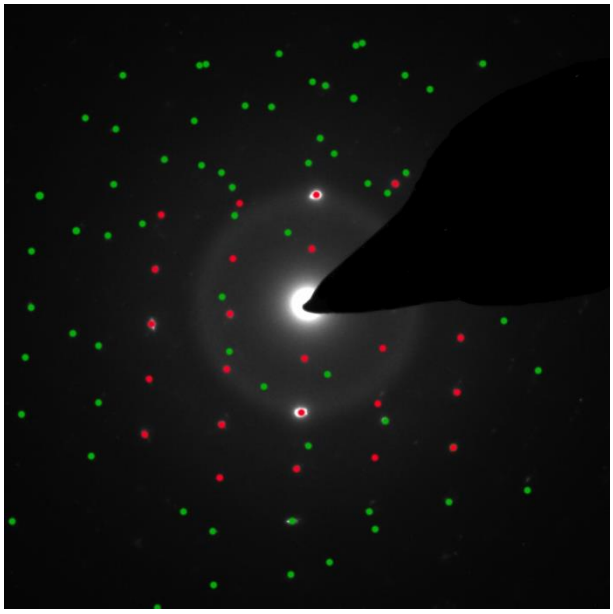

Figure 6.20. Replication of the SAED pattern in Figure 6.19 (d) in order to distinguish between the distinctive single crystal phase (red spots) and the remaining spots (green)

Table 6.11. Table of calculated d-spacings from the SAED pattern in Figure 6.19 (a) and is compared to hexagonal wurtzite Zinc Oxide (ZnO) (ICCD ref: 04-015-4060)

Measured d-spacing, Å	**Reference d-spacings, Å**	**h k i l**
5.35	-	-
2.80	2.81	$10\bar{1}0$
2.60	2.60	0002
2.48	2.47	$10\bar{1}1$
1.90	1.91	$10\bar{1}2$
1.75	-	-
1.48	1.48	$10\bar{1}3$
1.30	1.30	0004

Table 6.12. Table of calculated d-spacings from the SAED pattern in Figure 6.19 (c) and is compared to cubic zinc telluride (ZnTe) (ICCD ref: 04-012-6469)

Measured d-spacing, Å	**Reference d-spacings, Å**	**h k l**
3.51	3.51	111
2.13	2.15	220
1.83	1.83	311
1.76	1.75	222

Table 6.13. Table of calculated d-spacings from the different crystal phases determined in the SAED pattern in Figure 6.20, taken from Figure 6.18 (b)

Measured d-spacing, Å, for the red spots	**Measured d-spacing, Å, for the green spots**
5.32	4.04
3.80	3.45
3.43	3.24
2.86	3.15
2.71	2.58
2.56	2.18
2.44	2.13
1.99	2.10
1.89	1.94
1.71	1.88
1.42	1.81
-	1.37

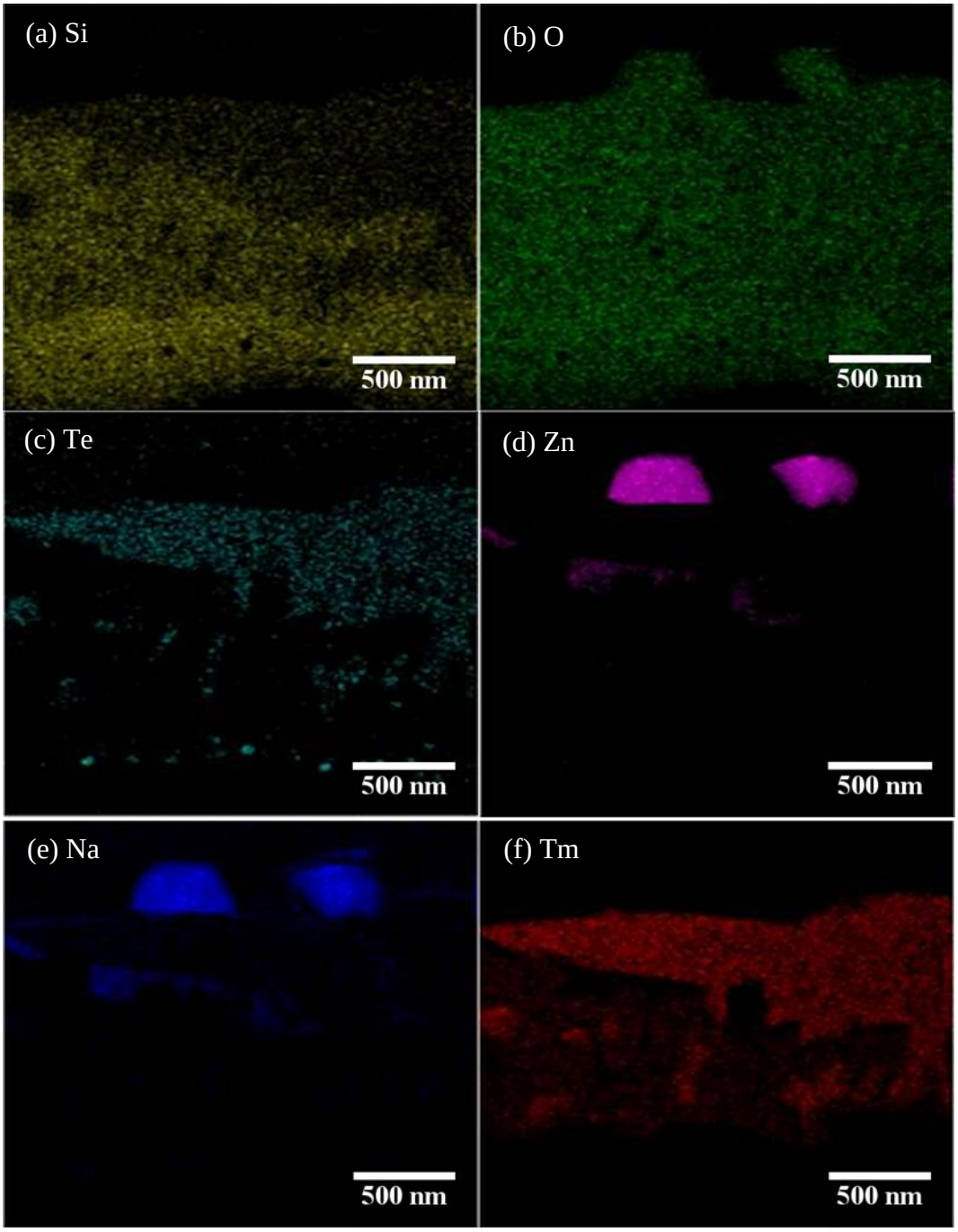

Figure 6.21. EDX maps of the region depicted in Figure 6.18 (b) of sample I100A, elemental maps include: (a) Si (K series); (b) O (K series); (c) Te (L series); (d) Zn (K series); (e) Na (K series); (f) Tm (L series).

Table 6.14. Table of the atomic percentages (at%) calculated from the EDX measurements of the regions illustrated in red in the cross sectional TEM images of I100A in Figure 6.18 (b). Concentrations of less than 1 at% have been marked as 'trace', while those with 0 at% detected are marked as nil.

Element ID	EDX 1 (at%)	EDX 2 (at%)	EDX 3 (at%)	EDX 4 (at%)	EDX 5 (at%)	EDX 6 (at%)	EDX 7 (at%)
Si	Trace	Trace	12.2	17.2	11.0	16.5	7.7
O	50.5	49.4	75.5	79.3	74.8	82.3	36.9
Te	Nil	Nil	Trace	Nil	Trace	Nil	11.7
Zn	28.2	29.0	Nil	Nil	Trace	Trace	38.5
Na	20.2	20.6	2.5	Trace	3.2	Nil	3.9
Tm	Nil	Nil	8.4	3.0	9.5	Trace	1.3

The FIB section of I100A imaged by TEM in Figure 6.18 and subsequent analysis reveals several key observations when related to previous samples as well as the surface viewed by SEM in Figure 6.16 prior to its extraction. Firstly, the platelet structures are found to be Na doped wurtzite ZnO crystallites, thus confirming the observations made by EDX measurements made in section 6.3.2. Secondly, the flat surface crystallites identified as Tm rich can now be linked to the surface crystal formations observed in Figure 6.9 and Figure 6.13 for I50A and I100A. This is known due to a good agreement between EDX and SAED analysis of these samples. Finally, the suspected phase difference between the left and right hand side of the area selected in Figure 6.16 does in fact correspond to one. This is found when observing the decrease in the abundance of crystallites from right to left of Figure 6.18 (b), compared to the sample surface in Figure 6.16. This is found to be an amorphous variant of the adjacent Tm rich crystallites, point EDX and accompanying elemental maps demonstrate a deficiency in Te, Na and Tm, suggesting a critical concentration of one or more of these elements is required before crystallisation can occur.

The variation in chemical composition from one region to another in the films discussed so far demonstrates some level of continuity. The surface embedded crystallites are found to be Tm-rich as well as having high concentrations of Si and

O with small amounts of Na, indicating that they are some form of silicate polymorph. Unfortunately the d-spacings from the SAED patterns do not match to a known crystal phase and shall be returned to in subsequent analysis with XRD for a more detailed discussion. This is in good agreement with the conclusions of the chapter 5, whereby α-cristobalite was inferred from the XRD spectrum. It was noted that the slight shift in the XRD spectrum may be attributed to an expansion of the unit cell due to an inclusion of some of the larger elements from the plasma phase. Although this does not confirm the assertion, it is compelling evidence worthy of consideration. It should also be noted that high resolution TEM imaging of a crystal plane could not be acquired due to beam damage of the sample.

With regard to the EDX mapping in Figure 6.21 as well that of previous maps, it is appropriate to note that the Zn Lα and Lβ lines very closely match the Na Kα and Kβ lines. An example of this proximity is given in Figure 6.22 for the EDX point analysis from Figure 6.18 (b) labelled '1' in red. Note that the abundance of Cu in this spectrum is attributed to the Cu in the sample holder and is an instrumental factor which cannot be removed.

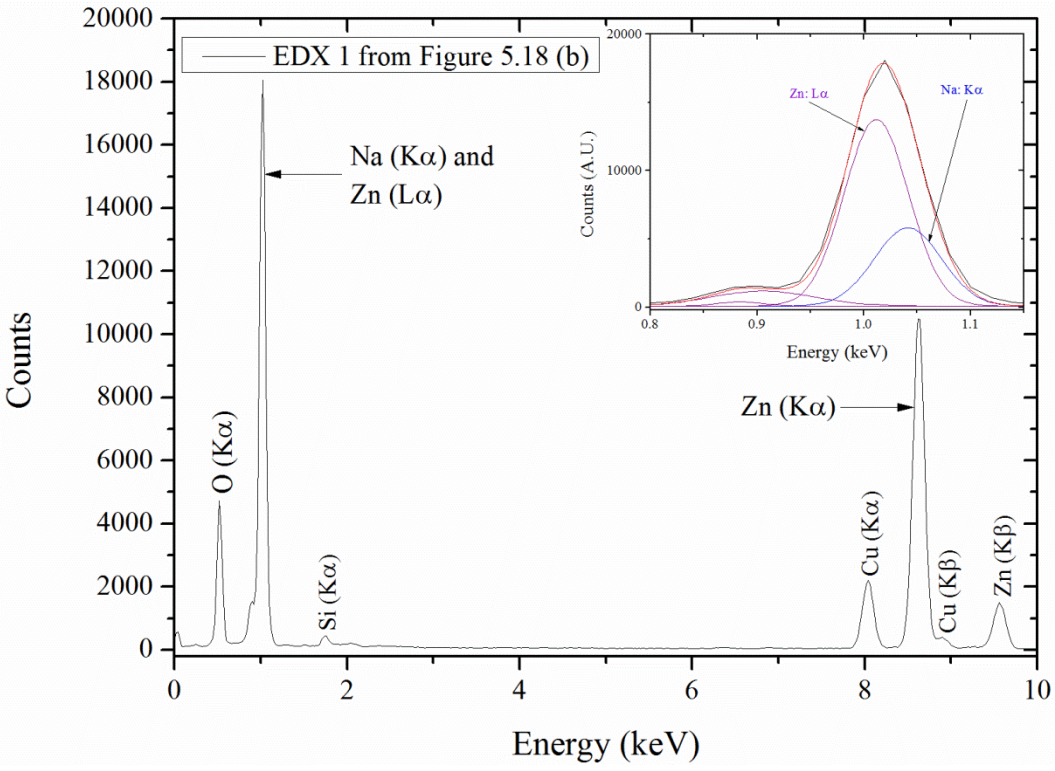

Figure 6.22. EDX spectrum of the region labeled '1' in Figure 6.18 (b) identified as a ZnO microplatelet. Inset shows an enhancement of the region 0.8 to 1.15 keV, composed of the Na: Kα and Zn: Lα lines.

From the fitting in the EDX spectrum in Figure 6.22, it is clear that the Zn Lα peak is dominant, however, the exact difference between the main Lα peak of Zn (1.012 keV) and the Kα peak of Na (1.041 keV) is only 0.03 keV. For accurate assessments of EDX data, such a proximity adds additional errors into the calculation of the chemical composition. This is emphasised further by considering the spacing between the data points of the EDX spectrum are only 0.02 keV and the spectral resolution of an EDX map is considerably lower for each pixel. For this reason, one must be cautious with regard to interpreting the Na concentration in a Zn-rich environment. The calculation of Zn concentration however should be largely unaffected from Na as the Zn Kα line is rather isolated as found in Figure 6.22.

The SAED pattern for one of these Zn rich crystallites in Figure 6.19 (a) shows a good correlation to that of a star quality standard reference pattern in the ICCD database for hexagonal wurtzite ZnO (ICCD ref: 04-015-4060), illustrated in Table 6.11. The agreement between the measured d-spacing to that of wurtzite ZnO can thus be related to the observed Zn rich crystallites in previous SEM and EDX analysis to deduce that they too are ZnO crystallites. The presence of small amounts of Na is to be expected because Na is a known dopant in ZnO crystallites as an acceptor dopant, thus, like ZnTe, making them a p-type semiconductor. This presents an interesting point for discussion, in that it suggests one could engineer such crystallites to become intrinsic semiconductors (undoped) or p-tpye depending on the composition of the starting target material. The apparent onset of ZnO growth occurring after that of ZnTe means the conditions for the growth of ZnTe crystallites could be tailored to dope according to a set regime. One could then switch to another target material *in situ*, inducing the growth of a different crystallite with a different doping regime. This is of great interest for the engineering of semiconductor crystallites as well as the breadth of functionality for this technique in comparison to conventional PLD.

ZnO crystallises as Rochelle salt (at rather high pressures), Zinc blende (when grown on a cubic substrate) or a hexagonal Wurtzite structure, whereby the Zn anion is surrounded by four O cations at the corners of a tetrahedron, and *vice versa*. The lack of high pressures and absence of a cubic crystal structure thus favours wurtzite formation. As identified in the SAED pattern in Figure 6.19 (a). What is important about this Wurtzite structure in the current context is that the unit

cell has two lattice parameters: a and c. The a-axis is the defined by the edge length of the hexagonal unit cell and the c-axis by its height, as depicted in the ball and stick diagram of a Wurtzite ZnO crystal of Figure 6.23.

A large anisotropic growth rate along the c-axis i.e. the [0001] direction can result in the formation of ZnO crystalline rods. Very often, this is the dominant growth mode (i.e. fastest) due to the high surface energy of the (0001) face. This is brought about due to the wurtzite structures lack of an inversion plane perpendicular to the c-axis, resulting in a polarity between these two possible surfaces [97]. Where a Zn polarity is designated (0001) or an O polarity as $(000\bar{1})$.

With reference to previous observations of the surface of the samples yet presented, a greater understanding can be reached with regard to the unusual crystal formations across the surface. In Figure 6.3 and Figure 6.4 for example, a range of different crystallographic structures are identified, all based upon a hexagonal crystal structure [99] with associated extremes in various dimension; apparent as elongated rods or platelets [224]. It is interesting therefore to draw a parallel to that of known ZnO crystal structures.

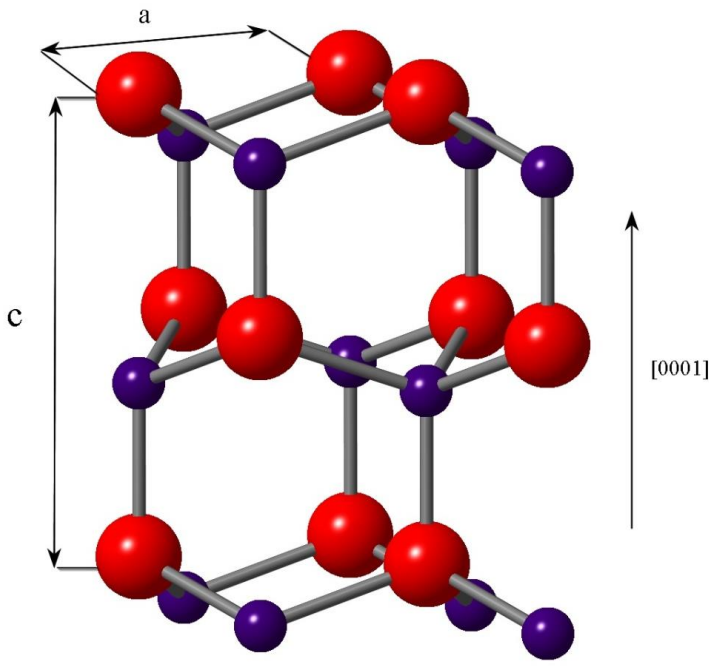

Figure 6.23. Ball and stick atomic structure of Wurtzite ZnO (O atoms are red balls, Zn atoms are purple balls) (constructed from ICCD ref: 04-015-4060)

ZnO crystalline rods come in the form of elongated hexagonal prisms, where the length and width are dictated by the experimental conditions [97]. Generally speaking, the lengths of the rods are limited by the availability of further Zn and/or O reactants, while the width can be somewhat more complex [224]. An interplay between both temperature and pressure has been identified as key parameters in dictating the width and relative alignment [225] of ZnO nanorods when produced by vapour deposition. It should be noted however that growth parameters identified in literature are very much specific to the fabrication process itself. In the present consideration, a comparatively more complex interaction is underway; whereby Zn is gradually being delivered to the substrate surface from the plasma phase alongside Te, Na and Tm, where each of these in conjunction with silicon, will be competing for the limited oxygen.

Another interesting trend in rod-growth mechanics identified by others is that a given Na concentration in a ZnO crystallite leads variations in the rate of growth along the [0001] direction [226]. The samples used in reference [226] were prepared by a sol-gel method where the (0002) peak of an XRD spectrum was found to be maximised at a doping concentration of 8 at%, which is indicative of extended growth and preferred orientation in the [0001] direction and a comparatively smaller growth in the lateral directions. Also of note, and what is particularly pertinent for the present discussion, is that when the Na concentration was doubled to 16 at% or halved to 4 at%, the (0002) XRD peak dropped significantly, relative to other peaks. Of course if this dataset were expanded, a more refined trend could be identified. These observations serve as reasonable evidence for an explanation of the disparity in crystalline structures which match that of ZnOs known formations. An example of this can be found in the micro- and nano-platelets depicted in Figure 6.4 (a) and (b). The high Na concentration described by EDX 1 and EDX 2 of Table 6.14, corresponding to similar structures supports this proposal. Furthermore, the rod-like propagations marked in Figure 6.6 under EDX 3 possess a Na concentration of approximately 10 at%, which directs a more rapid growth rate in the [0001] direction and thus are observed as more elongated structures. Furthermore, the topographical variation in the ZnO-like structures implies that it could in fact be the Na which is unevenly distributed across the surface of the sample, thus resulting in this large variety of ZnO crystallites.

A reasonable explanation for the significant Na compositional differences is that Na is highly soluble in SiO_2 [227] and a diffusion coefficient of approximately1.0 x 10^{-7} cm^2/sec. Na depravation on the surface could thus be attributed to its diffusion and integration into the SiO_2 matrix in the subsurface. The diffusion of Na into SiO_2 is likely to of occurred from the very early stages of fabrication, where it is identified in all regions of the modified layer through EDX measurements already discussed.

As was identified in section 5.3.3.4, Zn oxides in the plasma phase will preferentially reduce in the presence of Si, however, in the latter stages of fabrication for the present samples, much of the surface Si has already oxidised, this would therefore mean that the oxidation of Zn ions is thermodynamically favourable and ZnO crystallites can form. This point shall be returned to in section 6.5.

Such a theory for the formation of ZnO crystallites in the variety of shapes observed in Figure 6.3, Figure 6.4 and Figure 6.5 can again be used as a means to suggest the possibility of engineering such materials. In addition to this, such a suggestion serves as a key point in the proposition of this technique being worthy of considerable interest. The fundamental point being that it gives the opportunity to create favourable conditions for the growth of complex crystal structures based upon the given chemical considerations of the system itself. This includes the reduction of a starting target material; many oxides are comparably cheaper than their pure metallic counterparts due to reduced processing stages, thus adding considerable financial cost to a given fabrication process. Furthermore, when the conditions of the experiment are changed, i.e. the effective substrate or the interacting material, the formation of complex semiconductor oxides such as ZnO become favourable and are able to grow. A refinement of the control parameters instilled on the current PLD system, such as the *in situ* plasma analysis system described in section 3.1.1 could allow considerably more detailed analysis of these surface modified materials in relation to the nature of the plasma phase.

As an alternate to the proposed theory of Na induced structural changes in ZnO, there are other possibilities which must be considered on their own merit before coming to a conclusion as to the likely formation mechanism. The growth of platelets, as opposed to elongated structures along the c-axis (rods), relies upon a change in the rate of growth of a given crystal face. A change in preferential growth

direction for a ZnO crystallite has been attributed to the suppression of the [0001] growth direction by adsorption of OH^- ions on the (0001) face [104]. This leads to an increased growth in the $<2\bar{1}\bar{1}0>$ direction (i.e. perpendicular to the c-axis) and thus the formation of platelets as opposed to rods. It is reasonable to assume the existence of hydrogen in the chamber itself as a contaminant. Such as from the silicon substrate or in the tellurite glass target [228] as a result of its preparation outside of a glove box.

The proposition of H ions resulting in changes to the growth mechanics of the ZnO crystallites is well established and can be observed in other forms. These include crystal structures such as those depicted on the surface of sample I100A in Figure 6.5 for (a) capped-pyramid and (b) star-like tips of microrods. The formation mechanisms responsible for the growth of these structures has also been linked to the presence of OH^- during the fabrication stage [229]. In the present system, the occurrence of a certain type of 'tipped' micro-rod tends to be isolated to a specific bundle, i.e. a large concentration of star-like crystals will be found together, but not amongst a large concentration of the complete hexagonal prisms such as those in Figure 6.3, etc.

The nature of this division in crystalline formations is rather interesting for deducing their origin. As is known from literature, and explained earlier, the aforementioned ZnO crystal structures form in response to specific experimental conditions, for example an increase in H content, a change in the temperature or pressure of the reaction chamber, Na concentration etc. This indicates that across the surface, where these supersaturated nucleation sites have occurred, variations in the local environment have triggered changes in their growth mechanics.

It therefore appears likely that the influencing factors on the growth mechanics of ZnO crystallites could be a mixture of these two propositions. Firstly, the Na content in EDX 1 and 2 of Table 6.14 strongly suggests their formation is due to the influence of this dopant. The distinctive crystalline formations in Figure 6.5 (a) and (b) in combination with expected OH^- content in the starting target [228] linked to observations in literature [229] suggests it too has a fundamental role for modifications to the growth mechanics.

The effect of laser energy on the fabrication process overall when studied through these two samples thus far appears to simply relate to the abundance of

ablated material. This is reflected in the surface and subsurface features of I100A, fabricated at 100 μJ, appearing much more extensive yet consistent with those observed in I50A. This is most distinctive in the TEM cross sections when prepared by the standard methodology in Figure 6.9 and Figure 6.13 for I50A and I100A respectively as well as corresponding analysis. The Tm-rich crystallites are considerably more continuous across the surface for I100A, where they occupy large areas in the top down SE-SEM analysis in Figure 6.3 (a). As was identified for the samples presented in Figure 6.1, increases in laser energy appear to increase the amount of depositing material. The only significant difference in the samples is the formation of Te crystallites in the subsurface, formed in the early stages of fabrication as opposed to ZnTe. The partial separation of Tm-rich surface crystallites visible in Figure 6.9 of I50A, indicates they form individually and grow out of the glassy SiO_2 matrix. Extrapolating this growth mechanism to the observations of I100A leads one to conclude they eventually consume the surrounding amorphous SiO_2 and continue to develop into a continuous, polycrystalline surface layer.

From the TEM cross sections, what is also of note is that the observed interface between the oxide layer and the silicon substrate is energy independent for I50A and I100A. One may expect a more diffuse interface as expected from ordinary diffusion profiles [215], however the EDX mapping of both samples suggests a well-defined interface with the Si substrate. This shall be described in greater detail in section 6.3.4.

6.3.4. Crystallite characterization via X-ray diffraction

Each sample was analysed by XRD to better define the various crystal phases alluded to in previous electron microscopy analysis. ZnO, ZnTe and Te crystallites have already been identified as well as an as yet unidentified Tm-rich silicate crystal phase. Corresponding X-ray diffraction patterns for samples C570, I50A and I100A are provided in Figure 6.24, Figure 6.25, and Figure 6.26 respectively.

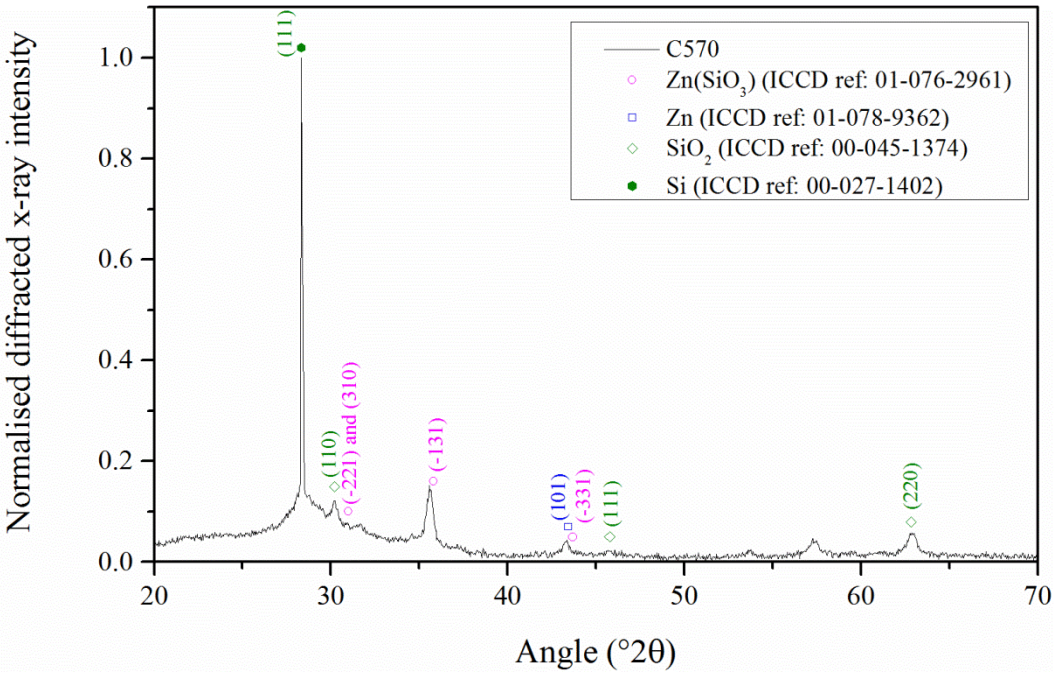

Figure 6.24. XRD spectrum of C570, including possible assigned phases for Si (⬢) (ICCD reference: 00-027-1402), hexagonal Zn (□) (ICCD reference: 01-078-9362), Stishovite SiO_2 (◇) and monoclinic Zn (SiO_3) (ICCD ref: 01-076-2961)

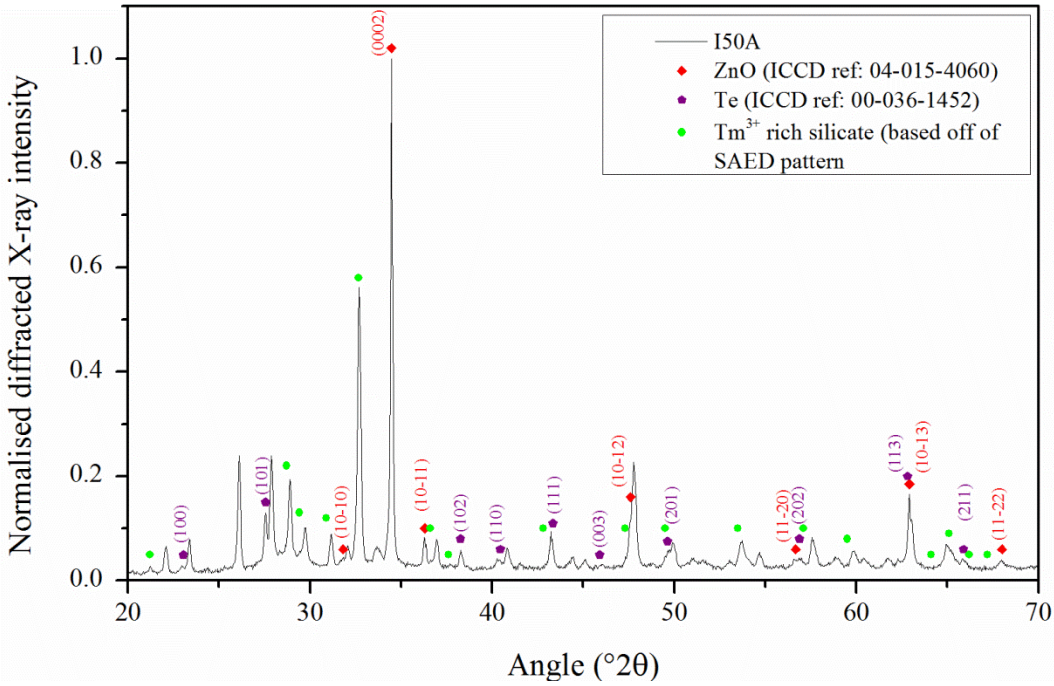

Figure 6.25. XRD spectrum of I50A, including the calculated d-spacings from measurements of the SAED pattern in Figure 6.10 (b) (●), hexagonal Zincite (ZnO) (◆) (ICCD reference: 01-071-6424) and hexagonal Tellurium (Te) (⬟) (ICCD reference: 00-036-1452)

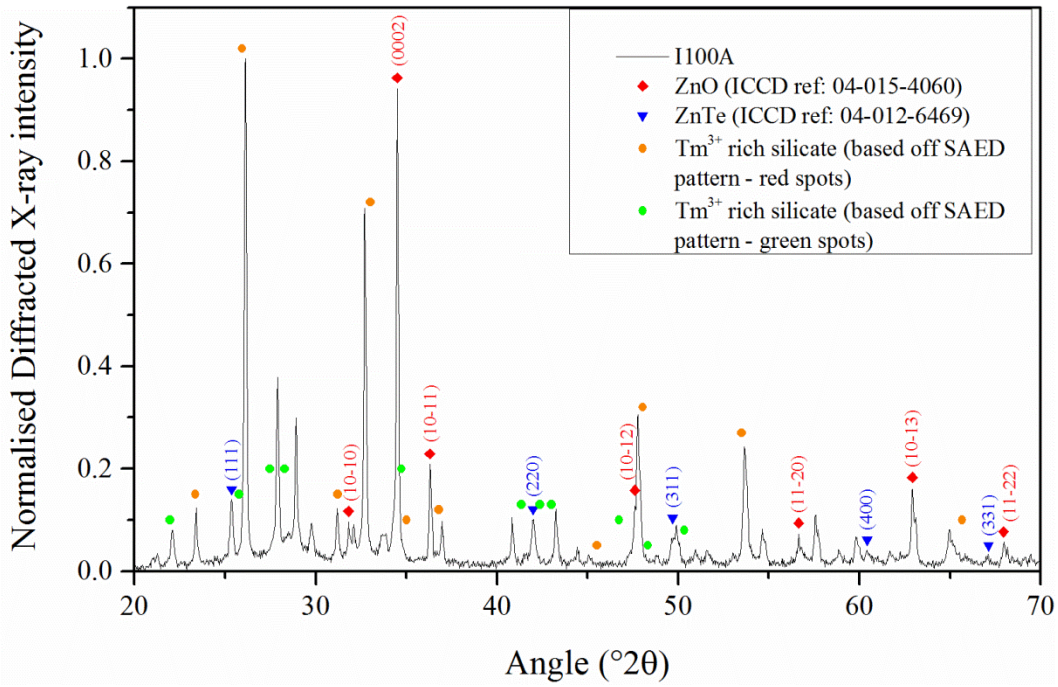

Figure 6.26. XRD spectrum of sample I100A, including the calculated d-spacings from measurements of the SAED pattern in Figure 6.20s red spots (●) and green spots (●), hexagonal Zincite (ZnO) (◆) (ICCD reference: 01-071-6424) and cubic Zinc Telluride (ZnTe) (▼) (ICCD reference: 04-012-6469)

As can be seen from the aforementioned figures, there is a certain degree of variation between each of the samples. Some of the peaks in each spectrum can be readily matched to that of the standard reference patterns. This includes Te (ICCD ref: 00-036-1452), ZnTe (ICCD ref: 04-012-6469) and ZnO (ICCD ref: 04-015-4060); in addition to these, n set of peaks which correspond to that of the d-spacings for the Tm rich crystallites identified for both I50A and I100A in Table 6.9 and Table 6.13, respectively. The angles (in º2θ) from these d-spacings were calculated and thus compared to the peak positions of some of the unassigned peaks still remaining for I50A in Table 6.15 and I100A in Table 6.16. Unfortunately, a matching phase for the XRD peaks allocated to the measured d-spacings from the SAED patterns of both I50A and I100A could not be found.

A clear match to the diffraction pattern of C570 could not be attained, however certain phases which appear to mach have been included in the figure. Most notably, this includes monoclinic Zn metal, Stishovite SiO_2 and hexagonal $Zn(SiO_2)$. These phases are however tentatively ascripted to this spectrum.

Table 6.15. Table comparing the calculated angles in º2θ from the SAED pattern data presented in Table 6.9 (column 1) for I50A to that of I50As XRD peaks in Figure 6.25 which best fit to them

calculated from corresponding SAED pattern		**º2θ from corresponding XRD pattern**	
º2θ	**d-spacing, Å**	**º2θ**	**d-spacing, Å**
21.2	4.19	21.2	4.19
28.7	3.11	28.9	3.09
29.4	3.04	29.7	3.01
30.9	2.89	31.2	2.86
32.7	2.74	32.7	2.74
36.6	2.45	36.9	2.43
37.6	2.39	37.7	2.38
42.8	2.11	-	-
47.3	1.92	47.3	1.92
49.5	1.84	49.9	1.83
53.5	1.71	53.7	1.71
57.1	1.61	57.6	1.60
59.5	1.55	59.8	1.55
64.1	1.45	-	-
65.1	1.43	65.0	1.43
66.2	1.41	-	-
67.2	1.39	-	-

Table 6.16. Table comparing the calculated angles in º2θ from the SAED pattern data presented in Table 6.13 of I100A for the red and green spots depicted in Figure 6.20 to that of I100As XRD peaks in Figure 6.26 which best fit to them

SAED pattern	**Calculated from corresponding SAED pattern**		**º2θ from corresponding XRD pattern**	
	º2θ	**d-spacing, Å**	**º2θ**	**d-spacing, Å**
Red spots	23.39	3.80	23.38	3.80
	25.96	3.43	26.11	3.41
	31.25	2.86	31.18	2.87
	33.03	2.71	32.73	2.73
	35.02	2.56	-	-
	36.81	2.44	36.98	2.43
	45.55	1.99	45.08	2.01
	48.10	1.89	47.80	1.90
	53.55	1.71	53.66	1.71
	65.70	1.42	64.96	1.43
Green spots	21.98	4.04	22.07	4.02
	25.80	3.45	-	-
	27.51	3.24	-	-
	28.31	3.15	27.91	3.19
	34.74	2.58	34.57	2.59
	41.38	2.18	40.84	2.21
	42.40	2.13	-	-
	43.04	2.10	43.25	2.09
	46.79	1.94	47.31	1.92
	48.38	1.88	-	-
	50.37	1.81	49.89	1.83

The peak positions recorded from XRD in Table 6.15 for sample I50A allocated compare very well to the measured d-spacings of Table 6.9 (converted to

º2θ for convenience) acquired from a SAED of a Tm-rich crystallite. Similarly, the deconvoluted SAED spots of Table 6.16 for I100A converted to º2θ compare well to the allocated XRD peaks between the calculated d-spacings in Table 6.9 (column 1).

This comparison between SAED data and XRD data is particularly useful in relation to understanding the d-spacings of I100A, where two distinctive sets of diffraction spots were identified in Figure 6.20. The mismatch of the d-spacings between these two sets, labelled red spots and green spots, suggest they stem from different crystallites. The repeating grid pattern of the red spots is indicative of a single crystal while the somewhat random array of green spots suggests they are from a collection of smaller crystallites, such as in Figure 6.19 (c). As stated earlier, a standard reference pattern to match either of these sets of peaks could not be identified. This includes the diffraction pattern from I50A in Figure 6.10 (b). The mismatch between the observed XRD spectrum and that of known silicate polymorphs, in combination with the significant doping indicated by EDX measurements suggests that the crystalline unit cell may have been significantly modified. This reduces the likelihood of identifying a standard reference pattern to identify this particular phase.

The identification of ZnO by comparison is very well established. The peak intensities are significantly shifted due to the average dimension and orientation of the crystallites. This has been discussed previously in relation to the results from literature [226], whereby a preferential growth in the [0001] direction results in an overall increase in the intensity of the (0002) peak. The overall height of the diffraction peak can therefore be understood as a representation of preferential orientation of the c-axis, directed away from the substrate itself. An example of this occurrence is depicted in Figure 6.3 (a). The orientation of these microrods may be related to the action of gravity, recalling the orientation of the substrate being directed down toward the plasma plume.

The standard data available on the ICCD database is related to powder diffractions patterns; whereby there is no preferential orientation, thus the relative peak intensities for a ZnO XRD spectrum can be related to this standard, allowing the relative orientation in this direction to be inferred. For this reason, the ratio of the peak intensities of (0002) to that of the $(10\bar{1}0)$ and $(10\bar{1}1)$ peaks is calculated and compared to those from the standard reference pattern (ICCD ref: 04-015-4060)

for ZnO in Table 6.17. It should be noted that the peak intensity measured for the (0002) in both I50A and I100A is that of the deconvoluted peak intensity

Table 6.17. Table comparing the ratio of the peak intensities of (0002) to $(10\bar{1}0)$ and $(10\bar{1}1)$ for both I50A and I100A acquired from their respective XRD spectrums. These values are also compared to the ratio from a standard ZnO reference pattern (ICCD ref: 04-015-4060)

Sample ID	**(0002): $(10\bar{1}0)$**	**(0002): $(10\bar{1}1)$**
I50A	25.0	12.5
I100A	9.79	4.48
Reference sample	0.71	0.39

Table 6.17 serves as significant evidence for the preferential growth rate of the ZnO crystallites along the c-axis, but also for their preferred orientation. The distinctive increase in these ratios for I50A relative to I100A can be understood in relation to the significant number of platelet formations on the surface of I100A. As depicted in Figure 6.4 (a), many of these platelets are orientated perpendicular to the microrods, i.e. the <0001> facet is orientated perpendicular to the surface. This would therefore increase the proportion of scattering from other crystal planes, such as the $(10\bar{1}0)$ and $(10\bar{1}1)$.

It is interesting to note the observation of hexagonal Te with no trace of diffraction from ZnTe in Figure 6.25 for I50A and *vice-versa* for I100A in Figure 6.26. As was observed for the two 30 minute samples in chapter 5, there appears to be a degree of variability in the likelihood of formation of ZnTe or Te, perhaps due to inhomogeneities in the target glass mixture or some other, as yet, unidentified cause.

6.3.5. Raman characterisation of surface modified materials

Analysis of samples in chapter 5 demonstrated that characterisation of the crystal structures through XRD as well as Raman spectroscopy is particularly useful. For this reason, both I50A and I100A were characterized using Raman spectroscopy, where I50A is presented in Figure 6.27 and I100A is presented in Figure 6.28. A deconvoluted spectrum of the region of interest for both samples in provided in the inset of those figures.

The Raman data for I50A demonstrates fluorescence as well as very weak traces of the phonon modes for ZnTe. This suggests that the concentration of ZnTe in I50A is below the threshold for detection in XRD [230]. The ZnTe photoluminescence interference in the Raman spectrum of I100A by comparison is clear.

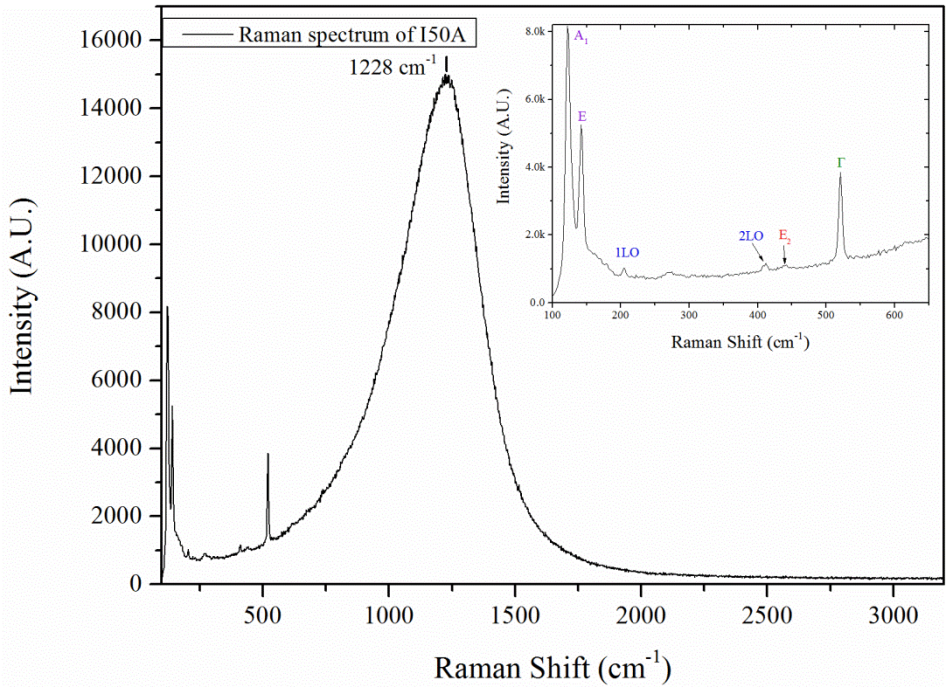

Figure 6.27. Raman spectroscopy of sample I50A with the peak position of the fluorescence marked at 1228 cm^{-1}. The inset shows the A_1 and E modes of hexagonal Te in purple, the 1LO and 2LO modes of ZnTe in blue, the E_2 mode of ZnO in red and the zero-centre one-phonon line (Γ) of Si in green.

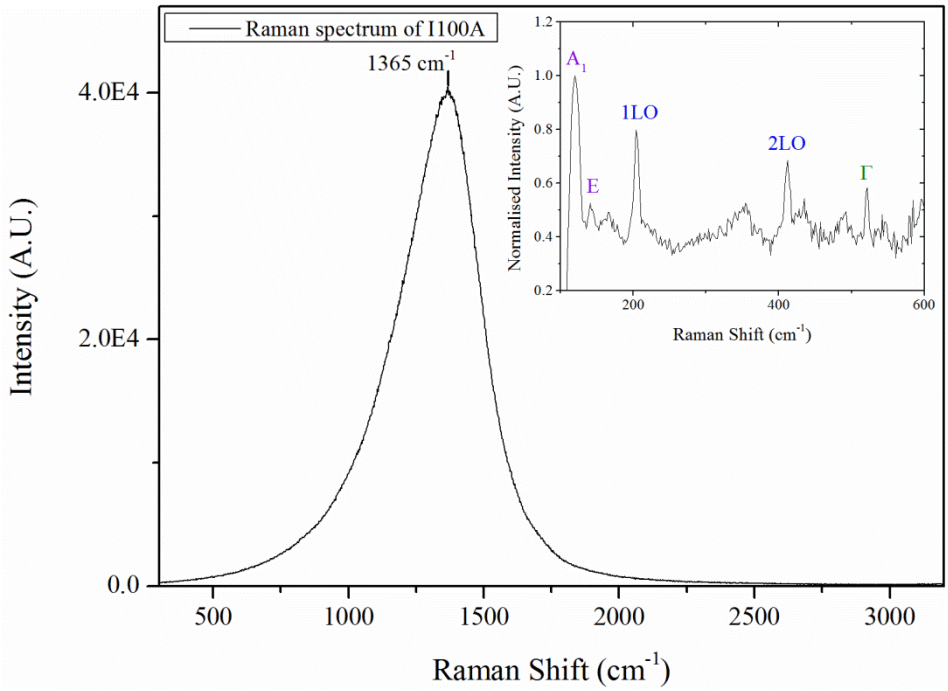

Figure 6.28. Raman spectroscopy of sample I100A with the peak position of the fluorescence marked at 1365 cm^{-1}. The inset shows the A_1 mode of hexagonal Te in purple, the 1LO and 2LO modes of ZnTe in blue and the zero-centre one-phonon line (Γ) of Si in green.

As with the identification of ZnTe phonon modes in I50A by Raman spectroscopy, Te phonon modes have also be identified in I100A. This again is due to the increased sensitivity of Raman spectroscopy to small concentrations of a particular phase in comparison to XRD. As with Chapter 5, Raman spectroscopy reaffirms the allocation of crystal phases to the XRD spectrum. In addition to the known ZnTe, Te and Si phonon modes, the Raman spectrum of I50A identifies a number of other minor peaks. One of which corresponds to ZnO. The additional peaks in I100A cannot necessarily be ascribed to a given phase due to the signal to noise ratio, thus only the sharp, distinctive peaks are marked. Unfortunately, the unidentified peaks of I50A could not be identified in relation to a known material.

The XRD spectrum of sample C570, the sample deposited 30 μJ, the lowest laser energy, is entirely dissimilar to the samples deposited with higher laser energy. This is particularly interesting with regard to considerations on the growth mechanisms of the sample. If one relates the lower laser energy simply to the abundance of ablated material, it would be logical to therefore expect a material akin to those presented in chapter 5 but perhaps somewhat more developed. Instead, there is no trace of any crystallites which have previously been observed. The cross

sectional SE-SEM analysis of C570 in Figure 6.2 (a) and (b) appears markedly different in the subsurface structure. The visible porosity and distinct interface with the silicon substrate suggests that this material, although fabricated at the same high temperature, does not have a modified surface, but is instead deposited. This represents an important conclusion, in that a laser fluence threshold must be overcome in order to trigger surface modification.

6.4. Raman and XRD characterisation of deposited materials

In order to test this, two further samples were fabricated at 30 µJ whereby the peak fabrication temperature was lowered to 300 ºC for sample C300 and 400 ºC for sample C400. Cross sectional SE-SEM images and XRD spectrums for C300 are found in Figure 6.29 while those corresponding to C400 are in Figure 6.30. In addition to this, Raman spectroscopy for each sample is provided in Figure 6.31.

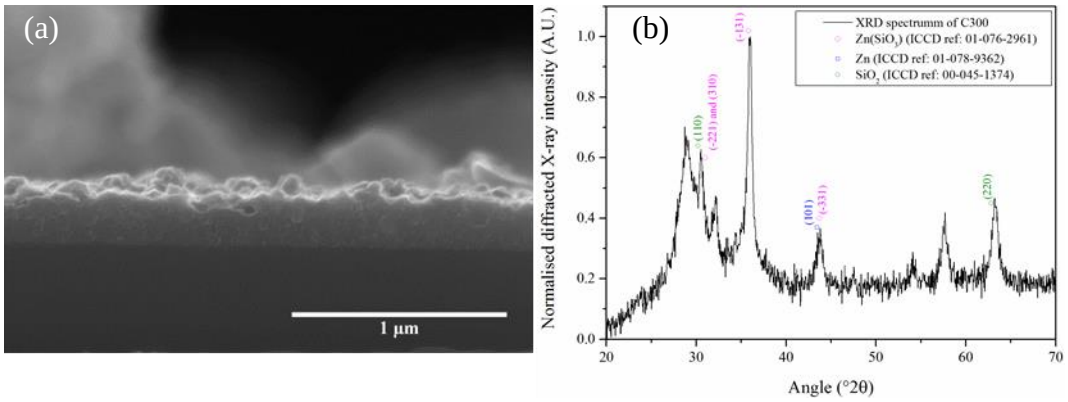

Figure 6.29. (a) Cross sectional SE-SEM image of C300, (b) XRD spectrum of C300

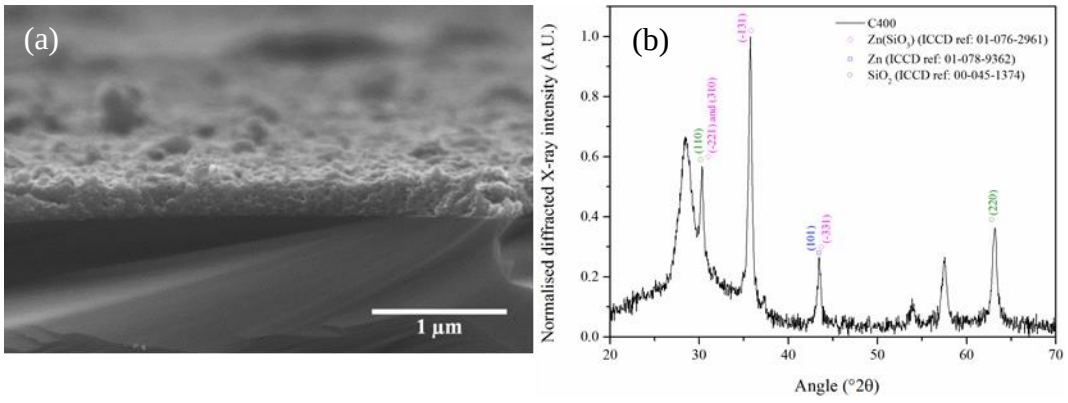

Figure 6.30. (a) Cross sectional SE-SEM image of C400, (b) XRD spectrum of C400

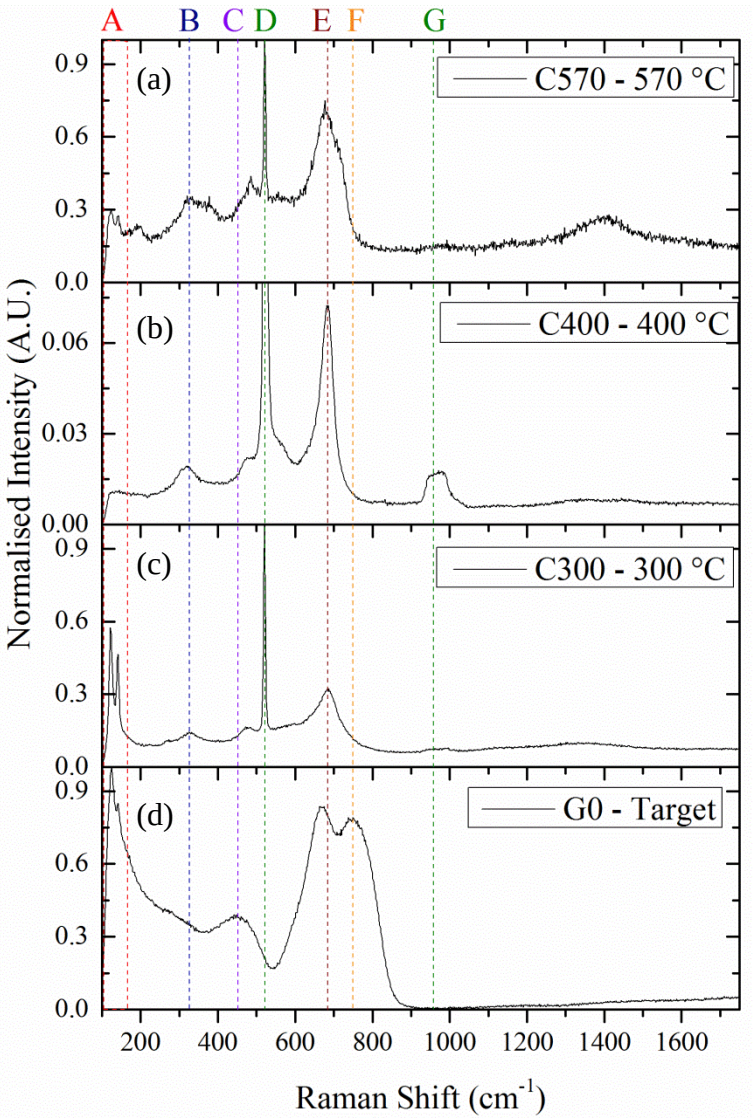

Figure 6.31. Raman spectrum of (a) C570, (b) C300, (c) C400, (d) G0. A to G label the peak positions of Raman vibrational modes described in the text. Note the change in scale (c) C400, this is due to the dominance of the Γ line of silicon which extends up to 1.0.

The SE-SEM images in Figure 6.29 and Figure 6.30 are suggestive of conventional deposition, where a very well defined interface, likened to the dry-run sample presented in chapter 5 is visible. This is of course a qualitative interpretation; however the Raman spectroscopy presented in Figure 6.31 is much more indicative as to its nature.

Firstly, note the distinct difference in the overall spectrum for all samples in Figure 6.31 in comparison to those of I50A and I100A discussed earlier. The primary peak differences are identified through the markers A to G on this figure. The main phonon modes for TeO_2 are distinguishable in the Raman spectrum of G0,

the starting glass target. The phonon modes for Te chains described in section 5.3.2.2 are also visible in addition to those related to the underlying Si substrate. The origin of each of the markers in Figure 6.31 are as follows [231]:

A. (122.5 and 142.0 cm^{-1}) A_1 and E modes of hexagonal Te chains
B. (327.5 cm^{-1}) ZnO doped with another oxide [232]
C. (453.0 cm^{-1}) Stretching and bending vibration of Te-O-Te linkages in TeO_4, $TeO_{3+\delta}$ polyhedral and TeO_3
D. (521.0 cm^{-1}) Zero-centre one-phonon line (Γ) of the crystalline silicon substrate
E. (684.0 cm^{-1}) Antisymmetric vibrations of Te-O-Te in $TeO_{3+\delta}$, TeO_3 and TeO_4 networks
F. (747.0 cm^{-1}) Stretching vibrations between tellurium and non-bridging oxygen atoms
G. (930-1000 cm^{-1}) 2To(X) and 2LO(L) phonon modes from the silicon substrate

The observation of these phonon modes is particularly indicative as to the abundance of TeO_x networks in the deposited material. This means that very little of the depositing material has interacted with the silicon substrate, i.e. oxidising it and thus facilitating the surface modification as with other samples. Fabricating materials at lower temperatures (300 and 400 °C for 1-5 and C300 respectively) demonstrates a clear trend to the formation of a deposited layer. This is most distinctive in the corresponding cross sectional SE-SEM images where an interface akin to that seen for the silicon thin films presented in Figure 4.6. The interface for sample C570, visible in Figure 6.2 however appears somewhat blurred by comparison. This may suggest that C570 was fabricated at close to a surface modification threshold in temperature and/or laser fluence. Samples described in Table 6.2 serve as a demonstration of the effects of temperature, whereby more than sufficient laser energy was used for sample G0-1, yet no surface modification is apparent. Operating below the laser fluence and temperature thresholds may be the reason why this fabrication mechanism has not been identified previously.

The observations made with regard to C570, C300 and C400 in relation to samples fabricated at higher laser energy presents the possibility for a competitive hypothesis as to how the surface modification is driven. The well-defined depth with which material appears at 1 hour as well as 4 hours, in combination with the observed deposition at lower laser energy suggests implantation may be occurring.

The process of implantation is best understood through the well-known fabrication method ion implantation. This technique utilizes an accelerated beam of ions to create thin layers of doped material on the surface of a given substrate. This concept was studied by Volkov *et al* [194], whereby Ge ions generated from femtosecond pulsed laser ablation were implanted into a Si substrate. This work demonstrated a peak concentration at 50 nm with a long tail extending to 400 nm. This point has been addressed previously but shall be returned to in light of the current observations.

An interesting way of questioning the possibility of implantation is through the observation of the velocity distribution of ions, accelerated via femtosecond pulsed laser ablation, with respect to laser energy. As noted in section 3.1.1, this cannot be done through the current instrumentation and thus one relies on the observations by others. The velocity distribution function itself follows a shifted Maxwell-Boltzmann distribution function, *f(v)* [233]:

$$\boldsymbol{f(v) = cv^2 exp\left(-\frac{m(v-u)^2}{2kT}\right)} \quad \textbf{(6.1)}$$

Where *v* is the total velocity, *u* the centre of mass or drift velocity (associated with the 'shifted' aspect of this relationship), *k* is Boltzmann's constant, *m* the particle mass and *T* is the temperature. The conformity of particles to this relationship, in combination with their identical kinetic energy, regardless of mass, was one of the first indications of the ions emanate directly from the surface. Additionally, this equation can be related to a basic understanding of the relative velocities of ions from one laser fluence to another. Amoruso *et al* [34] identified an important trend in this regard, whereby fast-ions, i.e. those most likely to implant, were found to increase in velocity with a corresponding increase in laser fluence. For a laser fluence of 0.8 J cm^{-2} for a 100 fs, 780 nm laser, the greatest velocity to be expected would be 160 km s^{-1} for silicon ions while the average of the fast ion component would travel at 29 km s^{-1}. It is expected that the velocity of Te and Zn ions would be considerably less due to the larger atomic number [34], however it is reasonable to assume that some degree of implantation would occur for the laser parameters employed for these experiments. What is not explained however is the formation of crystallites, which would require diffusion over distances which are not possible for such ions (Zn and Te) [214–216,234].

This therefore returns to the prospect of the diffusion of oxides being the root cause of the surface modification. Perhaps the most important aspect of this theory is the diffusion of oxygen into the underlying silicon lattice structure as it would therefore facilitate the diffusion of additional dopants into the structure, resulting in the crystal formations now under analysis. This point was introduced in chapter 5 and a good agreement was found between the proposed depth of the oxide layer, based upon the observed depth of subsurface crystallites. This same operation can now be carried out on observations made thus far for samples C570, I50A and I100A, but with a greater refinement of the depth profile for the oxide layer. The proposed diffusion depths, calculated from equation 4.5 in section 5.3.3.4, and the measured oxide layer thickness are compared in Table 6.18. Note the oxide thicknesses are measured from the top of the Tm-rich crystallites to the crystalline Si substrate interface. The results of the calculated depth for a sample fabricated at 30 minutes as well as D60-1 at 1 hour are also included.

Table 6.18. Table comparing the calculated depth of diffusion of oxygen into a crystalline silicon lattice at 30 minutes, 60 minutes and 240 minutes to that of the observed oxide depth for I50A and I100A. The thin film thickness of C570, C300 and C400 are also noted. E denotes the fs- laser energy in µJ, while T notes the temperature in °C. The depth of ZnTe crystallites in sample D60-1 (fabricated for 1 hour) is also included.

Sample	**E, µJ**	**T, °C**	**Fabrication time, s**	**Calculated depth, µm**	**Observed depth, µm**
D30-1	-	570	1800	0.18	-
D60-1	50	570	3600	0.36	0.3 ± 0.1†
C300	50	300	14400	1.43	0.3 ± 0.2
C400	50	400	14400	1.43	0.3 ± 0.2
C570	50	570	14400	1.43	0.6 ± 0.0
I50A	50	570	14400	1.43	1.2 ± 0.3
I100A	100	570	14400	1.43	1.4 ± 0.2

†Depth noted is that of the average penetration depth of ZnTe and is thus used as an approximation for the extent of the oxide depth.

The calculated depths in Table 6.18 for samples I50A and I100A are in good agreement with the observed depths and acts as good supporting evidence for diffusion being the primary pathway for this fabrication mechanism. As noted in previous SEM and TEM analysis, there is a degree of surface texturing, particularly on I50A, as well as undulations in the interface depth, making a precise measurement of the oxide depth difficult.

The thickness of the deposited samples is also of interest in the current discussion, whereby C570 as if a deposited material with a blurred interface, however the measured thickness implies some degree of diffusion. Again, this suggests the experimental parameters for C570 are not sufficient to encourage the growth of the crystallites of interest in this thesis.

6.5. Theoretical basis for the formation of ZnO crystallites

As was stated earlier, the formation of ZnO crystallites appears to occur between 1 to 4 hours after the start of a fabrication within the experimental parameters defined in this work. The question of how this may be occurring is one which can be reasoned through contemplation of the thermodynamics of the fabrication process. Firstly, it was established in section 5.3.3.4 that both Te and Zn would reduce in the presence of Si which enabled the formation of the oxide layer visible in the cross sectional TEM analysis of this chapter. Furthermore, the reduction process itself was deduced to aid in the formation of ZnTe and Te nanocrystallites, observed in samples discussed here and between 30 minutes and 1 hour. This raises two particularly important questions:

1. How has ZnO formed?
2. Where is the Te, which should be in abundance based upon the starting composition?

The answer to both of these questions is believed to be linked. Firstly, consider the thermochemical calculations presented in Figure 6.32 concerned with the formation of ZnO through various possible interactions. These reactions are considered beyond 1 hour, whereby the substrate is considered to be effectively silicate (or some variant which is unimportant in this context), i.e. where the Si is now completely oxidized. This therefore means that the interactions can now be considered to be between the reactants from the plasma phase and Zn metal. What

is important to note in this environment is that the Zn metal would be molten at 570 ºC (melting point 419 ºC) and is considered to be adhering to the surface.

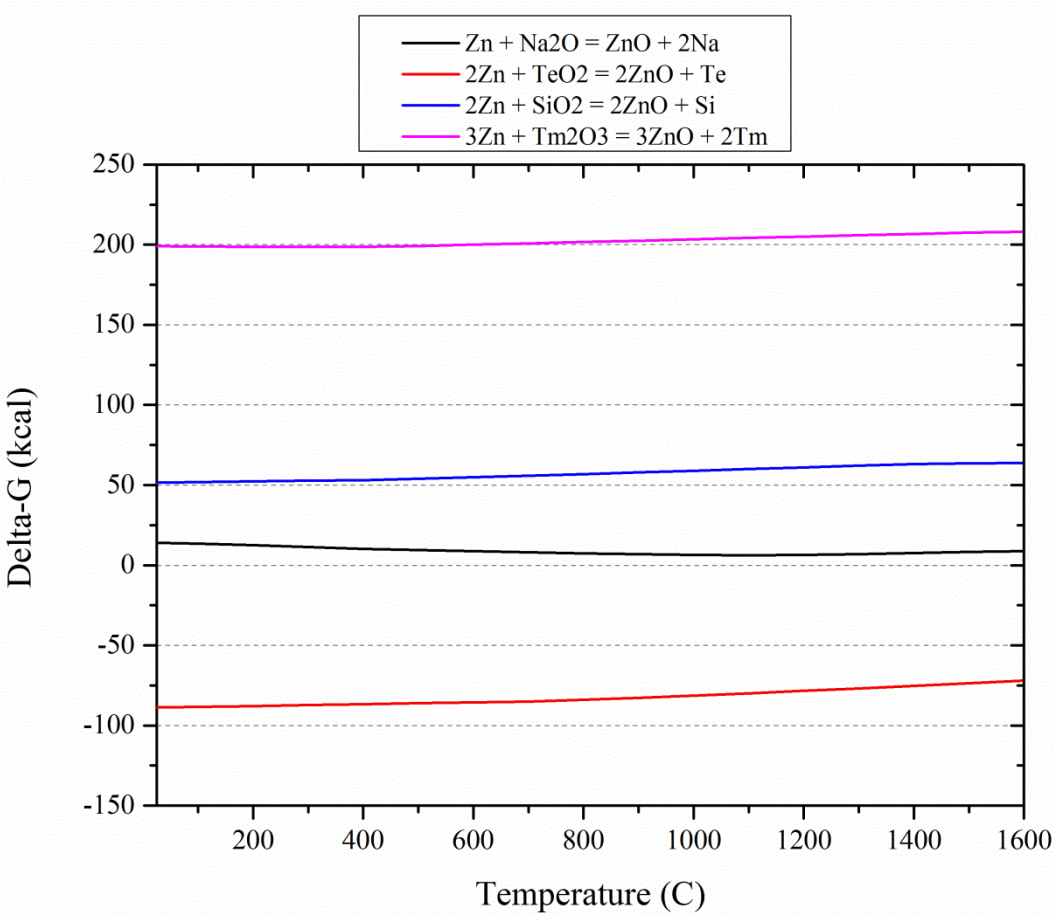

Figure 6.32. Graph of thermochemical calculations for the formation of ZnO from Zn and various other possible reactants in order to oxidise it.

From this figure, it is clear that the only possible means in which Zn can oxidise (other than reacting with gaseous O_2 or an unidentified oxide) is through the reduction of TeO_2, resulting in Te metal. One can therefore propose that following the formation of a sufficiently deep and complete oxide layer in the silicon substrate, Zn metal on the surface will oxidise through the reduction of TeO_2 and thus grow. This will of course result in an abundance of Te metal on the surface. As with Zn, Te will also be in a liquid state at 570 ºC (melting point 449 ºC). Metallic Te, should it be present on the surface of the substrate, would not oxidise in the same way as Zn did, as the conditions required for this would not be particularly favourable. This is illustrated through the various possible ways in which residual Te on the surface may oxidise in Figure 6.33.

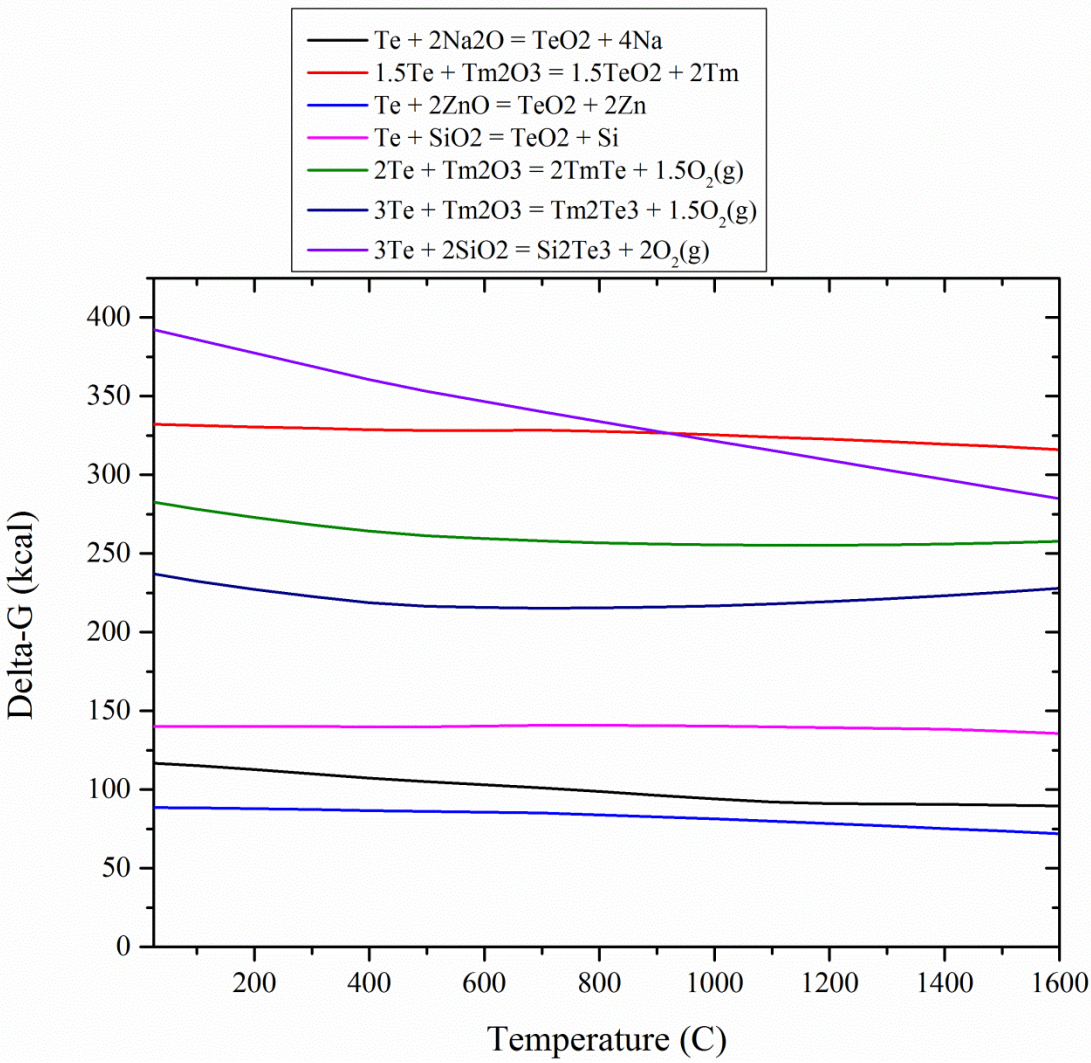

Figure 6.33. Graph of ΔG vs. temperature for various possible reactions to oxidise Te metal

The first question can thus be answered by the following: Molten Zn metal on the silica surface after 1 hour or more, produced through the oxidation of Si, can act as a catalyst for the formation of ZnO via the reduction of TeO_2. This process is therefore driven by incoming TeO_2 as well as further ZnO from the plasma phase.

The second question of why there is only very minute concentrations of Te detected in the surface modified materials can also be answered. Firstly, Te is not soluble in SiO_2 and is highly immobile due to its metallic character [215], meaning it cannot be expected to diffuse into the substrate. A molten liquid, suspended from a surface, can be expected to be somewhat unstable due to the constant impacts from the plasma phase, this is therefore expected to result in 'splashing'. Due to the

substrates orientation (i.e. upside down), any splashing would therefore project molten Te away from the substrate, thus resulting in the observed Te deficiency.

The degree of splashing can be inferred by considering the viscosity of Te metal. Sklyarchuk *et al* [235]studied the viscosity of molten Te over a wide range of temperatures including when doped with small quantities of transition metals. It was found that pure Te melts possess a viscosity of approximately 2.1 Pa s^{-1} at 570 °C. The viscosity of Zn by comparison is found to be approximately 2.5 Pa s^{-1} [236]. These two viscosity are relatively similar, however the slight elevation of Zn metals in combination with its tendency to oxidise would thus favour its stability.

One may postulate that further extending the fabrication process may result in the formation of a stable TeO_2 phase, however this is not of interest in the present work.

6.6. Conclusion

The results of the present chapter have identified significant developments in the surface modified material for samples fabricated over 4 hours. Extensive ZnO crystallisation has occured, where the growth mechanics are believed to be influenced by the relative Na content. Tm-rich silicate crystallites have formed on the upper surface, unfortunately their precise crystal structure could not be identified.

An approximate laser fluence threshold of > 0.18 J cm^{-2} for inducing the kind of surface modification described above and in chapter 5 is identified through XRD, Raman spectroscopy and cross sectional SEM. Furthermore, temperature appears to play a similar role, whereby fabrications at <570 °C results in the simple deposition. This is evident through the existence of Te-O-Te chains, identified in the Raman spectra. One can therefore deduce that both a sufficiently elevated temperature and laser fluence are required for the formation of crystallites such as ZnTe, Te, ZnO and the as yet unidentified Tm-rich silicate.

Good agreement if found between the calculated diffusion coefficient of O in Si and the observed oxide depth in TEM studies for the surface modified samples. These results are compared to those of the previous chapter where further evidence is supplied for the action of diffusion being the primary mechanism for surface modification.

The formation of ZnO has been described as beginning from a molten Zn catalyst which becomes oxidised as the oxidised silicon layer reaches a sufficient thickness. The primary route for Zn oxidation aside from gaseous O_2 is found to be the reduction of TeO_2. This is believed to result in significant molten Te, whereby its low viscosity and molten state encourage its removal from the material surface.

Chapter 7.
Femtosecond pulsed laser assisted surface modification of silicon substrates III: Engineering with gas type

One of the key aspects of any materials processing technique is the ability to control the outcome of that process. The current work has thus far presented a new branch of femtosecond pulsed laser based fabrication and processing techniques; this chapter aims to demonstrate some of the control mechanisms which can be implemented with respect to gas type.

The primary tool for the analysis of these samples is that of XRD, whereby changes in the preferred growth directions, orientations and relative abundances can thus be inferred. These are also corroborated with cross sectional TEM analysis, surface EDX measurements acquired through SEM and Raman spectroscopy.

7.1. Introduction

Control over the growth of materials so as to fabricate them in a precise manner is paramount to the success of a given fabrication technique. ZnO crystallites for example can be grown in an enormous array of shapes and sizes based upon a specific input of fabrication parameters [97]. This has aided in the development of ZnO based applications as well as presenting it as a highly versatile material for engineering [99].

The engineering of the material properties of rare earth doped materials is also of great importance. Control over the state of the crystalline host can have interesting effects upon the fluorescence characteristics of a rare earth ion [88,184,237] and therefore is of importance for the development of functional devices.

The proposed technique must therefore demonstrate similar capabilities in order to become competitive with established techniques. Simmilarly, a great exploration of the fabrication parameters used for these samples is of great interest. The impact of the background gas type is therefore identified as a key factor in

determining the fabrication mechanism. This is because Ar is not only inert, but also, to a certain extent, ensures that the environment remains oxygen depleted, thus oxidiation must proceed through other means. Fabrication in dilute O_2 environments therefore offers a means to explore the proposed growth mechanics and therefore challenge them.

7.2. Fabrication parameters

The primary samples discussed in this chapter are defined in Table 7.1 with fixed parameters provided in Table 7.2. These samples were prepared to serve as a comparison to the samples deposited in Ar. As noted in chapters 5 and 6, oxygen is a very important element in the formation each crystallite yet observed. Samples fabricated in an oxygen environment can therefore be expected to deviate somewhat from previous samples. Moreover, the use of oxygen as a background gas may indeed alleviate many of the questions raised in the previous chapters concerning the formation mechanisms of certain phases. Additionally, producing samples at 4 hours allows the full extent of these variations to be viewed in comparison to the observations provided in the previous chapter.

The inclusion of hydrogen in the sample I50H is intended to assist in the investigation of the ZnO crystallites and their properties. Much was discussed in the previous chapter regarding the presence of hydrogen in the TZN target and how that may of influenced the crystal properties. This sample is designed to further this discussion.

Table 7.1. Key fabrication parameters for the main samples discussed in this chapter. Others discussed in the text can be found in the previous chapters.

Sample ID	**Laser energy, (μJ)**	**Laser fluence (Jcm^{-2})**	**Gas type**
I50H	50	0.3	4% H in Ar
I100X	100	0.6	O_2
I50X	50	0.3	O_2

Table 7.2. Fixed experimental parameters for each sample produced for this chapter

Pressure	70 mTorr
Duration	4 hours
Target to substrate distance	70 mm
Laser spot size	1.7×10^{-4} cm^2
Substrate	Single crystalline Silicon (1 x 2 cm)
Target	G0 (Tm^{3+}:TZN, 3:77:10:10)
Temperature	570 °C

7.3. Results and discussion

7.3.1. Topographical characterisation of surface modified samples in difference background gasses

Each sample was studied by SEM to ascertain the topological features and thus compare them to previous results in order to identify any similarities or differences. Cross sectional SE-SEM images of I50H are provided in Figure 7.1 while a top-down image is provided in Figure 7.2 with corresponding elemental EDX maps acquired from that region which are depicted in Figure 7.3. Cross sectional and top-down SEM images of sample I100X and I50X are provided in Figure 7.5 and Figure 7.6 respectively. On the top down SEM images of each sample are marked regions from which EDX measurements were acquired, where Table 7.3, Table 7.4 and Table 7.5 illustrate the respective compositions by at%.

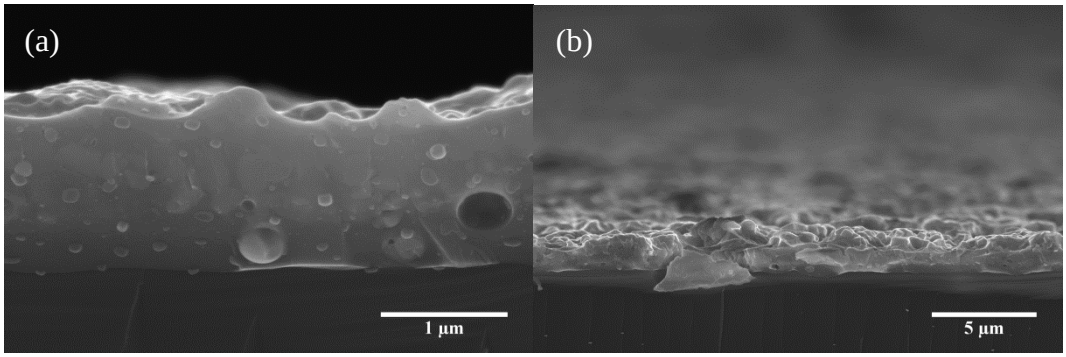

Figure 7.1. Cross sectional SE-SEM images of I50H. (a) High magnification image; (b) Low magnification image

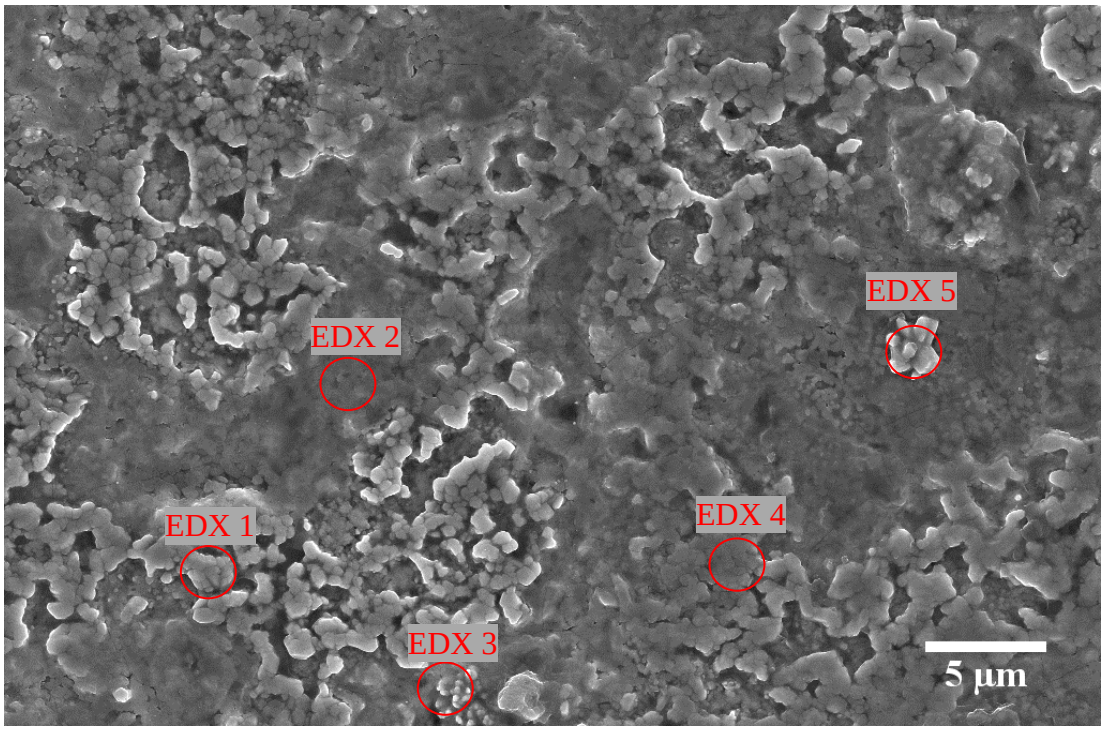

Figure 7.2. Top down SE-SEM image of I50H, including marked areas for spot EDX analysis in red. This area was also selected for EDX mapping which is presented in Figure 7.3

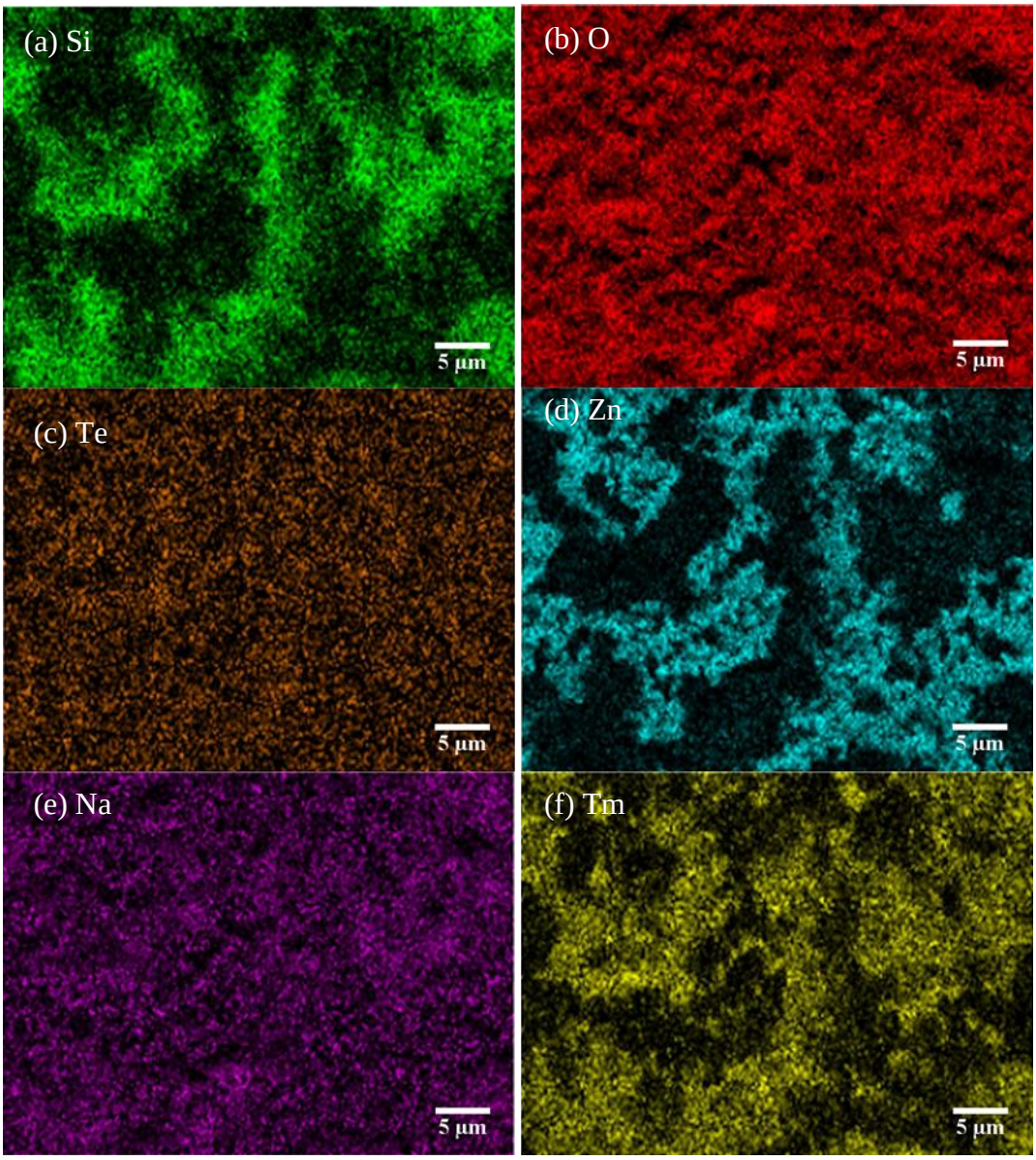

Figure 7.3. Elemental EDX maps of the surface of sample I50H depicted in Figure 7.2, (a) Si (K series); (b) O (K series); (c) Te (L series); (d) Zn (L series); (e) Na (K series) and (f) Tm (M series)

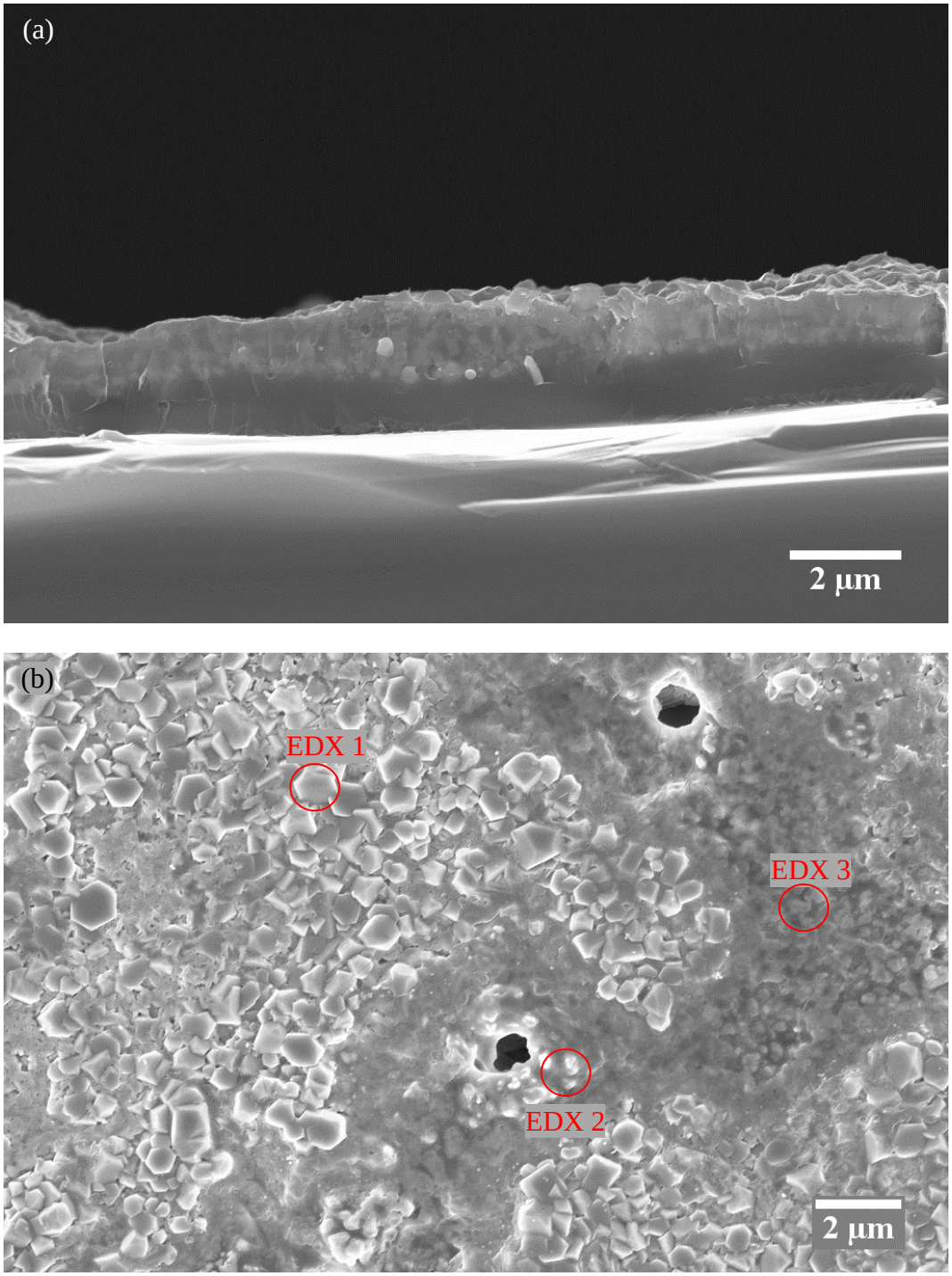

Figure 7.4. (a) Cross sectional SE-SEM image of I100X; (b) top down SE-SEM image of I100X including areas located for EDX analysis

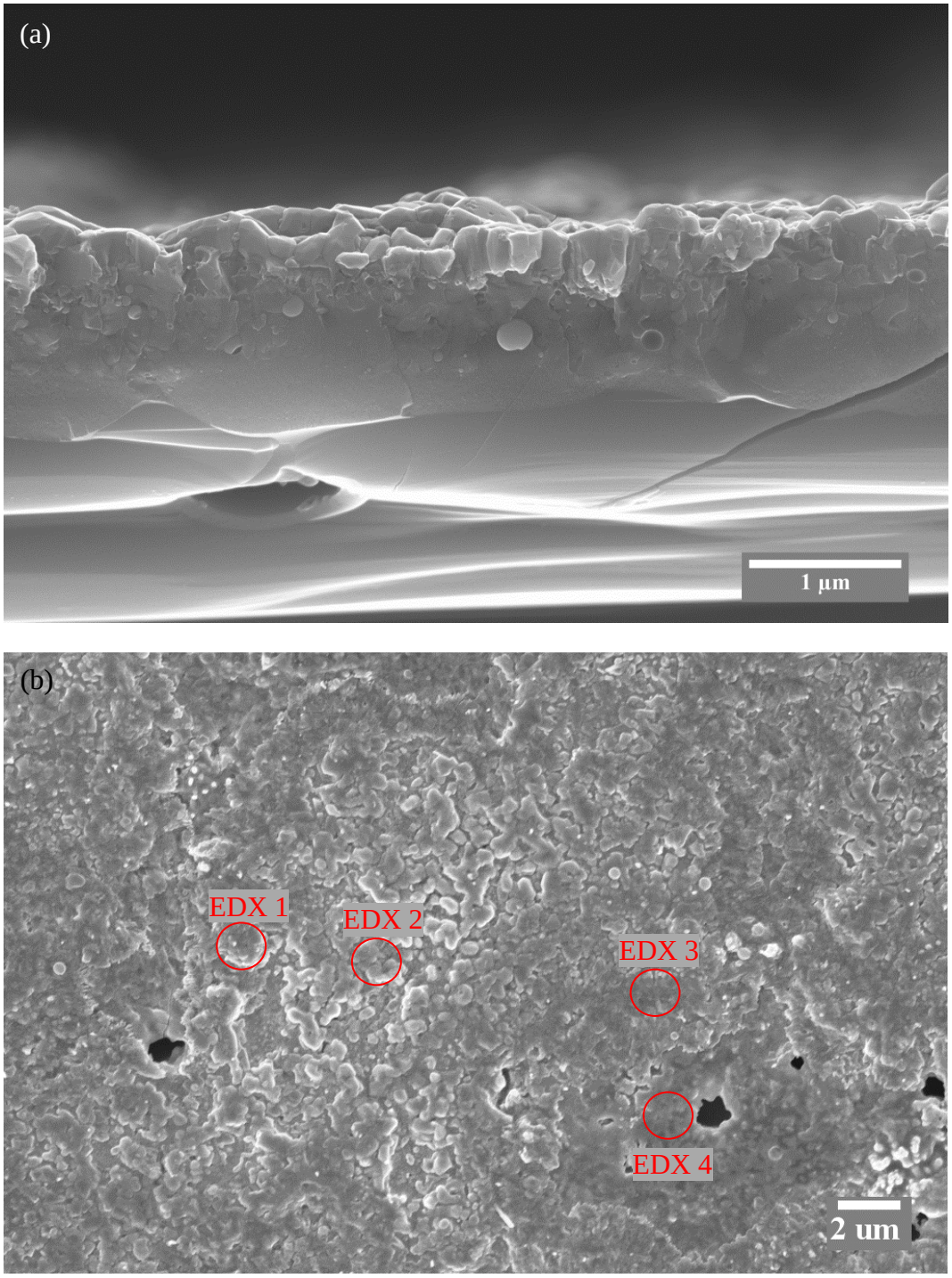

Figure 7.5. (a) Cross sectional SE-SEM image of I50X; (b) top down SE-SEM image of I50X including areas located for EDX analysis

Table 7.3. Table of the semiquantitative point EDX analysis from the surface of I50H in at%. The corresponding locations of the points are illustrated on Figure 7.2**.**

Element ID	EDX 1 (at%)	EDX 2 (at%)	EDX 3 (at%)	EDX 4 (at%)	EDX 5 (at%)
Si	1.5	19.8	22.3	3.4	1.8
O	40.2	50.2	43.7	44.3	42.7
Te	Trace	2.7	2.8	Trace	Trace
Zn	47.5	Trace	4.0	36.7	44.1
Na	8.0	16.0	13.9	12.7	10.5
Tm	1.9	11.2	13.4	2.0	Trace

Table 7.4. Table of the semiquantitative point EDX analysis from the surface of I100X in at%. The corresponding locations of the points are illustrated on Figure 7.4 (b)**.**

Element ID	EDX 1 (at%)	EDX 2 (at%)	EDX 3 (at%)
Si	Trace	18.3	15.2
O	43.7	55.0	57.1
Te	Trace	3.0	3.2
Zn	40.2	3.4	2.5
Na	13.1	9.6	8.6
Tm	1.7	10.7	13.4

Table 7.5. Table of the semiquantitative point EDX analysis from the surface of I50X in at%. The corresponding locations of the points are illustrated on Figure 7.5 (b)**.**

Element ID	EDX 1 (at%)	EDX 2 (at%)	EDX 3 (at%)	EDX 4 (at%)
Si	4.8	Trace	14.4	17.8
O	44.2	46.3	54.1	54.4
Te	Trace	Trace	2.0	4.3
Zn	32.1	38.5	12.3	2.1
Na	15.4	12.5	9.2	7.1
Tm	2.9	1.8	7.9	14.2

As can be seen in the SEM and EDX data presented for each sample, there are many similarities with the samples discussed in the previous chapter. The EDX mapping and point EDX measurements indicate each sample has Zn rich regions distributed across the surfaces, presumably ZnO. The Tm-rich silicate crystallites are also in abundance in the regions surrounding the ZnO crystallites. Moreover, the edge and protrusion contrast of the Zn-rich regions again suggests they are propagating from the surface. The chemical composition of the Tm-rich crystallites for each sample is also in good agreement with the results of the previous chapter. Qualitatively, the crystalline facets of the Zn rich regions match those previously observed. The higher laser energy used for the fabrication of I100X is reflected in the enhanced development of the Zn rich crystallites and again indicates that the higher laser energy simply increases the growth rate of these crystallites.

What is also identified on the surface of each of these samples is the existence of holes. These are noted to only occur within a segment of the Tm rich silicates. A magnified view of one of these holes is provided in Figure 7.6, whereby the base is visible as a smooth surface. As noted in chapter 6 when discussing the holes identified on the surface of I50A, there appears to be cracks surrounding the edges, propagating outward. It seems highly unlikely that such structures would form during the plasma deposition phase, as particles would easily deposit in them as they are directed toward the target, i.e. pointing down *in situ*. In addition to this, the surface energy of the heated substrate during fabrication would not favour the

formation of a well-defined hole. It is possible that these holes are simply formed by the removal of some of the surface material. Note the well-defined angular edges visible at the base of the hole which have been marked on in the inset of Figure 7.6. Both angles are equal to 144° however the perspective of this image is not sufficient to determine this angle accurately. If the hole was angled parallel to the viewing direction the measured angle would decrease, suggesting it may approach the angles matching a hexagon, i.e. the shape of many of the crystal structures observed thus far. Unfortunately it is not possible to identify the root cause of them at this time.

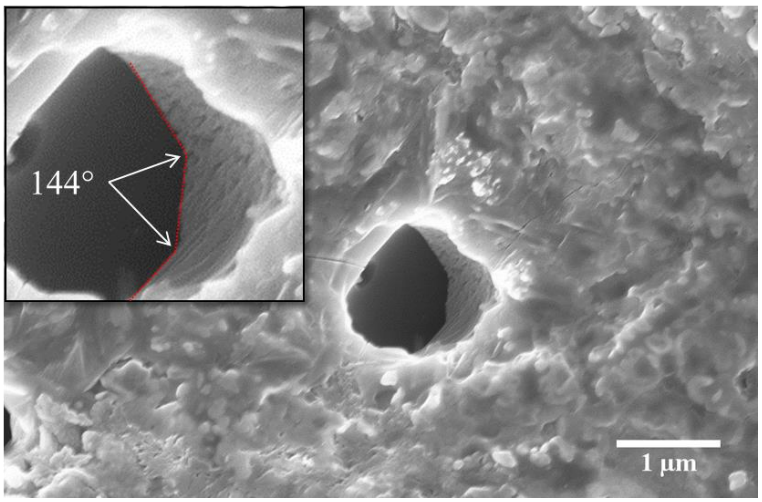

Figure 7.6. A hole on the surface of I100X acquired by SEM, inset shows a magnified view of the hole with the internal angles measured and illustrated

What is also distinctive in each of the cross sectional SEM images for samples I50H, I100X and I50X, is that there is also an abundance of subsurface crystallites. This is expected for sample I50H as the inclusion of H_2 in the Ar atmosphere during fabrication would not necessarily impeded the reduction of the depositing material. For samples I100X and I50X however, it suggests the early stages of formation have not been affected significantly by the abundance of O_2, thus still facilitating the formation of Te and/or ZnTe. One may expect the increased oxygen content to create a more extensive oxide layer on the Si surface prior to deposition. Recall there are a series of heating stages prior to reaching the 570 ºC fabrication temperature in which O_2 gas has already been added at a pressure of 70 mTorr. Should an initial oxide layer have formed, it does not appear to of altered the formation mechanism significantly and therefore provides more food for thought in subsequent analysis.

7.3.2. Cross sectional TEM analysis of surface modified samples in dilute O_2

In light of the identification of extensive subsurface particles in both I100X and I50X, it would be prudent to probe the structure of some of these crystallites and perhaps gain an insight into any changes due to the O content. For this reason, I50X was selected for TEM cross sectional analysis and prepared by focused ion beam (FIB) lithography in order to locate a suitable region to analyse. The region selected is highlighted in Figure 7.7 and the extracted region is given in Figure 7.8 following the final thinning stage with the Ga ions. TEM analysis of the entire visible area (i.e. that below 100 nm in thickness) is provided in Figure 7.9, while a higher magnification of the right hand side is given in Figure 7.10. Figure 7.10 has been marked to indicate the regions from which EDX point analysis (red circles) and SAED patterns (green circles) were taken. The compositional EDX data is provided in Table 7.7. The SAED patterns are presented in Figure 7.11 and the calculated d-spacings for the pattern identified as hexagonal Te is provided in Table 7.7 and compared to a star-quality reference pattern. As with previous discussions, the d-spacings recorded for the Tm-rich silicate crystallites shall be presented in combination with the XRD result for convenience of analysis. EDX mapping in Figure 7.13 acquired from the region depicted in Figure 7.12 was also carried out. Figure 7.12is a reoriented view of the area shown in Figure 7.9, reproduced for clarity. The material above the ZnO crystallites in these maps is composed of Pt from the FIB processing stage and has not been included in the elemental maps as it is not pertinent to the analysis.

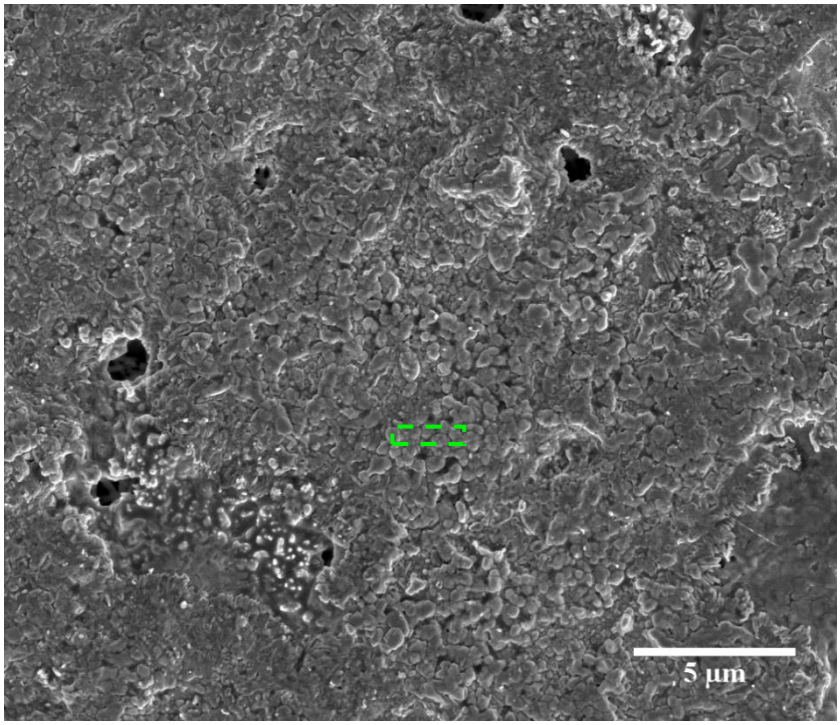

Figure 7.7. SE-SEM image of the surface of I50X, illustrating the section extracted by focussed ion beam (FIB) lithography for TEM analysis in green

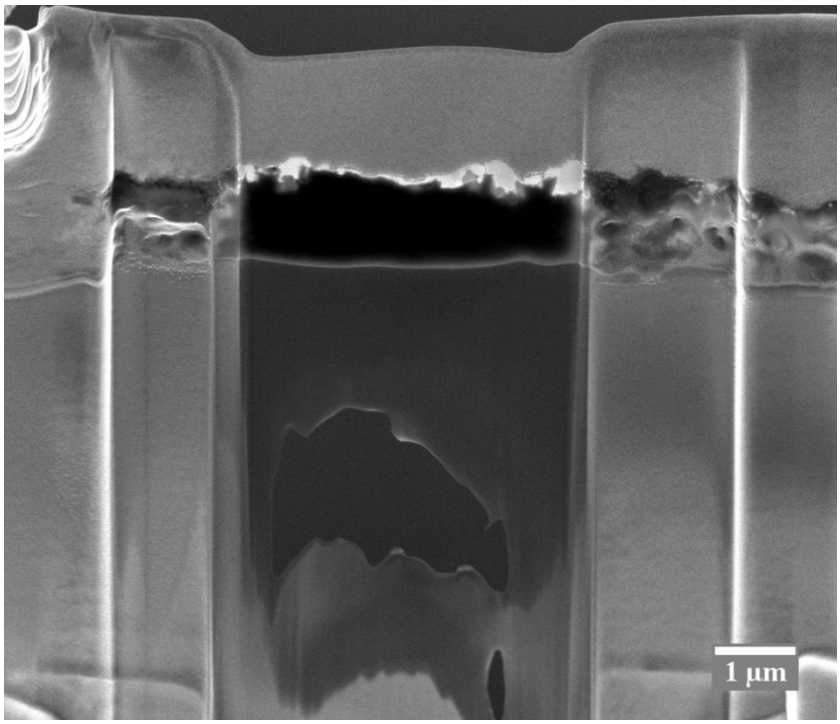

Figure 7.8. SE-SEM image of the I50X section extracted by FIB for TEM analysis following the final thinning stage

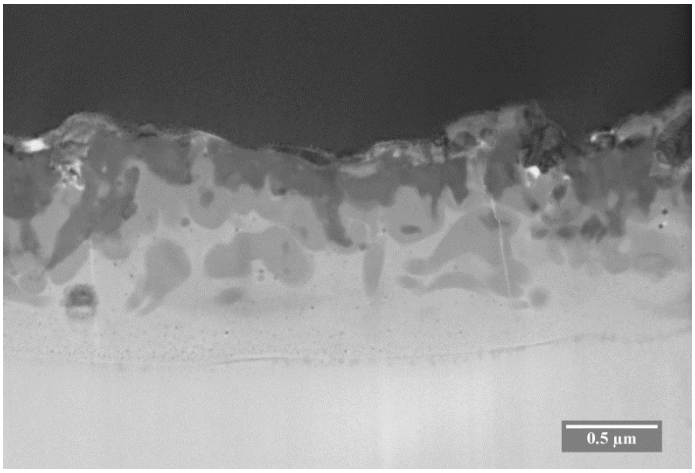

Figure 7.9. TEM image of the cross section of I50X prepared by FIB

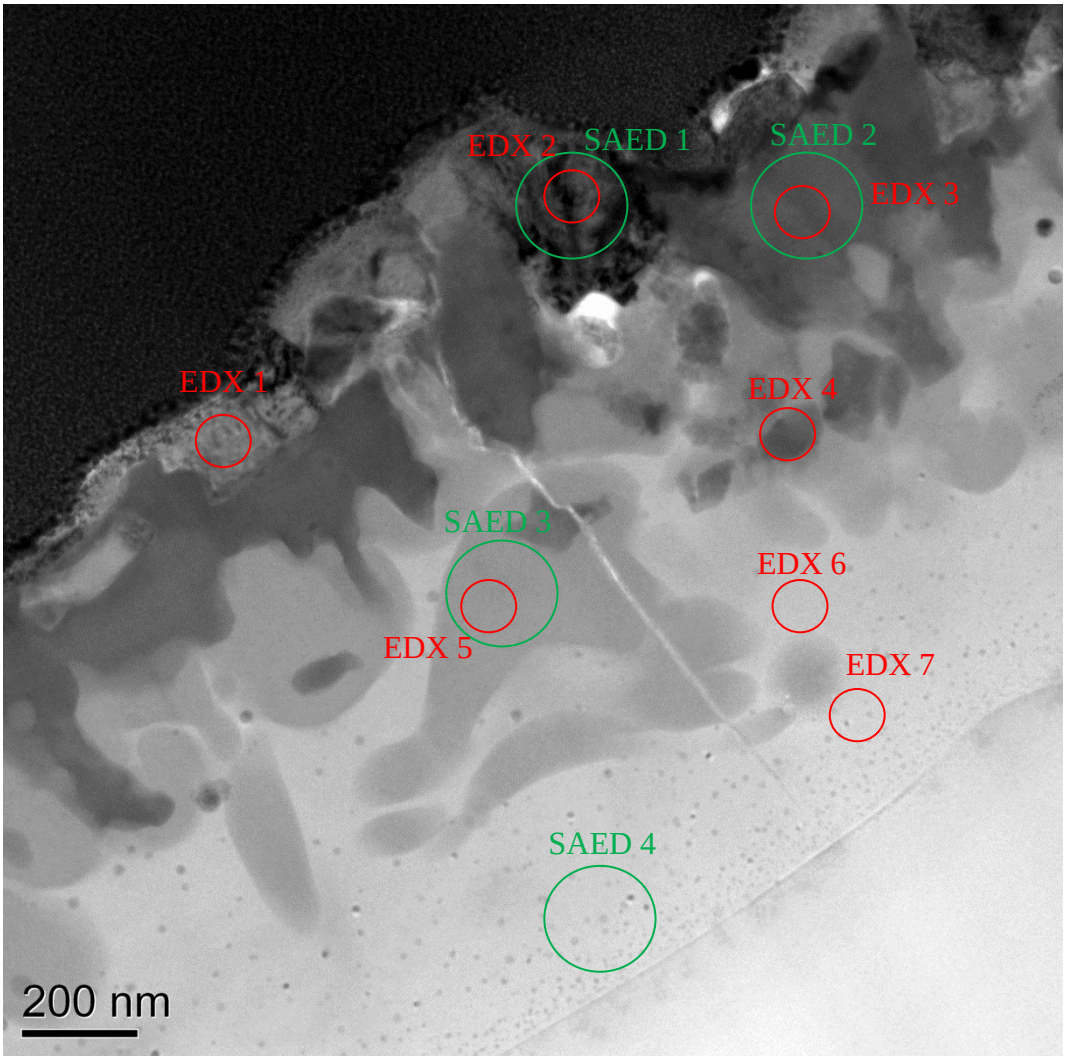

Figure 7.10. TEM image of the right hand side of the section extracted by FIB in Figure 7.9. Marked on the figure are the locations from which EDX point analysis (red circles) and SAED patterns (green circles) were acquired.

Table 7.6. Table of the calculated semi-quantitative chemical compositions in at% of the regions illustrated in Figure 7.10 with red spots. Compositions of less that 1 at% are marked as traces, while those with 0% are marked nil.

Element ID	**EDX 1 (at%)**	**EDX 2 (at%)**	**EDX 3 (at%)**	**EDX 4 (at%)**	**EDX 5 (at%)**	**EDX 6 (at%)**	**EDX 7 (at%)**
Si	Trace	Nil	10.9	14.1	16.4	16.4	16.5
O	55.1	51.0	75.1	77.2	79.0	78.9	75.1
Te	Nil	Nil	Trace	Trace	Nil	Nil	Trace
Zn	26.2	29.3	Nil	Nil	Nil	2.3	4.8
Na	18.1	19.3	2..8	1.0	Trace	1.1	1.7
Tm	Nil	Trace	10.2	7.2	4.4	1.1	1.4

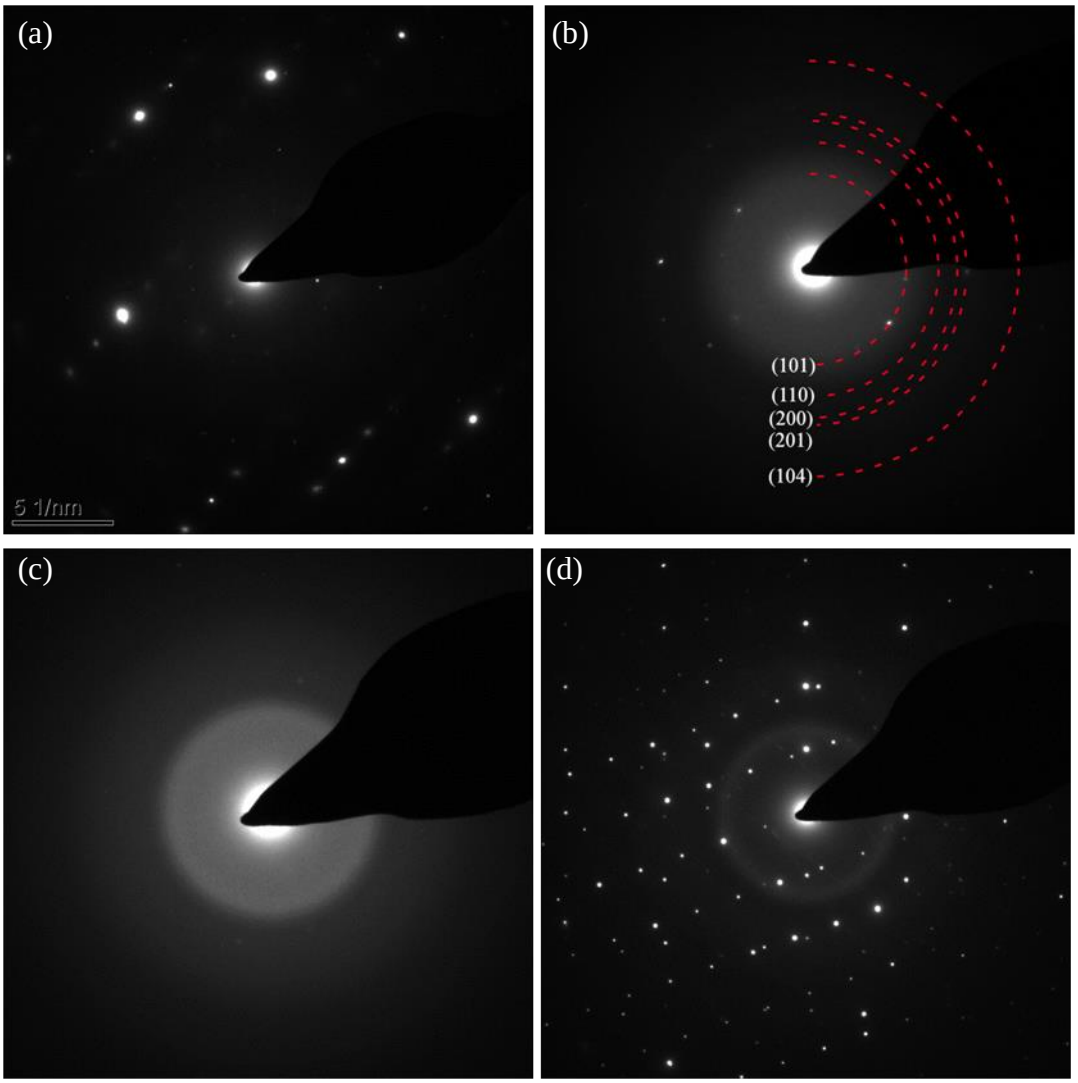

Figure 7.11. SAED patterns from the areas highlighted in Figure 7.10 (a) SAED 1 - ZnO; (b) SAED 2 – Tm rich silicate; (c) SAED 3 – Amorphous silica; (d) SAED 4 – Te nanocrystallites

Table 7.7. Table comparing the measured d-spacings recorded from the randomly orientated nanocrystalline pattern in Figure 7.11 (b) to standard d-spacing measurements for hexagonal Te (ICCD ref: 00-036-1452)

Observed d-spacings	**Reference d-spacings**	**h k l**
3.16	3.23	101
2.23	2.23	110
1.88	1.93	200
1.82	1.84	201
1.40	1.38	104

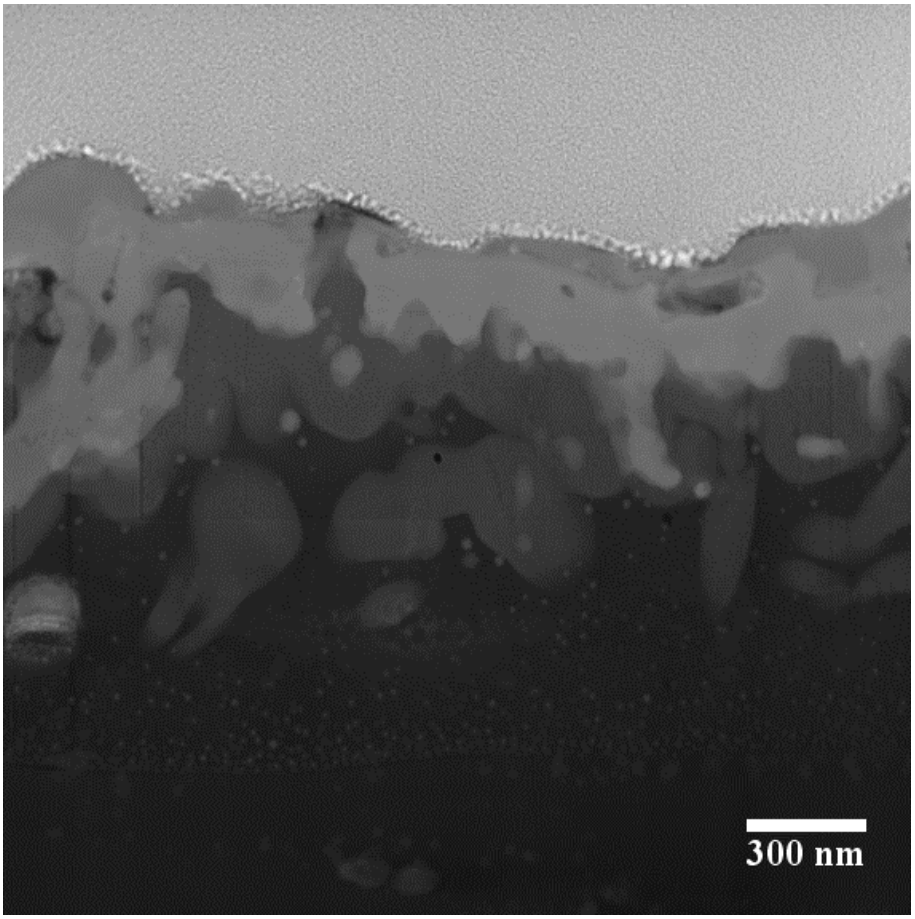

Figure 7.12. TEM image of the cross sectional area of I50X mapped by EDX spectroscopy. The elemental maps corresponding to this area are provided in Figure 7.13

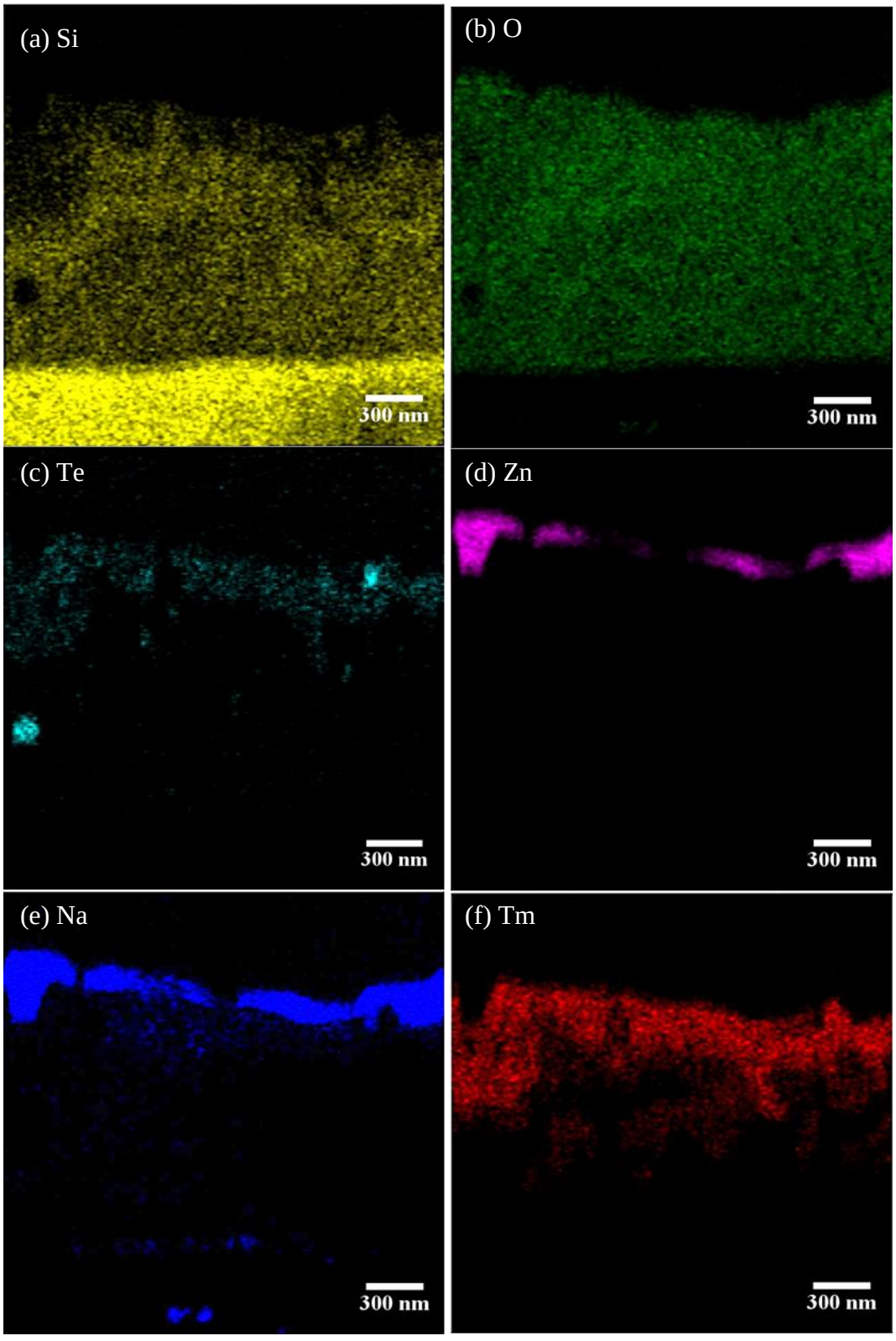

Figure 7.13. Elemental EDX maps generated from the area depicted in Figure 7.12 by the characteristic EDX lines for: (a) Si (K series); (b) O (K series); (c) Te (L series); (d) Zn (K series); (e) Na (K series) and (f) Tm (L series)

From the TEM image in Figure 7.9, it is clear that many of the crystalline structures observed for samples deposited in an Ar atmosphere are still prevalent in the samples fabricated in O_2. This is particularly true for the depth of the oxide layer, where the interface with the crystalline Si is found to be approximately 1.2 μm from the surface. Furthermore, the interface is once again found to be extremely abrupt and distinct, instead of the gradual transition otherwise expected for diffusion. This is significant in that it suggests the abundance of O_2 in the reaction chamber has not distinctly altered the formation mechanics for the oxide layer itself.

The observation of ZnO is also of interest in Figure 7.10 as it conveys a degree of wetting over the surface. This is inferred by the clear surface coating of the underlying Tm-rich crystallites with crystalline ZnO. This provides an interesting point for discussion on the current system. As was noted in chapter 6, wurtzite ZnO has a hexagonal crystalline structure. It was also noted that when grown on a cubic substrate, ZnO will often adopt a zinc blende crystal structure [99]. It is interesting to note at this point, based upon the clear adhesion of ZnO to the Tm-rich silicate in the EDX maps of Figure 7.12 is that β-cristobalite has a cubic structure. Recall that β-cristobalite is the high temperature variant believed to match the XRD data of D60-1 in described in section 5.3.3.2. Note that following the cooling procedure, as discussed, β-cristobalite would change to the α-phase instantaneously, i.e. the microscopic crystalline structure would be preserved. This would mean the Tm-rich crystallites (if they were originally a variation of cubic β-cristobalite) would remain as cubic crystallites and would not possess the hexagonal geometric structure identified on the surface of I100A in chapter 6. The unknown peaks identified for sample D60-1 were not however repeated in any of the previous samples fabricated for 4 hours and thus one may deduce that they may have been an intermediary phase, or simply a different phase altogether.

As was postulated in chapters 5 and 6, the reduction of the oxides from the plasma phase by Si is believed to favour the growth of an oxide layer in the Si substrate, thus resulting in an oxygen deficiency. The strong preference for any starting oxides to be reduced by Si was established in section 5.3.3.4. In combination with other favourable growth conditions, this was believed to explain the formation of crystallites such as Te and ZnTe. It would therefore appear that the O_2 in the PLD chamber was not sufficient to inhibit the growth of these crystallites and thus challenges this proposed hypothesis. One must recall however that the

TEM cross section of I50X is an astoundingly minute representation of the overall structure. Better characterised can thus be achieved in combination with XRD and Raman spectroscopy, as identified in earlier chapters and extended discussion shall therefore be reserved for these subsequent sections.

7.3.3. Crystallite characterisation via X-ray diffraction and Raman spectroscopy

TEM analysis of I50X identified distinct similarities between in general cross sectional structure with that of I50A discussed in chapter 6. Cross sectional TEM analysis can be rather misleading as to the overall crystallography of a given sample. For a more quantitative and overall crystallite characterisation, XRD and Raman spectroscopy were carried out on the samples of this chapter. The XRD and Raman spectrums of I50H are provided in Figure 7.14 and Figure 7.15 respectively and are matched to that of known crystallites. The XRD pattern corresponding to I100X is provided in Figure 7.16 and a Raman spectrum of its surface in Figure 7.17. The XRD pattern for I50X is found in Figure 7.18, while its respective Raman spectrum is provided in Figure 7.19.

The XRD peaks allocated to the Tm rich silicate crystallites in Figure 7.14 for I50H are based off the observed d-spacings in SAED patterns for I50A as well as those labelled ‘red spots’ from the SAED patterns for I100A.

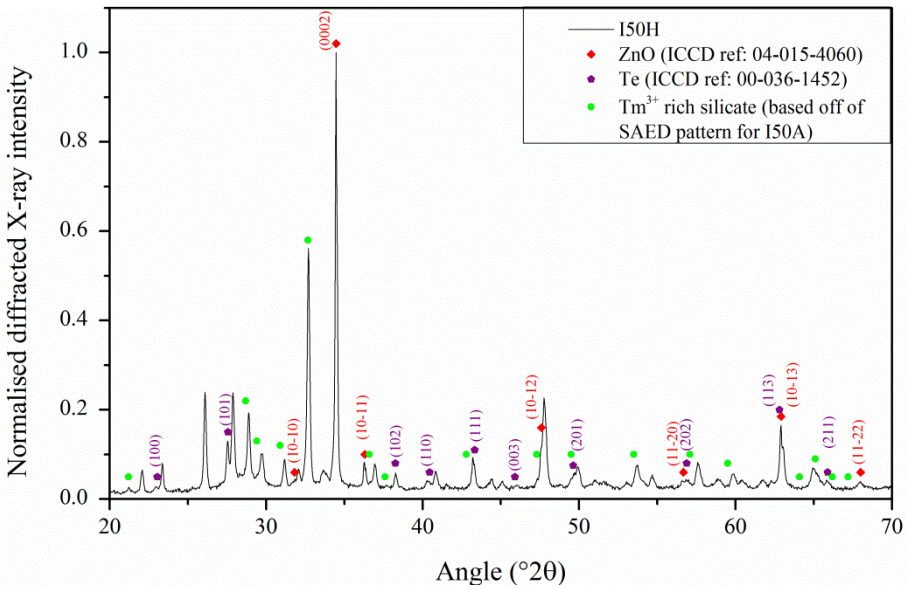

Figure 7.14. XRD spectrum of I50H, including the calculated d-spacings from measurements of the SAED pattern in Table 6.16 (●) for Tm rich crystallites in I50A, calculated d-spacings from SAED pattern of I100A (●), hexagonal ZnO (◆) (ICCD reference: 01-071-6424) and hexagonal Te (⬟) (ICCD reference: 00-036-1452)

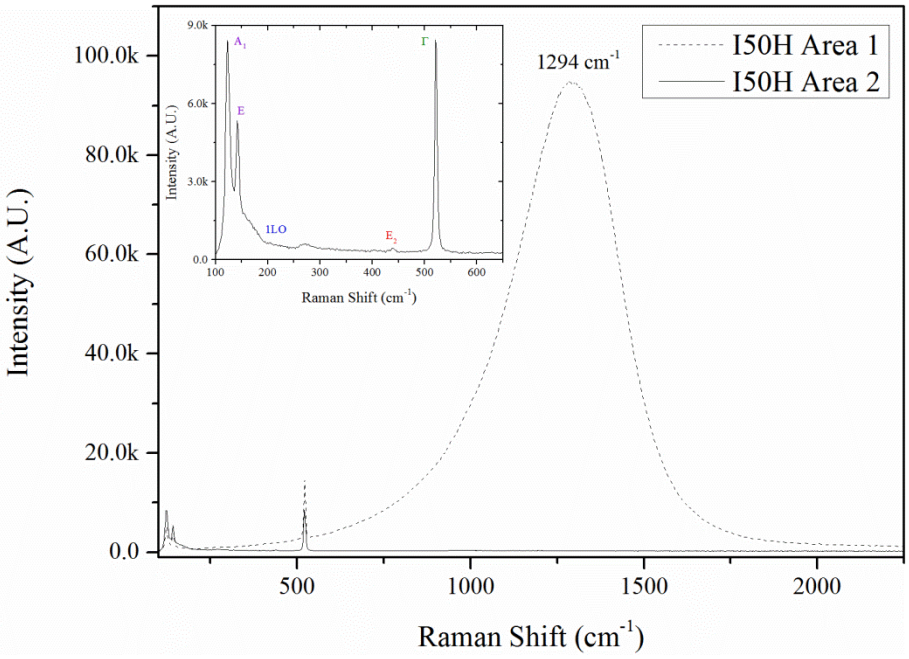

Figure 7.15. Raman spectrum of two areas of I50H with marked peaks corresponding to the Γ mode of Si in green, the E_2 mode of ZnO in red, the LO mode of ZnTe in blue and the A_1 and E modes of hexagonal Te in purple. Inset shows the lower frequency spectrum of Area 2

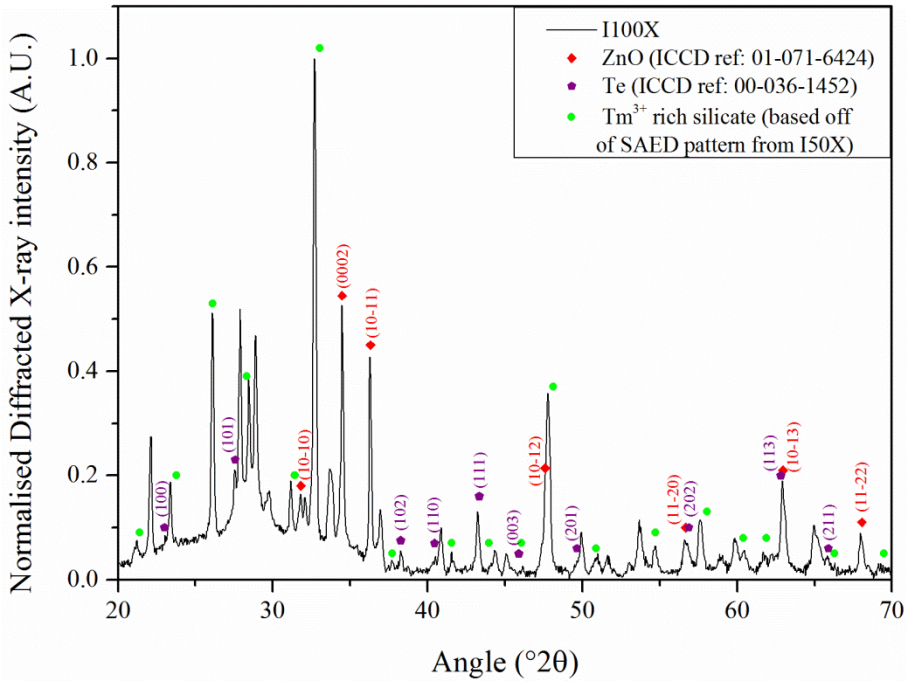

Figure 7.16. XRD spectrum of I100X, including the calculated d-spacings from measurements of the SAED pattern in Figure 7.11 (d) (●) for Tm rich crystallites in I50X, hexagonal ZnO (◆) (ICCD reference: 01-071-6424) and hexagonal Te (⬟) (ICCD reference: 00-036-1452)

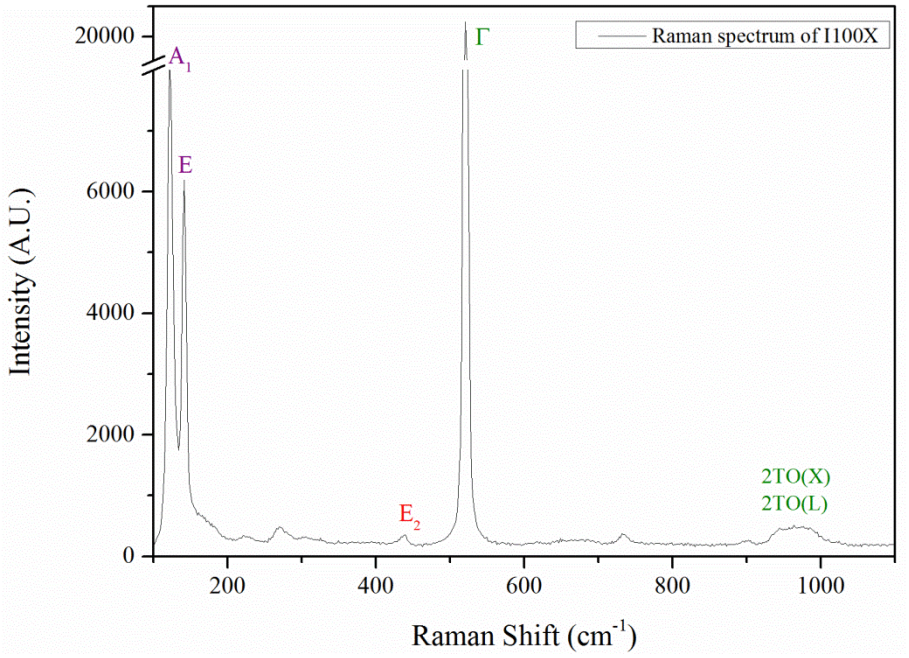

Figure 7.17. Raman spectrum of I100X with marked peaks corresponding to the Γ modes of Si in green, the E_2 mode of ZnO in red and the A_1 and E modes of hexagonal Te in purple.

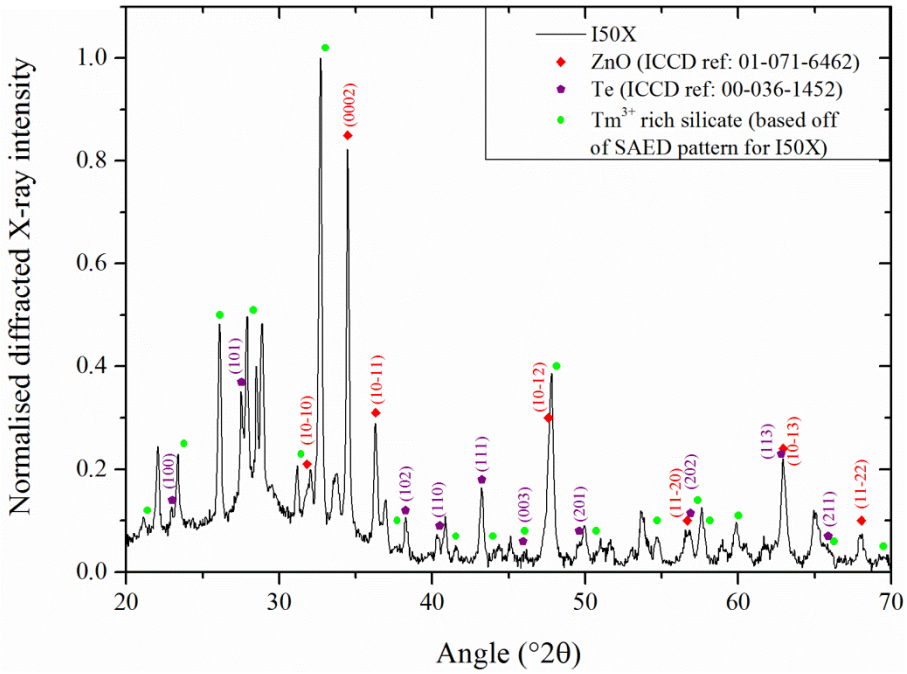

Figure 7.18. XRD spectrum of I50X, including the calculated d-spacings from measurements of the SAED pattern in Figure 7.11 (d) (●) for Tm rich crystallites, hexagonal ZnO (◆) (ICCD reference: 01-071-6424) and hexagonal Te (⬟) (ICCD reference: 00-036-1452)

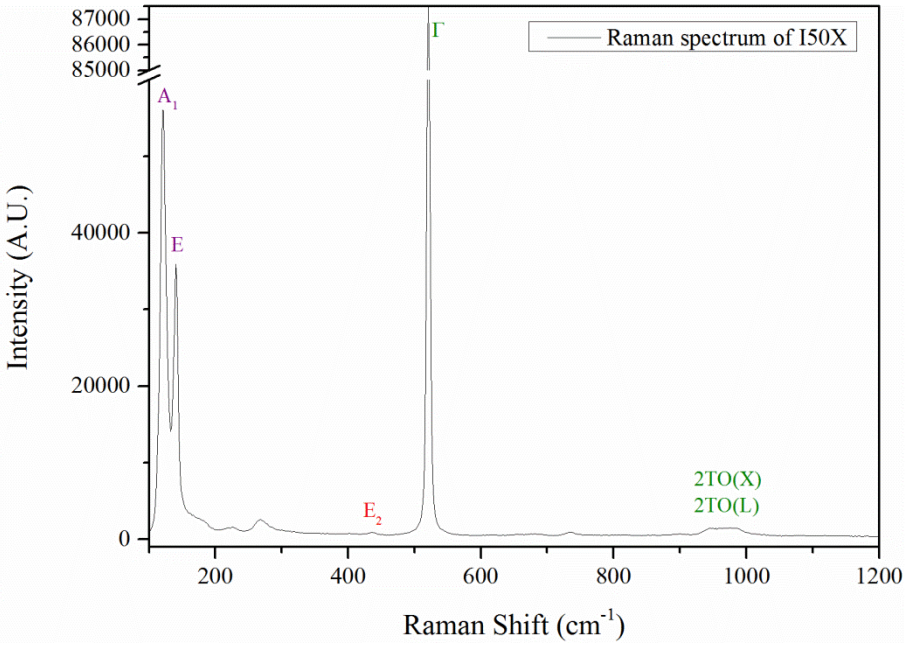

Figure 7.19. Raman spectrum of I50X with marked peaks corresponding to the Γ modes of Si in green, the E_2 mode of ZnO in red and the A_1 and E modes of hexagonal Te in purple.

The aforementioned XRD spectrums of I50H, I100X and I50X appear to possess many of the crystallographic features found in the samples discussed in chapter 6. This includes the matching XRD peaks for the Tm rich crystallites, Te nanocrystallites, hexagonal ZnO and occasionally ZnTe. ZnTe crystallites appear to be absent when fabrication occurs in an O_2 environment. No fluorescence was observed for any region studied for either I100X or I50X during Raman spectroscopy, which has been found to be the easiest way to identify their occurrence. This kind of relationship is also reflected in I50Hs Raman spectrum in Figure 7.15. Area 1 of Figure 7.15 was found to be rich in ZnTe and thus the resulting fluorescence obscured many of the spectral features, however no fluorescence was observed in area 2, suggesting an absence of ZnTe. The lack of peaks corresponding to ZnTe in I50Hs XRD spectrum in Figure 7.14 is attributed to the low concentration of this phase in the overall material. Below a concentration of approximately 1% by volume in a given material, a particular phase is not likely to appear beyond the noise level of an XRD scan. Raman spectroscopy is considerably more sensitive to individual areas and thus can be used to study different regions.

7.3.3.1. Characterisation of associated ZnO crystallite peaks

Closer inspection of the relative peak intensities corresponding to hexagonal ZnO in each samples respective XRD spectrums identifies interesting trends. Expressed in Table 7.8 is a comparison of the relative peak height for the dominant (0002) peak to that of the $(10\bar{1}1)$ peak of the wurtzite ZnO phase. For convenience, this ratio shall be designated κ. Recall that the $(10\bar{1}1)$ and $(10\bar{1}0)$ peaks of wurtzite ZnO correspond to the a-axis and thus are representative of growth perpendicular to the c-axis. A comparison to the $(10\bar{1}1)$ peak is easier to resolve than that to the $(10\bar{1}0)$ as it is not overlapped by any surrounding peaks, thus has been selected for comparison. Note that these comparisons are made between the heights recorded from spectra deconvoluted from the amorphous background.

Table 7.8. Table comparing the ratios of the (0002) peak to that of the $(10\bar{1}1)$ peak of wurtzite ZnO identified in the XRD spectrums of all samples where ZnO is observed. Included in this comparison is that of the standard reference pattern for wurtzite ZnO used thus far (ICCD ref: 01-071-6424).

Sample ID	**Laser energy during fabrication (μJ)**	**Gas type**	**(0002): $(10\bar{1}1)$ ratio, κ**
Reference spectrum	N/A	N/A	0.39
I50H	50	4% H_2 in Ar	8.40
I50A	50	Ar	12.5
I100A	100	Ar	4.48
I100X	100	O_2	1.18
I50X	50	O_2	3.02

The data presented in Table 7.8 can be reasoned through an understanding of the complex growth mechanisms involved in the formation of ZnO crystallites for the present system. As noted in the previous chapter, the inclusion of Na as a dopant during the formation of ZnO rod structures leads to significant variability in the preferential growth direction [226] depending on the local Na concentration. One can expect this to introduce a random factor into the overall growth direction as the distribution of Na across the sample surface is expected to fluctuate due to diffusion into the SiO_2 matrix. In order to first comprehend the differences in these ratios, it is convenient to begin with a comparison of the relative change in κ for the two pairs of samples fabricated in different gasses: I50A (50 μJ) and I100A (100 μJ) in Ar and I100X (100 μJ) and I50X (50 μJ) in O_2. Firstly, the relative increase in κ from I100A to I50A is found to be 2.56, while the same increase from I100X to I50X is found to be 2.79. Similarly, the relative increase in κ from I100X in O_2 to I100A in Ar is found to be 3.80, while I50X to I50A is 4.14. This demonstrates an interesting agreement between the relative change in the ZnO crystallite orientation and preferential growth direction for fabrication in either gas types based on a change in laser energy. It is acknowledged however that these ratios are for a very narrow set of samples, the agreement is worth considering.

The growth of ZnO crystallites, as noted, is well characterised by other fabrication techniques. This can therefore be extrapolated to describe the observations of the present system. It should be noted that the following discussion is hypothetical and used as a means to explore the crystal growth mechanisms. In order to develop a robust theory to explain the crystal growth, computer simulations coupled with a much more extensive experimental dataset should be pursued.

The growth of ZnO crystallites may proceed in one of two ways depending upon the gaseous environments considered. In dilute O_2, oxidation would proceed rapidly for the formation of ZnO. Such oxidation rates can be expected based upon the thermochemical calculations presented in Figure 7.20. The rapid oxidation rate would thus favour the nucleation of ZnO crystallites which would then grow as the experiment progresses. The availability of O_2 however would thus suggest that such crystallites would be Zn-limited in their growth. Moreover, their growth can be expected to have an isotropic character due to the Zn-limiting factor, thus ensuring crystallites will grow continually from exposed (0001) Zn facets. The ZnO surface coating observed in Figure 7.13 supports this rationale in that a surface coating has formed in favour of well-defined, isolated crystallites.

With regard to growth in an Ar gas environment, the growth can be considered to be O-limited, whereby the oxidation source is deemed to be TeO_2. This slower rate of oxidation would thus favour the formation of more extensive molten Zn zones described in chapter 6. Upon oxidation, a nucleation event can thus be considered, whereby a small, yet stable ZnO crystallite would form. This crystallite can be considered to be encapsulated in a molten Zn region, thus allowing the crystallite to re-orientate as the growth ensues. Note the higher surface energy on the {0001} plane favours growth in the c-axis. One may therefore postulate that a sufficiently long rod would re-orientated under gravity so as to descend from the surface. Again, recall the orientation of the substrate is directed toward the ground. Such re-orientation events would not be possible in the dilute O_2 environment due to molten Zn surface being negligible.

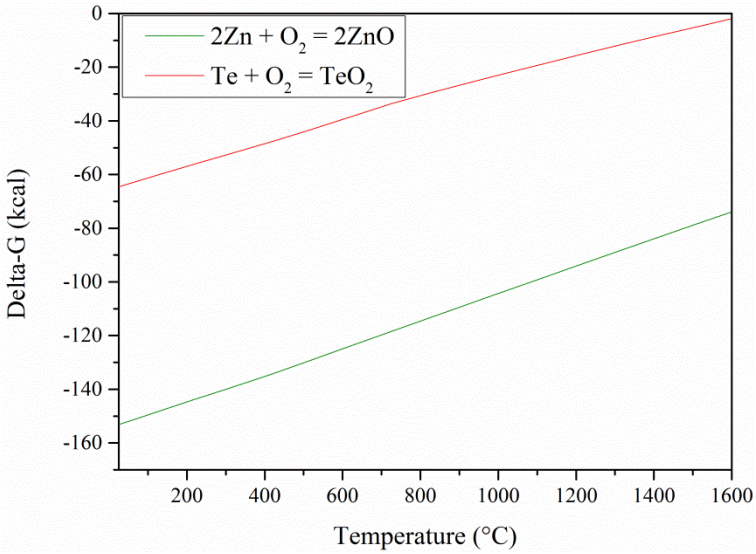

Figure 7.20. Thermochemical calculations for ΔG of the oxidation of Zn and Te by gaseous O_2 across a range of temperatures

Such a hypothesis does not contradict the growth of the wide microrod crystallites observed most distinctively for I100A and I100X. It merely proposes the circumstances in which a ZnO crystallite may become orientated in the initial stages of growth.

A satisfactory explanation of the observed increase in κ for samples fabricated with lower laser energy unfortunately could not be defined. Further experimentation may allude to a reasonable hypothesis in which to test, however the prolonged malfunction of the fs-PLD system prohibited exploration of this and other points.

As found in Figure 7.20, the formation of TeO_2 is expected to be favourable in dilute O_2. Oxidation would certainly favour the formation of TeO_2 from any reduced Te content that may have formed. However, the precise reason for the loss in Te content on the as-formed material remains unclear.

7.3.3.2. Characterisation of associated Tm-rich silica peaks

With the complete listings of diffracted X-ray peaks associated with the Tm-rich silica crystallites, as identified through SAED patterns of samples I50A, I100A and I50X, a comparison of relative peak positions can be carried out. In order to study this effectively, the XRD peaks most distinctively associated with the d-spacings calculated from SAED patters is identified. These are as follows:

22.1, 23.4, 26.1, 27.9, 32.7, 36.9, 40.8, 53.7 and 65.0 °2θ

The peak intensities of each spectrum was then normalised to the 32.7° peak, which is the most intense diffraction peak for all but I100A. In addition to this, a normalised set of peak intensities to the 26.1 °2θ diffraction peak of each spectrum was also collected. With these datasets, a comparison between each sample was made, whereby the normalised peak intensity of one peak was divided by that of other samples, as defined in the first row of Table 7.9 and Table 7.10. The rationale for this comparison is that if a degree of continuity exists for several samples in relation to a specific XRD peak, it would provide further evidence that such peaks are related to the same material. As found with the ZnO in section 7.3.3.1 however, discrepancies may occur should there be preferential orientation. The tables detailing the full list of these comparisons are provided in Table 7.9 for 32.7° and Table 7.10 for 26.1°.

Little or no correlation is identified for peaks normalised to 26.1°, suggesting is relates to a different phase, as indicated in the SAED data of I100A in Figure 6.26. Many of the peaks normalised to 32.7° however show a distinctive correlation and are thus ascribed to this phase. These include:

23.4, 27.9, 32.7, 36.9, 40.8, 53.7 and 65.0 °2θ

Note that the anomalous intensities when comparing I100A to other sample at 53.7° is due to the second reflection at double the 26.1° angle, i.e. 52.2°.

The isolation of the 26.1° peak in addition to the 52.2° peak would therefore suggests that this phase may be a form of silica. Thus the 26.1 and 52.2° XRD peak is tentatively ascribed to Quartz, as in the star reference spectrum for hexagonal quartz with the ICCD reference number 00-046-1045. The (101) peak of this phase is noted as 26.64°, thus is a reasonable assumption based upon observations in SAED, XRD and localised EDX measurements.

Table 7.9. Table comparing the relative intensities of XRD peaks asociated with Tm-rich silica when normalised to 32.7 °2θ for a range of samples.

	I100A/ I50A	**I100X/ I50X**	**I50H/ I50A**	**I50H/ I50X**	**I50A/ I50X**	**I100A/ I100X**	**I100X/ I50A**	**I100X/ I50H**
22.1	0.98	1.29	1.61	0.94	0.58	0.44	2.21	1.37
23.4	1.23	0.80	1.09	0.88	0.80	1.24	0.99	0.91
26.1	3.32	1.09	0.98	0.96	0.98	2.99	1.11	1.13
27.9	1.25	0.99	1.08	1.23	1.14	1.44	0.87	0.80
32.7	1.00	1.00	1.00	1.00	1.00	1.00	1.00	1.00
36.9	0.97	1.10	1.05	1.21	1.15	1.02	0.95	0.91
40.8	1.34	0.99	0.99	1.02	1.02	1.39	0.97	0.97
53.7	2.56	1.00	1.03	1.10	1.06	2.71	0.94	0.91
65.0	0.92	0.86	1.01	0.98	0.97	1.04	0.88	0.88

Table 7.10. Table comparing the relative intensities of XRD peaks asociated with Tm-rich silica when normalised to 26.1 °2θ for a range of samples.

	I100A/ I50A	**I100X/ I50X**	**I50H/ I50A**	**I50H/ I50X**	**I50A/ I50X**	**I100A/ I100X**	**I100X/ I50A**	**I100X/ I50H**
22.1	0.29	1.18	1.65	0.98	0.59	0.15	1.99	1.21
23.4	0.37	0.74	1.12	0.92	0.82	0.41	0.90	0.80
26.1	1.00	1.00	1.00	1.00	1.00	1.00	1.00	1.00
27.9	0.38	0.91	1.11	1.28	1.16	0.48	0.78	0.71
32.7	0.30	0.92	1.02	1.04	1.02	0.33	0.90	0.88
36.9	0.29	1.01	1.07	1.26	1.18	0.34	0.86	0.80
40.8	0.40	0.91	1.02	1.06	1.04	0.46	0.87	0.86
53.7	0.77	0.92	1.06	1.14	1.08	0.91	0.85	0.80
65.0	0.28	0.79	1.03	1.02	0.99	0.35	0.80	0.77

7.4. Conclusion

This chapter has detailed the effect of the background gas upon the growth of crystallites and their resulting microstructure. It has been found that fabrication in a dilute O_2 atmosphere has little or no effect on the resulting structure or the formation mechanisms of the oxide layer itself. Detailed analysis of the XRD spectrum for ZnO crystallites has however identified a degree of preferred orientation. It is found that this is subject to effects of laser energy as well as being deposited in a dilute Ar or O_2 atmosphere. A hypothesis is proposed for the improved orientation in an Ar atmosphere, based upon the mobility of crystallites in a molten Zn catalyst due to the O-limited growth.

A refinement of the associated d-spacings for the Tm-rich crystallites to the corresponding XRD spectrums is provided. It has revealed that a second crystalline phase exists within this collection which likely corresponds to hexagonal quartz.

The results of this chapter demonstrate that the growth mechanics of crystallites for these materials can be influenced by the set experimental parameters. A degree of continuity is inferred in this regard, suggesting the engineering of the crystallites relative size and orientation may be possible. Further work is required in order to fully explore these phenomena. Furthermore, one may expect similar effects from parameters which were fixed in this study, for example gas pressure and laser repetition rate.

Chapter 8.
Femtosecond pulsed laser assisted surface modification of silicon substrates IV: Optical characterisation

Previous chapters pertaining to the surface modification of silicon through the ablation of Tm^{3+} doped TZN glass has identified a variety of crystal types. Many of these crystals are found to be highly applicable in the field of photonics. The semiconductors ZnTe and ZnO for example fluoresce in the visible region, while Tm^{3+}-ions are well known for their optical mid-infrared emission.

This chapter describes the optical characterisation of these materials through photoluminescence and excitation spectroscopy. In so doing, a great deal of insight is be gained into the local crystalline environment encapsulating the Tm^{3+}-ions which complement the structural analysis of previous chapters significantly. Additionally, fluorescence characterisation of Er^{3+}-doped samples fabricated under similar conditions are also presented.

8.1. Introduction

Several crystalline materials fabricated in chapters 5, 6 and 7 have photonic applications. Optical applications of semiconductors is far reaching and of great interest to many areas of industry. The optical applicability of rare earth elements is also of great interest for the development of novel photonic devices such as lasers [231], optical amplifiers [238] and a variety of optoelectronic devices [78].

Within photonics, rare earth ions are often used as the gain medium [239] in laser based applications. Gain media may be pumped either electrically or optically and thus a conductive material is not necessarily required. The demonstration of photoluminescence from rare earth ions within a given host material is therefore of great interest. Host materials for rare earth ions are not found in abundance however; the low solubility of lanthanides makes them difficult to dope certain materials, particularly crystalline materials. Compositional analysis of the Tm^{3+}-rich crystallites described in this work for different samples has identified varying

concentrations of Tm^{3+}-ions, suggesting a range of concentrations may be possible. This is highly advantageous as it suggests the doping concentration can be controlled and thus tailored to the specific design requirement. It should be noted that rare earth elements are susceptible to concentration quenching, thus control of the doping concentration is paramount for optimising a possible device.

8.2. Sample specifications

The samples described in this chapter include those already described from previous chapters as well as a sample fabricated from Er^{3+} doped TZN (1 wt%, 80:10:10 mol%). The experimental variables used for the fabrication of these samples are provided in Table 8.1, in addition to this, the fixed parameters are provided in Table 8.2. Although many of these are repeated from previous chapters, it is appropriate to collect these into a single table for the purposes of this chapter.

Table 8.1. Table of the experimental variables used for the fabrication of samples described in this chapter. Note the Tm^{3+} doped TZN target is 3 wt%, while the Er^{3+}-doped sample is 1 wt%

Sample ID	**Temperature, °C**	**Laser energy, µJ**	**Laser Fluence, J cm^{-2}**	**Gas type**	**Duration, hours**	**Target**
I50H	570	50	0.30	4% H in Ar	4.0	Tm^{3+}:TZN
I50A	570	50	0.30	Ar	4.0	Tm^{3+}:TZN
I100A	570	100	0.60	AR	4.0	Tm^{3+}:TZN
I50X	570	50	0.30	O_2	4.0	Tm^{3+}:TZN
D30-1	570	50	0.30	Ar	0.5	Tm^{3+}:TZN
D60-1	570	50	0.30	Ar	1.0	Tm^{3+}:TZN
E50A	570	50	0.30	Ar	4.0	Er^{3+}:TZN

Table 8.2. Fixed fabrication parameters for the fabrication of the samples described in this chapter

Pressure	70 mTorr
Target to substrate distance	70 mm
Laser spot size	1.7×10^{-4} cm^2
Substrate	Single crystalline silicon

The target used for the fabrication of E50A was produced in the same way as described in section 3.1.2.1, but 1 wt% of Er_2O_3 was used in place of Tm_2O_3.

Optical characterisation is carried out using the Edinburgh instruments spectrophotometer described in section 3.2.1. Due to the wide 3.3 eV direct bandgap of ZnO, it was excited using 270 nm monochromated light from a broadband microsecond flash-lamp source. A visible bandpass filter was used to cover the entry into the monochromator connected to the visible photomultiplier tube (PMT) detector. This filter (named 668GK) absorbs >99% of 270 nm light while being ~95% transparent in the 320-620 nm range.

ZnTe has a bandgap of approximately 2.26 eV, thus can be excited with an Ar-ion laser. In order to resolve the subsequent emission from ZnTe however, the main 514 nm line from the Ar-ion laser cannot be utilised due to its proximity to the ZnTe emission line. This would significantly interfere with the detector and therefore a 488 nm bandpass filter was positioned in the beam path outside of the spectrometer. Such a filter allows the transmission of only the specified wavelength (to a given range) and attenuates all others. This ensures the excitation wavelength is set to 480 nm. This laser wavelength would still saturate and damage the detector should it be allowed to pass through to the visible PMT detector. To prevent this, another filter is positioned over the entry slit to the monochromator inside the spectrometer which filters >99% of the 480 nm laser light. To ensure the resulting signal can be collected, this filter is also ~95% transparent at 550 nm. The subsequent emission from the ZnTe crystallites can thus be detected using the visible-PMT detector.

For the characterisation of Tm^{3+} and Er^{3+}-ion emission, one must consult the energy level diagrams depicted in Figure 2.1 and Figure 2.2. The absorption

spectrum for these lanthanides and indeed the aforementioned semiconductors could not be acquired due to the dominant absorption by the silicon substrate.

Tm^{3+} doped samples were optically excited with a Ti:sapphire laser at 796 nm pumped with twin Ar-ion lasers. This is to excite the $^3H_4$ manifold of the Tm^{3+}-ions and thus instigate the well-known cross-relaxation process resulting in the $^3F_4 \rightarrow {}^3H_6$ decay. The subsequent emission was collected using an Edinburgh Instruments 301 NIR InGaAs detector. Due to an inability to chop the excitation source electronically as well as the associated weak emission from a thin film, the lifetime of this transition could not be acquired. A mechanical chopper was attempted, however a satisfactory decay curve associated with the Tm^{3+}-ion emission could not be extrapolated without incurring significant errors in its analysis.

Low temperature emission spectroscopy was conducted for the Tm^{3+} doped samples using an Oxford Instruments Optistat^{DN} cryostat whereby the sample can be controllably cooled from room temperature to 77 K using liquid nitrogen. Operating at lower temperatures reduces the available thermal energy for the lanthanides 4f-electrons and thus confines their occupancy to lower Stark levels. This applies to all manifolds in the system and thus offers better resolution of the individual crystal-field levels associated with a given transition.

8.3. ZnO photoluminescence spectroscopy

Due to the lack of a viable laser excitation source and the relatively sparse distribution of ZnO crystallites across each samples surface, only weak fluorescence intensities have been observed for each sample. As found in previous chapters, sample I100A is qualitatively determined to have the greatest abundance of ZnO crystallites, therefore it is reasonable that the emission spectrum for this sample is found to be the most intense. Although all other samples were studied in this way, only sample I100A was found to produce a discernible emission spectrum, as seen in Figure 8.1.

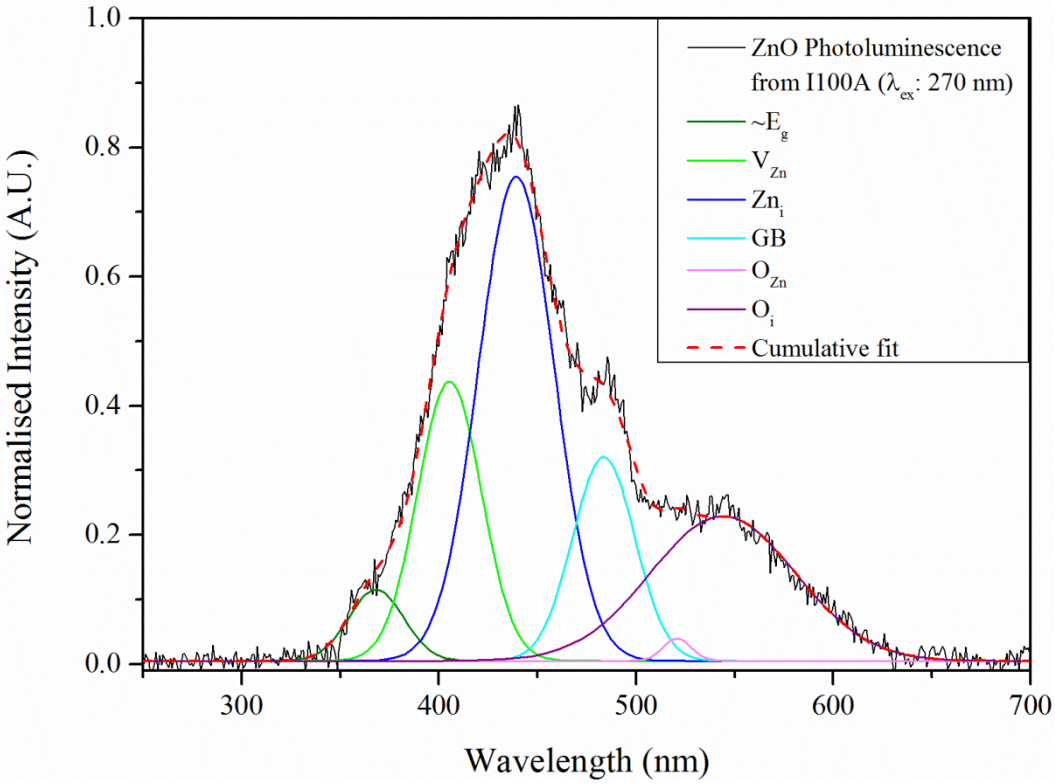

Figure 8.1. Deconvoluted photoluminescence spectrum of ZnO crystallites when excited (λ_{ex}) with 270nm monochomated light from a broadband μs flash-lamp. The labelled abbreviates are described in the text.

The spectral lineshape of Figure 8.1 is a deconvoluted depiction of transitions occurring from the ZnO conduction band edge to that of a series of characteristic defect states within the bandgap. The peak positions, full-width at half-maxima (FWHM) and integrated intensities of the sub-peaks in Figure 8.1 are provided in Table 8.3 and compared to literature. The definitions of the notation used to describe each sub-peak are as follows:

E_g – Near-band-edge transitions comprised of neutral donor-bound exciton emission (D°X) and donor-acceptor pairs (DAP). Factors influencing the position of this peak include Na-doping [240] and quantum confinement [103]

V_{Zn} – Zinc vacancies [241]

Zn_i – Interstitial zinc [241]

GB – Deep-level emission known as green band (GB) emission, believed to be due to oxygen vacancies [242]

O_{Zn} – Anti-site oxygen [241]

O_i – Interstitial oxygen [241]

Table 8.3. Table comparing the observed spectral features in Figure 8.1 from ZnO crystallites of I100A to that of literature

Peak ID	Peak position			FWHM		Normalised integrated intensity, A.U.
	Obs		Lit	Obs	Lit	
	nm	eV	eV	nm	nm	
~E_g	368.3	3.37	3.36 [241]	32.8	~10 [103,104]	0.28
V_{Zn}	405.4	3.06	3.06 [241]	37.9	~ 40 [243]	0.26
Zn_i	439.2	2.82	2.90 [241]	45.3	~100 [241]	1.00
GB	483.6	2.56	~2.5 [240,242]	37.2	~100 [244]	0.14
O_{Zn}	520.8	2.38	2.38 [241]	16.8	~100 [241]	0.55
O_i	544.0	2.28	2.28 [241]	86.8	~ 100 [241]	0.19

The data of Table 8.3 is compared to literature where possible. For the peak positions in which to observe the transitions within ZnO, there are ample references, however, for the FWHM it is non-existent. As a result, the FWHM values quoted stem from a visual interpretation of published ZnO emission spectrums. Note the transitions for Zn_i, GB, O_{Zn} and O_i are all listed as ~100 nm. This is because there is rarely a distinction in the spectra made between these peaks and thus no definitive value can be provided.

Table 8.3 conveys a reasonable agreement between the observed spectral features in Figure 8.1 of ZnO crystallites for I100A to those found in literature. These observations suggest a variety of defect states exist within the ZnO crystal lattice. Due to this sample being fabricated in an oxygen deprived environment, it is surprising that the intensity of the interstitial oxygen transitions is particularly high relative to other defect states. The observation of a green-band (GB) emission suggests there are also oxygen vacancies present. These contradictory observations

can be understood by comprehending the area in which this data is collected. The light focussed onto the surface of the sample can be estimated to have a spot size of hundreds of microns in diametre. This would encompass a variety of crystal formations, such as the microrods and platelets, as identified in chapter 6, where each may have differing concentrations of defect states. Although this cannot be quantified, it is supported by literature [241] and corresponds well with the conclusions of chapter 6 relating to the Na-concentration influencing the ZnO growth mechanics. The photoluminescence data published by Fang *et al* [241] is also a very close approximation of the data presented in Figure 8.1.

The increased FWHM of the ~E_g is attributed to the range in ZnO crystallite sizes observed in SEM images provided in section 6.3.2. The blue-shift of this peak is also attributed to the smaller ZnO particles, whereby the bandgap has expanded due to quantum confinement, resulting in shorter wavelengths of emitted photons [104]. Additionally, the degree to which the slits to the monochromator were open when acquiring this spectrum would of artificially added to this FWHM. Due to the minute ZnO quantity, the slits needed to be open rather wide in order to acquire a signal intensity.

It is acknowledged that ZnTe photoluminescence contributions to the spectrum in Figure 8.1 should be expected, however, a satisfactory fit with the corresponding spectral features (i.e. peaked at approximately 554 nm with a full-width at half-maxima (FWHM) of approximately 12 nm) could not be found. This may be due to insufficient excitation power from the monochomated flash-lamp to generate an observable fluorescence intensity from ZnTe. Alternatively, the sample this scan may simply be from a region of low ZnTe concentration.

8.4. ZnTe photoluminescence spectroscopy

Due to the applicability of the 488 nm Ar-ion laser line for the excitation of ZnTe, a considerably more refined photoluminescence (PL) spectrum can be acquired. The PL spectrum of ZnTe crystallites are presented in Figure 8.2 for (a) two areas of I100A and (b) D30-1 and D60-1.

The two areas of I100A were acquired by moving the sample laterally, without altering the position of the sample relative to the focal point of the laser. This ensures the laser remains focused on the surface of the sample. This can only

be achieved in one axis (side to side) due to the equipment available. In performing these lateral translations across the sample surface, the ZnTe PL intensity is found to vary continually; Figure 8.2 (a) is used to represent this. Without the ability to microscopically identify the area in which the 488 nm laser is focused upon, a correlation between surface features and underlying ZnTe cannot be accounted for, if any. These fluctuations are determined to be real due to attempts made to refine the focussing of the excitation source onto the sample surface.

No characteristic peak of ZnTe PL from D30-1 could be acquired. This could be attributed to a decreased concentration of ZnTe crystallites in the sample, thus emission may not be significant enough to be observed above the noise level of the detector. It could also be due to the particle sizes associated with this sample, which is expected to be much lower than D60-1. A reduction in particle size below ~10 nm would begin to induce quantum confinement upon the conduction and valence band states, thus increasing the bandgap. The 488 nm (2.58 eV) laser line is on the band edge of large (i.e. >10 nm) ZnTe crystallites, thus even a slight blue-shift in the excitation spectrum would be significant. This effect is clearly demonstrated by Jun *et al* [245] whereby blue-shifts of 0.50 and 1.0 eV were identified for particle sizes of 5.4 and 4.2 nm respectively. Thus if a significant yield of particles are below 10 nm exists in D30-1 and similar samples, very little excitation would occur using a 488 nm laser source.

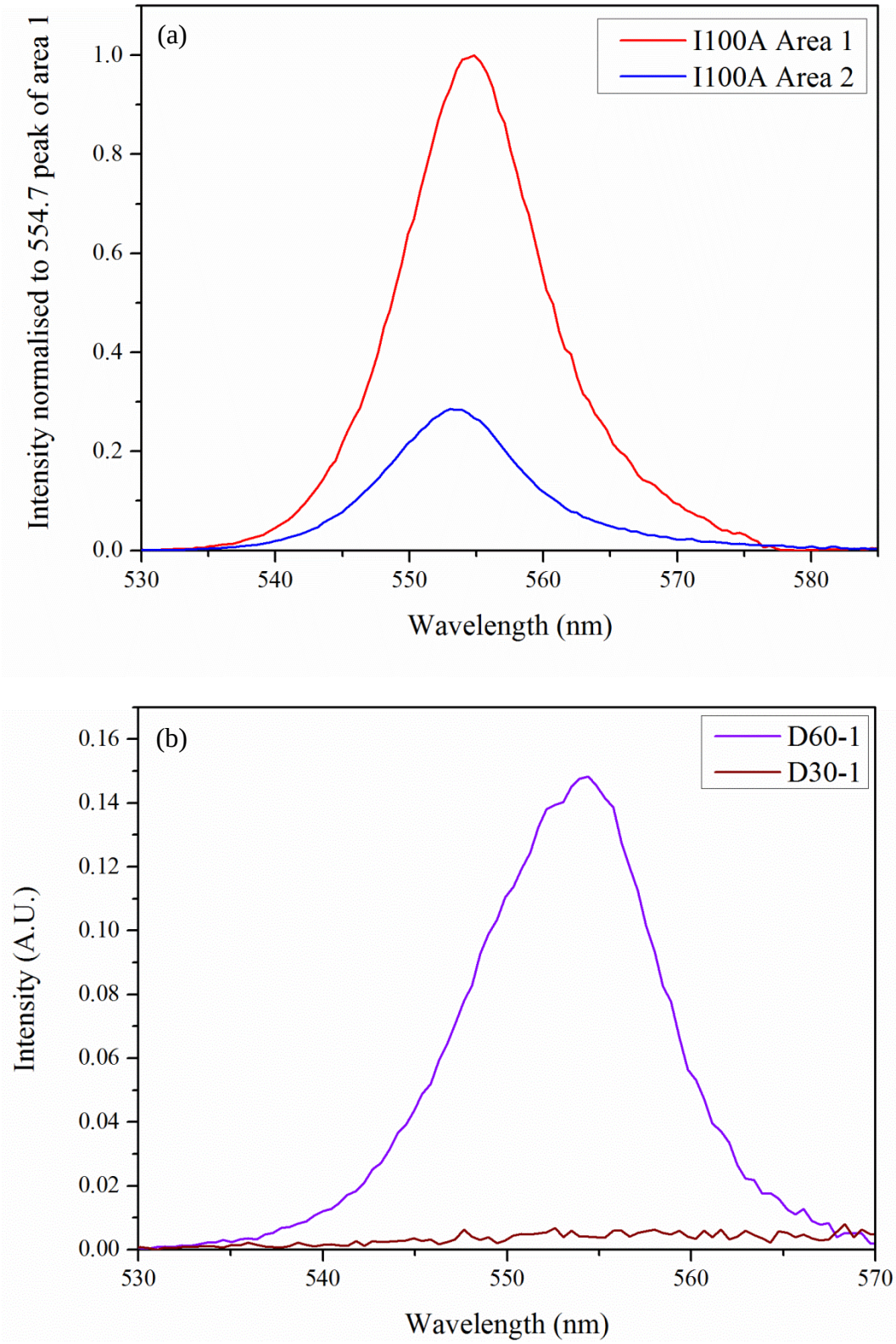

Figure 8.2. ZnTe photoluminescence spectroscopy when excited with 488 nm for (a) two areas of I100A, A1 and A2, (b) D30-1 and D60-1

The observed peak positions of ZnTe fluorescence from samples studied by Raman spectroscopy in earlier chapters have been compared to those found through conventional photoluminescence spectroscopy in Table 8.4. This is used to demonstrate the effectiveness of Raman spectroscopy in detecting both surface distributed and low concentrations of ZnTe compared to other techniques, but also for data comparison. The observed ZnTe fluorescence peak positions for each sample in Table 8.4 is found to be in good agreement with literature [246]. Furthermore, the observed peak fluorescence of all samples situated between 2.24 to 2.26 eV (554.7 to 548.8 nm) is in good agreement with the reported ZnTe bandgap at room temperature of 2.26 eV [247]. Note the slight blue-shift in the observed fluorescence from D30-1 and I50A. As noted earlier, if there are few ZnTe crystallites above 10 nm, the Ar-ion laser may not sufficiently excite the particles.

Table 8.4. Table comparing the peak emission wavelength from ZnTe recorded from Raman spectroscopy as well as conventional photoluminescence. Samples where emission could not be detected during photoluminescence spectroscopy are marked "–". Those where no fluorescence was detected by either method are discounted.

Sample ID	**Peak fluorescence from Raman spectroscopy (nm)**	**Peak fluorescence from PL (nm)**
I50H	550.6	-
I50A	548.6	-
I100A	552.8	554.7 / 553.4
D30-1	548.8	-
D60-1	550.0 / 553.1	554.2
Reference	-	550 [246]

8.5. Lanthanide optical characterisation

8.5.1. Tm^{3+}-doped TZN surface modified silicon materials

Prior to studying the photoluminescence of a lanthanide ion, it is prudent to acquire an excitation spectrum so as to ensure the pump source is optimised for the highest fluorescence intensity. Excitation spectra for I50H, I50A, I100A and I50X are thus provided in Figure 8.3. These excitations spectra have been power corrected to account for the change in laser power with adjustments in the emission wavelength of the Ti:Sapphire laser. The peak sample fluorescence intensity in Figure 8.3 at 1745 nm is found when excited with 789 nm for each sample.

For comparison to the surface modified samples, a fluorescence spectrum of the starting target glass G0 is provided in Figure 8.4. The distinctive inhomogeneous broadening is visible for the $^3F_4 \rightarrow {}^3H_6$ transition in Figure 8.4 due to the range of dipole environments in the glassy network. Note the $^3H_4 \rightarrow {}^3F_4$ transition is also visible in this spectrum peaked at 1.46 μm. The ratio of the relative peak intensity of the main $^3F_4 \rightarrow {}^3H_6$ (1.84 μm) decay to the $^3H_4 \rightarrow {}^3F_4$ transition is found to be 11.0. This indicates a high concentration of the Tm^{3+} dopant due to the larger tendency for ions to undergo cross-relaxation [248].

The fluorescence spectrums of I50H and I50A are compared in Figure 8.5 while those of I100A and I50X are provided in Figure 8.6. These two pairs are compared separately for reasons that will become clear later.

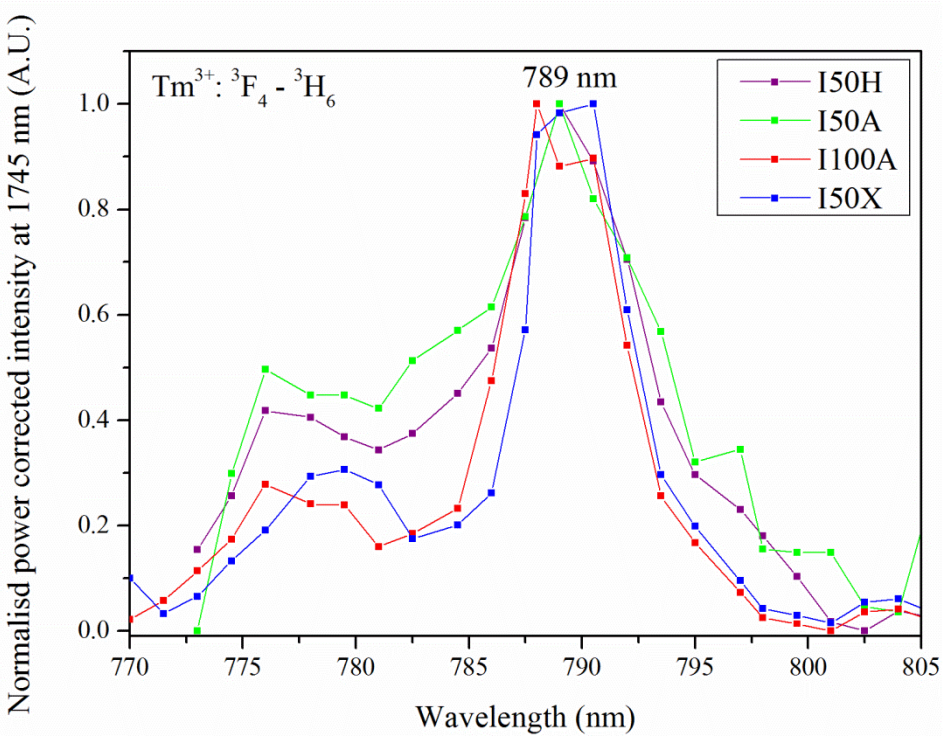

Figure 8.3. Tm^{3+} excitation spectrum surface modified samples I50H, I50A, I-9 and I50X

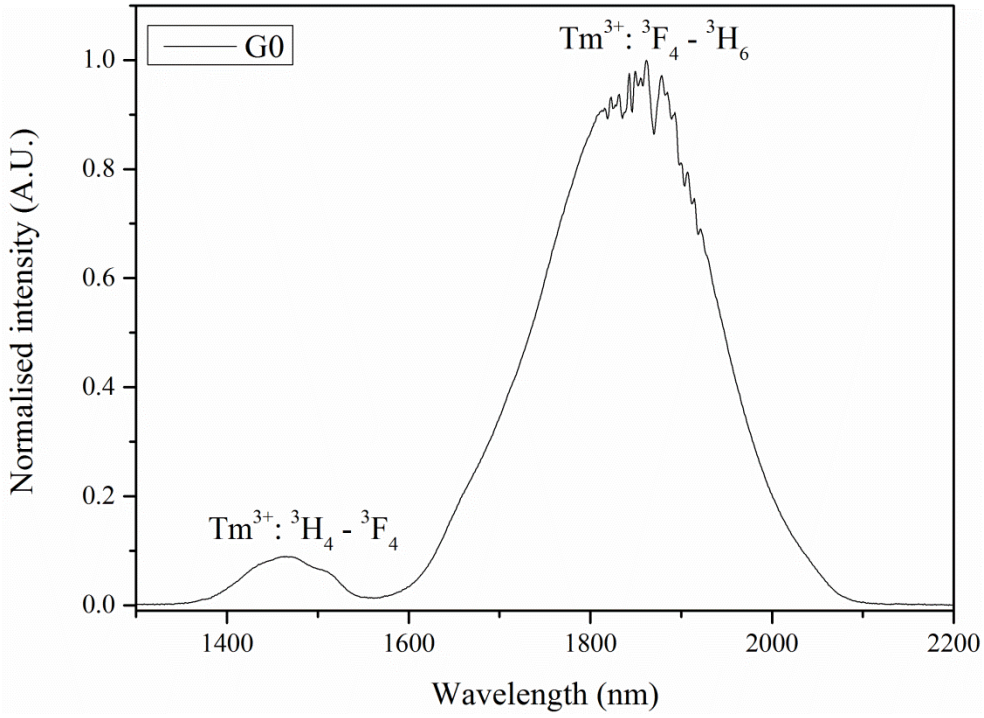

Figure 8.4. Fluorescence spectra of target glass material Tm^{3+}:TZN when excited with a 789 nm Ti:Sapphire laser source.

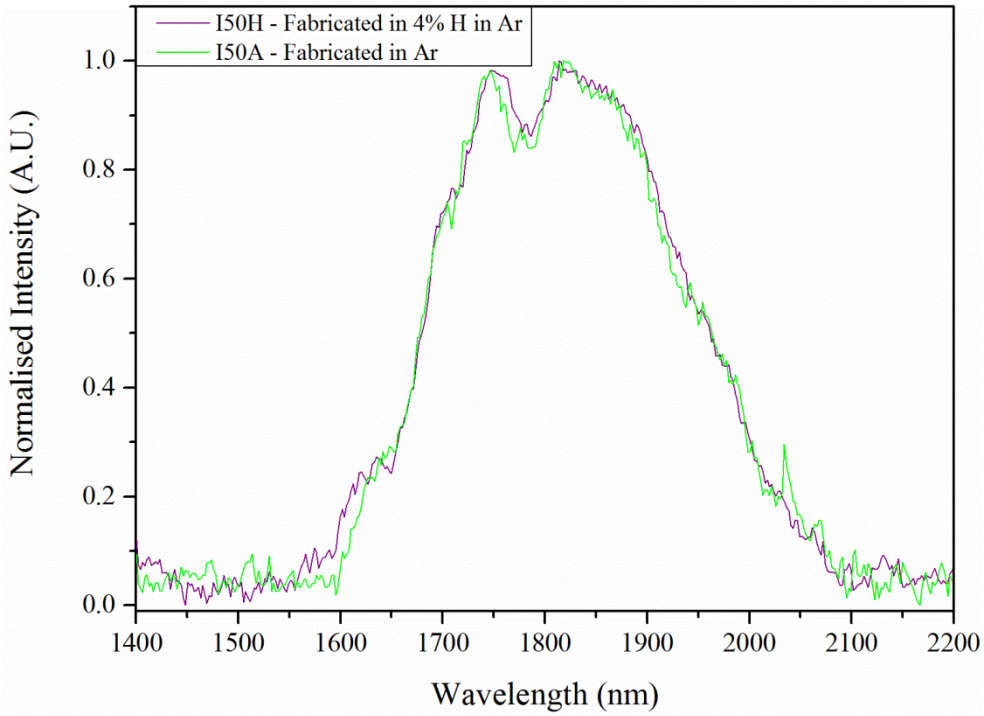

Figure 8.5. The combined normalised fluorescence spectra of I50H and I50A when excited by a 789 nm laser source

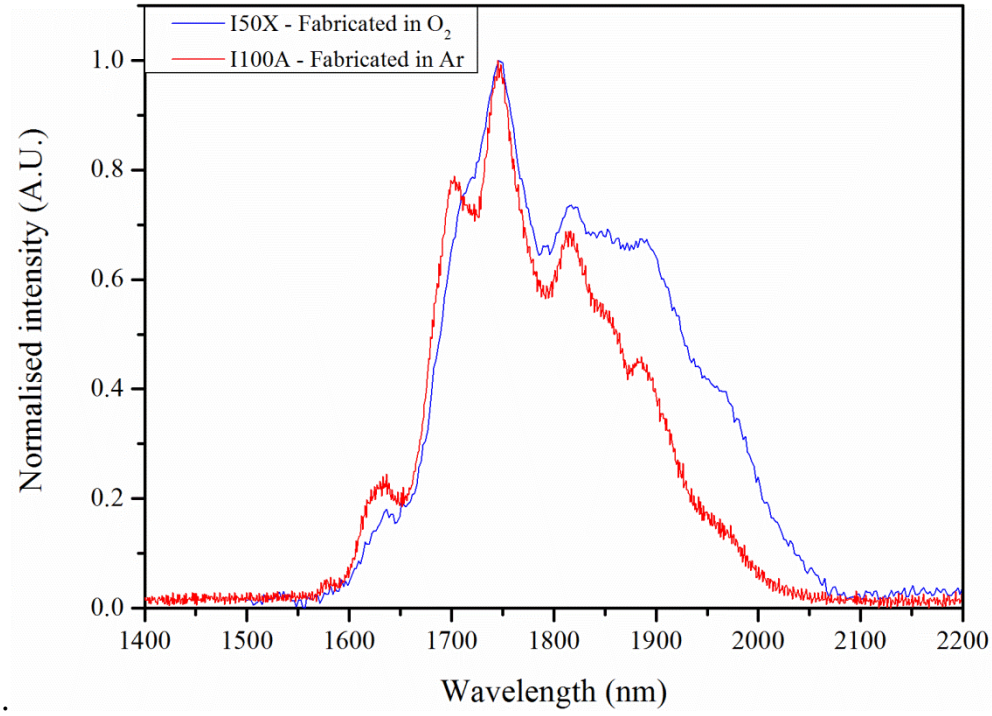

Figure 8.6. The combined normalised fluorescence spectra of I100A and I50X when excited by a 789 nm laser source

From all respective fluorescence spectra in Figure 8.5 and Figure 8.6, it is clear that the Tm^{3+}: $^3H_4$ to $^3F_4$ transition has been substantially quenched, so it is no longer visible. From the compositional analysis conducted in chapter 6 and 7, this can be reasoned in terms of the high Tm^{3+} concentration in the crystallites. EDX estimated this concentration to be approximately 8 at% for I100A and 10 at% for I50X. Such high concentrations suggest the lanthanide ions are very likely to be in close proximity. This significantly increases the probability that an excited Tm^{3+}-ion will decay from the $^3H_4$ manifold via the well-known cross-relaxation process Tm^{3+}: $^3H_6$, $^3H_4 \rightarrow {}^3F_4$, $^3F_4$ with a neighbouring Tm^{3+} ion in the ground state. This effect is most distinctive in Figure 8.6 due to the improved spectral resolution.

It would appear that in Figure 8.5 the spectral lineshape of both I50H and I50A are identical. This suggests there is no discernible difference in the generalized local crystalline environment for Tm^{3+}-ions these two samples. One can therefore deduce that the 4% hydrogen in the Ar atmosphere has a negligible effect on the crystal lattice of the Tm-rich silica crystallites so as to alter the crystal field acting upon the lanthanide dopant. If it had, this would be evident as differences in the fluorescence spectra. There is however a distinct different in the fluorescence lineshape of Figure 8.6 for sample I50X, fabricated at 50 μJ in O_2 and I100A, fabricated at 100 μJ in Ar. The FWHM for each respective fluorescence spectrum is provided in Table 8.5 to quantify this assertion.

Table 8.5. Table comparing the full-width at half-maxima (FWHM) for samples I50H, I50A, I100A and I50X for the Tm^{3+}: $^3F_4$ to $^3H_6$ transition, depicted in Figure 8.5 and Figure 8.6

Sample ID	**I50H**	**I50A**	**I100A**	**I50X**
FWHM, nm	284	284	181	236

The distinctive decrease in the FWHM for the sample I100A in Table 8.5 compared those fabricated with lower laser energies can be attributed the an increase in the crystallinity of the surface structures. This is also evidenced by the increased surface saturation with Tm-rich crystallites, whereby a more complete coverage was identified for I100A. The samples fabricated at 50 μJ by comparison are found to possess amorphous channels extending to the surface. Therefore it can be stated that the increase in the FWHM of Tm^{3+} emission is due to inhomogeneous broadening

due to an increased amorphous content in the materials. This has been confirmed during compositional analysis, such as in Figure 6.13 (a) for I100A.

It is interesting to note the distinguishable crystal-field splitting of the $^3F_4$ and ground state $^3H_6$-J multiplets of the Tm^{3+}-ion fluorescence for I100A. This can be seen in the distinctive spectral lines which form the observed fluorescence spectrum in Figure 8.6. For a more accurate determination of this splitting between the excited and ground J-level manifold, low temperature fluorescence spectroscopy was conducted for I100A. The fluorescence spectrum at 77 K for I100A is presented in Figure 8.7 while the discernible emission peak positions are provided in Table 8.6. A key observation to make with regard to the spectral features of Figure 8.7 is the distinctive shift in the emission band centre to longer wavelengths. This is due to the reduced thermal energy of the 4f electrons, thus causing them to occupy lower Stark levels within the $^3F_4$ and $^3H_6$ manifolds, effectively condensing them. This means Tm^{3+}-ions excited to the $^3F_4$ state are more likely to decay from a lower Stark level which is energetically closer to the $^3H_6$ ground state, thus the resulting photon emitted is of a longer wavelength.

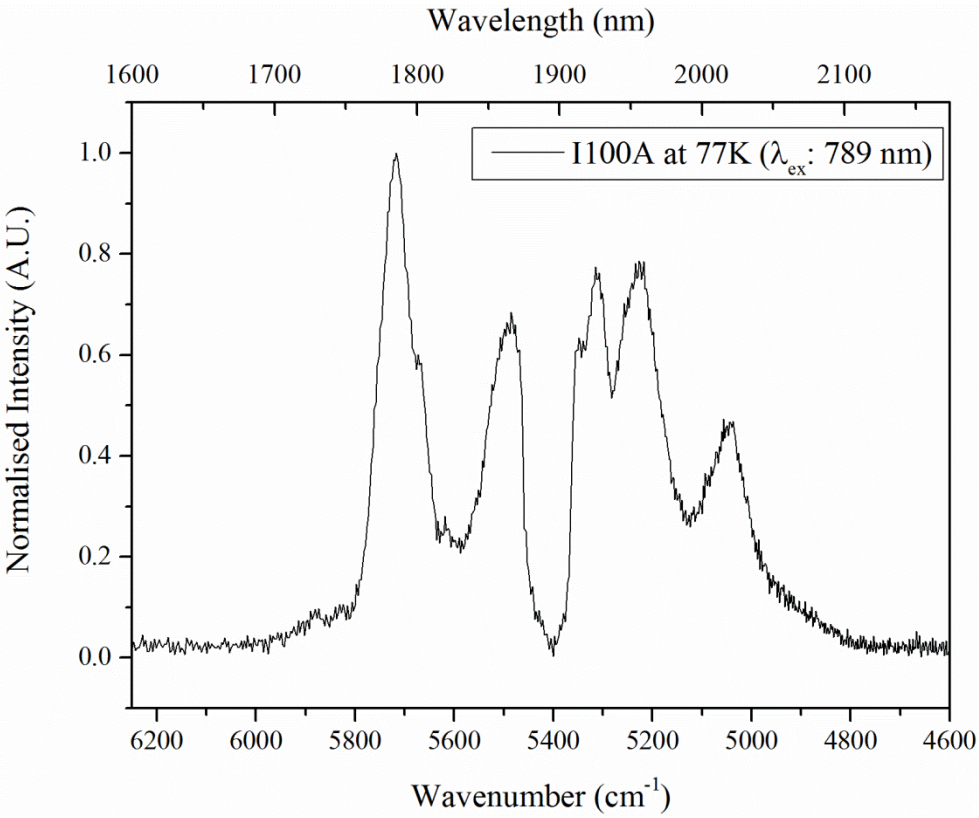

Figure 8.7. Low temperature fluorescence spectra for the $^3F_4$ to $^3H_6$ transition of Tm^{3+}-dopants in I100A when excited with 789 nm from a Ti:Sapphire laser.

Table 8.6. Table of main fluorescence peaks from the spectrum in Figure 8.7

Peak emission	
nm	**cm^{-1}**
1749	5717
1823	5486
1883	5311
1913	5235
1982	5052

It is now convenient to note the distinct similarities in the spectral lineshape between that observed for all samples and that observed for isomorphs of the trigonal $LiNbO_3$ crystal system, whereby Tm^{3+}-ions are found in sites with C_3 symmetry [71,249,250]. Distinctive similarities between the spectral lineshape of

the Tm^{3+}: $^3F_4$ to $^3H_6$ transition in a $LiTaO_3$ crystal, as seen in figure 5 of reference [71] in relation to the fluorescence spectra for I50H and I50A are noted. The similarities to this crystal-symmetry system for Tm^{3+}-ion fluorescence is perhaps most distinguishable in Figure 2 (b) of reference [70] in relation to I100A at room temperature. Note that the authors of reference [70] have incorrectly labelled the emission spectrum in the aforementioned figure, it should read '$^3F_4 \rightarrow {}^3H_6$'. This work also demonstrates a distinctive rise in the fluorescence intensity associated with the $^3F_4 \rightarrow {}^3H_6$ transition with increasing Tm^{3+}-dopant concentration. Unfortunately, no reason was provided in either publication as the difference in the spectral lineshape which is mimicked by Figure 8.5 and Figure 8.6. The former however lists the positions of the various stark levels which have been theoretically calculated for Tm^{3+}-ions in a site with C_3 symmetry. These have been reproduced in Table 8.7 for comparison to the current system.

Table 8.7. Table of the Tm^{3+} Stark energy levels theoretically expected for C_3 symmetry for the $^3F_4$ and $^3H_6$ manifolds as well as the overall splitting expected for each level. This table has been reproduced from that provided in Table 1 of reference [71] for Tm^{3+}: $LiTaO_3$

Multiplet	**Energy of Stark levels (cm^{-1})**	**Overall Splitting (cm^{-1})**
$^3F_4$	5678, 5689, 5708, 5927, 5985, 6026	348
$^3H_6$	0, 57, 115, 270, 365, 431, 530, 620	620

As noted earlier, due to the lack of absorption data, it is not possible to accurately determine the Stark levels of the various manifolds of the Tm^{3+}-dopants for this system. Additionally, this precludes the use of conventional Judd-Offelt calculations [251] for other fundamental phenomena related to lanthanide optical spectroscopy [252]. These limitations can, to a certain extent, be overcome by the application of the Stark levels derived from crystal field parameters described in Table 8.7 to the present spectroscopy data. The crystal field splitting for an induced electric dipole transition [253] such as Tm^{3+}:$^3F_4 \rightarrow {}^3H_6$ is often found to be somewhat consistent for different hosts, provided the site symmetry is identical. This is due to the filled 5s and 5p shells shielding of the 4f electrons from the local environment. This is noted in the earlier examples of $LiTaO_3$ and $LiNbO_3$. Note, however, that the C_3 point-symmetry has also been identified as one in which

pseudo-quadrupolar transitions, more commonly known as hypersensitive transitions, are possible [68]. For such transitions, the relative intensity compared to others may therefore be enhanced by up to a factor of 200 [254]. This principle is expressed by Tikhomirov *et al* [255] for Pr^{3+}-dopants in a variety of fluoride glasses. As alluded to in the work by Tikhomirov *et al*, the susceptibility of a hypersensitive transition to the encompassing ligands can be used as a probe for the lanthanides immediate elemental environment. The influencing factors identified from ligands have been identified as the coordination number, charge and the covalency. Based upon these considerations and the distinctive match between the aforementioned fluorescence spectra and the present work, one can deduce that the coordinating ligand is likely oxygen. If the ligand were Te, Na, Zn or Si, one would expect more distinctive differences in the spectral intensities of the transitions between Stark energy levels. The possibility of oxygen ligands is also supported by previous thermochemical calculations where Tm_2O_3 was found to be stable in all conceived scenarios, thus implying it remains as an oxide throughout the fabrication.

In order to assess the precise origin of the distinctive peaks noted in Table 8.6, a simple matrix calculation (not presented here) [66] was carried out of the Stark levels of the $^3F_4$ manifold against the $^3H_6$ ground state given in Table 8.7. The calculated transitions which best match the observed transitions of Table 8.6 is given in Table 8.8. It is important to note that the fluorescence spectrum in Figure 8.7 at 77 K still has contributions from other minor sub-peaks which cannot be accounted for by simple deconvolution. This is because it is not yet known if the Tm^{3+} ions occupy other sites of different point-symmetry which would in turn produce a different fluorescence spectrum. The results of Table 8.8 are therefore offered as a comparative test based upon the qualitative match to that of C_3-site Tm^{3+} fluorescence.

Table 8.8. Table comparing the main peaks described in Table 8.6 to the Stark energy levels most likely to be their origin.

Peak emission (cm^{-1})	**$^3F_4$ Stark level (cm^{-1})**	**$^3H_6$ Stark level (cm^{-1})**	**Calculated transition (cm^{-1})**	**Difference, (cm^{-1})**
5717	5985	270	5715	2 cm^{-1}
5486	5927	431	5496	10 cm^{-1}
	6026	530	5496	10 cm^{-1}
5311	5678	365	5313	2 cm^{-1}
5235	5678	431	5247	21 cm^{-1}
5052	5678	620	5058	6 cm^{-1}

Table 8.8 demonstrates a good agreement between the observed peak positions and those calculated for different Stark energy levels for respective manifolds of Tm^{3+} in a site with C_3 symmetry. With regard to the two possible routes of decay for the observed 5486 cm^{-1} peak, it is reasonable to assume that this transition is occurring from the 5927 cm^{-1} Stark level. This is because at lower temperatures, these lower levels will be more populated and thus transitions occurring from there would be more likely. The calculated mismatch between the observed emission peak at 5235 cm^{-1} and the calculated emission peak is attributed to contributions from unknown sub-peaks to the spectral lineshape. Note that this difference amounts to 4.5 nm.

The spectroscopy discussed thus far has conveyed compelling evidence for a crystal system where Tm^{3+}-dopants occupy a site with C_3 point-symmetry. This of course creates a complication, in that the only trigonal crystal phase of silica is α-Quartz which does not have a C_3 site available. Er^{3+}-doped silica for example can occupy one of 3 different point symmetries, including O_h, C_{3v} and C_{4v} [78]. The short range order of glassy silica can be considered to house all possible point-symmetries for lanthanide sites. This can therefore be applied to all unmodified variations of crystalline silica which suggests that the crystalline structure is not simply silica, but in fact a modified variant. The modification is likely caused by the identified inclusion of Na, observed through point EDX measurements.

Although the Te doping was identified through EDX mapping, the trace concentration calculated by point EDX analysis indicates its role in the modification of the crystal structure to be at most minor.

Although this does not offer a conclusive argument for the local structural environment of the Tm^{3+}-ions, it demonstrates compelling evidence for both the site symmetry and coordinating ligands in good agreement with literature. Such understanding can thus be incorporated into future deductions of the precise crystallography of the Tm-rich crystallites through more conventional means.

8.5.2. Er^{3+}-doped TZN surface modified silicon materials

An Er^{3+}-doped sample, named E50A, was also produced to demonstrate the applicability of this technique for use with other optically active lanthanide ions. Although all lanthanides are chemically very similar, as well as chemically inert in many ways, it is worthwhile demonstrating the similarities to the Tm^{3+}-doped sample discussed thus far. Raman spectroscopy of E50A is presented in Figure 8.8, where the phonon modes of ZnTe, Te and the well-known Si modes are marked and visible.

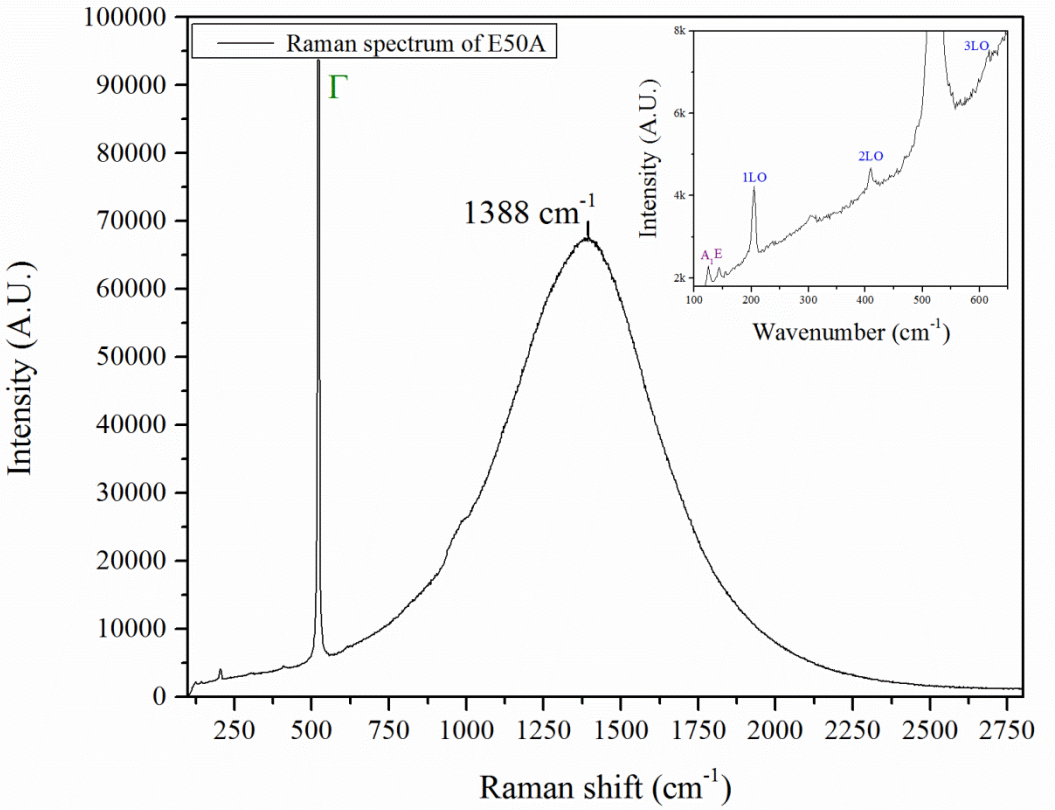

Figure 8.8. Raman spectroscopy of sample E50A with the peak position of the ZnTe fluorescence marked at 1388 cm^{-1}. The inset shows the A_1 and E modes of hexagonal Te in purple, the 1LO and 2LO modes of ZnTe in blue and the zero-centre one-phonon line (Γ) of Si in green

The Raman spectrum in Figure 8.8 is found to be in good agreement with the results of previous chapters as well as the ZnTe fluorescence (553.5 nm). The identification of the characteristic phonon modes for Te and ZnTe also confirm this.

The sample was also characterised by fluorescence spectroscopy using a 975 nm laser diode to excite the $^4I_{11/2}$ manifold of the Er^{3+}-dopants [256]. The observed fluorescence spectrum is provided in Figure 8.9 where the inset provides the decay profile of this transition. The fluorescence lifetime of this sample was measured to be 1.62 ms.

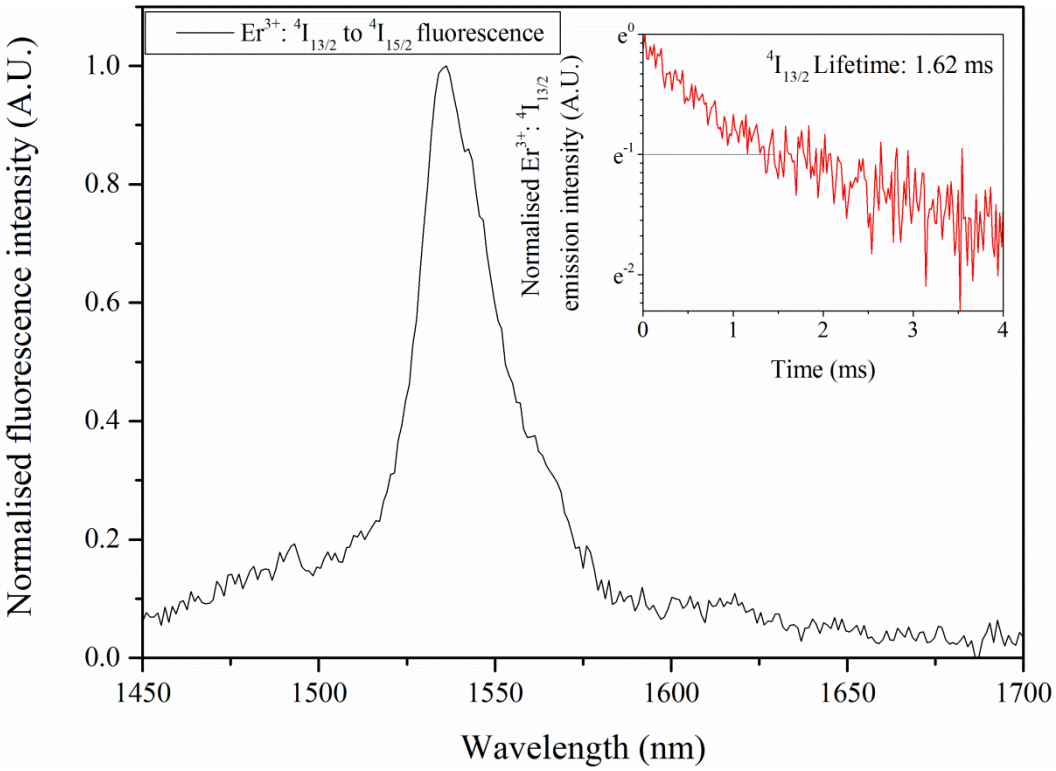

Figure 8.9. Fluorescence spectroscopy of Er^{3+}: $^4I_{13/2} \rightarrow {}^4I_{15/2}$ transition from sample E50A with an inset to show the radiative decay profile and lifetime.

The peak emission wavelength is found to be 1.54 μm and thus matches the well-known Er^{3+}: $^4I_{13/2} \rightarrow {}^4I_{11/2}$ transition [237]. Lidgard *et al* [257] has identified a lifetime of 1.6 ms for Er^{3+}-doped silica glass when Er^{3+}-ions are in high concentrations. This of course would vary for a crystalline equivalent, should it be able to crystallise. Recall that high concentrations of Tm^{3+}-dopants in I50X, fabricated under similar conditions, were identified in Table 7.6. High lanthanide concentrations are known to decrease the fluorescence lifetime of a given transition. This can be due to many reasons, such as clustering [258] or energy transfer processes to the host material [84].

Due to an imprecise understanding of the host material and therefore the quenching effects on the optical characteristics of the lanthanide ions, comparisons to literature become difficult. The known effect of concentration quenching on the optical characteristics of lanthanides already discussed is likely contributing to the observed results. This strongly suggests [259] that with a lower rare earth concentration, both the fluorescence intensity as well as the lifetime of these transitions can be significantly improved. 1.62 ms is however quite reasonable in

comparison to other host materials, particularly other crystallites. A selection of host materials and the associated lifetimes of the Er^{3+}: $^4I_{13/2} \rightarrow {}^4I_{15/2}$ fluorescence lifetimes are provided in Table 8.9 for comparison to the current observations.

Table 8.9. Table comparing the fluorescence lifetimes of Er^{3+}: $^4I_{13/2} \rightarrow {}^4I_{15/2}$ transitions in a variety of hosts

Host material	**$^4I_{13/2} \rightarrow {}^4I_{15/2}$ fluorescence lifetime, ms**	**Reference**
E50A	1.6	-
Silica	12.0	[259]
GaN	3.0	[260]
YAG	7.2	[261]
YSGG	3.4	[261]
GGG	4.9	[261]
Sodium tellurite glass	5.5	[184]

8.6. Conclusion

Photoluminescence spectroscopy has been used to characterise emission from ZnO, ZnTe, Er^{3+} and Tm^{3+}. The analysis of this data has also aided in understanding the nature of the associated crystallographic structure.

ZnO photoluminescence is observed when excited with 270 nm monochromated light from a broadband white light source. The deconvolution of this fluorescence reveals the existence of multiple defect states in the crystal lattice. These defect-related transitions are found to be in reasonable agreement with literature and have been used to further describe the nature of the ZnO crystal structure.

ZnTe photoluminescence is also observed when excited with the 488 nm Ar-ion laser line. The peak emission wavelength ranges from 548.6 to 554.8 nm and is in good agreement with observations reported in literature. Considerably lower intensities were identified for some samples however, for example D30-1, in relation to previous observations with Raman spectroscopy. This is reasoned by the higher collection rate of Raman spectroscopy as well as the identified surface fluctuations in ZnTe fluorescence.

The spectroscopic lineshape of Tm^{3+}-ion fluorescence is linked to the crystal-field splitting induced by C_3 site-symmetry. Possible decay pathways between Stark levels for the dominant peaks of the PL spectrum for the Tm^{3+}:$^3F_4 \rightarrow {}^3H_6$ transition are provided in relation to C_3 site-symmetry. The hypersensitive nature of this transition has been used to infer the most likely ligands coordinating the Tm^{3+}-ions which are determined to be oxygen. C_3 sites do not occur in crystalline silica hosts, thus the crystallite is determined to be a modified variant, likely due to sodium or possibly tellurium within the lattice.

Photoluminescence spectroscopy of the Er^{3+}:$^4I_{13/2} \rightarrow {}^4I_{15/2}$ decay in TZN surface modified silicon has been provided. The lifetime of this transition is found to be 1.6 ms and comparably shorter than in other hosts. This is attributed to concentration quenching, based on the compositional analysis of Tm^{3+}-dopants. If the concentration of lanthanide dopants could be controlled, it may be possible to dramatically improve the optical characteristics presented in this chapter.

Chapter 9.
Conclusions and for future work

The aims of this research have included an investigation into the deposition of rare earth doped silicon for optical and optoelectronic applications. Additionally, the exploration of the interaction of a femtosecond pulsed laser generated plasma phase with a given substrate material. The plasma-substrate interaction is often overlooked in femtosecond pulsed laser deposition (fs-PLD) literature. Furthermore, it was of great interest to determine if this interaction could be utilised for novel fabrication processes, but also to understand the mechanism of its action.

With these aims in mind, this chapter therefore provides a conclusion to the results achieved throughout this research project.

The deposition of silicon thin films upon inexpensive silica substrates provided a useful insight into the fs-PLD fabrication process. Raman spectroscopy identified the materials to be predominantly amorphous across a range of temperatures and experimental parameters. This identified a significant barrier in that the engineering of these materials to achieve efficient electrical devices was questionable. Fs-PLD of silicon p- and n-type silicon upon FTO coatings, topped with Al electrodes reaffirmed these doubts, where no electrical activity was observed. For this reason, the concept of directly depositing silicon upon thin conducting layers was abandoned. The principle reason for this, as shall be elaborated shortly, is the subplantation of the initial layers which destroy the conductive layer. Subplantation involves shallow implantation of the high energy plasma material. Although negligible in regular deposition, upon a thin conductive layer it proved catastrophic.

Silicon photonics remains a highly attractive focus of industry and thus the concept of an all-fs-laser processed photonic structure was challeneged. This began with the fabrication of rare earth doped silicon thin films, where fluorescence from Tm^{3+}: $^3F_4 \rightarrow {}^3H_6$ and Er^{3+}: $^4I_{13/2} \rightarrow {}^4I_{15/2}$ was demonstrated. Peak emission from Tm^{3+}-ions of 2.04 μm at room temperature was found to be significantly red-shifted relative to that reported in literature. Moreover a significant temperature dependency was observed for this transition, whereby the low temperature

photoluminescence more closely resembled that of Tm^{3+}-ion emission. At temperatures approaching ambient a broadband emission was observed to dominate with an associated fluoresce lifetime similar to that of the low temperature measurements.

These films, having demonstrated their emission characteristics, were then utilised for fs-laser processing for form integrated silicon photonic devices. This stage began with the fabrication of waveguide structures upon the rare earth doped silicon thin films. Attempts to optimised the waveguides to achieve a smooth side-wall finish, in order to minimie losses from the propagating light were therefore made. The optimum machining parameters were identified as a double pass of 1 μJ of laser energy with a translation speed of 2 mm/s to fabricate the channels. Although this was found to produce relatively smooth side walls, the waveguides themselves were found to be much too porous with rough surfaces, resulting in considerable losses in light propagation. For this reason, until the thin films can be produced to a very smooth surface finish, all-fs-laser waveguide production is not competitive with current alternatives.

As a considerable degree of research had been attempted previously to produce Er^{3+} doped silicon for photonic applications, comparison to such research was of great interest. The Er^{3+}-ion emission characteristics were found to closely resemble that reported in literature due to the dominant magnetic dipole character of this transition. This makes this transition particularly insensitive to the local environment. The rare earth ions were thus deduced to be within amorphous silicon particles. Alternative and more established fabrication methods however have demonstrated similar results, thus reducing the impact of such observations. The inability to form nanocrystallites directly via ultrafast laser ablation again limits the applicability of this technique for the fabrication of rare earth doped silicon materials.

The knowledge gained from the aforementioned investigation, particularly the photovoltaic study, led to the proposition that the interaction of the femtosecond laser generated plasma plume may be significantly altering the upper layer of the substrate. Thus a means to test this was established. Thermochemical calculations identified TZN glass (TeO_2, ZnO, Na_2O – 80:10:10 mol%) doped with a lanthanide ion could lead to an intriguing array of possible semiconductor and novel materials.

This form of fabrication had not been investigated before and was therefore of great interest as only minor developments have been made to describe the deposition process of fs-laser generated plasma.

It was found that by depositing the TZN glass onto a 570 °C heated silicon substrate considerable surface modifications would ensue. Following only 30 minutes of ablation, a silica layer is found to form through the reduction of the oxides in the plasma phase. The expansion of this SiO_2 layer is found to follow the calculated rate of diffusion for oxygen in silicon. In addition to this oxide layer expansions, it is found that the diffusion of some of the plasma constituents is now occurring. Although the diffusion of Na is expected to occur rapidly in SiO_2, Zn and Te also appear to diffuse. This is identified through the formation of ZnTe and Te crystallites. These crystallites are believed to form due to the diffusion of the oxide forms into SiO_2, where they are reduced by silicon dangling bonds. As this process continues, the Zn and Te cluster, crystallise and grow. Additionally, it is found that ZnTe is more stable under the experimental conditions and is more likely to form than isolated Te or Zn following a reduction reaction. Upon the surface of these substrates, unusual torroid structures are found to of formed which are clearly visible with an optical microscope and have an apparent depth profile.

As the experiment continues to 1 hour, the ZnTe crystallites are found to of increased in size and ZnTe florescence is now easily observable following 488 nm laser excitation. The oxide layer is also found to of expanded, in accordance with the calculated diffusion depth. The surface material of the substrate has now begun to coalesce, where disk-like particles are present. These disks are found to follow a log-normal size distribution, indicative of growth by coalescence. As these features are found to match similar experiments with TeO_2 powder targets, fabricated under identical conditions, it is reasoned they are composed of Te.

At 4 hour fabrication times, it is found that significant evolution of the surface layer has occurred. The ZnTe crystallites are found to of grown considerably in size yet still occupy a sedimentary layer below the surface. When fabricated in a dilute oxygen atmosphere however, no ZnTe is observed in the samples and instead Te crystallites are found to occur. Whether fabricated in O_2, Ar, or a 4%H in Ar gas mixture, there is significant crystallisation of a rare earth silicate. This crystallite is found to have rare earth concentrations of 10 at% or

more, which is considerably higher than the solubility of rare earths in bulk silica glass. The crystal structure however has remained somewhat elusive, where no XRD pattern is found to match it. Curiously, a very close match is identified for the stark level splitting of the Tm^{3+} emission from these crystallites to that of C_3 site symmetry. This is done through a novel approach to determining the local crystal field splitting as standard Judd-Offelt calculations are not possible due to the dominant Si absorption. These rare earth crystallites are found to occur in abundance across the entirety of the substrate surface.

Atop the rare earth silica crystallites are found ZnO crystallites of a wide range of shapes and sizes. The ZnO crystallites are found to form when a sufficiently thick oxide layer has formed, and thus silicon no longer reduces the ZnO on such a scale as at shorter times. These ZnO crystallites are found to have a certain sensitivity to the fabrication parameters. Through measuring the relative height of certain ZnO related XRD peaks, it was possible to determine the degree of alignment the crystallites possessed relative to the substrate face. When fabricated in at lower (50 μJ) laser energies, the ZnO crystallites grew with a preferential orientation of the c-axis directed away from the substrate surface. When fabricated at higher (100 μJ), this was found to be more randomly orientated. A similar effect was observed for fabricating in different gasses, where greater orientation away from the substrate surface was found for Ar, then 4% H in Ar and most random in O_2. This effect occurs due to the manner in which the ZnO crystallites form.

When fabricated in Ar, it is reasoned that growth of ZnO proceeds as oxygen-limited. Thus one may deduce that Zn exists on the surface of the substrate *in situ* in a liquid phase. As the SiO_2 layer reaches a sufficient thickness, the oxidation of the Zn can then proceed through the reduction of TeO_2 from the plasma phase. This results in slow growing ZnO from molten pools. Beyond a critical size, growth occurs preferentially along the c-axis, and thus extends the crystallites as rod formations. These re-orientate due to gravity and thus provide a greater preferential orientation. When fabricated in O_2, the growth is Zn limited, and therefore the existence of molten Zn pools on the substrate surface is highly unlikely and therefore the crystallites form in far more random orientations. A reasonable explanation for the effect of laser energy could not be clearly established.

The ZnO crystallites were found to have extensive defect related transitions in the visible regions. This meant that in a singular fabrication step, the formation of a depth separated ZnO, unknown rare earth silica crystallites and embedded ZnTe had been fabricated. This has tremendous applications in optics and optoelectronics if it can be more effectively guided. More importantly, relative to this the aims of this thesis, it indicates a significant diversion from conventional PLD.

Although much of the distribution of the ZnTe and ZnO appear to clustered laterally, it may be possible to create a more uniform distribution across the surface. This may be guided by greater experimentation with the pressure, which was not altered for the surface modification samples. This shall be addressed in full in the subsequent section.

Although fs-PLD was found to be a poor competitor to other fabrication techniques for silicon photonic and optoelectronic devices, the fabrication technique in general has been greatly developed. Instead of a distinct separation of the substrate and deposited material, there is now a significant and complex chemical interaction occurring between the two which is evolving with time. Through further experimentation, this could be better understood and developed for the production of novel photonic devices. This represents a major development for fs-laser ablation techniques and may turn it into a much more competitive fabrication technique.

9.1. Recommendations for future work

Based upon the principle observations made, i.e. the surface modification of a crystalline material based upon initial thermochemical calculations and theoretical designs, it is possible to greatly expand this work. The recommendations of future work can be divided into three categories: (1) further study of the fundamental interactions involved in this technique, (2) the development of the work presented in this thesis and (3) the exploration of different target/substrate/gas combinations. These shall be addressed below.

(1) Certain theoretical questions still remain for the interaction of the plasma phase with a given substrate. Firstly, the degree of implantation and subplantation is not yet known. These may be major contributors to the

initiation and progression of the surface modification, thus requiring dedicated investigation. Planned experiments could not be carried out to achieve this in the current work due to the prolonged mechanical failures of the PLD system. Specifically, this included using a mask layer (such as gold sputtered atop the silicon substrate) to cover half a then depositing across the whole sample. This would allow one to observe if extensive chemical interactions were occurring between the gold and the depositing material, or if, for example, the oxidation was not allowed to continue and hence the diffusion stopped. This would enable one to observe if it is primarily implantation driven (penetrates the gold and diffuses anyway) or is diffusion driven (does not penetrate the gold layer).

(2) For the current work, a refinement of the growth mechanics for ZnO is required. The prospect of engineering them by control of the gas type and laser energy is enticing, yet the results are not yet competitive with that of alternate techniques. Investigations varying other parameters such as pressure, laser repetition rate and elevated temperatures would undoubtedly yield further dependencies. Through careful and meticulous control of these parameters, it may be possible to engineer their structure to a high degree. The distribution of the surface crystallites is not yet known, however the growth mechanics in O_2 suggests it may be possible to influence their distribution. Furthermore, the rare earth doped silica crystal structure still requires defining. This could be achieved through the application of Rietveld refinement and if extensive beam damage can be avoided, tilting the sample during SAED analysis and constructing a stereograph could also assist in this regard. A major development which was not able to be tested in this thesis however is varying the cool down rate at the end of the experiment. If the cooling rate was substantially increase, would the extensive crystallisation still occur? Would some metastable characteristics appear? There is a lot which could be learnt through this unexplored parameter.

(3) Fabrication of materials based upon the fundamental principles outlined in this work could be extrapolated to a variety of other combinations. The selection of the starting materials must be based the chemical interactions between reactants, i.e. the plasma phase, the substrate and the gas type. This

can lead to an initial estimate of the possible materials which may form, thus drastically reducing the length of time required to deduce what is forming. One example of this is the reduction of silica by aluminium. This could conceivably form alumina and isolated silicon. Under preferable fabrication temperatures and cooling rates, this may form silicon nanocrystallites embedded in sapphire. The evolution of the material surface with respect to time should be considered; surface modification with one target for a given period of time, then with a different target and so on can easily be achieved with fs-PLD, yet may become extremely complex.

List of References

1. E. G. Gamaly, Physics Reports **508**, 91 (2011).

2. S. Amoruso, C. Altucci, R. Bruzzese, C. de Lisio, N. Spinelli, R. Velotta, M. Vitiello, and X. Wang, Applied Physics A **79**, 1377 (2004).

3. S. Amoruso, R. Bruzzese, N. Spinelli, R. Velotta, M. Vitiello, and X. Wang, Europhysics Letters (EPL) **67**, 404 (2004).

4. S. Amoruso, R. Bruzzese, N. Spinelli, R. Velotta, M. Vitiello, X. Wang, G. Ausanio, V. Iannotti, and L. Lanotte, Applied Physics Letters **84**, 4502 (2004).

5. D. Perez and L. Lewis, Physical Review Letters **89**, 1 (2002).

6. B. N. Chichkov, C. Momma, S. Nolte, F. von Alvensleben, and a. Tünnermann, Applied Physics A: Materials Science & Processing **63**, 109 (1996).

7. E. G. Gamaly and A. V. Rode, Progress in Quantum Electronics **37**, 215 (2013).

8. E. G. Gamaly, a. V. Rode, B. Luther-Davies, and V. T. Tikhonchuk, Physics of Plasmas **9**, 949 (2002).

9. C. H. Crouch, J. E. Carey, J. M. Warrender, M. J. Aziz, E. Mazur, and F. Y. Génin, Applied Physics Letters **84**, 1850 (2004).

10. B. Stuart, M. Feit, S. Herman, A. Rubenchik, B. Shore, and M. Perry, Physical Review. B, Condensed Matter **53**, 1749 (1996).

11. M. A. Green and M. J. Keevers, Progress in Photovoltaics: Research and Applications **3**, 189 (1995).

12. A. Mouskeftaras, S. Guizard, N. Fedorov, and S. Klimentov, Applied Physics A **110**, 709 (2012).

13. E. Gamaly, A. Rode, and B. Luther-Davies, Journal of Applied Physics **85**, 4213 (1999).

14. N. G. Semaltianos, S. Logothetidis, W. Perrie, S. Romani, R. J. Potter, S. P. Edwardson, P. French, M. Sharp, G. Dearden, and K. G. Watkins, Journal of Nanoparticle Research **12**, 573 (2009).

15. T.-H. Her, R. J. Finlay, C. Wu, S. Deliwala, and E. Mazur, Applied Physics Letters **73**, 1673 (1998).

16. P. A. G. O'Hare, Journal of Physical and Chemical Reference Data **22**, 1455 (1993).

17. Z. Zhao, G. Jose, T. T. Fernandez, T. P. Comyn, M. Irannejad, P. Steenson, J. P. Harrington, M. Ward, N. Bamiedakis, R. V Penty, I. H. White, and A. Jha, Nanotechnology **23**, 225302 (2012).

18. G. Jose, D. P. Steenson, M. Irannejad, and A. Jha, 2009 11th International Conference on Transparent Optical Networks 1 (2009).

19. M. K. Kim, T. Takao, Y. Oki, and M. Maeda, Japanese Journal of Applied Physics **39**, 6277 (2000).

20. S. Noel, J. Hermann, and T. Itina, Applied Surface Science **253**, 6310 (2007).

21. W. Kautek and J. Krueger, in *Laser Materials Processing: Industrial and Microelectronics Applications*, edited by E. Beyer, M. Cantello, A. V. La Rocca, L. D. Laude, F. O. Olsen, and G. Sepold (1994), pp. 600–611.

22. Y. Hirayama, H. Yabe, and M. Obara, Journal of Applied Physics **89**, 2943 (2001).

23. H. Kumagai, K. Midorikawa, K. Toyoda, S. Nakamura, T. Okamoto, and M. Obara, Applied Physics Letters **65**, 1850 (1994).

24. A. A. Oraevsky, L. B. Da Silva, A. M. Rubenchik, M. D. Feit, M. E. Glinsky, M. D. Perry, B. M. Mammini, W. Small, and B. C. Stuart, IEEE Journal of Selected Topics in Quantum Electronics **2**, 801 (1996).

25. A. Vogel and V. Venugopalan, Chemical Reviews **103**, 577 (2003).

26. A. V. Bulgakov, I. Ozerov, and W. Marine, Thin Solid Films **453-454**, 557 (2004).

27. J. Perrière, C. Boulmer-Leborgne, R. Benzerga, and S. Tricot, Journal of Physics D: Applied Physics **40**, 7069 (2007).

28. E. G. Gamaly, N. R. Madsen, D. Golberg, and a. V. Rode, Physical Review B **80**, 184113 (2009).

29. N. G. Semaltianos, S. Logothetidis, W. Perrie, S. Romani, R. J. Potter, S. P. Edwardson, P. French, M. Sharp, G. Dearden, and K. G. Watkins, Journal of Nanoparticle Research **12**, 573 (2009).

30. R. Ayouchi, R. Schwarz, L. Melo, R. Ramalho, E. Alves, C. Marques, L. Santos, R. Almeida, and O. Conde, Applied Surface Science **255**, 5299 (2009).

31. T. E. Glover, Journal of the Optical Society of America B **20**, 125 (2003).

32. E. G. Gamaly, Journal of Applied Physics **95**, 2250 (2004).

33. J. Jia, M. Li, and C. V. Thompson, Applied Physics Letters **84**, 3205 (2004).

34. S. Amoruso, G. Ausanio, a C. Barone, R. Bruzzese, L. Gragnaniello, M. Vitiello, and X. Wang, Journal of Physics B: Atomic, Molecular and Optical Physics **38**, L329 (2005).

35. R. V Volkov, D. M. Golishnikov, V. M. Gordienko, M. S. Dzhidzhoev, I. M. Lachko, B. V Mar'in, P. M. Mikheev, A. B. Savel'ev, D. S. Uryupina, and A. A. Shashkov, Quantum Electronics **33**, 981 (2003).

36. S. Amoruso, R. Bruzzese, X. Wang, and J. Xia, Applied Physics Letters **92**, 041503 (2008).

37. M. Murray, G. Jose, B. Richards, and A. Jha, Nanoscale Research Letters **8**, 272 (2013).

38. C. C. Garcia, H. Lindner, A. von Bohlen, C. Vadla, and K. Niemax, Journal of Analytical Atomic Spectrometry **23**, 470 (2008).

39. E. Millon, O. Albert, J. C. Loulergue, J. Etchepare, D. Hulin, W. Seiler, and J. Perrière, Journal of Applied Physics **88**, 6937 (2000).

40. V. Iannotti, S. Amoruso, G. Ausanio, X. Wang, L. Lanotte, A. C. Barone, G. Margaris, K. N. Trohidou, and D. Fiorani, Physical Review B **83**, 214422 (2011).

41. S. Amoruso, S. Tuzi, D. K. Pallotti, C. Aruta, R. Bruzzese, F. Chiarella, R. Fittipaldi, S. Lettieri, P. Maddalena, A. Sambri, A. Vecchione, and X. Wang, Applied Surface Science **270**, 307 (2013).

42. N. Li, X. Ni, R. Hong, T. Donnelly, X. Wang, S. Amoruso, and C. Wang, in *International Symposium on Photoelectronic Detection and Imaging*, edited by X. Chen, Y. Wang, Z. Zhou, and Q. Wang (Beijing, China, 2009), pp. 738109–738109–8.

43. R. Eason, in *Wiley-Interscience*, edited by R. Eason, Illustrate (Wiley-Interscience, 2007), p. 191.

44. G. Fu, Y. Wang, L. Chu, Y. Zhou, W. Yu, L. Han, and Y. Peng, EPL (Europhysics Letters) **69**, 758 (2005).

45. F. Xiong, Y. Y. Wang, V. Leppert, and R. P. H. Chang, Journal of Materials Research **8**, 2265 (2011).

46. X. Xu and D. a. Willis, Journal of Heat Transfer **124**, 293 (2002).

47. R. Le Harzic, N. Huot, E. Audouard, C. Jonin, P. Laporte, S. Valette, a. Fraczkiewicz, and R. Fortunier, Applied Physics Letters **80**, 3886 (2002).

48. C. Liu, X. Mao, S. S. Mao, R. Greif, and R. E. Russo, Analytical Chemistry **77**, 6687 (2005).

49. Z. Zhang, P. a. VanRompay, J. a. Nees, and P. P. Pronko, Journal of Applied Physics **92**, 2867 (2002).

50. M. Nastasi and J. W. Mayer, *Ion Implantation and Synthesis of Materials* (Springer, 2007), p. 277.

51. J. Davies and J. Denhartog, Canadian Journal of … **45**, (1967).

52. R. G. Wilson, Radiation Effects **46**, 141 (1980).

53. D. H. Lee and J. W. Mayer, Proceedings of the IEEE **62**, 1241 (1974).

54. D. Eaglesham and J. Michel, Applied Physics … **58**, 2797 (1991).

55. J. F. Gibbons, Proceedings of the IEEE **60**, 1062 (1972).

56. a. G. Cullis, T. E. Seidel, and R. L. Meek, Journal of Applied Physics **49**, 5188 (1978).

57. H. Ennen, G. Pomrenke, and A. Axmann, Journal of Applied Physics **57**, 2182 (1985).

58. H. Yang, K. Hong, and S. Feofilov, Journal of … **84**, 139 (1999).

59. G. Blasse, A. Meijerink, and C. de M. Donegá, Journal of Alloys and … **225**, 24 (1995).

60. R. Nakata, N. Hashimoto, and K. Kawano, Japanese Journal of Applied Physics **35**, L90 (1996).

61. M. Zinkevich, Progress in Materials Science **52**, 597 (2007).

62. C. Gorller-Walrand and K. Binnemans, in *Handbook on the Physics and Chemistry of Rare Earth Elements* (1998), pp. 101–264.

63. J. Wang, E. Vogel, and E. Snitzer, Optical Materials **3**, (1994).

64. Y. Ding, S. Jiang, B.-C. Hwang, T. Luo, N. Peyghambarian, Y. Himei, T. Ito, and Y. Miura, Optical Materials **15**, 123 (2000).

65. K. Gatterer, G. Pucker, H. . Fritzer, and S. Arafa, Journal of Non-Crystalline Solids **176**, 237 (1994).

66. J. B. Gruber, W. F. Krupke, and J. M. Poindexter, The Journal of Chemical Physics **41**, 3363 (1964).

67. J. B. Gruber, R. M. Yow, A. S. Nijjar, C. C. Russell, D. K. Sardar, B. Zandi, A. Burger, and U. N. Roy, Journal of Applied Physics **100**, 043108 (2006).

68. B. R. Judd, The Journal of Chemical Physics **44**, 839 (1966).

69. S. Payne, L. Chase, L. Smith, W. Kway, and W. Kruple, … , IEEE Journal Of **28**, (1992).

70. M. Quintanilla, E. Cantelar, J. a. Sanz-García, G. Lifante, G. a. Torchia, and F. Cussó, Journal of Luminescence **128**, 927 (2008).

71. I. Sokólska, W. Ryba-Romanowski, S. Gołąb, M. Baba, M. Świrkowicz, and T. Łukasiewicz, Journal of Physics and Chemistry of Solids **61**, 1573 (2000).

72. X. Zou, Journal of Non-Crystalline Solids **195**, 113 (1996).

73. M. Lourenço, R. Gwilliam, and K. Homewood, Optics Letters **36**, 169 (2011).

74. C. Rudowicz and P. Gnutek, Physica B: Condensed Matter **405**, 113 (2010).

75. P. Kik, M. de Dood, K. Kikoin, and A. Polman, Applied Physics Letters **70**, 1721 (1997).

76. A. Taguchi and K. Takahei, Journal of Applied Physics **83**, 2800 (1998).

77. G. S. Pomrenke, E. Silkowski, J. E. Colon, D. J. Topp, Y. K. Yeo, and R. L. Hengehold, Journal of Applied Physics **71**, 1919 (1992).

78. A. J. Kenyon, Progress in Quantum Electronics **26**, 225 (2002).

79. A. J. Kenyon, P. F. Trwoga, M. Federighi, and C. W. Pitt, MRS Proceedings **358**, 117 (2011).

80. A. K. Srivastava, Y. Sun, J. L. Zyskind, and J. W. Sulhoff, IEEE Photonics Technology Letters **9**, 386 (1997).

81. A. Mori, Y. Ohishi, and S. Sudo, Electronics Letters **33**, 863 (1997).

82. F. Priolo, G. Franzò, S. Coffa, A. Polman, S. Libertino, R. Barklie, and D. Carey, Journal of Applied Physics **78**, 3874 (1995).

83. R. T. Wegh, A. Meijerink, and R.-J. Lamminmäki, Journal of Luminescence **87-89**, 1002 (2000).

84. N. Hamelin, P. Kik, J. Suyver, K. Kikoin, A. Polman, A. Schönecker, and F. Saris, Journal of Applied Physics **88**, 5381 (2000).

85. G. S. Pomrenke, E. Silkowski, J. E. Colon, D. J. Topp, Y. K. Yeo, and R. L. Hengehold, Journal of Applied Physics **71**, 1919 (1992).

86. T. Oestereich, C. Swiatkowski, and I. Broser, Applied Physics Letters **56**, 446 (1990).

87. a. Zanatta and F. Freire, Physical Review B **62**, 2016 (2000).

88. V. F. Masterov, F. S. Nasredinov, P. P. Seregin, V. K. Kudoyarova, A. N. Kuznetsov, and E. I. Terukov, Applied Physics Letters **72**, 728 (1998).

89. R. Newman, Journal of Physics: Condensed Matter **335**, (2000).

90. M. Green, Progress in Photovoltaics: Research And 183 (2009).

91. S. E. Cross, B. Innes, M. S. Roberts, T. Tsuzuki, T. A. Robertson, and P. McCormick, Skin Pharmacology and Physiology **20**, 148 (2007).

92. W. J. E. Beek, M. M. Wienk, and R. A. J. Janssen, Advanced Materials **16**, 1009 (2004).

93. Z. L. Wang and J. Song, Science (New York, N.Y.) **312**, 242 (2006).

94. X. W. Sun and H. S. Kwok, Journal of Applied Physics **86**, 408 (1999).

95. D. C. Look, D. C. Reynolds, J. W. Hemsky, R. L. Jones, and J. R. Sizelove, Applied Physics Letters **75**, 811 (1999).

96. Z. L. Wang, Journal of Physics: Condensed Matter **16**, R829 (2004).

97. Z. Fan and J. G. Lu, Journal of Nanoscience and Nanotechnology **5**, 1561 (2005).

98. S. Baruah and J. Dutta, Science and Technology of Advanced Materials **10**, 013001 (2009).

99. V. A. Coleman and C. Jagadish, in *Zinc Oxide Bulk, Thin Films and Nanostructures*, edited by C. Jagadish and S. Pearton (Elsevier Ltd, 2006), pp. 1–20.

100. C. G. Van de Walle, Physical Review Letters **85**, 1012 (2000).

101. S. S. Lin, H. P. He, Y. F. Lu, and Z. Z. Ye, Journal of Applied Physics **106**, 093508 (2009).

102. R. Wallace, a. P. Brown, R. Brydson, K. Wegner, and S. J. Milne, Journal of Materials Science **48**, 6393 (2013).

103. G. Kiliani, R. Schneider, D. Litvinov, D. Gerthsen, M. Fonin, R. Ulrich, A. Leitenstorfer, and R. Bratschitsch, Optics Express **19**, 1641 (2011).

104. J. Li, S. Srinivasan, G. N. He, J. Y. Kang, S. T. Wu, and F. a. Ponce, Journal of Crystal Growth **310**, 599 (2008).

105. X.-P. Shen, A.-H. Yuan, Y.-M. Hu, Y. Jiang, Z. Xu, and Z. Hu, Nanotechnology **16**, 2039 (2005).

106. J. Perrière, E. Millon, W. Seiler, C. Boulmer-Leborgne, V. Craciun, O. Albert, J. C. Loulergue, and J. Etchepare, Journal of Applied Physics **91**, 690 (2002).

107. K. Patel, G. Solanki, J. Gandhi, and S. Patel, Chalcogenide Letters **6**, 393 (2009).

108. D. I. Kennedy, Journal of Applied Physics **38**, 4387 (1967).

109. K. Sato, M. Hanafusa, and A. Noda, Journal of Crystal … **215**, 1080 (2000).

110. G. Karczewski, S. Maćkowski, M. Kutrowski, T. Wojtowicz, and J. Kossut, Applied Physics Letters **74**, 3011 (1999).

111. J. Schrier, D. O. Demchenko, L.-W. Wang, and A. P. Alivisatos, Nano Letters **7**, 2377 (2007).

112. P. C. M. Planken, H.-K. Nienhuys, H. J. Bakker, and T. Wenckebach, Journal of the Optical Society of America B **18**, 313 (2001).

113. M. S. Rogers, C. P. Grigoropoulos, A. M. Minor, and S. S. Mao, Applied Physics Letters **94**, 011111 (2009).

114. W. B. Bridges, Applied Physics Letters **4**, 128 (1964).

115. J. Tauc and a Menth, Journal of Non-Crystalline Solids **8-10**, 569 (1972).

116. P. Scherrer, Nachrichten von Der Gesellschaft Der Wissenschaften Zu Göttingen, Mathematisch-Physikalische Klasse **1918**, 98 (1918).

117. J. I. Langford and A. J. C. Wilson, Journal of Applied Crystallography **11**, 102 (1978).

118. U. Holzwarth and N. Gibson, Nature Nanotechnology **6**, 534 (2011).

119. G. E. Lloyd, Mineralogical Magazine **51**, 3 (1987).

120. F. Arnal, P. Verdier, and P. Vincensini, Compt Rend Acad Sci **268**, 1526 (1969).

121. T. Tabata, R. Ito, and S. Okabe, Nuclear Instruments and Methods **94**, 509 (1971).

122. P. G. T. Howell, K. M. W. Davy, and A. Boyde, Scanning **20**, 35 (2006).

123. R. Castaing, Advances in Electronics and Electron Physics **13**, 317 (1960).

124. E. Terukov, V. Kudoyarova, a Kuznetsov, K. Koughia, G. Weiser, and H. Kuehne, Materials Science and Engineering B **81**, 161 (2001).

125. S. Eliezer, N. Eliaz, E. Grossman, D. Fisher, I. Gouzman, Z. Henis, S. Pecker, Y. Horovitz, M. Fraenkel, S. Maman, and Y. Lereah, Physical Review B **69**, 1 (2004).

126. S. Takajo, W. A. Kaysser, and G. Petzow, Acta Metallurgica **32**, 107 (1984).

127. J. Söderlund, L. Kiss, G. Niklasson, and C. Granqvist, Physical Review Letters **80**, 2386 (1998).

128. C. G. Granqvist and R. A. Buhrman, Solid State Communications **18**, 123 (1976).

129. D. Perez and L. Lewis, Physical Review B **67**, 1 (2003).

130. V. Margetic, T. Ban, F. Leis, K. Niemax, and R. Hergenröder, Spectrochimica Acta Part B: Atomic Spectroscopy **58**, 415 (2003).

131. F. Costache, S. Kouteva-Arguirova, and J. Reif, Applied Physics A **79**, 1429 (2004).

132. D. von der Linde and K. Sokolowski-Tinten, Applied Surface Science **154-155**, 1 (2000).

133. a. Borowiec and H. K. Haugen, Applied Physics Letters **82**, 4462 (2003).

134. B. Tan and K. Venkatakrishnan, Journal of Micromechanics and Microengineering **16**, 1080 (2006).

135. B. Tull, J. Carey, and E. Mazur, Mrs … **31**, 626 (2006).

136. B. Liu, Z. Hu, Y. Che, Y. Chen, and X. Pan, Applied Physics Letters **90**, 044103 (2007).

137. M. Murray, T. Toney Fernandez, B. Richards, G. Jose, and A. Jha, Applied Physics Letters **101**, 141107 (2012).

138. M. Murray, G. Jose, B. D. O. Richards, T. Toney Fernandez, and A. Jha, in *TMS2013 Spplemental*, edited by TMS (San Antonio, US, 2013).

139. M. Irannejad, G. Jose, A. Jha, and D. P. Steenson, Optical Materials **33**, 215 (2010).

140. M. Womack, M. Vendan, and P. Molian, Applied Surface Science **221**, 99 (2004).

141. I. Gordon, L. Carnel, D. Van Gestel, G. Beaucarne, and J. Poortmans, Progress in Photovoltaics: Research and Applications **15**, 575 (2007).

142. M. Yang, D. Huang, and P. Hao, Journal of Applied Physics **75**, 651 (1994).

143. D. Gracin, J. Sancho-Paramon, K. Juraić, a Gajović, and M. Ceh, Micron (Oxford, England : 1993) **40**, 56 (2009).

144. Z. Iqbal and S. Veprek, Journal of Physics C: Solid State Physics **377**, (1982).

145. G. Viera, S. Huet, and L. Boufendi, Journal of Applied Physics **90**, 4175 (2001).

146. V. Paillard, P. Puech, R. Sirvin, S. Hamma, and P. Roca i Cabarrocas, Journal of Applied Physics **90**, 3276 (2001).

147. C. Ossadnik, S. Vepvrek, and I. Gregora, Thin Solid Films **337**, 148 (1999).

148. E. Bustarret, M. Hachicha, and M. Brunel, Applied Physics Letters (1988).

149. D. Grojo, J. Hermann, and a. Perrone, Journal of Applied Physics **97**, 063306 (2005).

150. S. Stiffler, M. Thompson, and P. Peercy, Physical Review Letters **60**, 2519 (1988).

151. M. Brodsky, M. Cardona, and J. Cuomo, Physical Review B **16**, 3556 (1977).

152. J. Khajehpour, W. a. Daoud, T. Williams, and L. Bourgeois, The Journal of Physical Chemistry C **115**, 22131 (2011).

153. T. Oestereich, C. Swiatkowski, and I. Broser, Applied Physics Letters **56**, 446 (1990).

154. J. Tauc and a. Menth, Journal of Non-Crystalline Solids **8-10**, 569 (1972).

155. H. Search, C. Journals, A. Contact, M. Iopscience, and I. P. Address, Journal of Physics: Condensed Matter **10**, 1349 (1998).

156. M. Krishna and R. Friesner, The Journal of Chemical Physics **95**, 8309 (1991).

157. X. Zhao, O. Schoenfeld, S. Komuro, Y. Aoyagi, and T. Sugano, Physical Review B **50**, 18654 (1994).

158. J. Von Behren and T. Van Buuren, Solid State … **105**, 317 (1998).

159. B. Bahardoust, A. Chutinan, K. Leong, A. B. Gougam, D. Yeghikyan, T. Kosteski, N. P. Kherani, and S. Zukotynski, Physica Status Solidi (a) **207**, 539 (2010).

160. S. Guha, J. Y. United, and S. Ovonic, (2008).

161. M. V. Rama Krishna and R. A. Friesner, The Journal of Chemical Physics **95**, 8309 (1991).

162. W. Futako, K. Yoshino, C. M. Fortmann, and I. Shimizu, Journal of Applied Physics **85**, 812 (1999).

163. Y. Lifshitz, S. Kasi, J. Rabalais, and W. Eckstein, Physical Review B **41**, 10468 (1990).

164. F. R. Faller and a. Hurrle, IEEE Transactions on Electron Devices **46**, 2048 (1999).

165. V. Fthenakis, Renewable and Sustainable Energy Reviews **13**, 2746 (2009).

166. S. PIZZINI, M. ACCIARRI, S. BINETTI, D. CAVALCOLI, A. CAVALLINI, D. CHRASTINA, L. COLOMBO, E. GRILLI, G. ISELLA, and M. LANCIN, Materials Science and Engineering: B **134**, 118 (2006).

167. G. S. Bonett and R. M. Gerdes, Progress in Next-Generation Photovoltaic Devices, Iowa State, 2006.

168. C. Colinet, Journal of Alloys and Compounds **225**, 409 (1995).

169. a. B. Gokhale and G. J. Abbaschian, Bulletin of Alloy Phase Diagrams **9**, 574 (1988).

170. A. Gokhale, A. Munitz, and G. Abbaschian, Bulletin of Alloy Phase Diagrams **10**, 246 (1989).

171. A. Palenzona, P. Manfrinetti, S. Brutti, and G. Balducci, Journal of Alloys and Compounds **348**, 100 (2003).

172. a. B. Gokhale and G. J. Abbaschian, Bulletin of Alloy Phase Diagrams **9**, 582 (1988).

173. B. Chevalier, P. Lejay, J. Etourneau, and P. Hagenmuller, Solid State Communications **49**, 753 (1984).

174. M. Brandt, H. Fuchs, and M. Stutzmann, Solid State … **81**, 307 (1992).

175. D. Naturwissenschaften and J. Huh, (2010).

176. A. Campos and A. Meijerink, Journal of Physics and … **61**, 1489 (2000).

177. B. A. Andreev, Z. F. Krasil'nik, D. I. Kryzhkov, A. N. Yablonskii, V. P. Kuznetsov, T. Gregorkiewicz, and M. A. J. Klik, Physics of the Solid State **46**, 97 (2004).

178. P. G. Kik, M. J. a. de Dood, K. Kikoin, and a. Polman, Applied Physics Letters **70**, 1721 (1997).

179. F. Priolo, G. Franzò, S. Coffa, and A. Carnera, Physical Review B **57**, 4443 (1998).

180. J. Bonse, S. Baudach, J. Krüger, W. Kautek, and M. Lenzner, Applied Physics A: Materials Science & Processing **74**, 19 (2002).

181. C. Hnatovsky, R. S. Taylor, E. Simova, V. R. Bhardwaj, D. M. Rayner, and P. B. Corkum, Optics Letters **30**, 1867 (2005).

182. B. Corcoran, C. Monat, C. Grillet, D. J. Moss, B. J. Eggleton, T. P. White, L. O'Faolain, and T. F. Krauss, Nature Photonics **3**, 206 (2009).

183. K. Okamoto, Laser & Photonics Reviews **6**, 14 (2012).

184. A. Jha, P. Joshi, and S. Shen, Optics Express **16**, 13526 (2008).

185. a. R. Zanatta, Applied Physics Letters **82**, 1395 (2003).

186. J. S. Ha, C. H. Bae, S. H. Nam, S. M. Park, Y. R. Jang, K. H. Yoo, and K. Park, Applied Physics Letters **82**, 3436 (2003).

187. R. Teghil, D. Ferro, a Galasso, a Giardini, V. Marotta, G. Parisi, a Santagata, and P. Villani, Materials Science and Engineering: C **27**, 1034 (2007).

188. D. M. Hoffman, Polyhedron **13**, 1169 (1994).

189. Q. Yu, L. A. Jauregui, W. Wu, R. Colby, J. Tian, Z. Su, H. Cao, Z. Liu, D. Pandey, D. Wei, T. F. Chung, P. Peng, N. P. Guisinger, E. A. Stach, J. Bao, S.-S. Pei, and Y. P. Chen, Nature Materials **10**, 443 (2011).

190. K. Choy, Progress in Materials Science **48**, 57 (2003).

191. K. Petersen, U. Birkholz, and D. Adler, Physical Review B **8**, 1453 (1973).

192. M. Neumann-Spallart and C. Königstein, Thin Solid Films **265**, 33 (1995).

193. P. Temple and C. Hathaway, Physical Review B **7**, 3685 (1973).

194. R. V Volkov, D. M. Golishnikov, V. M. Gordienko, A. B. Savel'ev, and V. S. Chernysh, Quantum Electronics **35**, 33 (2005).

195. N. Burnham, D. Dominguez, R. Mowery, and R. Colton, Physical Review Letters **64**, 1931 (1990).

196. N. Da, a. a. Enany, N. Granzow, M. a. Schmidt, P. S. J. Russell, and L. Wondraczek, Journal of Non-Crystalline Solids **357**, 1558 (2011).

197. T. Chen, M.-S. Chiu, and C.-N. Weng, Journal of Applied Physics **100**, 074308 (2006).

198. E. Yildirim, in *Surface Chemistry of Solid and Liquid Interfaces*, 1st ed. (Wiley-Blackwell, Oxford, 2006), pp. 117–154.

199. F. Iskandar, L. Gradon, and K. Okuyama, Journal of Colloid and Interface Science **265**, 296 (2003).

200. J. Plateau, Philosophical Magazine Series 4 **14**, 1 (1857).

201. G. Xi, Y. Peng, W. Yu, and Y. Qian, Crystal Growth & Design 10 (2005).

202. T. D. Hatchard and J. R. Dahn, Journal of The Electrochemical Society **151**, A838 (2004).

203. E. Bustarret, M. A. Hachicha, and M. Brunel, Applied Physics Letters **52**, 1675 (1988).

204. J. Camacho, a. Cantarero, I. Hernández-Calderón, and L. González, Journal of Applied Physics **92**, 6014 (2002).

205. A. Pine and G. Dresselhaus, Physical Review B **4**, 356 (1971).

206. K. Ersching, C. E. M. Campos, J. C. de Lima, T. a. Grandi, S. M. Souza, D. L. da Silva, and P. S. Pizani, Journal of Applied Physics **105**, 123532 (2009).

207. G. Lucovsky, Physica Status Solidi (b) **49**, 633 (1972).

208. S. Hayashi, H. Sanda, M. Agata, and K. Yamamoto, Physical Review B **40**, (1989).

209. Z. Feng, S. Perkowitz, and P. Becla, Solid State Communications **78**, 1011 (1991).

210. W. Koch and S. K. Friedlander, Particle & Particle Systems Characterization **8**, 86 (1991).

211. J. M. Elzea, Clays and Clay Minerals **44**, 492 (1996).

212. R. Downs and D. Palmer, Am Mineral **79**, 9 (1994).

213. D. Hatch and S. Ghose, Physics and Chemistry of Minerals **17**, 554 (1991).

214. E. Janzén, Journal of Applied Physics **53**, 7367 (1982).

215. R. Espiau de Lamaestre, F. Jomard, J. Majimel, and H. Bernas, Journal of Non-Crystalline Solids **351**, 3031 (2005).

216. T. F. Lee, R. D. Pashley, T. C. McGill, and J. W. Mayer, Journal of Applied Physics **46**, 381 (1975).

217. B. Pajot, E. Artacho, C. A. J. Ammerlaan, and J.-M. Spaeth, Journal of Physics: Condensed Matter **7**, 7077 (1995).

218. R. Reynolds, D. Stroud, and D. Stevenson, Journal of The … **114**, (1967).

219. H. A. Schaeffer, J. Mecha, and J. Steinmann, Journal of the American Ceramic Society **62**, 343 (1979).

220. K. Reichelt and X. Jiang, Thin Solid Films **191**, 91 (1990).

221. G. Håkansson, L. Hultman, J.-E. Sundgren, J. E. Greene, and W.-D. Münz, Surface and Coatings Technology **48**, 51 (1991).

222. D. B. Laks, C. G. Van de Walle, G. F. Neumark, and S. T. Pantelides, Applied Physics Letters **63**, 1375 (1993).

223. B. Crowder and W. Hammer, Physical Review **150**, 541 (1966).

224. B. Cao and W. Cai, **28**, 680 (2008).

225. S. H. Dalal, D. L. Baptista, K. B. K. Teo, R. G. Lacerda, D. a Jefferson, and W. I. Milne, Nanotechnology **17**, 4811 (2006).

226. J. Lü, K. Huang, J. Zhu, X. Chen, X. Song, and Z. Sun, Physica B: Condensed Matter **405**, 3167 (2010).

227. R. Doremus, The Journal of Physical Chemistry **335**, 2212 (1964).

228. M. Naftaly, S. Shen, and a Jha, Applied Optics **39**, 4979 (2000).

229. Z. Zhang and J. Mu, Journal of Colloid and Interface Science **307**, 79 (2007).

230. L. D. Birkefeld, A. M. Azad, and S. A. Akbar, Journal of the American Ceramic Society **75**, 2964 (1992).

231. A. Jha, B. Richards, G. Jose, T. Teddy-Fernandez, P. Joshi, X. Jiang, and J. Lousteau, Progress in Materials Science **57**, 1426 (2012).

232. C. L. Du, Z. B. Gu, M. H. Lu, J. Wang, S. T. Zhang, J. Zhao, G. X. Cheng, H. Heng, and Y. F. Chen, Journal of Applied Physics **99**, 123515 (2006).

233. J. Reif, in *Laser-surface Interactions for New Materials Production*, edited by A. Miotello and P. M. Ossi (Springer Berlin Heidelberg, Berlin, Heidelberg, 2010), pp. 19–41.

234. F. Rollert, N. a. Stolwijk, and H. Mehrer, Materials Science and Engineering: B **18**, 107 (1993).

235. V. Sklyarchuk, Y. Plevachuk, S. Mudry, and I. Stec, Journal of Molecular Liquids **120**, 111 (2005).

236. D. S. Viswnath, T. K. Ghosh, D. H. L. Prasad, N. V. K. Dutt, and K. Y. Rani, *Viscosity of Liquids: Theory, Estimation, Experiment and Data* (Springer, Dordrecht, 2007), p. 575.

237. A. Kenyon, Current Opinion in Solid State and Materials Science **7**, 143 (2003).

238. S. Tanabe, Journal of Non-Crystalline Solids **259**, 1 (1999).

239. C. R. Giles and E. Desurvire, Journal of Lightwave Technology **9**, 271 (1991).

240. W. Liu, F. Xiu, K. Sun, Y.-H. Xie, K. L. Wang, Y. Wang, J. Zou, Z. Yang, and J. Liu, Journal of the American Chemical Society **132**, 2498 (2010).

241. Z. Fang, Y. Wang, D. Xu, Y. Tan, and X. Liu, Optical Materials **26**, 239 (2004).

242. Y. Yang, X. W. Sun, B. K. Tay, P. H. T. Cao, J. X. Wang, and X. H. Zhang, Journal of Applied Physics **103**, 064307 (2008).

243. S.-H. Jeong, B.-S. Kim, and B.-T. Lee, Applied Physics Letters **82**, 2625 (2003).

244. D. C. Reynolds, D. C. Look, and B. Jogai, Journal of Applied Physics **89**, 6189 (2001).

245. Y. Jun, C.-S. Choi, and J. Cheon, Chemical Communications **5769**, 101 (2001).

246. M. Shkir, G. Bhagavannarayana, M. a. Wahab, and K. K. Maurya, Optik - International Journal for Light and Electron Optics **124**, 1995 (2013).

247. A. Ebina and T. Takahashi, Journal of Crystal Growth **59**, 51 (1982).

248. B. D. O. Richards, Tellurite Glass Mid-infrared (1.9-2.1 Mm) Fibre Lasers, The university of Leeds, 2008.

249. G. Malovichko, V. Grachev, E. Kokanyan, and O. Schirmer, Physical Review B **59**, 9113 (1999).

250. G. Malovichko, V. Grachev, S. Okulov, E. Kokanyan, F. Henecker, a. Hofstaetter, and O. Schirmer, Physica Status Solidi (B) **243**, 409 (2006).

251. E. Rukmini and C. K. Jayasankar, Journal of Non-Crystalline Solids **176**, 213 (1994).

252. Y. Tian, R. Xu, L. Zhang, L. Hu, and J. Zhang, Journal of Applied Physics **108**, 083504 (2010).

253. R. Reisfeld and Y. Eckstein, Journal of Solid State Chemistry **5**, 174 (1972).

254. D. M. Gruen, The Journal of Chemical Physics **45**, 455 (1966).

255. V. K. Tikhomirov, M. Naftaly, and a. Jha, Journal of Applied Physics **86**, 351 (1999).

256. W. J. Miniscalco, Journal of Lightwave Technology **9**, 234 (1991).

257. A. Lidgard, A. Polman, D. C. Jacobsen, G. E. Blonder, R. Kistler, J. M. Poate, and P. C. Becker, Electronics Letters **27**, 993 (1991).

258. R. Y. C. Tsai, L. Qian, H. Alizadeh, and N. P. Kherani, Optics Express **17**, 21098 (2009).

259. A. Polman, Journal of Applied Physics **82**, 1 (1997).

260. J. T. Torvik, C. H. Qiu, R. J. Feuerstein, J. I. Pankove, and F. Namavar, Journal of Applied Physics **81**, 6343 (1997).

261. B. J. Dinerman and P. F. Moulton, Optics Letters **19**, 1143 (1994).